

# Slender-Body Hypervelocity Boundary-Layer Instability

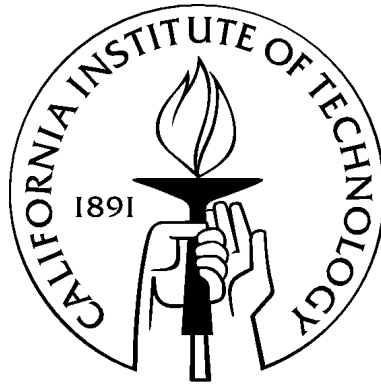
Thesis by

Nick Parziale

In Partial Fulfillment of the Requirements

for the Degree of

Doctor of Philosophy



California Institute of Technology

Pasadena, California

2013

(Submitted May 2013)

© 2013

Nick Parziale

All Rights Reserved

To Victoria, Susan, and Stephen

# Abstract

With novel application of optical techniques, the slender-body hypervelocity boundary-layer instability is characterized in the previously unexplored regime where thermochemical effects are important. Narrowband disturbances (500-3000 kHz) are measured in boundary layers with edge velocities of up to 5 km/s at two points along the generator of a 5 degree half angle cone. Experimental amplification factor spectra are presented. Linear stability and PSE analysis is performed, with fair prediction of the frequency content of the disturbances; however, the analysis over-predicts the amplification of disturbances. The results of this work have two key implications: 1) the acoustic instability is present and may be studied in a large-scale hypervelocity reflected-shock tunnel, and 2) the new data set provides a new basis on which the instability can be studied.

# Acknowledgements

Firstly, I would like to thank Joe Shepherd and Hans Hornung for the opportunity they afforded me in pursuing an advanced degree at Caltech. It was a privilege to work with them. They are accomplished scientists with “big” personalities; this made the work particularly rewarding because of the fun we had solving problems.

Without Bahram Valiferdowski, the quality of the work reported here would be comprised. Working with Bahram to make several key improvements to the tunnel-operation procedure helped make the experiments far more repeatable. I thank Bahram for more than his technical and engineering support, he is a close friend and it has been my pleasure to work with him.

I would like to thank Joe Jewell, my lab mate in T5. I have learned about many things from Joe, ranging from science to wine. His suggestions, efforts, and friendship have most certainly improved the quality of the work reported here, and my overall experience at Caltech. I would also like to thank Ivett Leyva for her support (including molybdenum nozzle throats and optical table legs) and friendship during my time at Caltech. Ross Wagnild of Sandia National Laboratories helped get the software package “STABL” running and provided valuable insight into boundary-layer stability calculations.

I would like to thank Guillaume Blanquart and Beverly McKeon for sitting on my thesis committee and the time they spent reviewing the work. In addition, Ravi Ravivhandran has been a mentor to me during my time at Caltech, and I thank him for that.

I would like to thank the members of the T5 and Explosion Dynamics Laboratory, past and present. It was my pleasure to work with Stuart Laurence on the shock surfing project. Also, Jason Damazo and I had many constructive conversations concerning high-speed imaging strategies. I became a close friend of Phil Boettcher's, and I am thankful for his encouragement. Sally Bane, Stephanie Coronel, Neal Bitter, Bryan Schmidt, and Remy Mevel have been a pleasure to work with.

At Caltech, I became close friends with Jon Mihaly, Jacob Notbolm, Jason Rabinovitch, Shannon Tronnick, Dan Turner-Evans, and Mumu Xu. In particular, I would like to thank Jason for his friendship and the time we spent working together on the 2013 Caltech Space Challenge and the Vertical Expansion Tube projects.

Tim Singler, Frank Cardullo, and James Pitarresi of SUNY Binghamton, and Walt Bruce of NASA Langley mentored, taught, and/or supported me early in my career, and I am grateful for that.

Without the base of support from my parents, Susan and Steven Parziale, and my brother and sister, Sabrina and Joseph Parziale, I would never have been able to come to Caltech. Frank Rampello, Chris Frlic, and Matt Moore have encouraged me from Long Island, and I thank them for that.

This work was an activity that was part of National Center for Hypersonic Laminar-Turbulent Research, sponsored by the "Integrated Theoretical, Computational, and Experimental Studies for Transition Estimation and Control" project supported by the U.S. Air Force Office of Scientific Research and the National Aeronautics and Space Administration (FA9552-09-1-0341).

Finally, I would like to thank Victoria Nardelli. She is everything.

# Contents

|  |            |
|--|------------|
| <b>Abstract</b>  | <b>iv</b>  |
| <b>Acknowledgements</b>  | <b>v</b>   |
| <b>Contents</b>  | <b>vii</b> |
| <b>List of Figures</b>   | <b>xi</b>  |
| <b>List of Tables</b>  | <b>xv</b>  |
| <b>1 Introduction</b>  | <b>1</b>   |
| 1.1 Design Implications of Boundary-Layer Transition . . . . . | 2          |
| 1.2 Paths to Transition and the Dominant Mechanism . . . . .   | 3          |
| 1.3 Geometrical Acoustic Motivation . . . . .                  | 6          |
| 1.3.1 Example Problems . . . . .                               | 8          |
| 1.3.2 High-Speed Boundary Layers . . . . .                     | 10         |
| 1.3.3 Summary . . . . .  | 15         |
| 1.4 Motivation For Hypervelocity Instability Study . . . . .   | 15         |
| 1.4.1 Energy Exchange and pdV Work . . . . .                   | 16         |
| 1.4.2 Simple Acoustic-Wave Attenuation Model . . . . .         | 18         |
| 1.5 Hypervelocity Transition in T5 . . . . .                   | 21         |
| 1.6 Project Scope and Outline . . . . .                        | 23         |

|          |   |           |
|----------|---|-----------|
| <b>2</b> | <b>Facility and Run Conditions</b>                        | <b>25</b> |
| 2.1      | Facility and Test Procedure . . . . .                     | 25        |
| 2.2      | Reservoir Conditions Calculation . . . . .                | 27        |
| 2.3      | Nozzle Calculation . . . . .                              | 28        |
| 2.3.1    | Nozzle Freezing Examples . . . . .                        | 29        |
| 2.4      | Cone Mean Flow Calculation . . . . .                      | 34        |
| 2.4.1    | Example Boundary-Layer Thicknesses . . . . .              | 34        |
| 2.4.2    | Comparison: DPLR to Similarity Solution . . . . .         | 35        |
| 2.4.3    | Thermo-Chemical Boundary-Layer Profiles . . . . .         | 38        |
| 2.5      | Uncertainty Estimate . . . . .                            | 42        |
| 2.5.1    | Reservoir Conditions Bias Uncertainty Estimate . . . . .  | 43        |
| 2.5.2    | Nozzle Calculation Bias Uncertainty Estimate . . . . .    | 44        |
| 2.5.3    | Cone Flow Calculation Bias Uncertainty Estimate . . . . . | 46        |
| 2.5.4    | Repeatability of Conditions . . . . .                     | 47        |
| <b>3</b> | <b>FLDI Measurement Technique</b>                         | <b>50</b> |
| 3.1      | Instability Measurement Technique Review . . . . .        | 50        |
| 3.2      | Focused Laser Differential Interferometry . . . . .       | 54        |
| 3.2.1    | Description of FLDI Setup . . . . .                       | 56        |
| 3.2.2    | Relation Between Density and Voltage . . . . .            | 57        |
| 3.2.3    | Bench Test: Evaluation of Sensitive Region . . . . .      | 60        |
| 3.2.4    | Bench Test: Equidistant Acoustic Wave . . . . .           | 61        |
| 3.2.5    | Integration Length Determination . . . . .                | 63        |
| 3.2.6    | Sensitivity to Wavelength . . . . .                       | 65        |
| 3.2.7    | Uncertainty Estimation . . . . .                          | 67        |
| <b>4</b> | <b>Results</b>  | <b>69</b> |
| 4.1      | Reflected-Shock Tunnel Noise Measurement . . . . .        | 69        |

|          |  |            |
|----------|--|------------|
| 4.1.1    | Motivation . . . . .   | 69         |
| 4.1.2    | Data . . . . .   | 71         |
| 4.1.3    | Discussion . . . . .   | 76         |
| 4.2      | Single Point FLDI Measurement . . . . .                      | 77         |
| 4.2.1    | Data . . . . .   | 77         |
| 4.2.2    | Discussion . . . . .   | 81         |
| 4.3      | Double Point FLDI Measurement - Development . . . . .        | 82         |
| 4.3.1    | Shock Tube Fill Gas Quality and Cleaning Procedure . . . . . | 83         |
| 4.3.2    | Data and Discussion . . . . .                                | 86         |
| 4.4      | Double Point FLDI Measurement - Air . . . . .                | 93         |
| 4.4.1    | Lower Enthalpy Conditions . . . . .                          | 94         |
| 4.4.2    | Higher Enthalpy Conditions . . . . .                         | 96         |
| 4.4.3    | Schlieren Visualization . . . . .                            | 99         |
| 4.5      | Double Point FLDI Measurement - N <sub>2</sub> . . . . .     | 100        |
| 4.5.1    | Lower Enthalpy Conditions . . . . .                          | 101        |
| 4.5.2    | Moderate Enthalpy Conditions . . . . .                       | 103        |
| 4.5.3    | Higher Enthalpy Conditions . . . . .                         | 105        |
| 4.5.4    | Schlieren Visualization . . . . .                            | 107        |
| 4.6      | Double Point FLDI Measurement - CO <sub>2</sub> . . . . .    | 108        |
| <b>5</b> | <b>Analysis</b>  | <b>112</b> |
| 5.1      | Experimental Amplification Factor . . . . .                  | 112        |
| 5.1.1    | Methodology . . . . .  | 112        |
| 5.1.2    | Uncertainty Estimate . . . . .                               | 114        |
| 5.1.3    | Results . . . . .  | 114        |
| 5.2      | PSE-Chem - Experiment Comparison . . . . .                   | 117        |
| 5.2.1    | Methodology . . . . .  | 117        |

|          |  |            |
|----------|--|------------|
| 5.2.2    | Results . . . . .  | 119        |
| <b>6</b> | <b>Conclusion</b>  | <b>131</b> |
| 6.1      | Introduction . . . . .                                       | 131        |
| 6.2      | Facility and Run Conditions . . . . .                        | 133        |
| 6.3      | FLDI Measurement Technique . . . . .                         | 133        |
| 6.4      | Results . . . . .  | 134        |
| 6.4.1    | Tunnel Noise . . . . .                                       | 134        |
| 6.4.2    | Single and Double Point FLDI Developement . . . . .          | 135        |
| 6.4.3    | Double Point FLDI Measurements . . . . .                     | 135        |
| 6.5      | Analysis . . . . .   | 136        |
|          | <b>Bibliography</b>  | <b>139</b> |
| <b>A</b> | <b>T5 Run Conditions</b>                                     | <b>157</b> |
| A.1      | Reservoir Conditions . . . . .                               | 157        |
| A.2      | Nozzle Exit Conditions . . . . .                             | 165        |
| A.3      | Edge Conditions . . . . .                                    | 169        |
| <b>B</b> | <b>Probe-Volume Locations and Boundary-Layer Thicknesses</b> | <b>173</b> |
| <b>C</b> | <b>Test-Section Vibration</b>                                | <b>176</b> |

# List of Figures

|      |   |    |
|------|---|----|
| 1.1  | Paths to Turbulence . . . . .   | 4  |
| 1.2  | Acoustic Mode in High-Speed Boundary Layer . . . . .                        | 5  |
| 1.3  | Comparison of Dominant Modes in a Supersonic Boundary Layer . . . . .       | 6  |
| 1.4  | Vector Addition for Tracing Acoustic Rays . . . . .                         | 8  |
| 1.5  | Goodman and Duykers Example Problem . . . . .                               | 10 |
| 1.6  | Munk Example Problem . . . . .  | 10 |
| 1.7  | Boundary-Layer Profiles for Geometric Acoustics . . . . .                   | 11 |
| 1.8  | Max Angles of Inclination for Acoustic Energy Trapping . . . . .            | 13 |
| 1.9  | Ray Traces for $M_E = 1$ . . . . .  | 13 |
| 1.10 | Ray Traces for $M_E = 6, T_W = T_{ad}$ . . . . .                            | 14 |
| 1.11 | Ray Traces for $M_E = 6, T_W = T_{ad}/10$ . . . . .                         | 14 |
| 1.12 | P-v Diagrams Illustrating Acoustic Absorption . . . . .                     | 18 |
| 1.13 | Relaxation Absorption Coefficient Time and Temperature Dependence . . . . . | 19 |
| 1.14 | Example Absorption Coefficient for CO <sub>2</sub> . . . . .                | 21 |
| 2.1  | T5 Schematic . . . . .  | 26 |
| 2.2  | Example Reservoir Pressure and Shock Timing Traces for Shot 2789 . . . . .  | 28 |
| 2.3  | Outline of Contoured Nozzle . . . . .                                       | 29 |
| 2.4  | Nozzle Calculation for Air. . . . .   | 30 |
| 2.5  | Nozzle Calculation for CO <sub>2</sub> . . . . .                            | 31 |
| 2.6  | Nozzle Calculation for N <sub>2</sub> . . . . .                             | 32 |

|      |   |    |
|------|---|----|
| 2.7  | Example Computed Boundary-Layer Thicknesses . . . . .                     | 34 |
| 2.8  | Example Velocity Profiles . . . . .                                       | 36 |
| 2.9  | Example Temperature Profiles . . . . .                                    | 37 |
| 2.10 | Evolution of Mass Fractions . . . . .                                     | 38 |
| 2.11 | Evolution of Temperature . . . . .  | 40 |
| 2.12 | $u \pm a$ Profiles. . . . .   | 42 |
| 2.13 | Overlay of the Computed Density, Cone, Shock, and Streamlines . . . . .   | 45 |
| 2.14 | Zoomed-in Presentation of Density Contours in Nozzle. . . . .             | 45 |
| 2.15 | Wall-Normal Distance from the Cone vs. the Radius in the Nozzle . . . . . | 46 |
| 2.16 | Examples of Repeatability . . . . .                                       | 48 |
| 3.1  | Annotated Schematic of the FLDI . . . . .                                 | 55 |
| 3.2  | Boundary-Layer Thickness and Beam Profile . . . . .                       | 59 |
| 3.3  | Bench Test Schematic and Results: Sensitive Region . . . . .              | 61 |
| 3.4  | Bench Test Schematic and Results: Equidistant Acoustic Wave . . . . .     | 62 |
| 3.5  | Density Eigenfunction and FLDI Probe Volume Sensitivity . . . . .         | 63 |
| 3.6  | Averaged Density Eigenfunction and Response Function . . . . .            | 65 |
| 3.7  | Sensitivity to Wavelength . . . . .                                       | 66 |
| 4.1  | Sources of Wind-Tunnel Noise . . . . .                                    | 70 |
| 4.2  | Tunnel Noise Time Traces . . . . .  | 72 |
| 4.3  | Frequency Spectrum of Tunnel Noise Time Traces . . . . .                  | 73 |
| 4.4  | Wavelength Spectrum of Tunnel Noise Time Traces . . . . .                 | 74 |
| 4.5  | Spectrogram of Tunnel Noise . . . . .                                     | 75 |
| 4.6  | Single Point FLDI Results Shot 2695 . . . . .                             | 78 |
| 4.7  | Single Point FLDI Results Shot 2702 . . . . .                             | 79 |
| 4.8  | Single Point FLDI Results Shot 2702 - Zoomed Time Trace . . . . .         | 80 |
| 4.9  | Spectrograms Showing Particulate Impact . . . . .                         | 84 |

|      |   |     |
|------|---|-----|
| 4.10 | Gas Opacity . . . . .   | 86  |
| 4.11 | Windowed Spectra Shot 2711 . . . . .                                      | 87  |
| 4.12 | Windowed Spectra Shot 2743 . . . . .                                      | 88  |
| 4.13 | Narrowband vs. Broadband Disturbance . . . . .                            | 88  |
| 4.14 | Cross-Correlations, Shots 2711, 2743 . . . . .                            | 89  |
| 4.15 | Spectrograms of Shot 2711 . . . . .                                       | 90  |
| 4.16 | Spectrograms of Shot 2743 . . . . .                                       | 91  |
| 4.17 | Spectra For Shots 2711 and 2743 . . . . .                                 | 92  |
| 4.18 | Traces and Cross-Correlations, Air, Low Enthalpy . . . . .                | 94  |
| 4.19 | PSD Estimates, Air, Low Enthalpy . . . . .                                | 96  |
| 4.20 | Traces and Cross-Correlations, Air, High Enthalpy . . . . .               | 97  |
| 4.21 | PSD Estimates, Air, High Enthalpy . . . . .                               | 98  |
| 4.22 | Schlieren Image of Instability in Air . . . . .                           | 100 |
| 4.23 | Traces and Cross-Correlations, N <sub>2</sub> , Low Enthalpy . . . . .    | 102 |
| 4.24 | PSD Estimates, N <sub>2</sub> , Low Enthalpy . . . . .                    | 103 |
| 4.25 | Traces and Cross-Correlations, N <sub>2</sub> , Medium Enthalpy . . . . . | 104 |
| 4.26 | PSD Estimates, N <sub>2</sub> , Medium Enthalpy . . . . .                 | 105 |
| 4.27 | Traces and Cross-Correlations, N <sub>2</sub> , High Enthalpy . . . . .   | 106 |
| 4.28 | PSD Estimates, N <sub>2</sub> , High Enthalpy . . . . .                   | 106 |
| 4.29 | Schlieren Image of Instability in N <sub>2</sub> . . . . .                | 108 |
| 4.30 | Traces and Cross-Correlations, CO <sub>2</sub> . . . . .                  | 109 |
| 4.31 | PSD Estimates, CO <sub>2</sub> . . . . .                                  | 110 |
| 5.1  | Amplification Factor SNR . . . . .  | 114 |
| 5.2  | Experimental Amplification Factor - All Shots . . . . .                   | 115 |
| 5.3  | Experimental Amplification Factor - Selected Shots . . . . .              | 117 |
| 5.4  | Amplification Factor Calculation Methodology . . . . .                    | 119 |
| 5.5  | Computational-Experimental Comparison, Air Low Enthalpy . . . . .         | 121 |

|      |   |     |
|------|---|-----|
| 5.6  | Computational-Experimental Comparison, N <sub>2</sub> Low Enthalpy . . . . .  | 123 |
| 5.7  | Computational-Experimental Comparison, CO <sub>2</sub> . . . . .              | 124 |
| 5.8  | Computational-Experimental Comparison, N <sub>2</sub> High Enthalpy . . . . . | 125 |
| 5.9  | Computational-Experimental Comparison, Air High Enthalpy . . . . .            | 127 |
| 5.10 | $U_E/(2\delta)$ Scaling . . . . .   | 129 |
| C.1  | Test Section Vibration . . . . .  | 176 |

# List of Tables

|      |   |     |
|------|---|-----|
| 1.1  | Characteristic Thermo-chemical Energies . . . . .                         | 16  |
| 2.1  | Uncertainty in Reservoir Conditions . . . . .                             | 43  |
| 2.2  | Uncertainty in Nozzle Conditions . . . . .                                | 46  |
| 2.3  | Uncertainty in Edge Conditions . . . . .                                  | 47  |
| 2.4  | Shot Series Data from Hornung (1992) . . . . .                            | 47  |
| 4.1  | Run Conditions - Tunnel Noise . . . . .                                   | 72  |
| 4.2  | RMS Tunnel Noise . . . . .  | 75  |
| 4.3  | Run Conditions - Single Point FLDI . . . . .                              | 80  |
| 4.4  | Single Point Edge Conditions . . . . .                                    | 81  |
| 4.5  | Double Point Edge Conditions - Dev. . . . .                               | 86  |
| 4.6  | Double Point Dev. Boundary Layer Instability Scaling . . . . .            | 93  |
| 4.7  | Double Point Edge Conditions - Dev. . . . .                               | 93  |
| 4.8  | Double Point Air Boundary Layer Instability Scaling . . . . .             | 99  |
| 4.9  | Double Point Edge Conditions - N <sub>2</sub> . . . . .                   | 101 |
| 4.10 | Double Point N <sub>2</sub> Boundary Layer Instability Scaling . . . . .  | 107 |
| 4.11 | Double Point Edge Conditions - CO <sub>2</sub> . . . . .                  | 108 |
| 4.12 | Double Point CO <sub>2</sub> Boundary Layer Instability Scaling . . . . . | 111 |
| 5.1  | Amplification Factor Data Summary . . . . .                               | 115 |
| A.1  | Tunnel Noise Tunnel Run Parameters . . . . .                              | 157 |

|      |   |     |
|------|---|-----|
| A.2  | Tunnel Noise Reservoir Conditions . . . . .                             | 158 |
| A.3  | Single Point Tunnel Run Parameters . . . . .                            | 158 |
| A.4  | Single Point Reservoir Conditions . . . . .                             | 158 |
| A.5  | Double Point Tunnel Run Parameters - Dev 1 Air . . . . .                | 159 |
| A.6  | Double Point Reservoir Conditions - Dev 1 Air . . . . .                 | 159 |
| A.7  | Double Point Tunnel Run Parameters - Dev 1 CO <sub>2</sub> . . . . .    | 159 |
| A.8  | Double Point Reservoir Conditions - Dev 1 CO <sub>2</sub> . . . . .     | 160 |
| A.9  | Double Point Tunnel Run Parameters - Dev 2 Air . . . . .                | 160 |
| A.10 | Double Point Reservoir Conditions - Dev 2 Air . . . . .                 | 160 |
| A.11 | Double Point Tunnel Run Parameters - Dev 2 CO <sub>2</sub> . . . . .    | 161 |
| A.12 | Double Point Reservoir Conditions - Dev 2 CO <sub>2</sub> . . . . .     | 161 |
| A.13 | Double Point Tunnel Run Parameters - Air . . . . .                      | 162 |
| A.14 | Double Point Reservoir Conditions - Air . . . . .                       | 162 |
| A.15 | Double Point Tunnel Run Parameters - N <sub>2</sub> . . . . .           | 163 |
| A.16 | Double Point Reservoir Conditions - N <sub>2</sub> . . . . .            | 163 |
| A.17 | Double Point Tunnel Run Parameters - CO <sub>2</sub> - AR:100 . . . . . | 164 |
| A.18 | Double Point Reservoir Conditions - CO <sub>2</sub> - AR:100 . . . . .  | 164 |
| A.19 | Tunnel Noise Nozzle Exit Conditions . . . . .                           | 165 |
| A.20 | Single Point Nozzle Exit Conditions . . . . .                           | 165 |
| A.21 | Double Point Nozzle Exit Conditions - Dev 1 Air . . . . .               | 166 |
| A.22 | Double Point Nozzle Exit Conditions - Dev 1 CO <sub>2</sub> . . . . .   | 166 |
| A.23 | Double Point Nozzle Exit Conditions - Dev 2 Air . . . . .               | 166 |
| A.24 | Double Point Nozzle Exit Conditions - Dev 2 CO <sub>2</sub> . . . . .   | 167 |
| A.25 | Double Point Nozzle Exit Conditions - Air . . . . .                     | 167 |
| A.26 | Double Point Nozzle Exit Conditions - N <sub>2</sub> . . . . .          | 168 |
| A.27 | Double Point Nozzle Exit Conditions - CO <sub>2</sub> . . . . .         | 168 |
| A.28 | Single Point Edge Conditions . . . . .                                  | 169 |

|      |   |     |
|------|---|-----|
| A.29 | Double Point Edge Conditions - Dev 1 Air . . . . .              | 169 |
| A.30 | Double Point Edge Conditions - Dev 1 CO <sub>2</sub> . . . . .  | 170 |
| A.31 | Double Point Edge Conditions - Dev 2 Air . . . . .              | 170 |
| A.32 | Double Point Edge Conditions - Dev 2 CO <sub>2</sub> . . . . .  | 171 |
| A.33 | Double Point Edge Conditions - Air . . . . .                    | 171 |
| A.34 | Double Point Edge Conditions - N <sub>2</sub> . . . . .         | 172 |
| A.35 | Double Point Edge Conditions - CO <sub>2</sub> . . . . .        | 172 |
| B.1  | Probe Volume Locations and Boundary-Layer Thicknesses . . . . . | 173 |

# Chapter 1

## Introduction

The study of boundary-layer transition (BLT) on hypersonic vehicles has been a subject of research for approximately a half century. Such continued support is indicative of the intricate and potentially rewarding nature of the topic. Knowing the state of the boundary layer is critical to the design of the vehicle.<sup>1</sup> The surface heating rate and skin friction are several times higher when the boundary layer has transitioned from laminar to turbulent. The primary design implications are that the thermal protection system must be more massive and the drag is increased when the boundary layer is turbulent. The current state of the art is to design a vehicle conservatively by sizing the thermal protection system over the entire vehicle to meet the requirements of turbulent boundary-layer heating rates. This is in large part due to the lack of a reliable transition location prediction tool. The growth of the disturbances in the boundary layer that precede transition is poorly understood, particularly at conditions where gas dissociation and vibrational excitation must be considered. A clearer understanding of the amplification process of disturbances in the boundary layer in this flight regime would allow for a more intelligent sizing of thermal protection systems. In this work, the acoustic boundary-layer instability is characterized with novel application of optical techniques in the previously unexplored regime where

---

<sup>1</sup>Reviews of the influence of BLT on high-speed vehicle design can be found in [Schneider \(2004\)](#), [Schmisser and Erbland \(2012\)](#), [Lau \(2008\)](#), and [Lin \(2008\)](#), the first offers an academic perspective, the second offers governmental perspective, and the last two offer perspectives from industry.

thermo-chemical effects are important.

## 1.1 Design Implications of Boundary-Layer Transition

A case study of such design implications is the apparent weight and cost savings on the National Aerospace Plane (NASP). The NASP was intended to be a single stage to orbit vehicle, capable of transporting people by “tak[ing] off from Dulles Airport, accelerat[ing] up to 25 times the speed of sound, attaining low Earth orbit or flying to Tokyo within 2 hours” (Reagan, 1986).

The questions surrounding transition prediction were made apparent in a report from the Defense Science Review Board on the NASP in 1988, “[t]he largest uncertainty is the location of the point of transition from laminar to turbulent flow. Estimates range from 20% to 80% along the body span. That degree of uncertainty significantly affects the flow conditions at the engine inlet, aerodynamic heat transfer to the structure and skin friction. These in turn affect estimates of engine performance, structural heating and drag. The assumption made for the point of transition can affect the design vehicle gross take off weight by a factor of two or more... In view of the potential impact of uncertainties in the transition location, this is by far the single area of greatest technical risk in the aerodynamics of the NASP program” (DSB, 1988). Prior to the NASP program’s cancellation in 1993, the Defense Science Review Board once again named boundary-layer transition as a critical area of fundamental uncertainty, “[b]oundary layer transition and scramjet performance cannot be validated in existing ground test facilities...” (DSB, 1992).

With certainty it can be said that BLT was a technical issue for the NASP and played some role in the program trajectory, which was funded with a total of  $\approx 1.69$

billion USD from FY 1985-1993.<sup>2</sup>

## 1.2 Paths to Transition and the Dominant Mechanism

The path to transition in boundary layers is a subtle subject. [Reshotko \(2008\)](#) notes that “[u]ntil about [1995], the predominant view of laminar-turbulent transition was centered around the slow linear amplification of exponentially growing (“modal”) disturbances..., preceded by a receptivity process to the disturbance environment and followed by secondary instabilities, further nonlinearity, and finally a breakdown to a recognizable turbulent flow.” [Reshotko \(2008\)](#) goes on to say that “[t]his picture had to be urgently reconsidered in the early 1990s with the emergence of a literature on transient growth,” which was motivated by the fact that “there are transition phenomena in flows that are linearly stable.” A flow-chart describing the paths to turbulence was devised by [Morkovin et al. \(1994\)](#), where focus is placed on understanding the subtleties of this process (Fig. 1.1, taken from [Fedorov \(2011\)](#)). In chapter 9 of [Schmid and Henningson \(2001\)](#) there is a thorough explanation of the developments on this topic.

For a sharp, slender body in low-speed flight, at zero angle of attack, [Tollmien-Schlichting](#) waves (“T-S waves”) are observed to be of large amplitude prior to boundary-layer transition; these disturbances were experimentally characterized by [Schubauer and Skramstad \(1948\)](#). This is in contrast to high-speed boundary layers on the same vehicle geometry, where a key instability mechanism is the high-frequency modes discovered by [Mack \(1984\)](#). These modes are primarily acoustic in nature, are always present if the boundary-layer edge Mach number is sufficiently large, and

---

<sup>2</sup>The funding figures can be found in [Schwelkart \(1997\)](#), which references the NASP Joint Program Office; he documents the NASP program from a historian’s perspective.

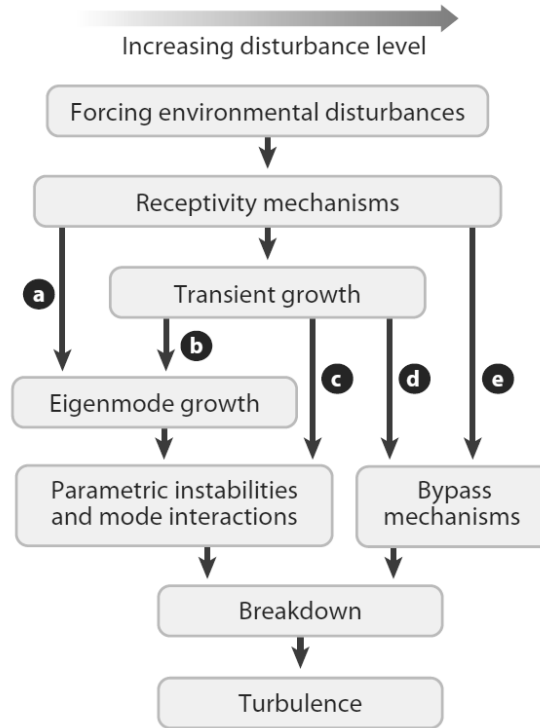


Figure 1.1: Flow-chart describing the paths to turbulence was devised by Morkovin et al. (1994), taken from Fedorov (2011) with permission.

can be the dominant instability mechanism when the wall temperature is sufficiently low compared to the recovery temperature. “They belong to the family of trapped acoustic waves. Owing to the presence of a region of supersonic mean flow relative to the disturbance phase velocity, the boundary layer behaves as an acoustic waveguide (schematically shown in [Fig. 1.2])” Fedorov (2011). Fedorov (2011) goes on to provide a thorough explanation of “Path A” in Fig. 1.1 for the case of high-speed boundary layers, supporting his conclusions of how the disturbances develop with detailed stability calculations.

Mack termed the dominant higher frequency mode the “second mode,” although Fedorov and Tumin (2011) suggest “that Mack’s definitions of modes are inconsistent with conventional usage of the term normal modes.” However, most researchers continue to use the terminology “second mode” to refer to the fast growing acoustic

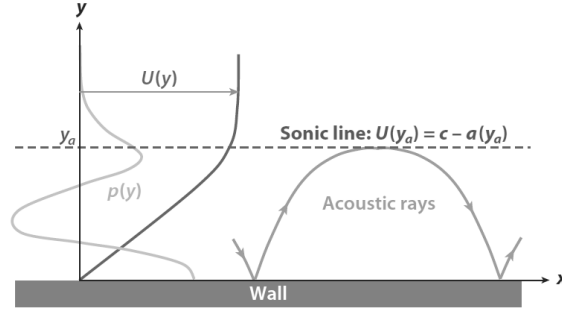


Figure 1.2: “Acoustic mode in a high-speed boundary layer, where  $U(y)$  is the mean-flow profile, and  $p(y)$  is the pressure disturbance profile.” reproduced from Fedorov (2011) with permission. The sonic line refers to where the local velocity ( $U(y)$ ) equals the difference between the disturbance phase speed ( $c$ ) and the local sound speed ( $a(y)$ ). This is the location of the critical layer, where disturbance amplitudes are typically large Mack (1984), Fedorov (2011).

instability discovered by Mack, and this is the terminology usage in this thesis. The larger growth rate of the acoustic instability relative to the “T-S waves” is seen in Fig. 1.3(a). Additionally, it is seen that the second mode of largest growth rate is two dimensional in nature. This second mode is the subject of study in this work. In Fig. 1.3(b), a linear stability diagram is shown for an example case in T5. The stream-wise imaginary wavenumber is shaded for values above 0, and more darkly for larger values. Note the exceedingly high frequency of the acoustic mode, and the narrowband at which it is most amplified. The most strongly amplified frequency is observed to decrease with increasing distance from the tip of the cone; this frequency is approximately equal to  $KU_E/(2\delta)$ , where  $K$  is a constant of proportionality,  $U_E$  is the edge velocity, and  $\delta$  is the boundary-layer thickness,<sup>3</sup> this scaling is shown in Fig. 1.3(b) as a thin white line. The constant of proportionality ( $K$ ) for a certain geometry is a function of (among other things) edge Mach number, because of the implication on disturbance-phase velocity (Fig. 9.1 of Mack (1984)), and boundary-layer temperature profile, because of the implication on disturbance wave number (Fig. 10.9

<sup>3</sup>In this work,  $\delta$  refers to  $\delta_{99}$ , where the local velocity in the boundary layer is 99% of the velocity at the boundary-layer edge.

of Mack (1984)). The theoretical framework for the scaling of the most strongly amplified frequency can be found in Mack (1984, 1987); experimental support of this scaling can be found in Kendall (1975), Demetriades (1977) and Stetson et al. (1983, 1984, 1989) (among many other reports). This scaling is extended to hypervelocity conditions in this work.

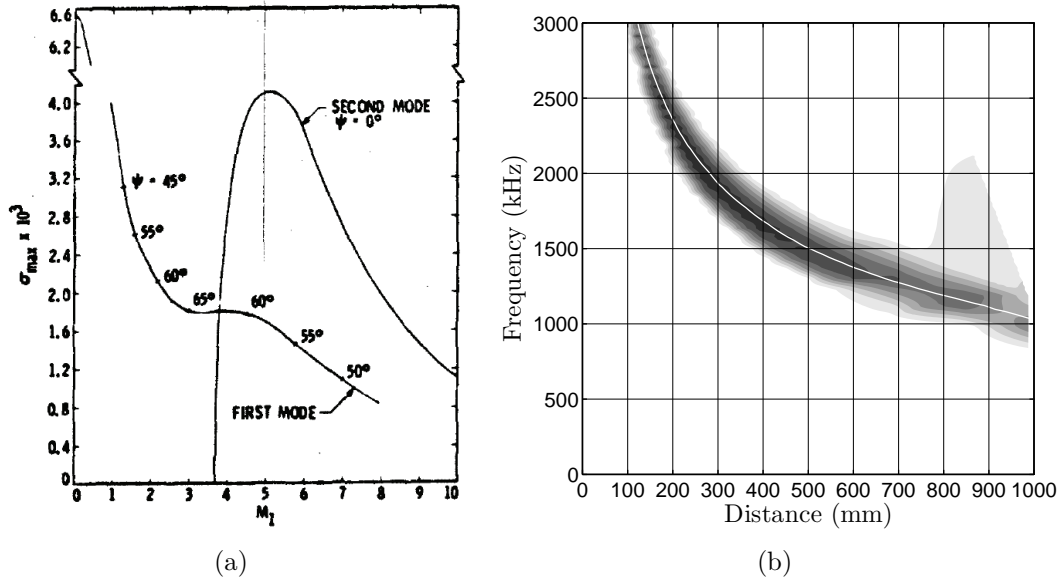


Figure 1.3: a: “Effect of Mach number of the maximum spatial amplification rate of the first and second mode waves... Insulated wall, wind-tunnel temperatures” Mack (1984). At above Mach 4 the acoustic mode, which is two dimensional in nature, dominates the first mode. b: Example linear stability diagram computed from PSE-Chem for flow over a 5 degree half-angle cone, as in shot 2789 in T5. The stream-wise imaginary wavenumber is shaded for unstable values, and more darkly for more unstable values. The  $KU_E/(2\delta)$  scaling of the most amplified frequency is shown as a thin white line, where  $K$  is a constant of proportionality that can range from 0.6-1.1.

### 1.3 Geometrical Acoustic Motivation<sup>4</sup>

In this section the acoustic instability is examined with a geometrical acoustic approach. The propagation of acoustic waves within the boundary layer is profoundly

<sup>4</sup>This material is adapted from Parziale et al. (2013b).

influenced by the velocity and sound speed gradients created by the action of viscosity and heat conduction within the layer. These gradients form a waveguide that may trap acoustic waves and provide a mechanism for the formation of large amplitude disturbances. This suggests that geometrical acoustic analysis of these waveguides can provide insights into the potential for boundary-layer acoustic instability. Here, we outline the basics of geometric acoustics, apply the ray-tracing technique to example problems, and then to high-speed boundary layers. The refractive behavior of different high-speed boundary-layer profiles is compared.

The approach follows the classical ray-tracing approach to geometrical acoustics in which the propagation of a wave-front is calculated by computing the paths (rays) along which a point on the wave-front moves (Pierce, 1989, Thompson, 1972). From a physical point of view, geometrical acoustics is a high-frequency approximation that is valid when: 1) the wavelengths are small compared to the geometrical features in the flow, in this case the thickness of the boundary layer; 2) the amplitude and front curvature do not vary too rapidly along the wave-front; 3) cusps or folds (caustics) do not form in the wave-front. In high-speed boundary-layer profiles, the most amplified acoustic wavelength is known to be approximately 2 boundary-layer thicknesses (Mack, 1984) and caustics are known to form (G. A. Kriegsmann and E. L. Reiss) so we acknowledge from the outset that our results may be limited in quantitative applicability and will be more qualitative in nature.

The rate of change of the position of a point  $x_p$  on the wave-front can be written as,

$$\frac{dx_{pi}}{dt} = n_i c + v_i = v_{ray,i} \quad (1.1)$$

where  $v_i$  is the local velocity,  $c$  is the local sound speed, and  $n_i$  is the unit normal to the wave-front  $\tau_i$  (Fig. 1.4). The speed of the wave-front normal to itself ( $c + n_i v_i$ ) is in general different than the magnitude of the ray velocity  $|n_i c + v_i|$ . The evolution of the unit normal  $n_i$  is cumbersome to compute directly, so the formulation by Pierce

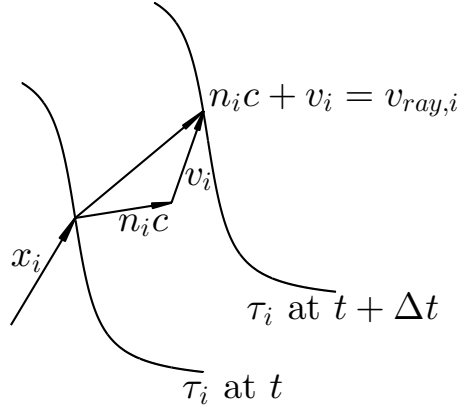


Figure 1.4: Vector addition to find the velocity of the rays.

(1989) is used where the wave-front is described in terms of the wave-slowness vector

( $s_i = \nabla\tau_i$ ),

$$\frac{dx_i}{dt} = \frac{c^2 s_i}{\Omega} + v_i, \quad (1.2a)$$

$$\frac{ds_i}{dt} = -\frac{\Omega}{c} \frac{dc}{dx_i} - \sum_{j=1}^3 s_j \frac{dv_j}{dx_i}, \quad (1.2b)$$

where,

$$\Omega = 1 - v_i s_i, \quad (1.3a)$$

$$s_i = \frac{n_i}{c + n_i v_i}. \quad (1.3b)$$

### 1.3.1 Example Problems

Solutions to two example problems are presented here to provide basic insight into geometric acoustics as well as to test our numerical methods. The first test problem is an adaptation from the work of [Goodman and Duykers \(1962\)](#). Analytic solutions for ray paths are found for a quiescent gas with a parabolic sound speed profile of the form  $c = c_0 + \alpha^2 y^2$ , with  $1/c^2 = (1/c_0^2)(1 - y^2/L^2)$ , and  $L = \sqrt{c_0/2\alpha^2}$ . In the

example presented here,  $c_0 = 340$  m/s,  $\alpha = \sqrt{c_0/10}$ , and a rigid boundary at  $y = 0$  is imposed. The solution for a ray path with initial angle of inclination to the horizontal  $\theta_0$ , is

$$y/L = \sin \theta_0 \sin (x/(L \cos \theta_0)). \quad (1.4)$$

This solution (solid line) and results from numerically integrating Eqs. 1.2 (circular markers) are shown to agree favorably in Fig. 1.5. In this scenario,  $s_x$  is a constant, per Eq. 1.2b. To calculate the point at which acoustic rays are refracted back to the surface, it is recognized that the ray direction is parallel to the unit normal,  $n$ , when horizontal (Pierce, 1989), and from Eq 1.3b,

$$s_x = \frac{\cos \theta_0}{c_0 + \cos \theta_0 v_{x0}} = c_h + v_{xh}, \quad (1.5)$$

where the subscript 0 indicates the local value at ray origin, and the subscript  $h$  indicates the local value where the ray is horizontal. Using this observation, the wall-normal distance where the ray is refracted back to the surface can be obtained algebraically. The predicted height (dashed line) shows favorable agreement with the analytic and numerical results in Fig. 1.5. Note that the acoustic rays are refracted towards a sound speed minimum, consistent with the vertical component of Eq. 1.2b.

The second test problem is ray-tracing through the Sound Fixing and Ranging (SOFAR) channel, as previously computed by Munk (1974), who assumed that the sound speed in the ocean,  $c$ , varies as  $c = c(y) = c_1(1 + \epsilon(\eta(y) + e^{-\eta(y)} - 1))$ , due to temperature and density gradients, where  $c_1 = 1.492$  km/s,  $\epsilon = 0.0074$ ,  $\eta = \eta(y) = (z - z_1)/(z_1/2)$ , and  $z_1 = 1.3$  km. Numerical integration of Eqs. 1.2 with this sound speed profile gives reasonable visual agreement with Munk's results, although precise quantitative comparison is not possible (Fig. 1.6). Acoustic rays are observed to be refracted to a sound speed minimum, which is consistent with Eq. 1.2b.

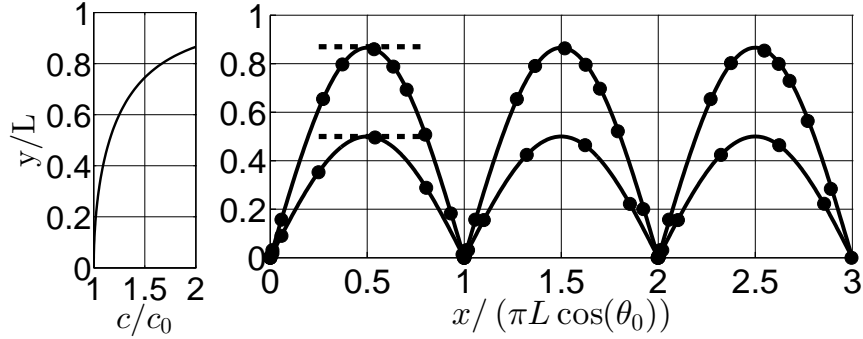


Figure 1.5: A slight modification to the problem posed by Goodman and Duykers (1962), with the analytical solution (solid line), numerical integration (circular markers), and predicted turning height (dashed line) showing good agreement. Initial angle of inclination of acoustic ray to the surface:  $\theta_0 = 30^\circ, 60^\circ$ . The sound speed profile is plotted on the left.

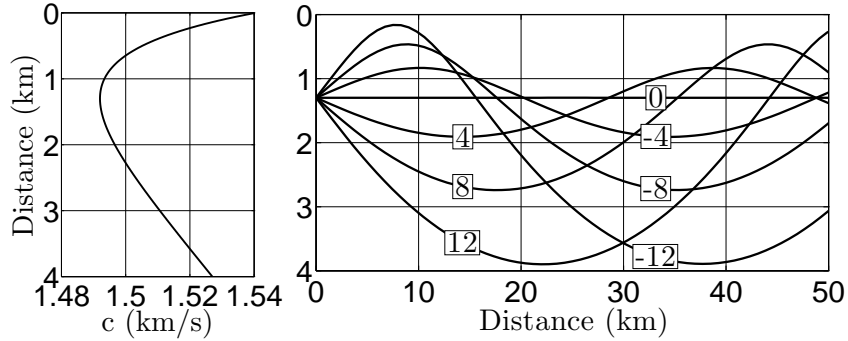


Figure 1.6: Replication of the case done by Munk (1974), tracing acoustic rays through the SOFAR channel. The ordinate marks depth from the ocean surface, and the initial angle of the ray to the horizontal is denoted in degrees by a number overlaid on the line.

### 1.3.2 High-Speed Boundary Layers

Geometric acoustic implications for a selection of high-speed boundary-layer profiles are presented in this section. Boundary-layer profiles are computed using the similarity solution for a laminar, compressible, perfect-gas flow on a flat plate (White, 2006). It was noted in the previous section that acoustic rays tend to be refracted towards sound speed minima. The mean flow of the boundary layer modifies this and the rays are refracted towards  $u + c$  minima, consistent with the vertical component of Eq. 1.2b. Three different profiles are presented in Figs. 1.7(a), 1.7(b), and 1.7(c)

to illustrate a range of  $u + c$  profiles that are possible.

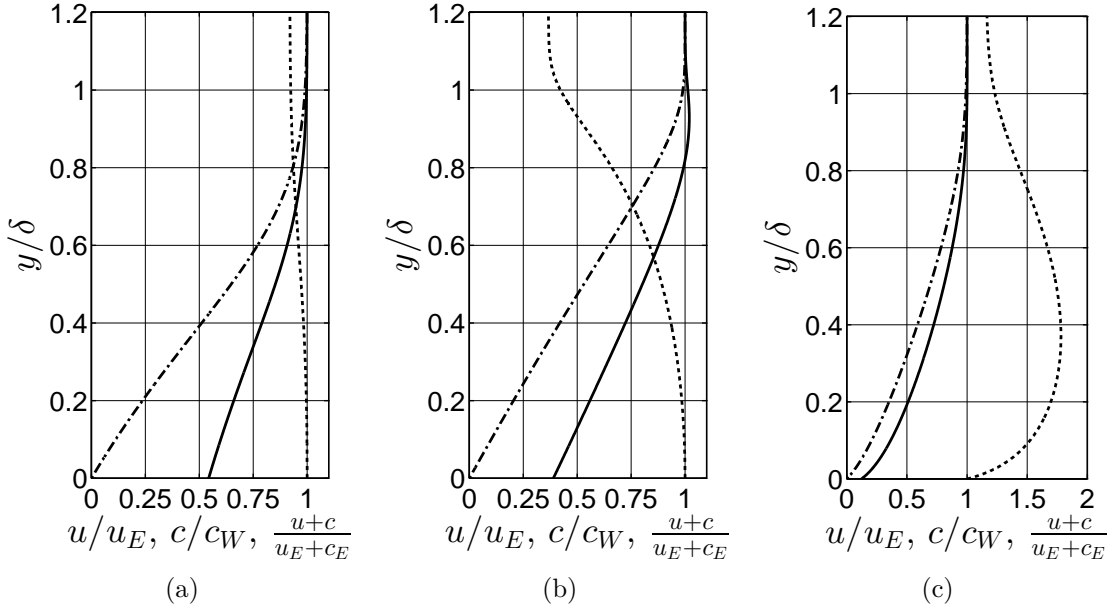


Figure 1.7: a: Boundary-layer profile for  $M_E = 1$ ,  $\gamma = 7/5$ ,  $T_W = T_{ad}$ . b: Boundary-layer profile for  $M_E = 6$ ,  $\gamma = 7/5$ ,  $T_W = T_{ad}$ . c: Boundary-layer profile for  $M_E = 6$ ,  $\gamma = 7/5$ ,  $T_W = T_{ad}/10$ . Each velocity profile ( $u/u_E$ ) is normalized by the edge value (dash-dot). Each sound speed profile  $c/c_W$  is normalized by the value at the wall (dashed). Each combined profile  $(u + c)/(u_E + c_E)$  is normalized by the edge values (solid).

Using Eq. 1.5, and assuming that the flow is locally parallel, the maximum angle that is refracted back to the surface can be found. We postulate that the larger this angle, the more unstable the boundary layer due to the larger amount of acoustic energy trapped within the layer. The maximum angle of inclination is computed for rays originating at the surface of the plate for a range of Mach numbers ( $M_E = 0.25-8$ ) with an adiabatic wall and three different ratios of specific heats in Fig. 1.8(a). The maximum angle increases with increasing Mach number, reaching a constant value for  $M_E \geq 5$ . Wall temperature ratio ( $T_W/T_{ad}$ , where  $T_{ad}$  is the adiabatic wall temperature) is another important parameter in determining the maximum initial angle of inclination for rays originating at the surface of the plate (Fig. 1.8(b)); at  $M_E = 6$ , colder walls are observed to trap more acoustic rays. In Fig. 1.8(c), the

wall normal distance of the origin of the acoustic ray is varied for an adiabatic plate with  $M_E = 6$ . Fewer rays are trapped as the ray origin is translated from the surface. The results in Figs. 1.8(a), 1.8(b), and 1.8(c) do not change with  $Re_x$ , where  $x$  is the distance from the leading edge, because the flow field is assumed to be locally parallel and the boundary-layer profiles are self-similar.

The non-parallel nature of the flow field can be included by interpolating the velocity and sound speed profiles calculated from the similarity solution for a certain range of  $Re_x$  and solving Eqs. 1.2. In Fig. 1.9, ray traces originating from the surface of an adiabatic flat plate with  $M_E = 1$  and  $\gamma = 7/5$  with an initial angle of inclination of  $\theta_0 = 56^\circ, 57^\circ, 58^\circ$  are observed to bracket the value predicted in Fig. 1.8(a). The edge Mach number is increased to 6 for the rays in Fig. 1.10 and ray traces with an initial angle of inclination of  $\theta_0 = 67^\circ, 68^\circ, 69^\circ$  bracket the maximum value predicted in Fig. 1.8(a). Changing the boundary condition at the wall to  $T_W = T_{ad}/10$  should increase the maximum initial angle of inclination per Fig. 1.8(b). This is reflected in the rays with an initial angle of  $\theta_0 = 82^\circ, 83^\circ, 84^\circ$ .

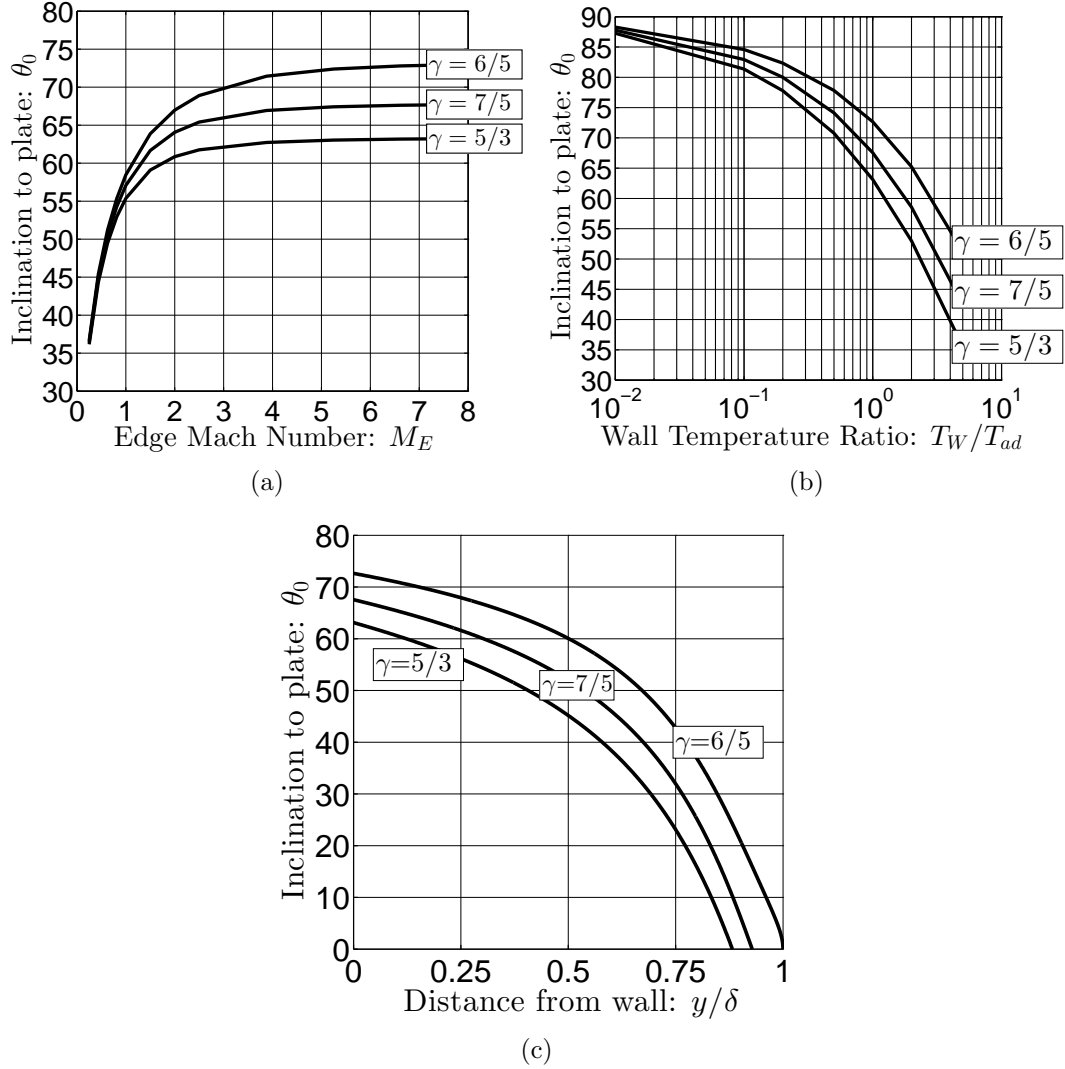


Figure 1.8: a: Largest angle of inclination to the plate of acoustic ray that is refracted back to the surface,  $M_E = 0.25 - 8$ ,  $\gamma = 6/5, 7/5, 5/3$ ,  $T_W = T_{ad}$ . b: Largest angle of inclination to the plate of acoustic ray that is refracted back to the surface,  $M_E = 6$ ,  $\gamma = 6/5, 7/5, 5/3$ ,  $T_W = KT_{ad}$ , where  $K$  is varied between  $10^{-2}$  and 5. c: Largest angle of inclination to the plate of acoustic ray that is refracted back to the surface at different wall normal origins,  $M_E = 6$ ,  $\gamma = 6/5, 7/5, 5/3$ ,  $T_W = T_{ad}$ .

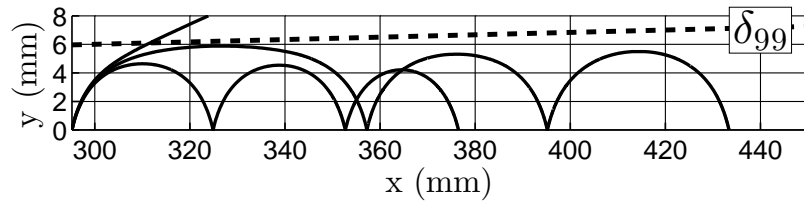


Figure 1.9: Ray traces for  $M_E = 1$ ,  $\gamma = 7/5$ ,  $T_W = T_{ad}$ , with  $\theta_0 = 56^\circ, 57^\circ, 58^\circ$  at  $Re_{x0} = 1 \times 10^5$ .

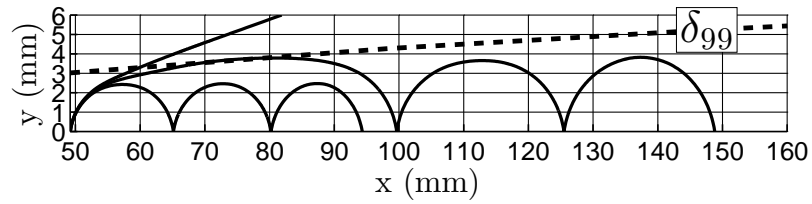


Figure 1.10: Ray traces for  $M_E = 6$ ,  $\gamma = 7/5$ ,  $T_W = T_{ad}$ , with  $\theta_0 = 67^\circ, 68^\circ, 69^\circ$  at  $Re_{x0} = 1 \times 10^5$ .

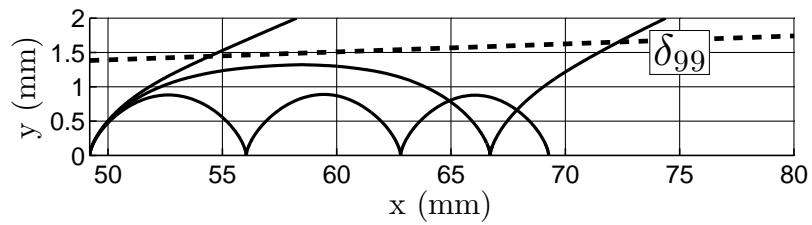


Figure 1.11: Ray traces for  $M_E = 6$ ,  $\gamma = 7/5$ ,  $T_W = T_{ad}/10$ , with  $\theta_0 = 82^\circ, 83^\circ, 84^\circ$  at  $Re_{x0} = 1 \times 10^5$ .

### 1.3.3 Summary

Ray-tracing in high-speed boundary layers has been used to explore the potential for acoustic energy trapping as function of edge Mach number, wall temperature ratio, and thermodynamic parameters. We proposed a figure of merit for acoustic energy trapping as the critical angle of inclination for rays originating in the boundary that are trapped, i.e., these rays always stay within the boundary layer. Using this concept, we find that an increasing amount of acoustic energy is trapped with increasing edge Mach number ( $M_E$ ), and decreasing wall temperature ratio ( $T_W/T_{ad}$ ). These trends agree qualitatively with the results of high-speed boundary-layer stability calculation by Mack (1984).

## 1.4 Motivation For Hypervelocity Instability Study

“High-enthalpy” or “hypervelocity” fluid-mechanics research is the study of high-speed flow fields “that are both hypersonic and high velocity, rather than merely hypersonic” (Stalker, 1989). The term “hypersonic” generally refers to flows with a characteristic Mach number of greater than five, but the term “high velocity” is more relative. Following Hornung (1993), we estimate the ordered-kinetic energy of the free-stream gas flowing over a vehicle moving at  $U_\infty$  as  $U_\infty^2/2$ ; so, a vehicle moving at 3 km/s or 6 km/s results in ordered kinetic energies of 4.5 MJ/kg or 18 MJ/kg, respectively. These large ordered kinetic energies can be of the same order as the characteristic thermo-chemical energy scales in a flow-field of interest; for example, the characteristic energies of dissociation ( $D$ ) and vibrational excitation ( $E_\nu$ ) for  $N_2$ ,  $O_2$ , and  $CO_2$  are listed in Table 1.1.<sup>5</sup> When the free-stream ordered kinetic energy is a significant fraction of the characteristic energy of dissociation or vibration, these

---

<sup>5</sup>The tabulated thermo-chemical data is adapted from McQuarrie (2000). For  $CO_2$ , the reaction  $CO_2 \rightarrow CO + \frac{1}{2}O_2$ , and the lowest energy doubly degenerate mode of vibrational excitation are considered.

effects can be present in the flow-field.

Table 1.1: Characteristic thermo-chemical energies

|            |            |            |               |               |                |
|------------|------------|------------|---------------|---------------|----------------|
| $D_{N_2}$  | $D_{O_2}$  | $D_{CO_2}$ | $E_{\nu N_2}$ | $E_{\nu O_2}$ | $E_{\nu CO_2}$ |
| 33.6 MJ/kg | 15.4 MJ/kg | 6.3 MJ/kg  | 1000 kJ/kg    | 590 kJ/kg     | 180 kJ/kg      |

For blunt-body flows, dissociation of the free-stream gas can occur, which can result in lower temperature and higher density than if the gas were thermo-chemically frozen. This can change the shockwave shape and stand-off distance over a vehicle, which can change the surface pressure distribution and heat-flux.

An essential aspect of studying hypersonic slender-body boundary-layer instability at high enthalpy is characterizing the energy exchange between the thermo-chemical and fluid-mechanical processes. These effects are termed “high-enthalpy effects” on boundary layers. Thermo-chemical processes are only relevant at high-enthalpy conditions where the ordered kinetic energy of the flow is high enough so that chemical reactions and relaxation processes occur. If the energy is high enough, and if the fluid-mechanical and thermo-chemical processes proceed at comparable time scales, then energy exchange may occur.

Of particular interest is the exchange of energy between the high-frequency acoustic instability in a hypersonic boundary layer and molecular vibrational relaxation processes. For certain conditions, the time scale of the instability which goes as the edge velocity on twice the boundary-layer thickness ( $f \approx U_E/(2\delta)$ ) is of the order 1 MHz. Vibrational relaxation processes can be of this time scale at conditions in a hypersonic boundary layer, so energy exchange may occur, and the instability could be damped.

### 1.4.1 Energy Exchange and pdV Work

In a non-equilibrium gas, the sound speed is not unique because the thermodynamic state is defined by three variables, i.e., mass-specific entropy can be defined as  $s =$

$s(p, \rho, q)$ , where  $q$  is a non-equilibrium variable (Vincenti and Kruger, 1965). The frozen sound speed ( $a_f^2 = (\partial p / \partial \rho)_{s,q}$ ) is evaluated with  $q$  fixed, and the equilibrium sound speed ( $a_e^2 = (\partial p / \partial \rho)_{s,q^*}$ ) is evaluated with the non-equilibrium variable  $q = q^*$  at its value if the gas were in local equilibrium. The ratio of frozen sound speed to equilibrium sound speed ( $a_f/a_e$ ) is a measure of the capacity of a gas to absorb acoustic energy.

Following section 4 of chapter 8 in Vincenti and Kruger (1965), a model of a piston harmonically oscillating in a constant area duct occupied by a non-equilibrium gas can be used as an example of how acoustic waves may be damped by an exchange of energy with the gas. An indication of the absorption of acoustic energy can be shown on a  $P$ - $v$  diagram.  $P$ - $v$  cycles of an acoustic wave oscillating at angular frequency  $\omega$  with the time scale of relaxation  $\tau$  show that an ellipse of finite width is traced when the pressure and density of the gas are out of phase (Fig. 1.12(a)). If the sound-speed ratio ( $a_f/a_e$ ) is fixed at a number that is larger than unity, and the time scale matching is varied, the ellipse thickness varies with the time scale ( $\omega\tau$ ), and is thickest when the scale is of order 1. The ellipse thickness indicates the possibility of  $pdV$  work, which may be interpreted as an exchange of energy from the acoustic wave to the internal energy of the gas; the broader the ellipse, the greater the energy exchange. Qualitatively, two requirements for energy exchange are evident: 1) the time scales of relaxation and acoustic wave oscillation must be similar, and 2) the gas must have sufficient internal vibrational or rotational energy so that energy exchange is possible.

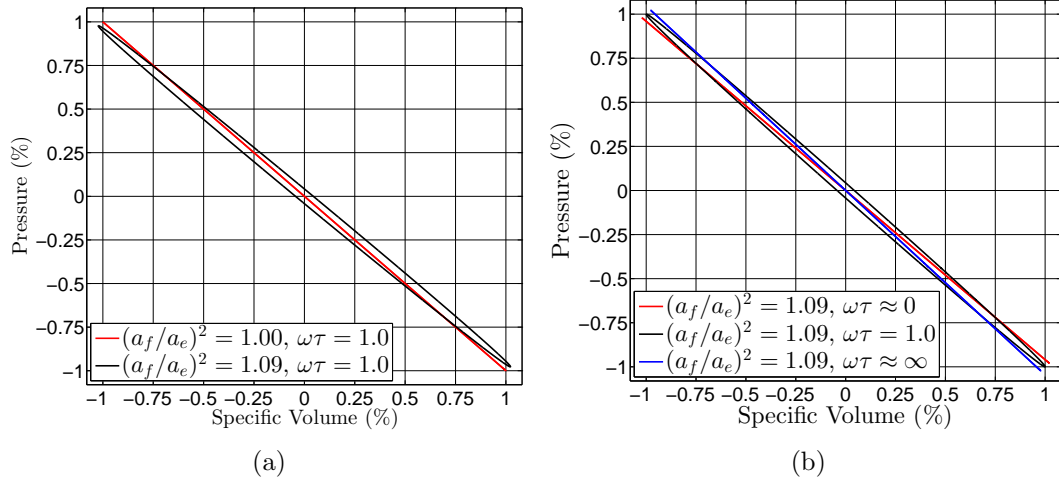


Figure 1.12: a:  $P$ - $v$  cycles of an acoustic wave with a time scale match ( $\omega\tau = 1$ ), with different ratios of sound speed ( $a_f/a_e$ ) b: for a fixed sound-speed ratio ( $a_f/a_e$ ),  $P$ - $v$  cycles for disparate time-scale ratios ( $\omega/\tau$ ). This illustrates the two requirements for  $pdV$  energy exchange: 1) the time scales of relaxation and acoustic wave oscillation must be similar, and 2) the gas must have sufficient internal energy so that energy exchange is possible.

### 1.4.2 Simple Acoustic-Wave Attenuation Model

A simple acoustic-wave attenuation model is introduced in this subsection. Following the development in [Pierce \(1989\)](#) and [Thompson \(1972\)](#), the absorption coefficient  $\alpha_a$  for a gas where there is a small contribution to the heat capacity from the vibrational degree of freedom ( $c_{v,i} \ll c_p$ ) can be written as,

$$\alpha_a = \alpha_c + \sum_i \alpha_{r,i}, \quad (1.6a)$$

$$\alpha_c = \frac{\mu\omega^2}{2\rho_L a_f^3} \left( \frac{4}{3} + \frac{\gamma_f - 1}{\text{Pr}} \right), \quad (1.6b)$$

$$\alpha_{r,i} = \frac{\pi(\gamma_f - 1)c_{v,i}}{\lambda c_p} \frac{\omega\tau_i}{1 + (\omega\tau_i)^2}. \quad (1.6c)$$

Here,  $\alpha_c$  is the classic absorption coefficient due to viscous and thermal attenuation,  $\mu$  is the viscosity,  $\rho_L$  is the mean local density,  $a_f$  is the frozen sound speed,  $\gamma_f$  is the frozen ratio of specific heats, and Pr is the Prandtl number. Additionally,  $\alpha_{r,i}$  is the absorption by relaxation process  $i$  with relaxation time  $\tau_i$ , and,  $\lambda$  and  $\omega$

are the wavelength and angular frequency of the acoustic wave, respectively;  $c_{v,i}$  is the constant-volume specific heat contribution from a relaxation process  $i$  (e.g. the vibrational mode of  $N_2$ ), and  $c_p$  is the equilibrium constant-pressure specific heat.

The classic absorption coefficient result is from Stokes and Kirchhoff, so it is termed SK attenuation (Thompson, 1972). Also in Thompson (1972), the SK attenuation results are supported by summarized experimental data up to a time scale where the collision rate becomes comparable; the scale  $\mu\omega/P = 0.1$  is suggested, where  $\mu$  is the local viscosity,  $\omega$  is the angular frequency of the disturbance, and  $P$  is the local pressure. This implies that the SK attenuation coefficient can be used to  $\approx 5$  MHz for conditions in a typical boundary layer during a T5 test.

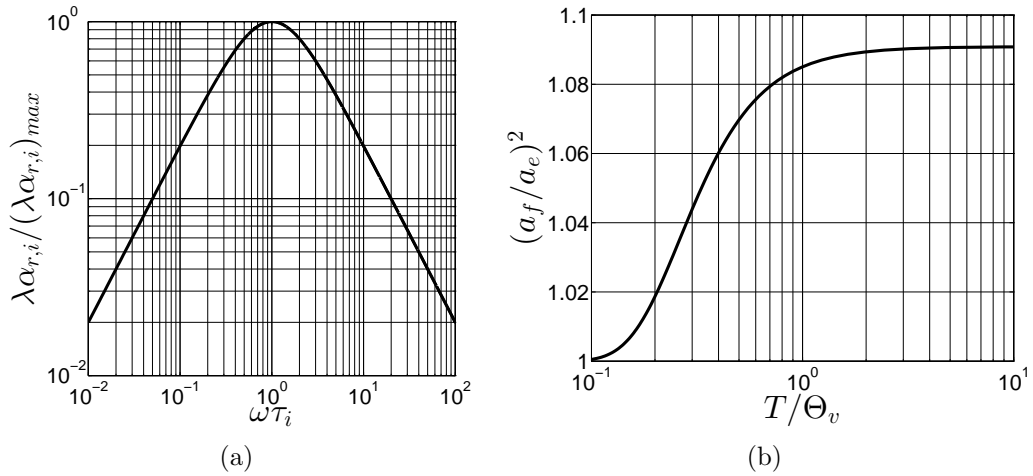


Figure 1.13: a: The absorption coefficient for a single relaxation process normalized by its maximum value illustrating the time scale dependence. b: The ratio of frozen to equilibrium sound speed as a function of the ratio of the temperature ( $T$ ) to characteristic vibrational temperature ( $\Theta_v$ ) for a linear polyatomic molecule with a single non-degenerate relaxing vibrational degree of freedom.

From Eq. 1.6c it is clear that the absorption coefficient due to a relaxation process is highly time scale dependent, this is highlighted in Fig. 1.13(a). Additionally, the frozen to equilibrium sound-speed ratio ( $a_f/a_e$ ) is an indicator of the magnitude of  $(\lambda\alpha_{r,i})_{max}$ . For a chemically frozen gas, this is a function of the extent to which a vibrational degree of freedom is excited. The temperature dependence for a lin-

ear polyatomic molecule with a single non-degenerate relaxing vibrational degree of freedom is highlighted in Fig. 1.13(b).

The absorption coefficient for  $\text{CO}_2$  is of particular interest because there is a doubly-degenerate vibrational mode at moderate characteristic temperature,  $\Theta_v = 960$  K; this is relatively low compared with the characteristic temperatures of vibration for  $\text{N}_2$  and  $\text{O}_2$ , which are 3374 K and 2260 K, respectively. The implication is that  $\text{CO}_2$  has a relatively high capacity to attenuate high-frequency waves, possibly even those in the boundary layer of a high-speed vehicle. The assumption that the contribution to the specific heat capacity from the vibrational degree of freedom is small ( $c_{v,i} \ll c_p$ ) is not valid in the temperature ranges discussed here. For this reason, the wavenumber is found from the dispersion relation for a relaxing gas given as Eq. 10-8.7 in Pierce (1989), and the imaginary portion is reported as the absorption coefficient.

An example absorption coefficient curve (Fig. 1.14(a)) highlights the relative spectrum of attenuation due to SK dissipation and vibrational relaxation for  $\text{CO}_2$  at  $P = 25$  kPa,  $T = 1500$  K. These results show attenuation of  $\approx 5\text{-}30\%$  per wavelength over a large frequency band. This is a large value for the absorption coefficient when compared with that of  $\text{N}_2$  for the same conditions (Fig. 1.14(b)).

In these calculations, the relaxation rates for  $\text{CO}_2$  and  $\text{N}_2$  are taken from Camac (1966) and Millikan and White (1963), respectively. In Camac (1966), it is observed that all four vibration modes relax at the same rate, and the data are summarized along with eight other references where vibrational relaxation data were reported at lower temperatures. Gaydon and Hurlle (1963) caution that “[t]he relaxation of carbon dioxide is very sensitive to the presence of impurities,” which can effectively reduce the relaxation time. The thermodynamic data were calculated using statistical mechanics, as in McQuarrie (2000). The thermodynamic properties are checked against the tabulated data for  $\text{CO}_2$  and  $\text{N}_2$  in chemical-thermodynamic equilibrium

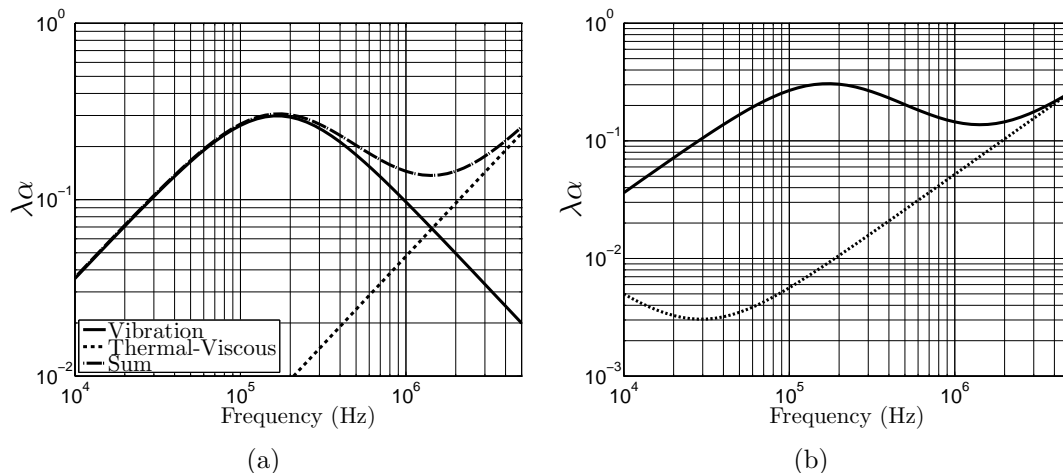


Figure 1.14: a: Absorption coefficient for  $\text{CO}_2$  at  $P = 25$  kPa,  $T = 1500$  K. The solid line represents the total absorption coefficient, which is the sum of the viscous-thermal term (dotted line), and the term due to the vibrational relaxation (dash-dot line). b: Absorption coefficient for  $\text{N}_2$  (dotted line) and  $\text{CO}_2$  (solid line) at  $P = 25$  kPa,  $T = 1500$  K.

in [McBride et al. \(2002\)](#) using Cantera ([Goodwin, 2003](#)). The viscosity is evaluated from curve fits as in [Blottner et al. \(1971\)](#).

## 1.5 Hypervelocity Transition in T5

Boundary-layer stability and transition in high-enthalpy facilities has been studied extensively for 20 years in the T5 hypervelocity shock tunnel. [Germain \(1993\)](#) and [Germain and Hornung \(1997\)](#) conducted a series of transition experiments on a sharp 5 degree half-angle cone at zero angle of attack in the T5 hypervelocity shock tunnel. Transition Reynolds number was measured for a range of free-stream conditions and gasses. The transition Reynolds number was determined by noting the location of departure of laminar heating rates. The surface heating rates were measured by heat-transfer gauges constructed of type E thermocouples (manufactured by Medtherm Corporation) that were mounted flush to the surface. [Germain](#) found that the transition Reynolds number increases with increasing reservoir enthalpy, when normalized by the reference conditions. This effect is more pronounced in gasses

with lower dissociation and vibrational energies. Additionally, resonantly enhanced shadowgraphy was used to characterize the flow structures. Based on these results, [Germain and Hornung](#) proposed that the dominant instability mechanism was the Tollmien-Schlichting mode in those experiments.

Transition and stability work on a sharp 5 degree half-angle cone in T5 continued in the 1990's, as reported in [Adam \(1997\)](#) and [Adam and Hornung \(1997\)](#). They too note that transition Reynolds number increases as the reservoir enthalpy is increased, and this effect is more pronounced in CO<sub>2</sub> than in air. Adam then used the tabulated transition Reynolds numbers based on reference temperature and found the results to be “within striking distance” of Re-entry F free-flight data reported in [Wright and Zoby \(1977\)](#). Adam also used BLIMPK<sup>6</sup> to compute the non-similar non-equilibrium boundary-layer profiles on the cone to understand the extent to which the frictional heating affected the thermo-chemical properties of the boundary layer, i.e., quantifying the dissociation level of different gases at different condition as a function of distance along the cone surface.

Boundary-layer stability control research then followed in T5, as reported in [Rasheed \(2001\)](#) and [Rasheed et al. \(2002\)](#). In that work, researchers used a novel passive scheme to damp the acoustic instability in a hypervelocity boundary layer on a five degree half-angle cone. Half of the surface of the test article was allocated to serve as a smooth control, and the opposing half was an ultrasonically absorptive surface. The transition Reynolds number on the smooth surface was consistent with previous work, while the half with the ultrasonic absorptive surface exhibited significant increases in transition Reynolds number. Because the passive boundary-layer instability control scheme was aimed at damping the acoustic instability, and the scheme proved effective in increasing the transition Reynolds number, one might conclude that the most unstable mode is acoustic in nature, not the viscous or Tollmien-Schlichting

---

<sup>6</sup>BLIMPK stands for Boundary Layer Integral Matrix Procedure with Kinetics, and more information can be found in [Bartlett and Kendall \(1968\)](#).

mode as suggested in [Germain \(1993\)](#) and [Germain and Hornung \(1997\)](#).

[Fujii \(2001\)](#) and [Fujii and Hornung \(2003\)](#) investigated attachment line boundary-layer transition on a swept cylinder in T5. Most relevant to the present work were the efforts made to quantify the role of energy exchange between the boundary-layer instability and the fluid, which is described in detail in [Fujii and Hornung \(2001\)](#). They proposed that if the time scale of a relaxation process in gas is nearly matched to the time scale of the acoustic instability in the boundary layer, significant energy may be scrubbed from the instability. This removal of energy from the boundary-layer instability would ultimately manifest itself as an increase in boundary-layer transition Reynolds number. Quantitative results for absorption were computed from a model of high-frequency sound waves propagating through a relaxing gas.

Further boundary-layer instability control research has continued in T5, as reported in [Leyva et al. \(2009a,b\)](#) and [Jewell et al. \(2011, 2012, 2013\)](#). In this research, the ultimate goal is to increase the transition Reynolds number in a test gas by introducing a different gas with lower dissociation and vibrational energies than the test gas. By introducing a gas into the boundary layer that has thermo-chemical properties which may attenuate acoustic waves, the researchers suggest that the acoustic instability will be damped, and the transition Reynolds number will be increased.

## 1.6 Project Scope and Outline

The disturbances preceding boundary-layer transition on a slender body at hypervelocity flight conditions are characterized in this work. A sharp five-degree half-angle cone at zero angle of attack is used as the test article because of the canonical nature of the geometry. Ground testing was performed in the T5 hypervelocity free-piston driven reflected-shock tunnel to enable the study of thermo-chemical/fluid-dynamic energy exchange.

In chapter 2, operation of the T5 facility is described; the test procedure and calculation of run conditions are presented with examples and estimates of error. In chapter 3, the focused laser differential interferometry technique (FLDI) is used to measure the hypervelocity boundary-layer disturbances and is characterized. In chapter 4, results from the application of the FLDI technique to T5 flows are presented; tunnel noise and boundary-layer disturbance spectra are highlighted. The results of experiments where narrowband boundary-layer disturbances were observed at two stations are analyzed in chapter 5. In chapter 6, the project is summarized.

# Chapter 2

## Facility and Run Conditions

The test facility and method of calculating the run conditions are described in this chapter. The test procedure is described in detail, noting alterations to past efforts. The run conditions are calculated in three stages, the reservoir, the nozzle, and then the mean flow over the cone. The propagation of error in these calculations is estimated. Comments are made on the repeatability of T5 tunnel operation. Example profiles are provided throughout this chapter for context.

### 2.1 Facility and Test Procedure

All measurements are made in T5, the free-piston driven reflected-shock tunnel at the California Institute of Technology (Fig. 2.1). It is the fifth in a series of shock tunnels designed to simulate high-enthalpy real gas effects on aerodynamics of vehicles flying at hypervelocity speeds through the atmosphere. More information regarding the capabilities of T5 can be found in [Hornung \(1992\)](#).

An experiment is conducted as follows: a 120 kg aluminum piston is loaded into the compression tube/secondary reservoir junction. A secondary diaphragm (mylar, 127  $\mu\text{m}$  thick) is inserted at the nozzle throat at the end of the shock tube near the test section and a primary diaphragm (stainless steel, 7-10 mm thick) is inserted at the compression tube/shock tube junction. The test section, shock tube, and compression

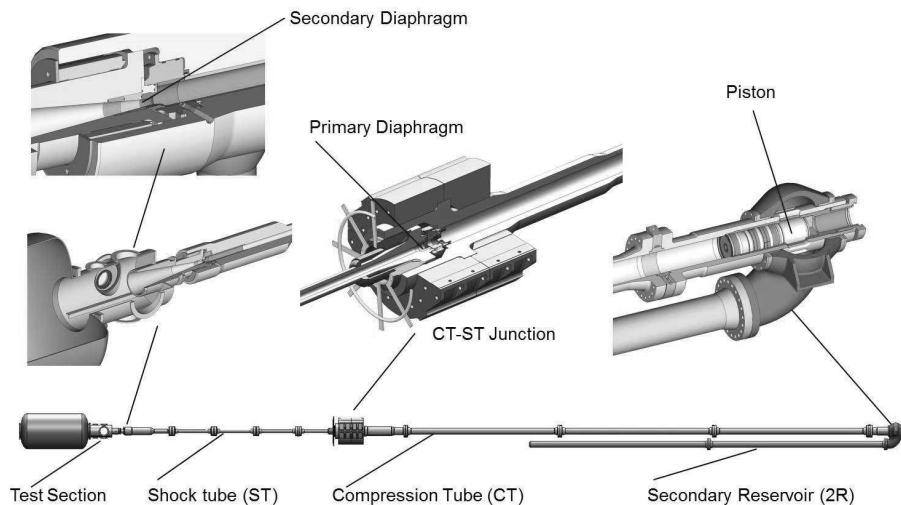


Figure 2.1: A schematic of T5 with a blown up view of each of the major sections.

tube are evacuated. The shock tube is filled with the test gas (in the present study, air,  $\text{CO}_2$ , or  $\text{N}_2$  to 20-150 kPa), the compression tube is filled with a He/Ar mixture to  $\approx 45$ -150 kPa and the secondary reservoir is filled with air to  $\approx 2$ -11 MPa. The air in the secondary reservoir is released, driving the piston into the compression tube. This piston motion adiabatically compresses the driver gas of the shock tunnel to the rupture pressure of the primary diaphragm ( $\approx 20$ -120 MPa). Following the primary diaphragm rupture, a shock wave propagates in the shock tube, is reflected off the end wall, breaking the secondary diaphragm and re-processing the test gas. The test gas is then at high temperature ( $\approx 2000$ -9000 K) and pressure ( $\approx 15$ -80 MPa) with negligible velocity, and is then expanded through a converging-diverging contoured nozzle to  $\approx$  Mach 5.5 in the test section.

Throughout the testing campaign for this work, it became apparent that there was opportunity to improve the quality of the flow over the model. Improvement was made by using higher quality gas to fill the shock tube and by cleaning the shock tube more thoroughly between experiments. The quality of the gas used to fill the shock tube, and the shock tube cleaning procedure were fixed after shot 2760 because consistent instability-measurement results were obtained. Fixing the experimental

procedure was concurrent with the conclusion of the development phase of the project. A more thorough explanation and examples of inconsistent and consistent instability-measurement results are found in section 4.3.1.

## 2.2 Reservoir Conditions Calculation

Initial shock tube pressure  $P_1$ , measured primary shock speed  $U_S$ , and reservoir pressure  $P_R$ , are used to compute the reservoir conditions for each shot. The primary shock speed and initial shock tube pressure are used to calculate the thermodynamic state of the gas after being processed by the primary and reflected-shock waves, assuming thermo-chemical equilibrium. The gas pressure behind the reflected-shock wave is changed isentropically, assuming chemical-thermodynamic equilibrium, to the measured reservoir pressure to account for the weak expansion or compression waves that are reflected between the contact surface and the shock tube end. Thermo-chemical calculations are performed using Cantera (Goodwin, 2003) with the Shock and Detonation Toolbox (Browne et al., 2006). The appropriate thermodynamic data are found in the literature (Gordon and McBride, 1999, McBride et al., 2002). The reservoir conditions for each experiment are tabulated in section A.1.

An example from shot 2789 shows the reservoir pressure time traces from the north and south gauges<sup>1</sup> in Fig 2.2(a). The mean between the gauges of the time-average during the steady pressure period is shown in the text box along with the standard deviation which serves as an estimate of error in the measurement.

An  $X-t$  diagram for shot 2789 is shown as Fig. 2.2(b). The pressure traces of the four stations in the shock tube and the reservoir are plotted at their spatial locations. The shock speed is calculated by dividing the transit distance by the transit time. The shock speed between station 4 and the reservoir transducer is not reported because

---

<sup>1</sup>The north and south notation refers to the orientation of the pressure transducers that are separated by 180° at the shock tube end.

the reservoir pressure tap is not designed for accurate time of arrival measurements. The shock speed between stations 3 and 4 is used for the thermo-chemical equilibrium calculations because it is estimated by  $X-t$  diagram that this location corresponds to the steady portion of the test gas slug (Bélanger, 1993).

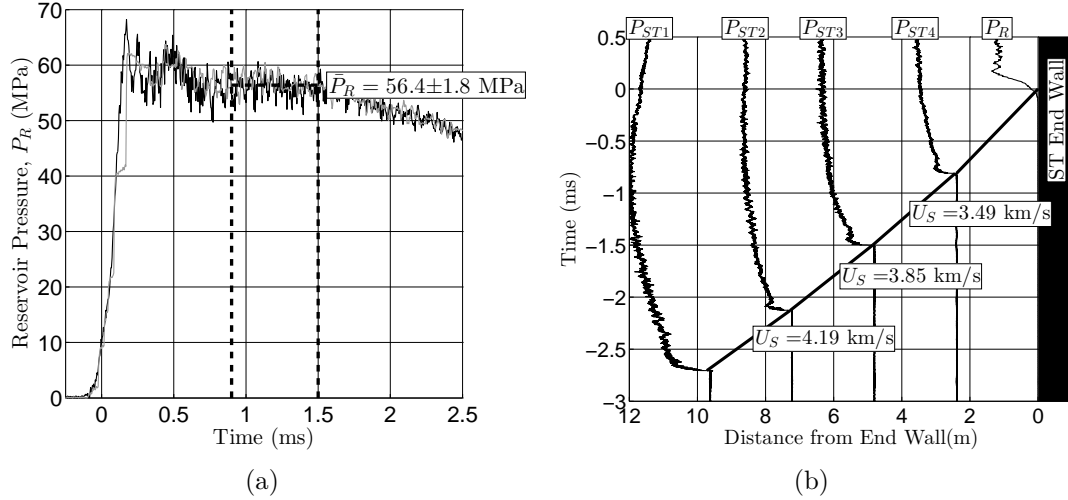


Figure 2.2: Left: Example reservoir pressure trace from shot 2789. In the reservoir pressure trace, the north gauge’s trace is black; the south gauge’s trace is gray. Right:  $X-t$  diagram showing the propagation of the incident shock of speed  $U_S$ , as well as pressure traces at 5 stations along the shock tube from shot 2789.

## 2.3 Nozzle Calculation

The steady expansion through the contoured nozzle (outline in Fig. 2.3) from the reservoir to the free-stream is modeled by the axisymmetric, reacting Navier-Stokes equations as described in by Candler (2005), Johnson (2000), and Wagnild (2012). The translational and rotational degrees of freedom are assumed to be in equilibrium. The vibrational degree of freedom is allowed to deviate with equilibrium with the translational/rotational modes. The boundary layer on the nozzle wall is assumed to be turbulent and modeled by one equation as in Spalart and Allmaras (1992) with the Catrisa and Aupoix (2000) compressibility correction. The grid is generated by the commercial tool, Gridgen.

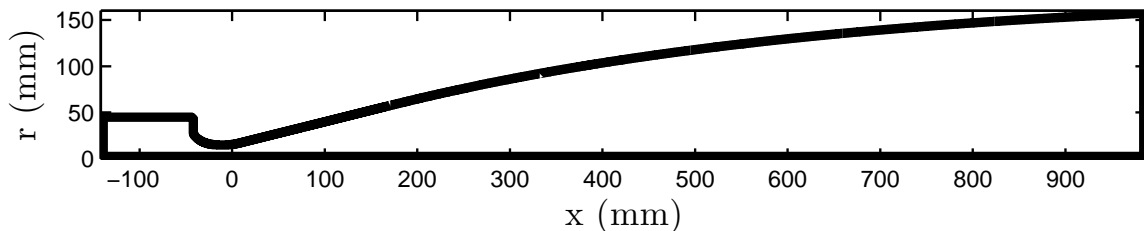


Figure 2.3: An outline of the T5 contoured nozzle of area ratio 100.

### 2.3.1 Nozzle Freezing Examples

The term *nozzle freezing* is used to indicate when a chemical-thermodynamic reaction rate is not high enough to match the characteristic time scale in the nozzle. Typically, reaction rates are a strong function of temperature, and reactions cease if the temperature drops too rapidly, hence the term *freezing*. This is a known issue in ground-testing because the gas at the exit of the nozzle can be partially dissociated and vibrationally excited relative to the desired free-stream condition that corresponds to a free-flight condition. This issue and others pertaining to high-speed ground-testing are discussed in broader context in [Stalker \(1989\)](#) and [Hornung \(1993\)](#).

The aim of the subsequent discussion is to give quantitative examples of the freezing effect by showing the computed evolution of the translational/rotational temperature ( $T_{t/r}$ ), the vibrational temperature ( $T_v$ ),<sup>2</sup> and the chemical composition along the centerline in the nozzle when the test gas is air, CO<sub>2</sub>, and N<sub>2</sub> at nominally similar reservoir conditions (reservoir enthalpy  $h_R \approx 9$  MJ/kg, and reservoir pressure  $P_R \approx 17$  MPa)<sup>3</sup>.

For air as the test gas, the translation/rotational and vibrational temperatures do not have a discernible difference from each other, but are elevated relative to a free-flight condition (Fig. 2.4(a)). NO and O are frozen downstream of the location

<sup>2</sup>The vibrational temperature ( $T_v$ ), is a figure that defines the quantity of energy that excites the vibrational degree of freedom. This is not to be confused with the characteristic temperature of vibration,  $\Theta_v = h\nu/k_b$ , where  $h$  is Planck's constant,  $k_b$  is Boltzmann's constant, and  $\nu$  is the frequency of the oscillator.

<sup>3</sup>the detailed conditions for shots 2767, 2773, and 2791 are tabulated in section [A.1](#)

$A/A^*=10$ , reducing the amount of  $O_2$  and  $N_2$  present at the nozzle exit (Fig. 2.4(b)), where  $A/A^*$  is the area ratio with respect to the area at the nozzle throat,  $A^*$ .

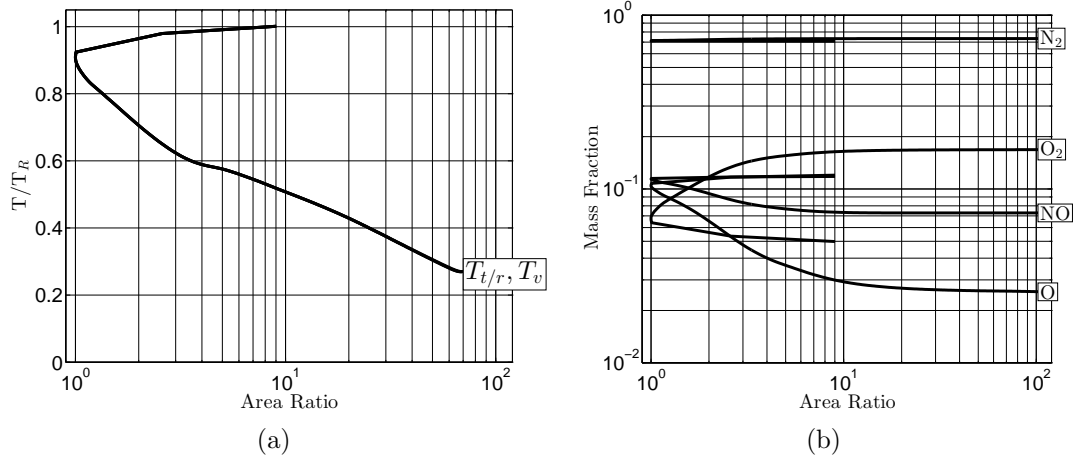


Figure 2.4: Air shot (2767). Labels are placed at the nozzle exit (area ratio 100), the other end of each line segment represents the value at the reservoir (area ratio 9). The area ratio of 1 denotes the converging-diverging nozzle throat. Left: Translation/rotational temperature  $T_{t/r}$  and vibrational temperature  $T_v$  for air. The subscript  $R$  denotes the value at the reservoir. Right: Species recombination in the nozzle for air.

To assess the effect of the dissociation products of air being frozen in the flow, the difference in free-stream enthalpy and velocity is chosen to differentiate between the gas in its computed thermo-chemical non-equilibrium state (Fig. 2.4(b)) with a comparable equilibrium state. Cantera is used to compute the equilibrium thermo-chemical state of the gas at the same free-stream temperature and pressure. At that temperature and pressure, the air is nearly totally recombined ( $y_{NO} < 0.02\%$ )<sup>4</sup>, and the free-stream enthalpy is 625 kJ/kg lower ( $\approx 7\%$  of the reservoir enthalpy,  $h_R$ ), resulting in an increase in velocity of 160 m/s (4%).

With  $CO_2$  as the test gas, the translation/rotational and vibrational temperatures also do not have a discernible difference from each other, but are elevated relative to a free-flight condition (Fig. 2.5(a)).  $CO$  and  $O_2$  concentrations are chemically frozen downstream of the location  $A/A^*=10$  at levels substantially higher than equilibrium

<sup>4</sup> $y_i$  is the mass fraction of species  $i$ .

at the nozzle exit, reducing the amount of  $\text{CO}_2$  in the test gas(Fig. 2.5(b)). The energy required to dissociate  $\text{CO}_2$  is lower than for  $\text{O}_2$  and  $\text{N}_2$  (quantitative values of relative dissociation levels can be found for all conditions in section A.1). Because it does not have correspondingly higher recombination rates,  $\text{CO}_2$  experiments tend to have more free-stream dissociation than air or  $\text{N}_2$  experiments at similar reservoir conditions. Comparing  $\text{CO}_2$  experiments relative to air experiments for similar reservoir conditions, the gas at the nozzle exit is of lower velocity and lower Mach number because it is hotter and more dissociated.

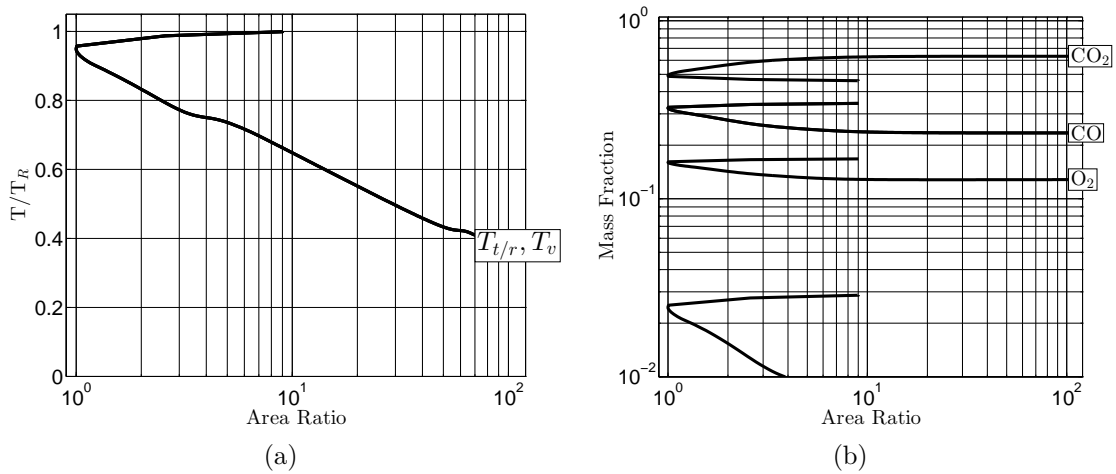


Figure 2.5:  $\text{CO}_2$  shot (2791). Labels are placed at the nozzle exit (area ratio 100), the other end of each line segment represents the value at the reservoir (area ratio 9). The area ratio of 1 denotes the converging-diverging nozzle throat. Left: Translation/rotational temperature  $T_{t/r}$  and vibrational temperature  $T_v$  for  $\text{CO}_2$ . The subscript  $R$  denotes the value at the reservoir. Right: Species recombination in the nozzle for air. The unlabeled line in (b) is the species O.

Dissociation products of  $\text{CO}_2$  being frozen in the flow also cause a difference in free-stream enthalpy and velocity between the gas in its computed thermo-chemical non-equilibrium state (Fig. 2.5(b)) and a corresponding equilibrium state. At the same free-stream temperature and pressure, but in thermo-chemical equilibrium, the  $\text{CO}_2$  is nearly totally recombined (99.8%), and the free-stream enthalpy is 2.4 MJ/kg lower ( $\approx 27\%$  of  $h_R$ ), resulting in an increase in velocity of 700 m/s (22.5%). This loss due to thermo-chemical freezing is significantly more important for  $\text{CO}_2$  shots

than for air or N<sub>2</sub> shots.

With N<sub>2</sub> as the test gas, the translation/rotational and vibrational temperatures do have a discernible difference from each other, and are elevated relative to an equilibrium condition at the nozzle exit (Fig. 2.6(a)). N<sub>2</sub> has a higher dissociation energy relative to air and CO<sub>2</sub>, and is high relative to the reservoir enthalpy in this example, so there is almost no N at the nozzle exit (Fig. 2.6(b)). Comparing N<sub>2</sub> shots to air shots, the gas at the nozzle exit is colder, less dissociated, and has higher velocity and higher Mach number.

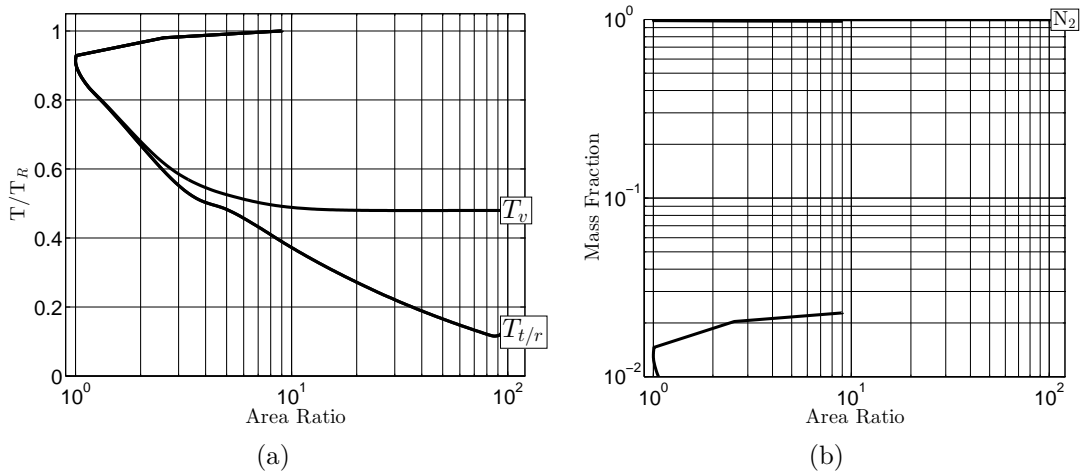


Figure 2.6: N<sub>2</sub> shot (2773). Labels are placed at the nozzle exit (area ratio 100), the other end of each line segment represents the value at the reservoir (area ratio 9). The area ratio of 1 denotes the converging-diverging nozzle throat. Left: Translation/rotational temperature  $T_{t/r}$  and vibrational temperature  $T_v$  for N<sub>2</sub>. The subscript  $R$  denotes the value at the reservoir. Right: Species recombination in the nozzle for air. Labels are placed at the nozzle exit, the other end of each line segment represents the value at the reservoir. The unlabeled line in (b) is the species N.

An estimate of the loss in free-stream velocity for shot 2773 due to the freezing of the N<sub>2</sub> in a partially vibrationally excited state can be estimated by following [Vincenti and Kruger \(1965\)](#). Neglecting contributions from electronic effects, the mass-specific internal energy can be written as

$$e = RT^2 \frac{\partial \ln Q}{\partial T} = RT_{t/r}^2 \frac{\partial \ln Q_t}{\partial T_{t/r}} + RT_{t/r}^2 \frac{\partial \ln Q_r}{\partial T_{t/r}} + RT_v^2 \frac{\partial \ln Q_v}{\partial T_v}, \quad (2.1)$$

where  $Q$  is the partition function, which for the translational (subscript  $t$ ), rotational (subscript  $r$ ), and vibrational (subscript  $v$ ) degrees of freedom are

$$Q_t = \left( \frac{2\pi mkT_{t/r}}{h^2} \right)^{3/2} V, \quad (2.2a)$$

$$Q_r = T_{t/r}/\Theta_r, \quad (2.2b)$$

$$Q_v = \frac{1}{1 - \exp(-\Theta_v/T_v)}, \quad (2.2c)$$

where  $T_{t/r}$  is the translational/rotational temperature,  $T_v$  is the vibrational temperature,  $m$  is the mass of  $N_2$ ,  $k$  is Boltzmann's constant, and  $h$  is Planck's constant.

This results in the internal energy

$$e = \frac{3}{2}RT_{t/r} + RT_{t/r} + \frac{\Theta_v/T_v}{\exp(\Theta_v/T_v) - 1}RT_v. \quad (2.3)$$

For shot 2773,  $T_{t/r} = 804$  K so the contribution to the internal energy is 597 kJ/kg, and  $T_v = 3163$  K so the contribution is 525 kJ/kg. If we assume that the vibrational temperature were to relax to the translational temperature,  $T_v = 804$  K, the contribution to the internal energy would be 15 kJ/kg. To assess what effect this has on the free-stream velocity the free-stream mass-specific enthalpy,  $h = e + p/\rho$ , is written as

$$h = \frac{7}{2}RT_{t/r} + \frac{\Theta_v/T_v}{\exp(\Theta_v/T_v) - 1}RT_v. \quad (2.4)$$

The free-stream enthalpies of the gas when vibrationally excited and in thermodynamic equilibrium are 1.4 MJ/kg and 850 kJ/kg, respectively. The total enthalpy of the flow is  $h + u^2/2 = 9.05$  MJ/kg, so that if the gas were in thermodynamic equilibrium, the free-stream velocity would be 128 m/s or 3.3% higher.

## 2.4 Cone Mean Flow Calculation

The mean flow over the cone is computed by the reacting, axisymmetric Navier-Stokes equations with a structured grid, and is part of the STABL software suite which uses a data-parallel lower-upper relaxation (DPLR) method, as described by [Wright et al. \(1996\)](#), [Johnson \(2000\)](#) and [Johnson et al. \(1998\)](#). For each experiment, the computed mean flow properties are tabulated in section [A.3](#) at the upstream FLDI probe volume.

### 2.4.1 Example Boundary-Layer Thicknesses

Examples for the same three cases described in section [2.3.1](#) for air, CO<sub>2</sub>, and N<sub>2</sub> are presented here to show the effects of changing the test gas on some mean flow characteristics. Firstly, a comparison for a fixed reservoir condition shows that as the test gas is changed, the boundary-layer thickness and Reynolds number vary ([Fig. 2.7\(a\)](#)).

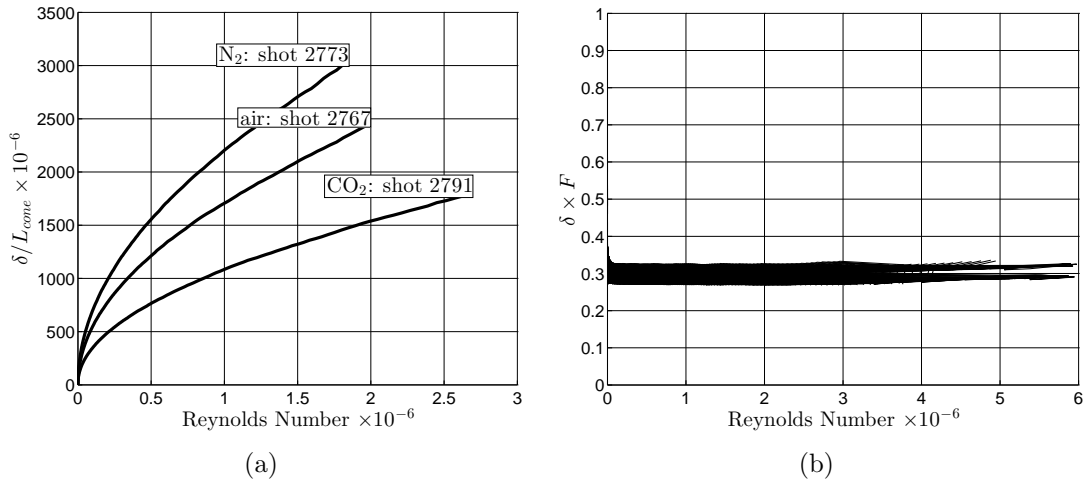


Figure 2.7: Left: Boundary-layer thicknesses for shots 2767, 2773, and 2791. The Reynolds number  $Re_s$  is based on the distance from the cone tip, and the highest Reynolds number corresponds to the end of the 1 meter long cone. Right: An effort to collapse the boundary-layer thickness with the scaling  $\delta \propto M_E^2 / \sqrt{Re_s/C_W}$  for 36 experiments (shots 2761 through 2797).  $F = 1/s\sqrt{Re_s/C_w} / (5 + (1/10 + 1/5(\gamma_E - 1)M_E^2))$ .

It is hypothesized that the most important parameters of the boundary layer typical on a five degree half-angle cone during runs in T5 are the edge Mach number  $M_E$ , the Reynolds number based on distance from the tip of the cone  $Re_s$ , and the wall temperature ratio  $T_W/T_E$ . Following [White \(1991\)](#), the wall temperature ratio can be incorporated into the scaling of the boundary-layer thickness by approximating the Chapman-Rubesin parameter  $C_W = \rho_W \mu_W / (\rho_E \mu_E)$  as  $C_W \approx (T_W/T_E)^{-1/3}$ . A slight modification to the semi-empirical formula that appears in [White \(1991\)](#),

$$\delta \times F = \delta/s \sqrt{Re_s/C_w} / (5 + (1/10 + 1/5(\gamma_E - 1)M_E^2)) \approx 0.3, \quad (2.5)$$

appears to collapse the boundary-layer thicknesses from shot 2761 through 2797 fairly well ([Fig. 2.7\(b\)](#)). This incorporates a broad range of CO<sub>2</sub>, N<sub>2</sub>, and air shots whose conditions are tabulated in detail in [section A](#). This is a correlation, so it can only be used inside the range of conditions it is based on, and for estimation purposes only.

### 2.4.2 Comparison: DPLR to Similarity Solution

In [Fig. 2.8\(a\)](#), the velocity profiles computed with DPLR at edge Reynolds numbers of  $0.25 \times 10^6$ ,  $0.50 \times 10^6$ , and  $1.00 \times 10^6$  for shot 2767 (air) are shown, along with the similarity solution. The similarity solution requires the edge Mach number and ratio of specific heats as inputs; it is evaluated with (dash-dot) and without (dashed) the contribution from the vibrational degree of freedom. The DPLR computations and the similarity solutions are quantitatively close in this range of Reynolds numbers. For shot 2773 (N<sub>2</sub>), the velocity profiles are computed with DPLR and the similarity solution with the Mach number and ratio of specific heats evaluated with (dash-dot) and without (dashed) the contribution from the vibrational degree of freedom ([Fig. 2.8\(b\)](#)); there is also no significant difference. [Fig. 2.8\(c\)](#) shows velocity profiles for CO<sub>2</sub>, shot 2791, computed with DPLR, and the similarity solution with the Mach

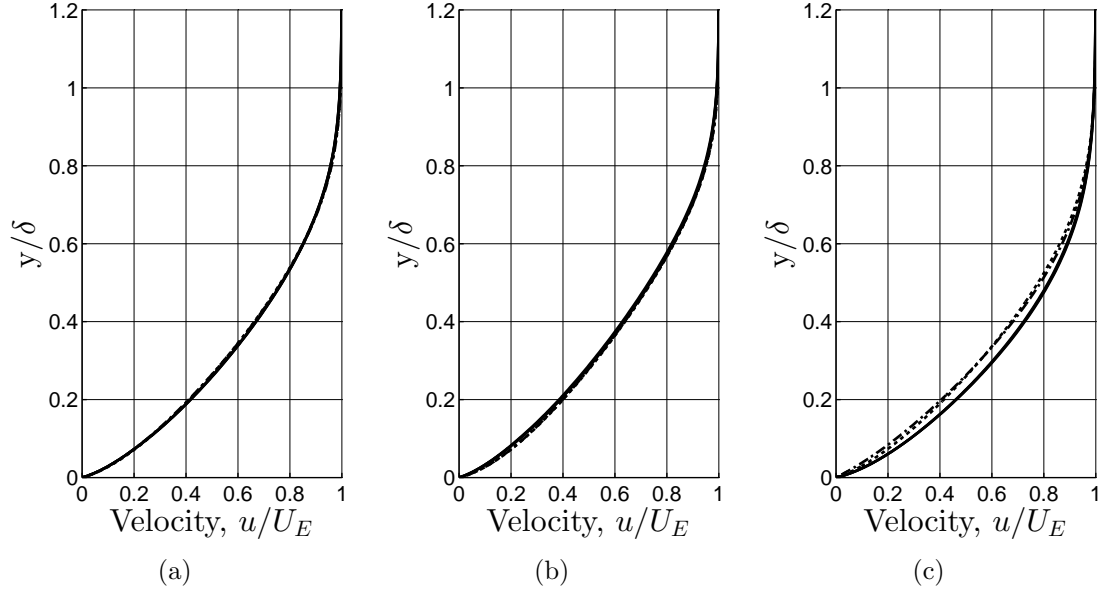


Figure 2.8: The similarity solution requires the edge Mach number and ratio of specific heats as inputs, and is evaluated with (dash-dot) and without (dashed) the contribution from the vibrational degree of freedom. The DPLR solution for several Reynolds numbers is represented by solid lines. Left: Velocity profiles for air, shot 2767, computed with DPLR, and the similarity solution. Center: Velocity profiles for  $N_2$ , shot 2773, computed with DPLR, and the similarity solution. Right: Velocity profiles for  $CO_2$ , shot 2791, computed with DPLR, and the similarity solution.

number and ratio of specific heats evaluated with (dash-dot) and without (dashed) the contribution from the vibrational degree of freedom. The similarity solution predicts a slightly lower velocity as compared with the DPLR computation. The slightly lower velocity in the similarity solution in a  $CO_2$  flow may be the result of estimating the Chapman-Rubesin parameter  $C = \rho\mu/(\rho_E\mu_E)$  that appears in the momentum and energy equation as a function of the temperature similarity variable  $g$ , as  $C = \rho\mu/(\rho_E\mu_E) = g^{-1/3}$ ; [White \(2006\)](#) states that this approximation is for air, so applying it to  $CO_2$  may introduce an error. The normalized velocity profiles computed by DPLR for the different test gases show no first-order type differences.

The temperature profiles for the same cases reveal behavior that more clearly discriminates between the test gases at the same nominal reservoir condition. The similarity solution without (dashed) the contribution from the vibrational degree of

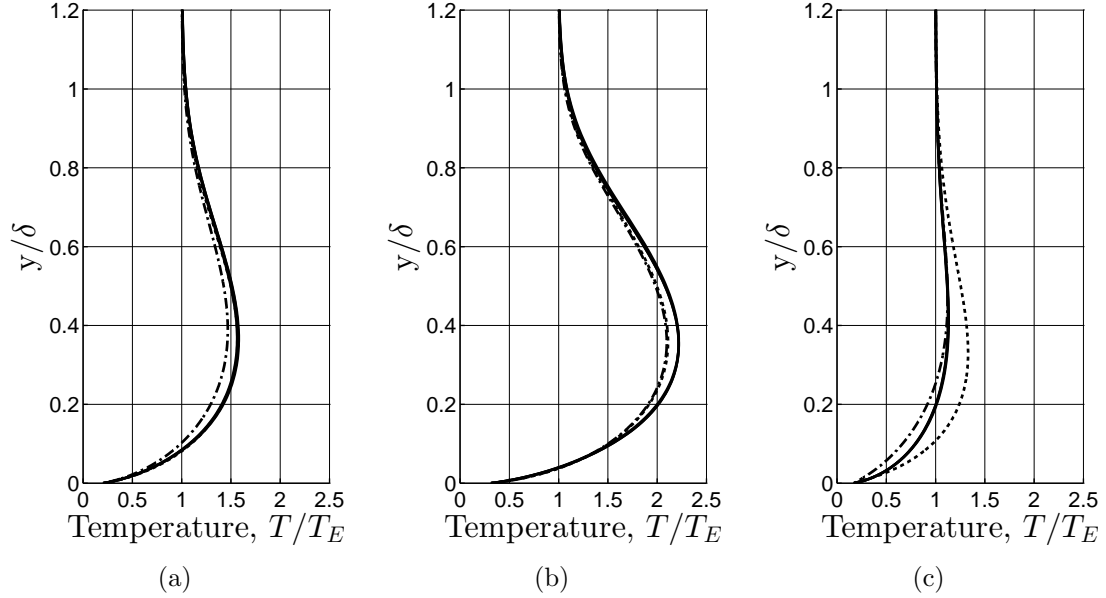


Figure 2.9: The similarity solution requires the edge Mach number and ratio of specific heats as inputs, and is evaluated with (dash-dot) and without (dashed) the contribution from the vibrational degree of freedom. The DPLR solution for several Reynolds numbers is represented by solid lines. Left: Temperature profiles for air, shot 2767, computed with DPLR, and the similarity solution. Center: Temperature profiles for  $N_2$ , shot 2773, computed with DPLR, and the similarity solution. Right: Temperature profiles for  $CO_2$ , shot 2791, computed with DPLR, and the similarity solution.

freedom appears to match the  $T_{t/r}$  calculated by DPLR at edge Reynolds numbers of  $0.25 \times 10^6$ ,  $0.50 \times 10^6$ , and  $1.00 \times 10^6$  for shot 2767 (air, Fig. 2.9(a)) and shot 2773 ( $N_2$ , Fig. 2.9(b)). The calculated  $T_{t/r}$  from DPLR for shot 2791 ( $CO_2$ ) appears to split the temperature profiles calculated from the similarity solution when the edge Mach number and ratio of specific heats are evaluated with (dash-dot) and without (dashed) the contribution from the vibrational degree of freedom (Fig. 2.9(c)). The temperature profiles for the different gases at the same nominal run condition exhibit significant differences when compared to one another.

### 2.4.3 Thermo-Chemical Boundary-Layer Profiles

The evolution of the chemical-thermodynamic profiles of the boundary layer is of interest. At similar reservoir conditions, the mass fraction profiles are plotted at several Reynolds numbers for air,  $N_2$ , and  $CO_2$  in Fig 2.10. The mass fraction profiles show no significant evolution. Furthermore, the mass fractions plotted in Fig. 2.10 are nearly identical to those used as the inputs to the mean flow solver in section A.2. At these conditions, the flow is very nearly chemically frozen.

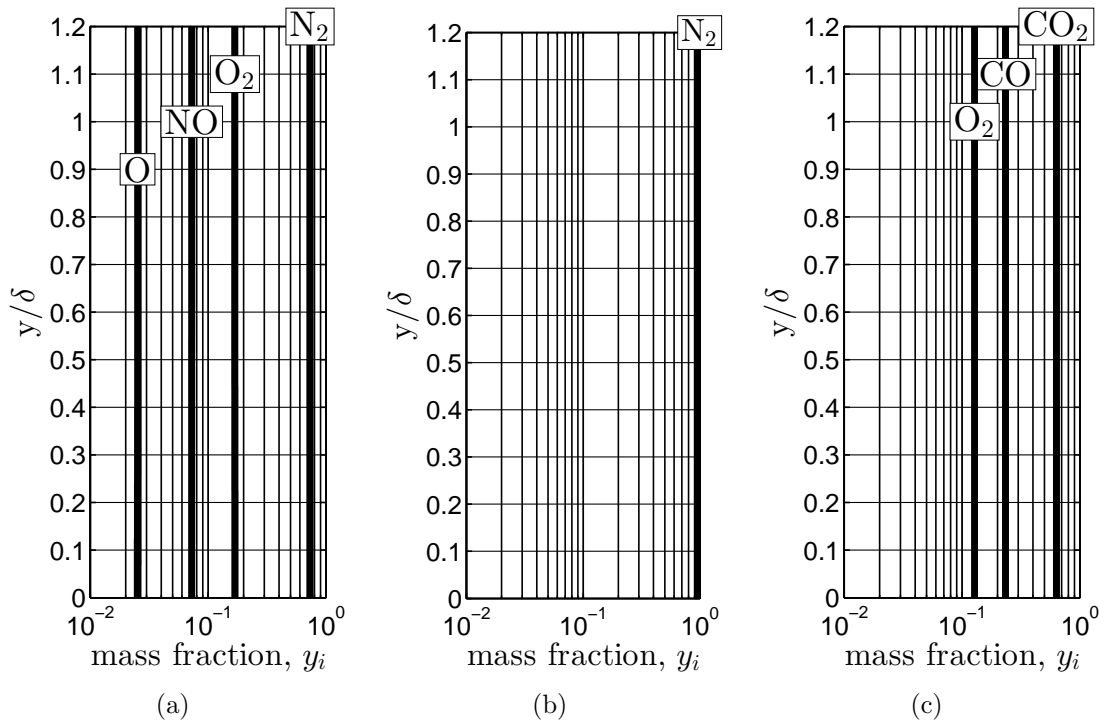


Figure 2.10: Left: Mass fractions profiles for shot 2767, air, at  $Re_E = 0.25, 0.50,$  and  $1.00 \times 10^6$ ; the profiles show no change. Center: Mass fractions for shot 2773,  $N_2$ , at  $Re_E = 0.25, 0.50,$  and  $1.00 \times 10^6$ ; the profiles show no change. Right: Mass fractions for shot 2791,  $CO_2$ , at  $Re_E = 1.00, 5.00 \times 10^4,$  and  $1.00 \times 10^6$ ; the profiles show no change.

The evolution of profiles of translational/rotational temperature,  $T_{t/r}$ , and vibrational temperature,  $T_v$ , show more interesting behavior (Fig. 2.11). The profiles of  $T_{t/r}$  and  $T_v$  for shot 2767 (air) show the time scale of the evolution of temperature is on the order of one cone length. Temperature profiles at  $Re_E = 0.25, 0.50,$  and

$1.00 \times 10^6$  display typical relaxation behavior in the boundary layer. Note that the vibrational relaxation occurs more quickly at the point in the boundary layer where the temperature is higher as compared with the apparent lack of relaxation at the boundary-layer edge. From Figs. 2.10(a) and 2.11(a), at these reservoir conditions, air appears to be chemically frozen, and is vibrationally active with a time scale on the order of one flow length ( $L_{cone}/U_E$ ).

The evolution of the  $T_v$  profiles for shot 2773 ( $N_2$ ) show very little relaxation to the  $T_{t/r}$  profiles at  $Re_E = 0.25, 0.50$ , and  $1.00 \times 10^6$  (Fig. 2.11(b)). The boundary condition at the wall is satisfied,  $T_v = T_{t/r} = 297$ , and the gas at the boundary-layer edge and further from the wall is vibrationally hot ( $T_{t/r} < T_v$ ). This results from the free-stream flow having energy frozen in vibrational modes that were excited in the reservoir (Fig. 2.6(a)). From Figs. 2.10(b) and 2.11(b), at these reservoir conditions,  $N_2$  appears to be chemically frozen, and nearly vibrationally frozen, except for the boundary condition at the wall.

For shot 2791 ( $CO_2$ ), the evolution of the  $T_v$  profiles show rapid relaxation to the  $T_{t/r}$  profiles at  $Re_E = 1.00, 5.00 \times 10^4$ , and  $1.00 \times 10^6$  (Fig. 2.11(c)). The relaxation process is nearly complete at an edge Reynolds number of  $5.00 \times 10^4$ . This corresponds to a time scale on the order of  $\delta/U_E$ . Figs. 2.10(c) and 2.11(c) indicate that at these reservoir conditions,  $CO_2$  appears to be chemically frozen, and vibrationally active at time scales similar to the scaling of the acoustic instability  $\approx 1.25\delta/U_E$ . In part, this is what makes studying instability in  $CO_2$  flows in a reflected-shock tunnel relevant.

The Landau and Teller (1936) formulation of translational/rotational and vibrational energy exchange used in Johnson (2000) and Wagnild (2012) as the vibrational energy source term is

$$Q_{t/r-v} = \sum_{i=1}^{nd} \rho_i \frac{e_{v-eq} - e_v}{\tau_i}, \quad (2.6)$$

where  $i$  is a polyatomic species,  $nd$  is the number of polyatomic species,  $\rho_i$  is density of

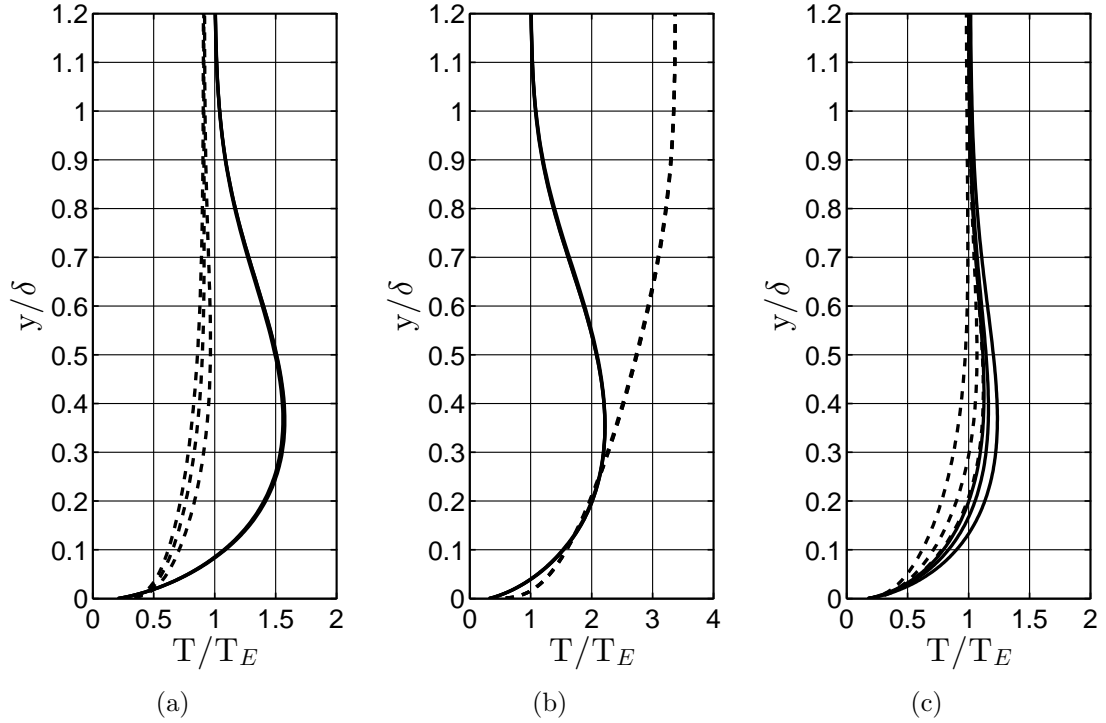


Figure 2.11: DPLR computations. In each plot, profiles at three Reynolds numbers are shown,  $T_v$  is dashed,  $T_{t/r}$  is solid, they relax towards each other as  $Re_s$  increases. Left: Temperature profiles for shot 2767, air, at  $Re_E = 0.25, 0.50,$  and  $1.00 \times 10^6$ ; the profiles show relaxation. Center: Left: Temperature for shot 2773,  $N_2$ , at  $Re_E = 0.25, 0.50,$  and  $1.00 \times 10^6$ ; the profiles show no change. Right: Temperature for shot 2791,  $CO_2$ , at  $Re_E = 1.00, 5.00 \times 10^4,$  and  $1.00 \times 10^6$ ; the profiles show rapid relaxation.

the polyatomic species,  $e_v$  is the local vibrational energy,  $e_{v-eq}$  is the local equilibrium vibrational energy. The weighted time scale of relaxation for species  $i$  is

$$\tau_i = \frac{\sum_{r=1}^{ns} \rho_r / M_r}{\sum_{r=1}^{ns} \rho_r / M_r / \tau_{i,r}}, \quad (2.7)$$

where  $r$  is the collisional partner,  $\rho_r$  is the density of the collisional partner,  $M_r$  is the molecular weight of the collisional partner, and  $\tau_{i,r}$  is the relaxation of polyatomic species  $i$  with collisional partner  $r$ . For  $N_2$ ,  $O_2$ ,  $NO$ , and  $CO$ , the semi-empirical curve

fits from [Millikan and White \(1963\)](#) are used and have the form

$$\tau_{i,r} = \exp(A_{i,r}T^{-1/3} + B_{i,r})/P, \quad (2.8a)$$

$$A_{i,r} = 1.16 \times 10^{-3} \mu_{i,r}^{1/2} \theta_{v,i}^{4/3}, \quad (2.8b)$$

$$B_{i,r} = -0.015 A_{i,r} \mu_{i,r}^{1/4} - 18.42, \quad (2.8c)$$

$$\mu_{i,r} = \frac{M_i M_r}{M_i + M_r}, \quad (2.8d)$$

where  $P$  is in atmospheres, and  $\theta_{v,i}$  is the characteristic temperature of vibration of species  $i$ . For  $\text{CO}_2$ , the four vibrational modes relax at the same rate, and the relaxation rates are taken from the fits to the data in [Camac \(1966\)](#),

$$\tau_{\text{CO}_2} = \exp(36.5T^{-1/3} - 3.9)/P, \quad (2.9)$$

where  $\tau_{\text{CO}_2}$  is in microseconds,  $T$  is in Kelvin, and  $P$  is in atmospheres.

From Eqs. [2.7](#), [2.8](#), and [2.9](#), using the edge conditions as representative properties (tabulated in section [A.3](#)), quantitative estimates of characteristic times scales of relaxation can be made. For shot 2767 (air),  $\tau_{\text{N}_2}$ ,  $\tau_{\text{O}_2}$ , and  $\tau_{\text{NO}}$  are calculated to be 29 ms, 150  $\mu\text{s}$ , and 2 ms, respectively. Due to the faster relaxation time and moderate mass fraction,  $\text{O}_2$  likely dominates the translational/rotational and vibrational transfer of energy per Eq. [2.6](#) in air flows near these reservoir conditions. This qualitatively matches the previously observed relaxation time scale of  $L_{\text{cone}}/U_E = 1 \text{ m}/3700 \text{ m/s} \approx 270 \mu\text{s}$  (Fig. [2.11\(a\)](#)). The observed lack of vibrational relaxation for shot 2773 ( $\text{N}_2$ ) is again apparent, as the calculated relaxation time is  $\tau_{\text{N}_2} = 950 \text{ ms}$ .

For shot 2791 ( $\text{CO}_2$ ),  $\tau_{\text{CO}_2}$ ,  $\tau_{\text{O}_2}$ , and  $\tau_{\text{CO}}$ , are 2.3  $\mu\text{s}$ , 85  $\mu\text{s}$ , and 4 ms, respectively. Because of the high mass fraction, fast relaxation time, and multiple relaxing vibrational modes,  $\text{CO}_2$  likely dominates the translational/rotational and vibrational transfer of energy per Eq. [2.6](#) in  $\text{CO}_2$  flows near these reservoir conditions. The previously observed relaxation time ( $\delta/U_E = 1 \text{ mm}/3000 \text{ m/s} \approx 0.33 \mu\text{s}$ ), is close to the

order of the calculated value for  $\tau_{\text{CO}_2}$ .

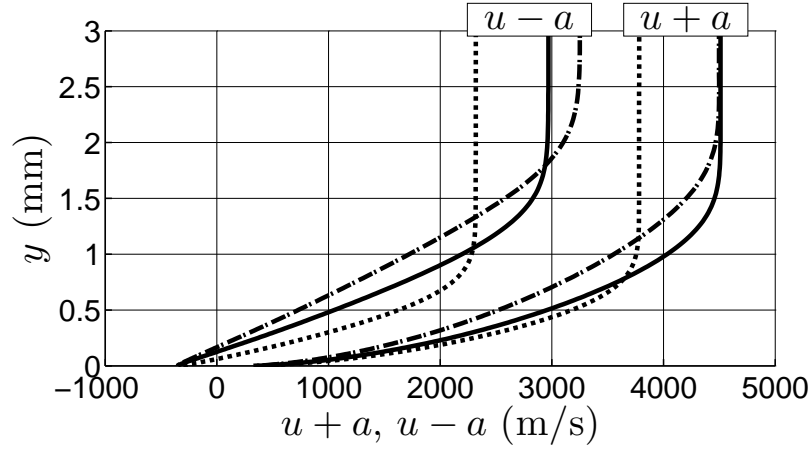


Figure 2.12:  $u \pm a$  profiles at edge Reynolds number of  $1 \times 10^6$  for shot 2767 (air, solid line), shot 2773 ( $\text{N}_2$ , dash-dot line), shot 2791 ( $\text{CO}_2$ , dashed line).

According to [Fedorov \(2011\)](#), modes of instability in high-speed boundary layers have time scales and length scales close to those of fast and slow acoustic waves, in particular when close to the leading edge or tip of an article. The dimensional  $u \pm a$  profiles are plotted in Fig. 2.12, noting that the sound speed does not include the contribution(s) from the vibrational degree(s) of freedom. The difference between  $u \pm a$  with and without the contribution from the vibrational degree of freedom is small (max  $\approx 2\%$ ).

## 2.5 Uncertainty Estimate

In this section, the uncertainty associated with the run conditions is estimated. The bias uncertainty is propagated through the data processing procedure. The repeatability is discussed and supported with an FLDI example and a reference to earlier work.

### 2.5.1 Reservoir Conditions Bias Uncertainty Estimate

An estimate of the bias error of the reservoir conditions is made in this subsection. The north and south reservoir pressure gauge time traces from shot 2789 are plotted in Fig 2.2(a). The mean between the gauges of the mean during the steady pressure period is boxed along with the standard deviation which serves as an estimate of error in the measurement.

The uncertainty in shock speed due to viscous deceleration effects is estimated to be 5%. The uncertainty in shock speed due to time of arrival measurement error is estimated to be 5%. Combining these two errors in primary shock speed in a root-mean-squared sense results in an uncertainty estimate of 7%.

The bias uncertainty in the reservoir conditions is estimated by considering the propagation of error as in [Kline and McClintock \(1953\)](#), [Coleman and Steele \(1999\)](#), and [Beckwith et al. \(2007\)](#). It is assumed that the uncertainty in the input parameters ( $P_1$ ,  $P_R$ , and  $U_S$ ) will dominate the uncertainty that results from the calculation method and the uncertainty in the tabulated thermodynamic data. The uncertainty  $u$  in reservoir parameter  $Q_R$  is estimated as

$$u_{Q_R} = \sqrt{\left(u_{U_S} \frac{\partial Q_R}{\partial U_S}\right)^2 + \left(u_{P_R} \frac{\partial Q_R}{\partial P_R}\right)^2 + \left(u_{P_1} \frac{\partial Q_R}{\partial P_1}\right)^2}, \quad (2.10)$$

noting that derivatives cannot be found analytically and are approximated by the finite difference method. Additionally, the input variables  $P_1$ ,  $P_R$ , and  $U_S$  are not correlated. Results from this estimate are tabulated in Table 2.1.

Table 2.1: Uncertainty in Reservoir Conditions

| Q    | Input |       |       | Output  |       |                      |           |           |          |       |       |
|------|-------|-------|-------|---------|-------|----------------------|-----------|-----------|----------|-------|-------|
|      | $P_1$ | $P_R$ | $U_S$ | $h_R$   | $T_R$ | $\rho_R$             | $y_{N_2}$ | $y_{O_2}$ | $y_{NO}$ | $y_N$ | $y_O$ |
|      | (kPa) | (MPa) | (m/s) | (MJ/kg) | (K)   | (kg/m <sup>3</sup> ) | (-)       | (-)       | (-)      | (-)   | (-)   |
|      | 70.0  | 56.4  | 3491  | 11.9    | 6934  | 24.53                | 0.696     | 0.024     | 0.115    | 0.017 | 0.147 |
| u    | 0.5   | 1.8   | 244   | 1.3     | 480   | 2.36                 | 0.005     | 0.010     | 0.012    | 0.010 | 0.017 |
| u(%) | 0.7   | 3.2   | 7.0   | 11      | 7     | 10                   | 0.7       | 43        | 11       | 62    | 11    |

## 2.5.2 Nozzle Calculation Bias Uncertainty Estimate

In this subsection, the bias uncertainty of the nozzle calculation is estimated. The steady expansion of flows in thermo-chemical non-equilibrium is known to be sensitive to inputs, particularly the static conditions (Ebrahim and Hornung, 1973, 1975). The solver for the mean flow over the cone requires values from a single point (a single value, not a field, for density, temperature, etc.). To best estimate what the appropriate values are for this point, uncertainties due to the propagation of error in the inputs to the nozzle code and uncertainty due to spatial inhomogeneity from the output of the nozzle code are combined in a root-means-squared sense.

The nozzle code requires  $T_R$ ,  $\rho_R$ , and mass fractions ( $y_i$ ) as inputs from the reservoir calculation. The mass fractions are not considered as inputs in the following uncertainty estimate because they are determined by  $T_R$  and  $\rho_R$ . It is assumed that the uncertainty in the input parameters dominates uncertainty that results from the calculation method and the uncertainty in the tabulated thermodynamic/kinetic data. The uncertainty  $u$  in nozzle exit parameter  $Q_X$  is estimated as

$$u_{Q_X} = \sqrt{\left(u_{T_R} \frac{\partial Q_X}{\partial T_R}\right)^2 + \left(u_{\rho_R} \frac{\partial Q_X}{\partial \rho_R}\right)^2 + 2\Upsilon_{(T_R, \rho_R)} \frac{\partial Q_X}{\partial T_R} \frac{\partial Q_X}{\partial \rho_R} u_{T_R} u_{\rho_R}}, \quad (2.11)$$

noting that derivatives cannot be found analytically and are approximated by the finite difference method. The correlation between  $T_R$  and  $\rho_R$  is included in this analysis as the third term in the square root in Eq. 2.11, where the correlation coefficient is  $\Upsilon_{(T_R, \rho_R)}$ . Choosing  $\Upsilon_{(T_R, \rho_R)} = 0$  or  $\Upsilon_{(T_R, \rho_R)} = \pm 1$  results in little change in the value for  $u_{Q_x}$  ( $\approx 0.1\%$ ), so that obtaining a value for  $\Upsilon_{(T_R, \rho_R)}$  is not necessary.

Additionally, there is uncertainty in the nozzle exit conditions due to spatial inhomogeneity. In Fig. 2.13 an overlay of contours of density in the nozzle, the five degree half-angle cone, the oblique shock wave, and streamlines illustrate the calculated spatial inhomogeneity as it pertains to this test series. Contours of density

are chosen for illustration of the inhomogeneity because density has the largest spatial standard deviations. The shock angle and streamlines are calculated from the [Taylor, G. I. and Maccoll, J. W.](#) solution, assuming a nominal exit condition.

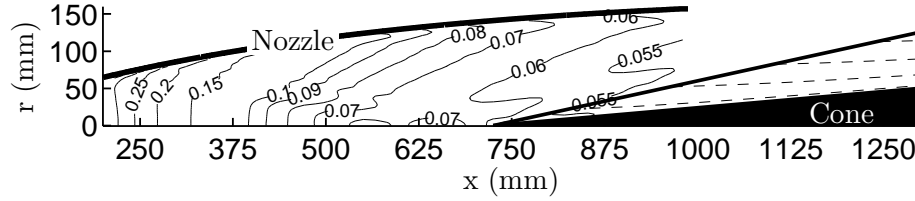


Figure 2.13: An overlay of the computed density, cone, shock, and streamlines for shot 2789. The units of density are  $\text{kg/m}^3$ . The shock angle and streamlines are calculated from the [Taylor, G. I. and Maccoll, J. W.](#) solution. Density represents the largest spatial standard deviations.

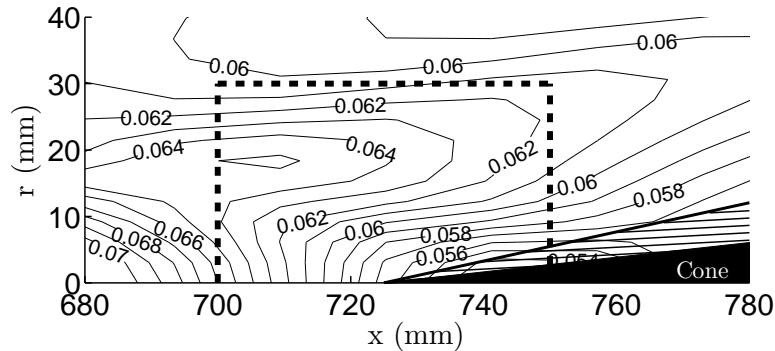


Figure 2.14: Zoomed-in presentation of density contours in nozzle.

The nominal exit condition is obtained by inspecting the volume of fluid that is most important to boundary-layer analysis. We assume this to be the volume of gas with streamlines that nearly intersect the boundary layer at the end of the cone. For all experiments in this work no boundary-layer thickness exceeds 4 mm at the end of the 1 m long cone, so the volume of gas that is to be spatially averaged has a radius of 30 mm (Fig. 2.15). The length of the volume of gas to be averaged over is the estimated uncertainty in the measured cone position, in this example  $725 \pm 25$  mm

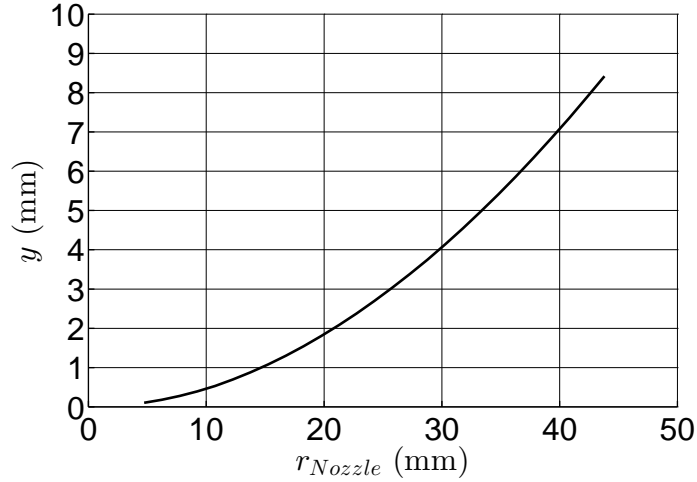


Figure 2.15: The wall normal distance from the cone vs. the radius in the nozzle.

(Fig. 2.14). The spatial inhomogeneity is assumed to be the standard deviation of the parameters in the chosen volume. The estimate of uncertainty in the calculated values, per Eq. 2.11, and the spatial inhomogeneity are combined in a RMS sense and tabulated in Table 2.2.

Table 2.2: Uncertainty in Nozzle Conditions

| Q    | Input                            |              | Output         |                                  |                |              |               |              |                  |                  |                 |              |              |
|------|----------------------------------|--------------|----------------|----------------------------------|----------------|--------------|---------------|--------------|------------------|------------------|-----------------|--------------|--------------|
|      | $\rho_R$<br>(kg/m <sup>3</sup> ) | $T_R$<br>(K) | $U_X$<br>(m/s) | $\rho_X$<br>(kg/m <sup>3</sup> ) | $P_X$<br>(kPa) | $T_X$<br>(K) | $Tv_X$<br>(K) | $M_X$<br>(-) | $y_{N_2}$<br>(-) | $y_{O_2}$<br>(-) | $y_{NO}$<br>(-) | $y_N$<br>(-) | $y_O$<br>(-) |
|      | 24.5                             | 6934         | 4322           | 0.060                            | 32.4           | 1824         | 1837          | 4.97         | 0.734            | 0.168            | 0.071           | 0.000        | 0.027        |
| u    | 2.4                              | 480          | 216            | 0.006                            | 5.67           | 274          | 276           | 0.35         | 0.001            | 0.008            | 0.002           | 0.000        | 0.008        |
| u(%) | 9.6                              | 6.9          | 5              | 10                               | 18             | 15           | 15            | 7            | 0.1              | 5                | 2.5             | -            | 30           |

### 2.5.3 Cone Flow Calculation Bias Uncertainty Estimate

The bias uncertainty in the cone mean flow solution is estimated in this subsection by assessing the effects of the code inputs on the conditions at the edge of the boundary layer. Again, it is assumed that the uncertainty in the input parameters ( $U_X$ ,  $T_X$  and  $\rho_X$ ) will dominate the uncertainty that results from the calculation method and the uncertainty in the tabulated thermodynamic/kinetic data. The uncertainty  $u$  in cone

edge parameter  $Q_E$  is estimated as

$$u_{Q_E} = \sqrt{\left(u_{U_X} \frac{\partial Q_E}{\partial U_X}\right)^2 + \left(u_{T_X} \frac{\partial Q_E}{\partial T_X}\right)^2 + \left(u_{\rho_X} \frac{\partial Q_E}{\partial \rho_X}\right)^2}, \quad (2.12)$$

noting that derivatives cannot be found analytically and are approximated by the finite difference method. The edge parameters are sampled at the location of the upstream FLDI probe volume. The results are tabulated in Table 2.3.

Table 2.3: Uncertainty in Edge Conditions

| Q    | Input |                      |       | Output |                      |       |       |          |       |            |
|------|-------|----------------------|-------|--------|----------------------|-------|-------|----------|-------|------------|
|      | $U_X$ | $\rho_X$             | $T_X$ | $U_E$  | $\rho_E$             | $P_E$ | $T_E$ | $T_{VE}$ | $M_E$ | $\delta_U$ |
|      | (m/s) | (kg/m <sup>3</sup> ) | (K)   | (m/s)  | (kg/m <sup>3</sup> ) | (kPa) | (K)   | (K)      | (-)   | ( $\mu$ m) |
|      | 4322  | 0.060                | 1824  | 4248   | 0.074                | 46    | 2084  | 1949     | 4.57  | 1183       |
| u    | 216   | 0.006                | 274   | 212    | 0.010                | 7     | 313   | 313      | 0.37  | 118        |
| u(%) | 5     | 10                   | 15    | 5      | 14                   | 15    | 15    | 15       | 8     | 10         |

## 2.5.4 Repeatability of Conditions

In this subsection, the variation of run conditions from shot to shot in the reflected-shock tunnel is commented on, and examples of repeatable experiments are presented. In [Hornung \(1992\)](#), the results from a series of five experiments in T5 are presented with the goal of conveying how repeatable the reservoir conditions are. The shock speed and reservoir pressure have low standard deviations on a shot to shot basis (Table 2.4). This is one reason of why researchers that use T5 can seek trends in their work with confidence.

Table 2.4: Shot Series Data from [Hornung \(1992\)](#)

| Shot         | 140  | 141  | 142  | 143  | 144  | STD         |
|--------------|------|------|------|------|------|-------------|
| $U_S$ (km/s) | 4.76 | 4.72 | 4.76 | 4.74 | 4.78 | 0.02 (< 1%) |
| $P_R$ (MPa)  | 57   | 55   | 58   | 60   | 60   | 2.12 (< 4%) |

During the tunnel noise campaign that is discussed in detail in section 4.1, a Pitot rake was installed at the nozzle exit. The Pitot rake was instrumented with

PCB113a21 piezo-electric pressure transducers and a PCB483M89 signal conditioner. The signals were sampled at 500 kHz. Pitot pressure measurements at nominally the same run conditions show that, at each location, the difference in Pitot pressure is no more than 4% different from each other, except for the value near the nozzle wall (150 mm) (Fig. 2.16(a)). The Pitot pressure measurement nearest to the wall was not found to be reliable, possibly due to the nozzle-wall boundary layer or an unknown experimental blunder.

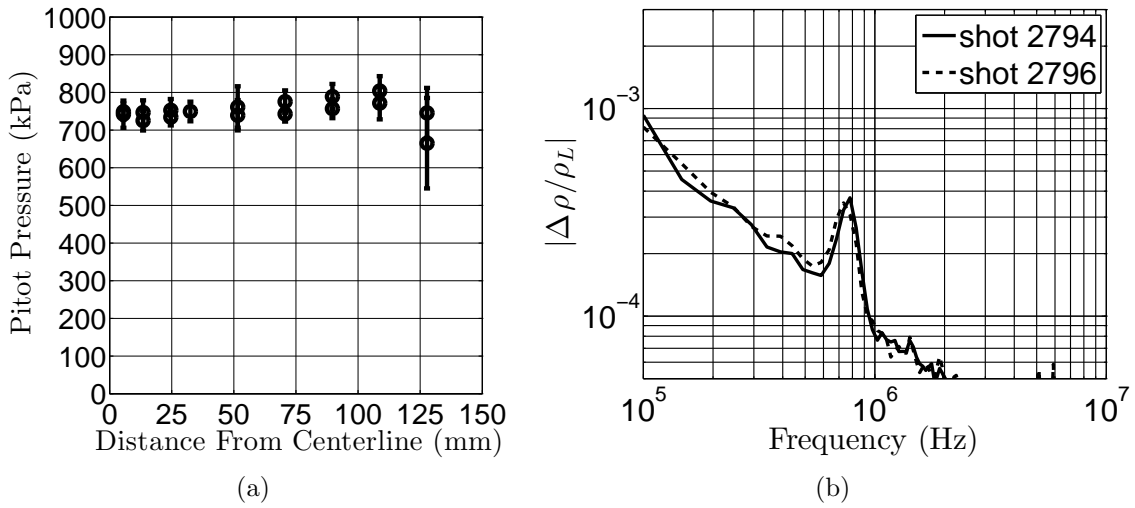


Figure 2.16: a: Pitot pressure measurements for shots 2691 and 2692. These shots are performed at nearly the same operating conditions in air, and the Pitot pressures at each location are no more than 4% different from each other, except for the value near the nozzle wall (150 mm). The error bars represent the standard deviation of the signal during the test time. b: Two instability measurements from shots 2694 and 2696 ( $\text{CO}_2$ ). These measurements are at the same nominal reservoir condition and at the same spatial location on the cone. Note two aspects of agreement, the peak amplitude and the peak frequency.

The agreement of two consecutive Pitot pressure measurements is useful, but this evidence may be met with skepticism if a researcher would claim this repeatability can be extended to something as sensitive as the instability of a hypervelocity boundary layer. The most amplified frequency in a hypervelocity boundary layer is  $f \approx 0.8U_E/(2\delta)$ , noting that  $\delta \propto M_E^2/\sqrt{Re_s/(T_W/T_E)^{-1/3}}$  (Fig. 2.7(b)). This indicates that the peak frequency is a strong function of the velocity and thermodynamic

state at the edge of the boundary layer. Repeating the peak frequency at the same nominal reservoir conditions would indicate excellent repeatability of the velocity and static conditions at the boundary-layer edge. Furthermore, repeatability of the peak amplitude in acoustic instability at the same nominal reservoir conditions would indicate a small shot to shot variation of the noise environment. Excellent shot to shot agreement for a CO<sub>2</sub> shot is presented in Fig. 2.16(b). Shot to shot repetition of the velocity and thermodynamic state at the edge of the boundary layer, and repeating the tunnel noise environment is crucial for researchers who seek trends in hypervelocity boundary-layer instability, as is done in this work.

# Chapter 3

## FLDI Measurement Technique

The focused laser differential interferometry (FLDI) measurement technique is presented in this chapter. For context, past research efforts to make instability measurements within a high-speed boundary layer are reviewed. The experimental setup, the methodology of extracting quantitative results, bench test results, and uncertainty estimates are included.

### 3.1 Instability Measurement Technique Review

Measurements of the instability within the boundary layer on a sharp right circular cone at zero angle of attack at hypersonic Mach numbers have been made with a number of measurement techniques. [Kendall \(1975\)](#), [Demetriades \(1977\)](#) and [Stetson et al. \(1983, 1984, 1989\)](#) appear to have made the first measurements of the acoustic instability with hot-wire anemometry. Demetrides observed that the frequency of the instability,  $f$ , is proportional to the velocity at the boundary-layer edge  $U_E$ , and inversely proportional to the boundary-layer thickness,  $\delta$ :  $f \propto KU_E/(2\delta)$ , where  $K$  is a constant of proportionality, typically of value 0.6-0.9. In [Kimmel et al. \(1996\)](#), extensive circumferential, streamwise, and wall-normal space-time correlations of detailed hot-wire anemometry data form the basis of some understanding of the boundary-layer instability structure.

Piezo-electric pressure transducers with a resonant frequency of up to 1 MHz are commercially available; these can be flush mounted to the surface of the test article to record high-speed pressure fluctuations in the boundary layer. [Fuji \(2006\)](#) used pressure transducers placed along a generator of a 5 degree half-angle cone to assess the effect of a wavy-wall roughness on the growth of the boundary-layer instability. [Fuji et al. \(2011\)](#) used the surface mounted pressure transducers to measure the second-mode instability and its growth rate along a generator of the cone. Additionally, the non-linear phase-coupling of the disturbances was analyzed by the bicoherence method in that report. [Casper \(2009\)](#) and [Berridge \(2010\)](#) have made hypersonic boundary-layer instability measurements with the same piezo-electric pressure transducers, performing their tests in a low-disturbance hypersonic facility.

Fast-response heat-flux gauges have also been utilized to measure the high-frequency fluctuations in a hypersonic boundary layer. The atomic layer thermopile (ALTP) developed by [Roediger et al. \(2008\)](#) is claimed to have a frequency response of up to 1 MHz. [Roediger et al. \(2009\)](#) utilized ALTP gauges to measure the second-mode instability waves and compare the experimentally observed growth rates to growth rates calculated from linear stability theory. [Heitmann et al. \(2011\)](#) utilized such heat-flux gauges to measure instabilities that are artificially excited in a hypersonic boundary layer with a pulsed Nd:YAG laser.

The grid and lens style focused schlieren setup was developed by [Boedeker \(1959\)](#) and refined by [Weinstein \(1993\)](#) and [Garg and Settles \(1998\)](#). It is a candidate for high-speed measurement of density fluctuation because of the fast response time and nonintrusive nature. [VanDercreek \(2010\)](#), [VanDercreek et al. \(2010\)](#) utilized this technique in their research, making measurements of the second-mode instability with the focused-schlieren deflectometer as well as with piezo-electric pressure transducers. Good agreement in the narrowband spectral content between the focused schlieren setup and the pressure transducers was demonstrated. Resonantly enhanced focused-

schlieren work in T5 has yielded some promising results ([Parziale et al., 2011](#)). Peaks in the spectral content at frequencies consistent with the acoustic instability were found along with detection of turbulent bursts; however, the method of resonantly enhanced focused-schlieren makes quantitative interpretation of the results difficult. [Hofferth et al. \(2013\)](#) used the focused schlieren technique to measure the second-mode waves in a low-disturbance wind tunnel. The high SNR allowed bispectral analysis of the data. Additionally, the researchers used the focused schlieren technique to assess the sensitivity of the most amplified disturbance to the cone's angle of attack.

Optical tracking of turbulent spots in the boundary layer on a cone has been reported from T5. This was done by introducing trace amounts of a seed gas with a strong line-strength (vaporized lithium) to the test gas, and focusing the spontaneous emission from a point of interest (the boundary layer) onto a fiber-coupled photodetector ([Parziale et al., 2012a](#)). The data reduction scheme in this report was complex and exhibited large error bounds. This work was ultimately unsuccessful in measuring the boundary-layer instability.

Two-beam laser differential interferometry (LDI) is a measurement technique that was used to experimentally characterize gas-dynamic flows by Smeets and George at the French-German Research Institute of Saint-Louis (ISL) in the 1970's ([Smeets, 1972, 1973, 1974, 1977, Smeets and George, 1973](#)). The technique is sensitive to changes in optical path length that are related to density by the Gladstone-Dale relation. Smeets and George proposed dozens of iterations of the two-beam interferometer which were cleverly applied to demonstrator-type problems in non-steady gas-dynamics, steady compressible aerodynamics, and acoustics. Each of these iterations of the LDI are clearly described with well annotated schematics in the previously cited reports.

[Laderman and Demetriades \(1976\)](#) used the LDI method as a boundary-layer

transition detection tool at Mach 3; they used a line-of-sight integrating LDI to detect increases in the RMS fluctuations in the boundary layer and related the increases in RMS fluctuation to transition to turbulence. [Azzazy et al. \(1985, 1986, 1987\)](#) discusses the LDI as a turbulence detection tool in a shear-layer, on a wind-tunnel wall at low subsonic Mach number, and in a Mach 2.36 boundary layer. They appear to have made measurements of transition in the shear-layer and on the subsonic wind-tunnel wall, even resolving some low frequency ( $< 100$  kHz) spectral content. They discuss the possibility of “transition signal” detection in a Mach 2.36 boundary layer with LDI, but the electronics used in that study were of insufficient frequency response, and this could be one reason why they were unable to resolve any instability or transition signals at Mach 2.36.

[O’Hare \(1985\)](#) used a form of LDI slightly different from that of Smeets and George to detect hypersonic boundary-layer transition. The LDI in [O’Hare \(1985\)](#) was a line-of-sight integrating setup that imaged a shift in the fringe pattern formed on a wind tunnel wall by two beams, one of which probed the boundary layer, the other traversed the mean flow outside of the boundary layer. What appear to be second-mode type frequencies were observed to have some agreement with hot-wire anemometry, although the SNR was poor and the frequency response appeared to be adequate only up to less than 200 kHz. [Collicott et al. \(1996\)](#) suggests the use of the LDI to make measurements of the instability in a Mach 4 boundary layer, but follow-up reports cannot be readily found. Finally, [Schneider \(2004\)](#) suggests that measurements of boundary-layer instability in impulse high-enthalpy hypersonic wind tunnels, such as T5, would be “difficult.”

## 3.2 Focused Laser Differential Interferometry

To measure the acoustic instability on a slender body in a large scale hypervelocity ground-test facility (such as the T5 reflected-shock tunnel), six requirements of the diagnostic are clear: 1) high sensitivity to an unstable quantity in the boundary layer, 2) high temporal resolution of the measurement technique ( $> 10$  MHz), 3) high spatial resolution to resolve the small wavelength of the disturbance ( $< 1$  mm), 4) insensitivity to mechanical vibration, 5) the capability to have a small focal volume near the surface of the cone, and 6) a straightforward and repeatable means of extracting quantitative data from the technique.

The focused laser differential interferometer (FLDI) meets these requirements. To build on what has been reported in the literature, two essential aspects for instability measurement with the LDI method are identified as the ability to *focus*, and advances in *technology*.

The ability to focus, or make localized measurements of fluctuation, is necessary because the turbulent shear-layers from the nozzle wall (noted as TSL in Fig. 3.1) in our test facility can dominate a line-of-sight integrating optical measurement technique.<sup>1</sup> The ability to probe only a small volume, especially in the spanwise direction, significantly raises the achievable SNR relative to a line-of-sight integrating scheme. Smeets (1973) utilized a scheme very similar to the one presented in this work. He made measurements of localized turbulent fluctuations in a free-jet desktop type experiment. Quantitatively characterizing instabilities on a test article in a large-scale impulse hypersonic facility requires careful optical design. The layout is nominally the same as in Smeets (1973), but the dimensions, kinematics, and plane of laser beam separation are specifically designed for the purposes of hypervelocity instability

---

<sup>1</sup>This assertion is likely true for many conventional supersonic/hypersonic wind tunnels. This assertion may even be true of high-speed low-disturbance tunnels because the “quiet core” may be surrounded by regions of flow that are affected by noise radiated from a turbulent boundary layer on the nozzle wall.

measurement. The system is described in the following section 3.2.1.

Advances in technology have been crucial to the success of the measurement. Low-cost high vertical-resolution digitizers that are able to operate at high sampling rate for long duration are now available. This allows researchers to perform exceedingly detailed measurements at sufficient speed for instability work. Additionally, high-speed, low-cost, low-noise amplifiers are also now available. High-quality amplifiers allow researchers to be prudent in how they wire the experiment for digitization, specifically: how the signal is terminated, so that ambient electrical noise (RF) may be reduced to acceptable levels.

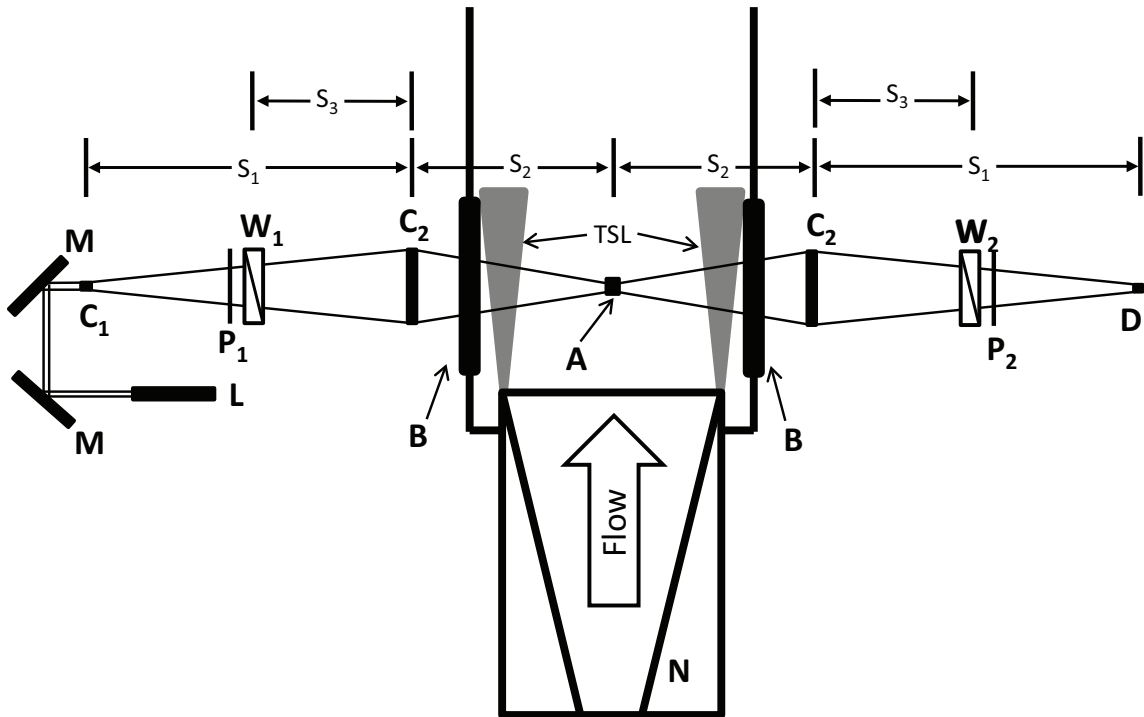


Figure 3.1: Annotated schematic of the FLDI. TSL, turbulent shear layer, L, Laser; M, mirror; C<sub>1</sub>, 10 mm focal length lens; C<sub>2</sub>, 300 mm focal length lens; P, polarizer; W, Wollaston prism; B, BK7 window; A, probe volume; D, photodetector; N, nozzle,  $s_1 = 718$  mm,  $s_2 = 515$  mm,  $s_3 = 300$  mm

### 3.2.1 Description of FLDI Setup

The laser used in this experiment is a Spectra-Physics Excelsior diode pumped solid state continuous-wave laser (532 nm wavelength, 200 mW power). The high quality beam ( $\text{TEM}_{00}$ ) does not require additional beam conditioning for use as an interferometer. Following the optical path in Fig. 3.1, starting from the laser (L), the beam is turned by a periscope arrangement for precise directional control. The beam is expanded by a lens,  $C_1$  (10 mm focal length), and linearly polarized by  $P_1$  at  $45^\circ$  to the plane of separation of the first Wollaston prism,  $W_1$  (United Crystals). The normal to the plane of separation of  $W_1$  is chosen to be orthogonal to streamlines in the boundary layer of the five degree half-angle cone. The prism splits the light by a narrow angle (2 arc minutes) into orthogonally polarized beams. The separation of the beams is fixed at  $350 \mu\text{m}$  by a lens,  $C_2$  (300 mm focal length), while the diameter of the beams is reduced to small values in the center of the test section. This arrangement creates two beams with orthogonal polarization that traverse much of the same optical path. The orthogonally polarized beams do not share the same optical path within  $\pm 10$  mm of the focal point (along the beam direction, centered at A in Fig. 3.1). In this region the beams are calculated to be less than  $100 \mu\text{m}$  in diameter, and traverse separate but very closely spaced volumes; they are  $350 \mu\text{m}$  apart (assuming  $1/e^2$  Gaussian beam propagation, [Siegman \(1986\)](#)). It is primarily within this small focal region that the diagnostic is sensitive to changes in optical path length (OPL). The spatial resolution of the technique ( $700 \mu\text{m}$ ) is set by doubling the beam spacing to satisfy the Nyquist sampling theorem. Beyond the beam focus, the optical paths are again common and an additional lens,  $C_2$  (300 mm focal length), re-focuses the beams. The second Wollaston prism,  $W_2$ , and polarizer,  $P_2$ , recombine and then mix the orthogonally polarized beams, such that the interference will be registered as irradiance fluctuations by the photodetector. The response of the photodetector (22.5 V battery biased FDS100 photodiode) is amplified at a gain of 5 for the single

probe volume system and 25 for the double probe volume system (SRS SR445) and digitized at 100 MHz by a 14-bit Ethernet oscilloscope (Cleverscope CS328A-XSE); all leads are terminated at 50 Ohms.

### 3.2.2 Relation Between Density and Voltage

The FLDI technique detects differences in phase primarily due to the density differences at the two focal regions, which are separated in the streamwise direction, making the interferometer sensitive to spatial density differences in the streamwise direction. A relation between the fluctuations in density and output voltage from the photodetector is needed for post-processing. This relation is found by considering the region within  $\pm 10$  mm of the focal point, along the beam direction (where the optical paths are not common), to be a two-beam differential interferometer.

Interference of the two beams with electric fields  $E_1$  and  $E_2$  occurs along the transmission axis of the second polarizer,  $P_2$ . The two electric fields have amplitude  $A_i$ , wavenumber  $k$ , angular frequency  $\omega$ , and phase  $\phi_i$ ,

$$E_1 = A_1 \exp(j(kz - \omega t + \phi_1)), \quad (3.1a)$$

$$E_2 = A_2 \exp(j(kz - \omega t + \phi_2)). \quad (3.1b)$$

The relation for irradiance at the photodetector's surface,  $I_d$ , due to change in phase is found by superimposing electric fields,  $E = E_1 + E_2$ , as

$$I_d = \langle EE^* \rangle = \langle (E_1 + E_2)(E_1 + E_2)^* \rangle, \quad (3.2a)$$

$$I_d = A_1^2 + A_2^2 + 2A_1A_2 \cos(\phi_2 - \phi_1), \quad (3.2b)$$

$$I_d = I_1 + I_2 + 2\sqrt{I_1I_2} \cos(\Delta\phi), \quad (3.2c)$$

where  $\Delta\phi$  is the phase change at the beam focus, and the amplitude  $A_i$  is the square

of the irradiance,  $I_i$ .  $I_1$  and  $I_2$  are equal,  $I_1 = I_2 = I_0$ . The relation between the change in optical path length and the change in phase (Born and Wolf, 1997) is

$$\Delta\phi = \frac{2\pi}{\lambda_0}\Delta OPL \approx \frac{2\pi}{\lambda_0}L\Delta n, \quad (3.3)$$

where  $L$  is the integration length over the phase object in the focal region,  $\Delta n$  is the change in refractive index between the two beams, and  $\lambda_0$  is the wavelength of the laser. From the Gladstone-Dale relationship (Liepmann and Roshko, 1957),

$$n = K\rho + 1, \quad (3.4)$$

where  $K$  is the Gladstone-Dale constant, Eq. 3.3 becomes

$$\Delta\phi = \frac{2\pi}{\lambda_0}LK(\rho_{\parallel} - \rho_{\perp}) = \frac{2\pi}{\lambda_0}LK\Delta\rho. \quad (3.5)$$

The change in phase,  $\Delta\phi$ , is due to the difference in density,  $\rho_{\parallel} - \rho_{\perp} = \Delta\rho$ . The densities are the instantaneous local densities interrogated by the beams polarized parallel ( $\rho_{\parallel}$ ) and orthogonal ( $\rho_{\perp}$ ) to the streamlines in the boundary layer. The two beams are spaced 350  $\mu\text{m}$  apart, and the phase object is integrated over the OPL,  $L$  (within  $\pm 10$  mm of the focal point). The integration length over the phase object is found by inspecting an overlay (Fig. 3.2) of the calculated boundary-layer thickness and calculated beam profile (assuming Gaussian beam propagation). The determination of the integration length is described in more detail in section 3.2.5.

For comparison between experiments it is more convenient to think of density changes in non-dimensional terms. Normalizing  $\Delta\rho$  by the mean local density  $\rho_L$ , makes Eq. 3.5,

$$\Delta\phi = \frac{2\pi}{\lambda_0}LK\rho_L\frac{\Delta\rho}{\rho_L}. \quad (3.6)$$

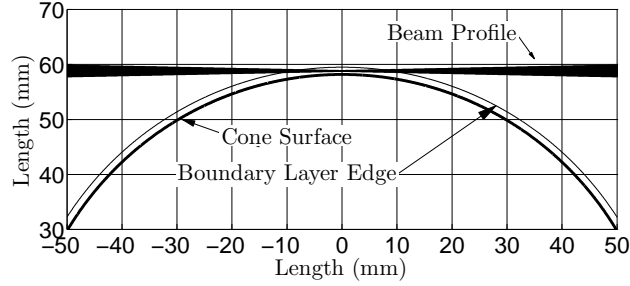


Figure 3.2: Overlay of the calculated boundary-layer thickness and calculated beam profile (assuming Gaussian beam propagation)

The potential response of the photodetector,  $V$  is expressed as

$$V = I\mathcal{R}R_L, \quad (3.7)$$

where  $\mathcal{R}$  is the responsivity of the photodiode and  $R_L$  is the load resistance. A relation for the normalized change in density in terms of the output voltage of the photodetector and several fixed parameters in the experiment is found by combining Eqs. 3.2, 3.6 and 3.7 as

$$\frac{\Delta\rho}{\rho_L} = \frac{\lambda_0}{2\pi KL\rho_L} \sin^{-1} \left( \frac{V}{V_0} - 1 \right). \quad (3.8)$$

The interferometer is set to the most linear part of a fringe before each experiment, so there is a  $\pi/2$  rad phase shift introduced, and  $V_0 = 2I_0\mathcal{R}R_L$ . During the experiments, the phase shift,  $\Delta\phi$ , is less than  $\pi/3$  rad, so there is no fringe ambiguity.

For all shots, the wall-normal distance from the surface of the cone to the volume being probed by the FLDI is measured with a Mitutoyo dial-indicator, translating a razor-blade cutoff normal to the surface of the cone. Wall-normal distances range from 450-990  $\mu\text{m}$ , and the uncertainty is estimated to be  $\pm 50 \mu\text{m}$ ; this is the calculated beam diameter, which is noted to be twice the precision of the dial-indicator. The distance from the cone tip is measured with a measuring tape. Probe volume

distance from the cone tip ranges from 627-783 mm. The uncertainty is estimated to be  $\pm 1$  mm, which is the precision of the measuring tape. Throughout the test campaign the following are changed to optimize the experimental setup: the number of probe volumes, probe volume wall-normal distance, and probe volume distance from the cone tip. Detailed records of these values and local boundary-layer thickness are tabulated in appendix B. The nose-tip radius is measured to be  $400 \mu\text{m}$  with a Mitutoyo caliper. Following Rotta (1966) and Stetson (1983), the entropy layer swallowing distance for all cases is calculated to be no more than 90 mm, or less than 15% of the distance from the cone tip to any probe volume; therefore, the cone may be considered “sharp” at the probe-volume locations.

### 3.2.3 Bench Test: Evaluation of Sensitive Region

This subsection describes a bench test designed to experimentally evaluate the sensitive region of the FLDI. A subsonic turbulent  $\text{CO}_2$  jet is traversed in the horizontal spanwise direction along the direction of beam propagation (schematic in Fig. 3.3(a)). The metric used to evaluate the size and character of the sensitive region in the spanwise direction is the amplitude of fluctuation at the focus relative to the amplitude of fluctuation at a distance from the focus. The rms value of the phase function,

$$rms(\Delta\phi) = \sqrt{\frac{1}{N} \sum_{i=1}^N (\Delta\phi_i)^2}, \quad (3.9)$$

is used as the measure of fluctuation, where  $N$  is the number of samples and  $\Delta\phi$  (as in Eq. 3.6) in terms of the potentials  $V$  and  $V_0$ , is,

$$\Delta\phi = \sin^{-1} \left( \frac{V}{V_0} - 1 \right). \quad (3.10)$$

The bench tests were conducted in the following manner: 1) Place the nozzle

approximately 2 millimeters from the focus of the FLDI (this initial position is shown in Fig. 3.3(a)), 2) record data for 15 milliseconds, 3) translate the nozzle a small distance in the spanwise direction, 4) record data for 15 milliseconds, 5) repeat steps 3 and 4 until perturbations in the oscilloscope readout are no longer perceptible. The jet was confirmed to be subsonic by high-speed schlieren visualization.

The results of this bench test demonstrate the decrease in response of the FLDI with increase in distance from the focus (Fig. 3.3(b)). The  $1/e$  folding in rms response of the FLDI to a subsonic  $\text{CO}_2$  jet is  $\approx 10$  mm from the focus.

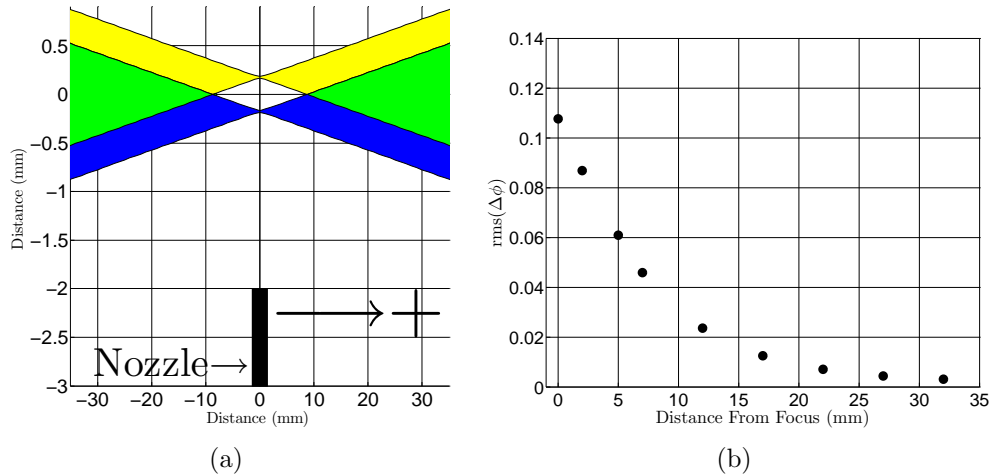


Figure 3.3: a: A sketch of the small  $\text{CO}_2$  nozzle and laser beam profile. The arrow ( $\rightarrow +$ ) denotes the direction in which the nozzle is traversed. The yellow shaded area denotes where the laser is polarized in the streamwise direction. The blue shaded area denotes where the laser is polarized normal to the page. The green shaded region denotes the area where the two laser beams overlap. b: The results of the bench test; the results demonstrate the decrease in response of the FLDI with increasing distance from the sensitive region.

### 3.2.4 Bench Test: Equidistant Acoustic Wave

This subsection describes a bench test designed to assess the similarity in response of two FLDIs aligned along one generator of the cone. The question is posed: is the response the same if an identical disturbance is imposed on each identically constructed detector? In this example, the upstream probe volume is located  $627 \pm 1$  mm from

the cone tip, the downstream probe volume is located  $718 \pm 1$  mm from the cone tip.

To make the disturbance, a pulsed Nd:YAG laser (New Wave Research Gemini-200, 200 mJ, 5 ns pulse), is focused to a point by a 200 mm focal length lens to ionize a spot of gas when the probe volumes interrogate ambient air with no mean flow. This ionized spot of gas acts as a spherical piston and creates a weak blast wave. If the time of arrival of the disturbance at each of the probe volumes is nearly identical, and it is assumed that the weak blast wave is symmetric, the disturbance amplitude at each of the probe volumes can be assumed to be nearly identical (schematic in Fig. 3.4(a)). The result of a such a test (Fig. 3.4(b)) indicates that the upstream and downstream FLDI signals are nearly identical. The difference in single shot peak response is less than 3.5%. The experiment is conducted five times and the difference in response is found to be repeatable. This procedure is repeated every  $\approx 20$  shots, or when there the results from the previous shot indicate misalignment.

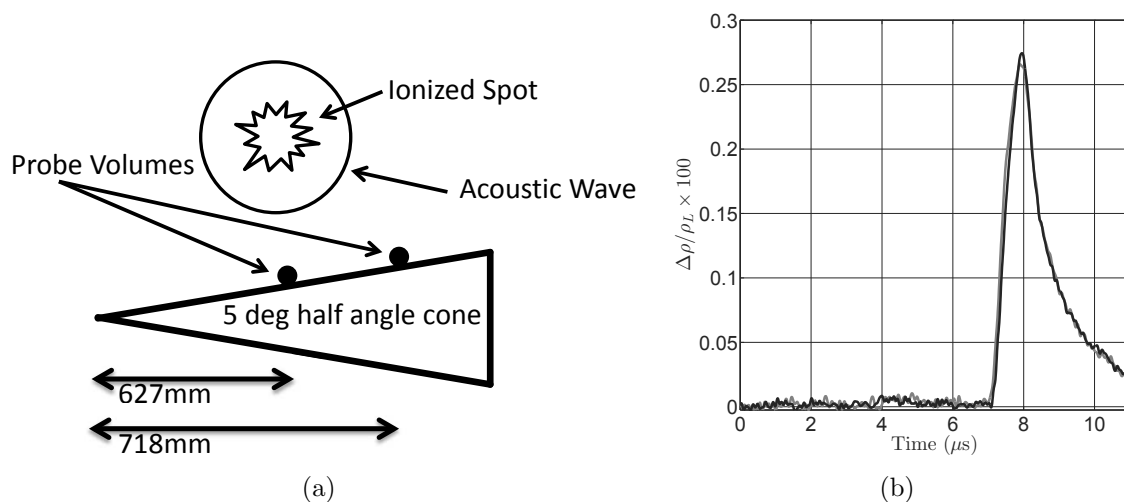


Figure 3.4: a: A sketch of the bench test arrangement. The upstream and downstream probe volumes are denoted by circles. The ionized spot of gas is located equidistant from both detectors so that it creates a disturbance that is nearly identical at both probe volumes. b: The results of the bench test, the probe volume at 627 mm is in black, the probe volume at 718 mm is in gray. The results show that the upstream and downstream interferometers respond similarly to a nearly identical disturbance.

### 3.2.5 Integration Length Determination

The FLDI has a finite sensitive region in the spanwise, streamwise, and wall-normal direction. In addition, the quantity that is being probed, density, has an eigenfunction that is not uniform in the wall-normal direction. It is the purpose of this subsection to present what quantity is being registered at the photodetector. A case representative of experiments in T5 is examined as an example.

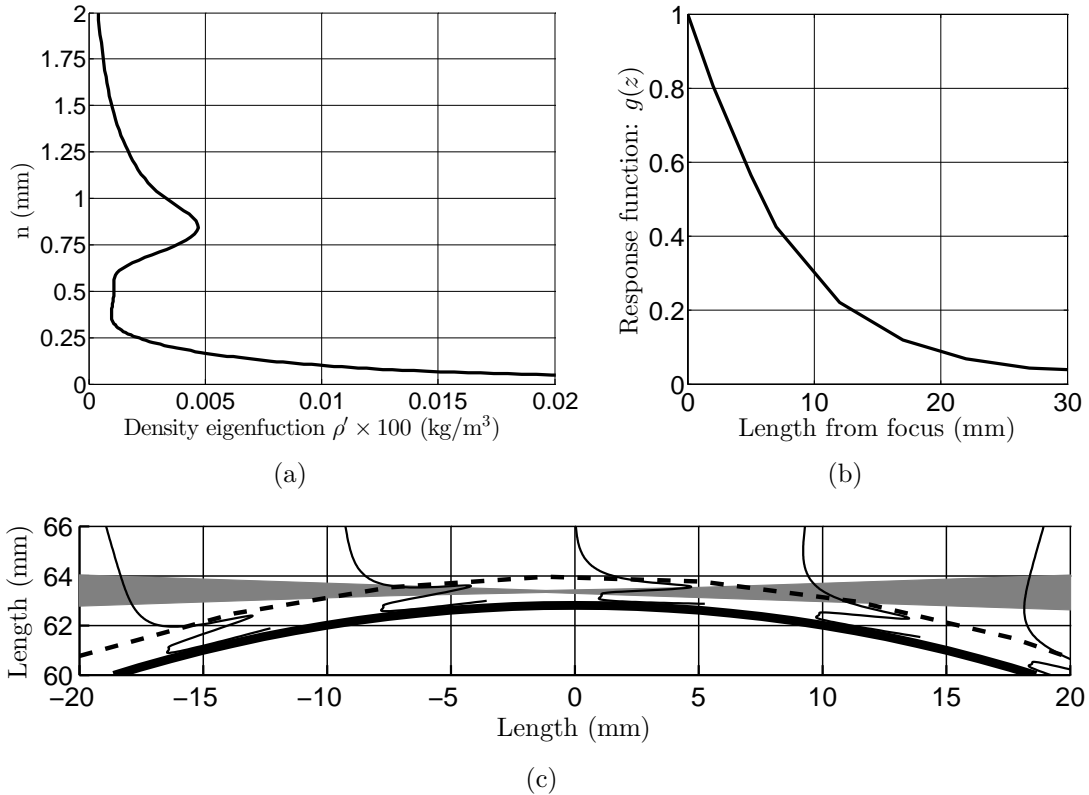


Figure 3.5: a: Eigenfunction at an unstable frequency for the downstream probe volume for shot 2789 (air) as a function of wall-normal distance.  $n$  is the wall-normal distance. b: Response function for the FLDI system as a function of distance from the focus. The length from the focus is  $z$ . c: Overlay of cone surface (solid thick line), calculated boundary-layer thickness (dashed line), density eigenfunction (solid thin lines), and laser beam profile (gray filled area). The zero of the abscissa is the focus of the beam, and distance along this direction is denoted by  $z$ .

The eigenfunction of density is assumed to be characteristic of the disturbance being probed by the FLDI. An eigenfunction at an unstable frequency (1236 kHz) for the downstream probe volume for shot 2789 is calculated from the STABL suite

and presented in Fig. 3.5(a). It highlights the variation in the wall-normal direction ( $n$ ) of the density eigenfunction amplitude, note the maximum near the critical layer<sup>2</sup> located 60-80% of boundary-layer thickness from the wall. The results of the bench test where the CO<sub>2</sub> jet was traversed from the focus (Fig. 3.3(b)) are normalized by the value at the focus and presented in Fig. 3.5(b) as the response function,  $g(z)$ , where  $z$  is the distance from the focus along the beam path, in the spanwise direction.

An overlay of the cone surface, calculated boundary-layer thickness, density eigenfunction, and laser beam profile is presented in Fig. 3.5(c). To assess the effects of the non-uniformity in response function along the length from the laser beam focus (Fig. 3.5(b)), the density eigenfunction (Fig. 3.5(a)), and curvature of the cone on the changes in OPL that are registered at the photodetector, we average the density eigenfunction,  $\overline{\rho}(z)$ , that is probed by the laser beam, and scale this value by the response function,  $g(z)$ , at the corresponding distance from the focus (Fig. 3.6(a)).

It is possible to make an estimate of the expected change in phase that would be registered at the photodetector with information about the spatial distribution of the registered density perturbations, assuming that the disturbances are two dimensional in nature. This is approximated by

$$\Delta\phi = \frac{2\pi}{\lambda_0} K \int_{-\infty}^{\infty} \overline{\rho}(z)g(z)dz. \quad (3.11)$$

Evaluating this integral by quadrature, the estimated change in phase is  $\approx 7.5e^{-4}$  rad. A comparison between this estimated change in phase and a sample experimental result, where the change in phase is evaluated from the data as in Eq 3.10, is favorable, as the spectrum of the phase change for shot 2789 at the downstream probe volume is presented in Fig. 3.6(b). The frequency range of interest is centered around the peak that appears in Fig. 3.6(b), and the observed change in phase is in the range  $4-8e^{-4}$  rad.

---

<sup>2</sup>The critical layer is introduced in the illustration in Fig. 1.2.

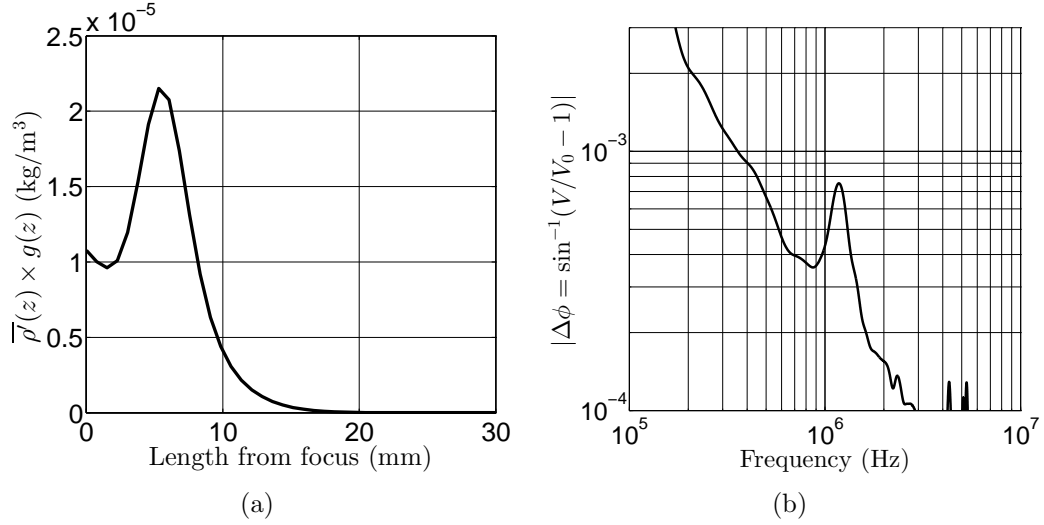


Figure 3.6: a: Averaged eigenfunction that is probed by the laser beam, scaled by the response function at the corresponding distance b: Phase change in frequency space of the downstream detector for shot 2789.

Finally, with the understanding of how the optical technique is probing the disturbances in the boundary layer, the integration length can be estimated. Inspecting the scaled, vertically averaged density eigenfunction amplitude (Fig 3.6(a)), there is a clear decline in response at  $\approx \pm 10$  mm, this is chosen as the integration length. At the extremes of the parameter space covered in this work, the boundary-layer thickness ranges from 1.1-2.5 mm, but, the integration length will change by less than 10%, primarily due to the large curvature of the cone relative to the boundary-layer thickness (reference Fig. 3.5(c)). Discrepancies due to change in integration length are conservatively included in the uncertainty estimation (section 3.2.7).

### 3.2.6 Sensitivity to Wavelength

The sensitivity of the technique to disturbance wavelength due to experimental setup is discussed in this subsection. The FLDI technique is able to probe only a small volume over the surface of a test article because the sensitive leg and reference leg share much of the same optical path, except near the focus. This optical arrangement

results in a setup that has a different sensitivity to different wavelengths.

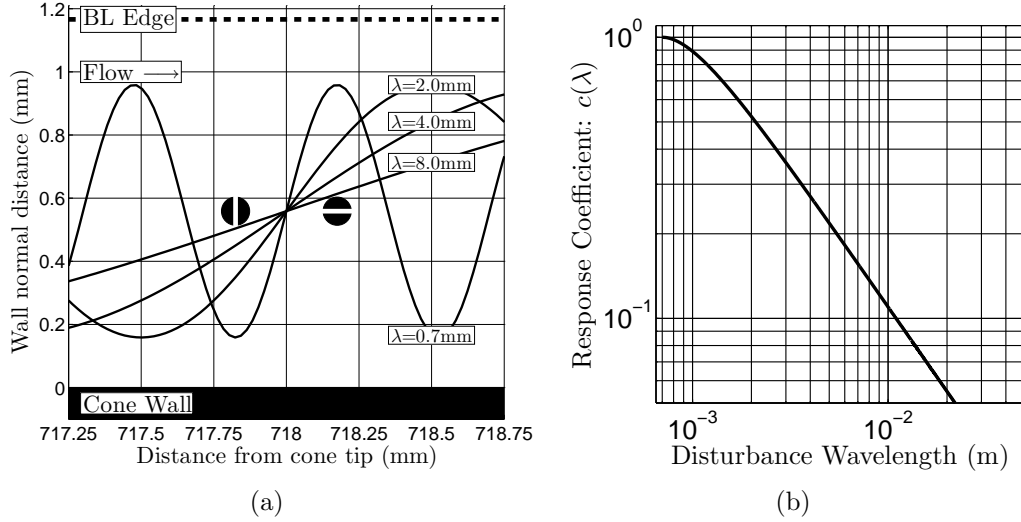


Figure 3.7: a: Streamwise view of the down-stream probe volume. Four sinusoids representative of boundary-layer disturbances of equal amplitude with wavelengths: 0.7, 2, 4, and 8 mm. The two circles represent the beam polarized in the streamwise and wall-normal direction, with a hash mark denoting each. b: Response of the detector as a function of wavelength.

A sketch of a streamwise slice of the flow field of interest at the downstream probe volume for shot 2789 shows the location of the laser beams, calculated boundary-layer edge, and four sinusoids intended to be representative of boundary-layer disturbances in density (Fig. 3.7(a)). The density disturbances are assumed to have the form  $\rho' = \rho_A \exp(i(2\pi s/\lambda - \omega t))$ , with the same amplitude  $\rho_A$ , and wavelengths  $\lambda = 0.7, 2, 4, 8$  mm. The distance along the cone surface is  $s$ , the frequency is  $\omega$ , and time is  $t$ . Referencing Fig. 3.7(a), at the Nyquist wavelength, the response of the FLDI will be at its maximum, and the change in density registered by the FLDI,  $\Delta\rho = \rho_{\parallel} - \rho_{\perp}$ , will be the density disturbance amplitude,  $\rho_A$ . For wavelengths longer than  $700 \mu\text{m}$ , the spatial change in density ( $\Delta\rho = \rho_{\parallel} - \rho_{\perp}$  as in Eq. 3.5), will decrease for a disturbance of the same amplitude. A quantitative estimate of the response coefficient,  $c(\lambda)$ , is made as

$$c(\lambda) = \sin\left(\frac{2\pi l_b/2}{\lambda}\right), \quad (3.12)$$

where  $l_b$  is the beam spacing. This coefficient demonstrates the behavior of reduced response with increasing wavelength (Fig. 3.7(b)).

The sensitivity to wavelength can complicate the interpretation of broadband spectra of density disturbances, in particular for the shock tunnel noise experiments presented in section 4.1. A correction using the coefficient in Eq 3.12 can be made if the time scale in the flow field is easily eliminated with a characteristic velocity. This is the case in the free-stream noise measurements, as the free-stream velocity is the obvious choice. The results of the tunnel noise measurements with and without this correction based on wavelength are discussed in section 4.1. The application of this correction to spectra of disturbances in the boundary layer is not as simple because the choice of velocity is not trivial.

### 3.2.7 Uncertainty Estimation

The systematic error stemming from applying Eq. 3.8 to the raw data is found by considering the propagation of uncertainty in  $\Delta\rho/\rho_L$  as a function of all the input parameters (Kline and McClintock, 1953, Beckwith et al., 2007). The largest sources of systematic error are considered to be the uncertainty introduced by the assumed integration length,  $L$  in Eq. 3.3 (assumed to be 20%), the quantization error in the potentials,  $V$  and  $V_0$  (assumed to be the 14-bit quantization error), and the magnitude of the local density  $\rho_L$  (assumed to be 20%). This leads to an error of approximately 20% in the magnitude of  $\Delta\rho/\rho_L$ , with a 95% confidence interval. There is systematic error in the magnitude of  $\Delta\rho/\rho_L$  from the spectral content estimation in each of the segments, this is approximately 20% in the magnitude of  $\Delta\rho/\rho_L$ , with a 95% confidence interval. Combining the errors from processing the data and estimating their spectra in a root-mean-squared sense, the systematic error is bounded at 30% (95% confidence interval).

Random error from electrical noise and mechanical vibrations can be estimated

by inspecting the spectral content of the signal immediately preceding the test time. Approximately 100 ms before the test begins, vibration from the piston launch (to compress the driver gas) is transmitted through the steel rails the entire shock tunnel rests on. By applying the identical signal processing scheme to the time just before the test, as used during the test, errors from ambient electrical noise and facility vibration can be bounded. In the 100 kHz to 10 MHz frequency band, the spectral content from vibration and electrical noise is less than 0.5% in the magnitude of  $\Delta\rho/\rho_L$  (95% confidence interval).

Random error from the FLDI's imperfect focusing ability comes from the optical technique having to traverse the core flow and turbulent shear layer from the turbulent boundary layer on the nozzle wall (refer to Fig. 3.1). The core flow and turbulent shear layer could introduce additional noise to the measurement of the probe volume. This issue is addressed in section 4.2.

# Chapter 4

## Results

### 4.1 Reflected-Shock Tunnel Noise Measurement

Experimental results that were conducted to quantify the tunnel noise are presented in this section. The measurements are made with the FLDI optical technique described in section 3. Motivation for such a survey is described, and the literature for high-speed wind-tunnel noise is briefly reviewed. The results show the perturbations in density are not a strong function of the reservoir enthalpy. During one experiment, exceptional levels of noise were detected; this singular result is attributed to non-ideal operation of the shock tunnel. The presented results indicate that RMS density fluctuations of  $\approx 1\%$  are achievable with attention to tunnel cleanliness. In addition, the spectral content of density fluctuation does not change throughout the test time.

#### 4.1.1 Motivation

The boundary-layer receptivity problem makes the characterization of the noise environment in the free-stream of any wind tunnel a key aspect of studying transition in ground-test ([Morkovin, 1969](#), [Reshotko, 1976](#), [Saric et al., 2002](#), [Fedorov, 2003](#)). Extensive reviews of the effect of tunnel noise on high-speed boundary-layer transition have been made by [Schneider \(2001, 2004\)](#).

The sources of disturbances in a supersonic wind tunnel are illustrated in Fig. 4.1.

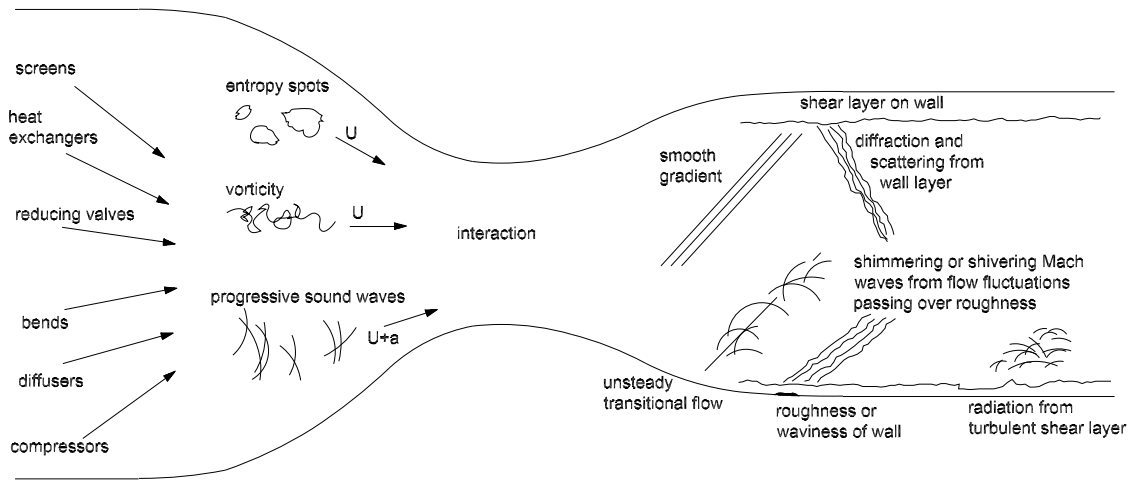


Figure 4.1: Sources of wind-tunnel noise. Taken from [Schneider \(2008\)](#) with permission. The major sources of disturbances in a reflected-shock tunnel are noted to be the turbulent boundary layer on the nozzle wall and/or the entropy fluctuations being advected from the reservoir of the facility ([Schneider, 2001](#)).

The major sources of disturbances in a reflected-shock tunnel are noted to be the turbulent boundary layer on the nozzle wall and/or the entropy fluctuations being advected from the reservoir of the facility ([Schneider, 2001](#)). Researchers have found some correlation of the tunnel-noise environment to the boundary-layer transition location ([Pate and Schueler, 1969](#), [Pate, 1971a,b, 1974](#)). The concern of tunnel environment and its effects on boundary-layer instability work has led to the development of hypersonic wind tunnels with low disturbance levels ([Blanchard et al., 1996](#), [Schneider, 2008](#), [Hofferth et al., 2013](#)). Hypersonic instability and transition work has been successful in these low-disturbance wind tunnels; however, they are not able to produce hypervelocity flows where fluid-dynamic/thermo-chemical interactions can exist. So, if a researcher is to study hypervelocity instability, it is prudent to characterize the noise of the test facility.

Pitot pressure measurements are typically made to quantify the perturbations in the test gas ([Bounitch et al., 2011](#), [Rufer and Berridge, 2012](#)). In a reflected-shock tunnel, this is difficult because: 1) The bandwidth of commercially available piezo-

electric pressure transducers is too low ( $< 1$  MHz) to cover the frequency band of importance. 2) The pressure transducers must be flush mounted to avoid resonances in any sort of protective cavity (McGilvray et al., 2009). Flush mounting the transducer causes excessive thermal loading and puts them at risk for particulate impact after the passage of the test gas. 3) It is uncertain that flush mounted pressure transducers in a Pitot probe configuration produce a faithful representation of the noise level in a supersonic or hypersonic free-stream. The interaction of free-stream fluctuations with the bow-shock wave that forms in front of the transducer may thwart the goal of resolving a wide range of disturbance length scales (Maheash et al., 1995). This interaction is known to be a function of the obliqueness (Moore, 1954) and the strength (Lee et al., 1997) of the shock wave. Furthermore, the complexity of the subsonic flow field behind the bow-shock wave may further obscure the fidelity of free-stream disturbance measurement, especially in the frequency domain.

Non-intrusive optical methods are an alternative to direct mechanical measurement. One approach described by Marineau and Hornung (2010) was tracking the unsteadiness of the bow-shock wave in front of a blunt body in the T5 test section. Using an edge detection algorithm with high-speed schlieren cinematography, they were able to track bow-shock motion in the 10 kHz range. This frequency response is not adequate for applications to hypervelocity boundary-layer instability work, where time scales in excess of 3 MHz must be resolved. The FLDI is fit for the job.

### 4.1.2 Data

A test series using the FLDI measurement technique for a series of seven shots (conditions in Table 4.1) was executed to investigate the noise in the free-stream flow of T5. The test-matrix was designed to hold the reservoir pressure ( $P_R$ ) constant while varying the reservoir enthalpy ( $h_R$ ) through the useful range of conditions in T5.

Seven band-pass filtered (5 kHz to 20 MHz) time traces of density perturbations

Table 4.1: Run Conditions - Tunnel Noise

| Shot | $P_R$ | $h_R$   | $T_R$ | $U_X$ | $\rho_X$             | $P_X$ | $T_{t/rX}$ | $T_{vX}$ | $M_X$ | $Re_X^{Unit}$ |
|------|-------|---------|-------|-------|----------------------|-------|------------|----------|-------|---------------|
|      | (MPa) | (MJ/kg) | (K)   | (m/s) | (kg/m <sup>3</sup> ) | (kPa) | (K)        | (K)      | (-)   | (1/m)         |
| 2684 | 46.6  | 8.0     | 5331  | 3677  | 0.059                | 18.9  | 1113       | 1116     | 5.47  | 4.9E+6        |
| 2686 | 49.5  | 13.9    | 7591  | 4629  | 0.041                | 24.6  | 2014       | 2016     | 5.00  | 2.9E+6        |
| 2687 | 49.3  | 15.9    | 8141  | 4891  | 0.036                | 25.0  | 2248       | 2250     | 4.94  | 2.5E+6        |
| 2691 | 41.8  | 5.5     | 4200  | 3114  | 0.071                | 14.1  | 683        | 694      | 5.93  | 6.7E+6        |
| 2692 | 42.4  | 5.3     | 4081  | 3053  | 0.075                | 14.0  | 646        | 657      | 5.98  | 7.2E+6        |
| 2693 | 49.6  | 8.6     | 5583  | 3790  | 0.059                | 20.9  | 1216       | 1218     | 5.39  | 4.8E+6        |
| 2694 | 49.9  | 17.8    | 8570  | 5118  | 0.034                | 25.8  | 2451       | 2453     | 4.90  | 2.3E+6        |

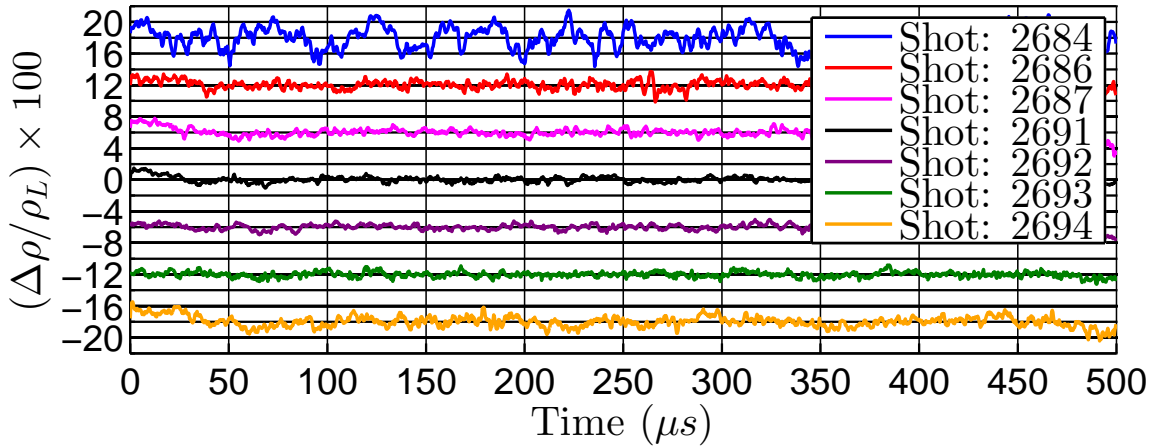


Figure 4.2: Filtered time traces of  $\Delta\rho/\rho_L \times 100$  (filter cutoffs: 5 kHz to 20 MHz). Each trace is offset 6% along the ordinate. Note that shot 2684 has a notably larger amplitude than the other shots.

(Fig. 4.2) illustrate that the noise level is similar through the range of reservoir enthalpy  $h_R$ , other than shot 2684, which has a larger RMS than the other experiments. This is explained by understanding the process of running T5. Polyurethane buffers slow the piston to a stop after the primary diaphragm is ruptured (refer to Fig. 2.1), these buffers were destroyed during the prior experiment (shot 2683). The destroyed buffers introduced material to the shock tube which was not completely removed during the normal cleaning process that is executed after each experiment. During the startup process of shot 2684, this buffer material was introduced to the flow, and registered as large fluctuations by the interferometer.

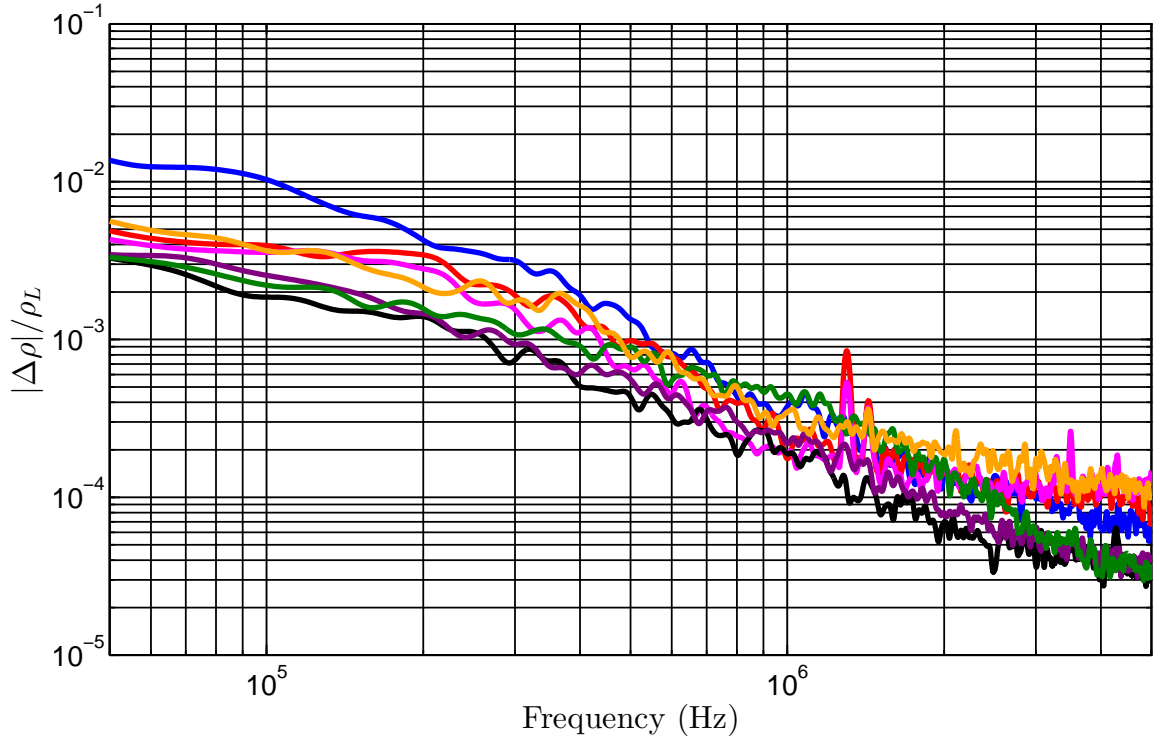


Figure 4.3: Frequency spectrum of tunnel noise time traces. Legend in Fig. 4.2. The four RF spikes at 1.3, 1.4, 3.5 and 6 MHz should be disregarded, these peaks appear when the tunnel is not in operation.

The spectrum<sup>1</sup> of the time traces (Fig. 4.3) further illustrates the similarity for all tests other than shot 2684. The noise measured in the free-stream during shot 2684 appears to be of larger amplitude than other experiments at lower frequencies ( $< 300$  kHz).

Applying Taylor's hypothesis, the data is presented in amplitude-wavelength space (Fig. 4.4, bottom). The free-stream velocity (Table 4.1) is used as the velocity scale. Additionally in Fig. 4.4, the wavelength spectrum is corrected for the sensitivity of the FLDI technique to wavelength, as discussed in section 3.2.6. When plotted in this fashion, the spectra (other than shot 2684) appear to collapse within the uncertainty limits and there is a clear separation between shot 2684 and the other shots.

Further interpretation of the results in Fig. 4.4 are given in Table 4.2. RMS density

<sup>1</sup>The data are digitized at 100 MHz. The spectral content of the single-side amplitude is estimated using the discrete Fourier transform with 50% overlapping 50 kHz Hann windows.

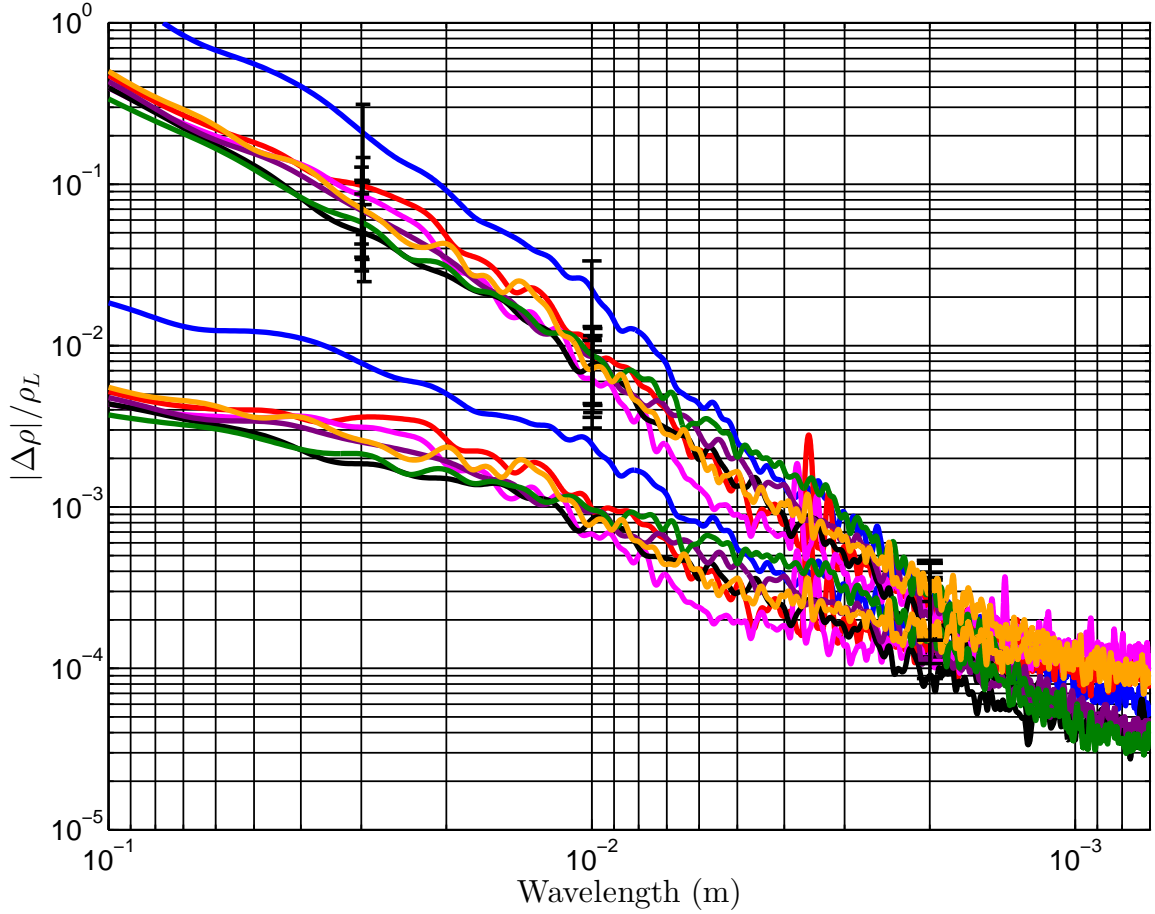


Figure 4.4: Wavelength spectrum of tunnel noise time traces. Legend in Fig. 4.2. There are two sets of wavelength spectrum plots of the same data. The lower amplitude data has not been corrected for the sensitivity of the FLDI technique to wavelength. The high amplitude data has been corrected for the sensitivity of the FLDI technique to wavelength. Error estimate from section 3.2.7.

fluctuations are tabulated at different bandpass wavelengths for each experiment. It is desirable to understand the amplitude of the RMS density fluctuations at length scales of relevance to transition work being conducted in T5, so comparing the scaling of the most unstable wavelength in the boundary layer on a five degree half-angle cone, ( $\approx 2\delta \approx 2\text{-}4\text{ mm}$ , Fedorov (2011)) to the measured frequency content of free-stream disturbance is a logical step. This perspective of the most unstable wavelength relative to the range of band pass wavelengths is important. For wavelengths most relevant to acoustic mode boundary-layer instability, the RMS tunnel noise is  $\approx 1\%$  (Table 4.2).

Table 4.2: Summary of RMS density fluctuations at different bandpass wavelengths. The quantity  $\text{rms}(\rho/\rho_L)\times 100$  is tabulated for each shot.

| Cutoff |                   | Shot# |      |      |      |      |      |      |  |
|--------|-------------------|-------|------|------|------|------|------|------|--|
| Long   | Short             | 2684  | 2686 | 2687 | 2691 | 2692 | 2693 | 2694 |  |
| 100 mm | 700 $\mu\text{m}$ | 5.96  | 2.37 | 2.11 | 1.38 | 1.57 | 1.50 | 2.37 |  |
| 50 mm  | 700 $\mu\text{m}$ | 3.69  | 1.84 | 1.49 | 0.85 | 1.05 | 1.00 | 1.43 |  |
| 25 mm  | 700 $\mu\text{m}$ | 1.68  | 1.00 | 0.75 | 0.50 | 0.61 | 0.64 | 0.77 |  |

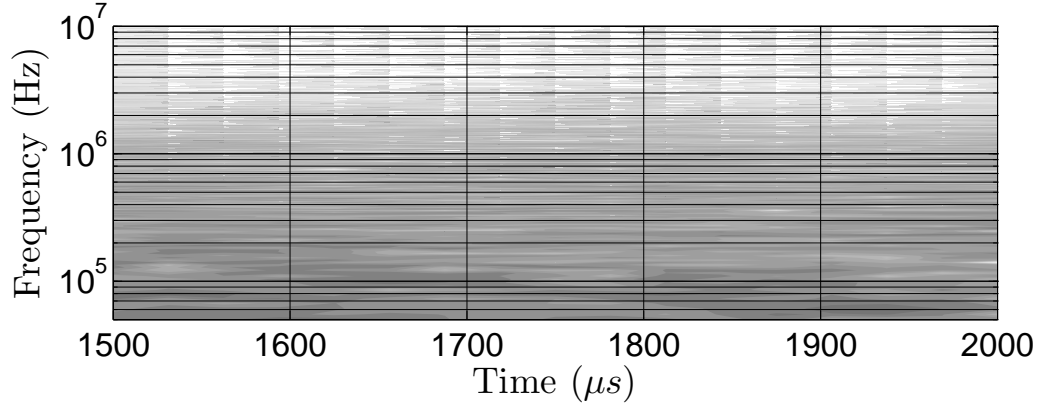


Figure 4.5: Spectrogram (contours of power spectral density, plotted in time-frequency space) of shot 2693, this illustrates how the spectral content of the fluctuations in the free-stream evolve throughout the test time. It is seen there are no clear trends in frequency-time space.

Examination of the spectral content evolution of fluctuations throughout the test time is important because there are complex non-steady wave systems in the reservoir of a reflected-shock tunnel during the starting process and steady run time. The concern is that weak non-steady waves or driver gas contamination (Sudani and Hornung, 1998) may manifest themselves during the test time as trends in noise, i.e., the spectral content will shift because the driver gas (helium) leaks into the useful test flow. This point is addressed by constructing a spectrogram<sup>2</sup> of the data presented in Fig. 4.2. An example (Fig. 4.5) shows contours of  $10\log_{10}(|\text{PSD}|)$  in time-frequency space. The data indicate no clear trends in noise throughout the test time. The other experiments show a similar lack of trend in noise during the run time of the tunnel.

<sup>2</sup>A spectrogram is made by estimating the power spectral density (PSD) of 10 kHz Hann windows with a 50 % overlap using the Welch method.

### 4.1.3 Discussion

The FLDI has been implemented in T5 to measure the free-stream noise levels over a range of reservoir enthalpy, keeping the reservoir pressure fixed. The RMS levels of free-stream fluctuations in density are quite similar through the range of reservoir enthalpy explored, except for one experiment. The larger RMS response in the exceptional experiment can be attributed to an event in the tunnel on the prior experiment, an experimental blunder. The present results indicate that RMS density fluctuations of  $\approx 1\%$  are achievable with attention to tunnel cleanliness. The data indicate no clear trends in the spectral content of density fluctuation throughout the test time. In addition, the frequency content at above 500 kHz is of considerably smaller magnitude than the levels below 500 kHz, indicating that measurements of the acoustic instability in hypervelocity boundary layers can be carried out in T5.

Evidence of correlation between the tunnel noise and run conditions is sought using forward and reverse stepwise regression, the results from shot 2684 are omitted from this exercise because it is identified as an outlier due to error in executing the experiment. The parameters chosen to seek correlation with the tunnel noise are  $P_R$ ,  $h_R$ ,  $Re_X^{Unit}$ ,  $M_X$ , and shot number. All data are centered and then normalized by their standard deviation. The p-value to enter or leave the regression model is 0.1. The forward selection analysis begins with no parameters in the regression model, the reverse selection analysis begins with all parameters in the regression model. No parameters are included in the final regression models found by the forward or reverse selection analysis, which indicates that the data are consistent with the null hypothesis,<sup>3</sup> so no parameters are found to be strongly correlated with tunnel noise.

---

<sup>3</sup>Stepwise regression is the use of an F-statistic to test models with and without a potential term at each step. If a term is not currently in the model, the null hypothesis is that the term would have a zero coefficient if added to the model. If there is sufficient evidence to reject the null hypothesis, the term is added to the model. Conversely, if a term is currently in the model, the null hypothesis is that the term has a zero coefficient. If there is insufficient evidence to reject the null hypothesis, the term is removed from the model ([MathWorks](#), [Draper and Smith, 1998](#)).

There are additional sources of noise that may vary with run condition, such as:

- 1) The contoured nozzle is being used at slightly off design conditions in this study.
- 2) For increasing reservoir enthalpy, the contact discontinuity has a higher impedance mismatch. The higher the impedance mismatch, the lower the noise transmitted into the driven section from the driver section. [Paull and Stalker \(1992\)](#) studied this effect in expansion tubes.
- 3) Perturbations in entropy originating in the reservoir. These effects on free-stream noise are difficult to quantify with the current technique.

## 4.2 Single Point FLDI Measurement<sup>4</sup>

The first measurements of the boundary-layer instability on a slender body at hypervelocity conditions are presented in this section ([Parziale et al., 2013](#)). A single point FLDI system was constructed and implemented in the T5 hypervelocity shock tunnel to achieve this goal. Density disturbances in the boundary layer of less than 0.5%, or  $\approx 4e^{-5}$  kg/m<sup>3</sup> are observed at over 1 MHz.

### 4.2.1 Data

During these experiments, the FLDI technique was used to try to measure the disturbances in the boundary layer, the state of which is largely laminar at the measurement point (based on time-averaged heat-flux correlations). The run conditions are tabulated in [Table 4.3](#). Two examples ([Fig. 4.6](#) and [Fig. 4.7](#)) are presented where both turbulent bursts and narrowband wave packets are detected; the spectral content estimation in these examples is obtained using Welch's method, with 50% overlapping 20  $\mu$ s Hann windows.

The FLDI response for shot 2695 ([Fig. 4.6](#)) reveals interesting phenomena at 1650  $\mu$ s and 1915  $\mu$ s; 40  $\mu$ s segments centered at 1650  $\mu$ s, 1800  $\mu$ s, and 1915  $\mu$ s are

---

<sup>4</sup>This material is adapted from [Parziale et al. \(2013\)](#).

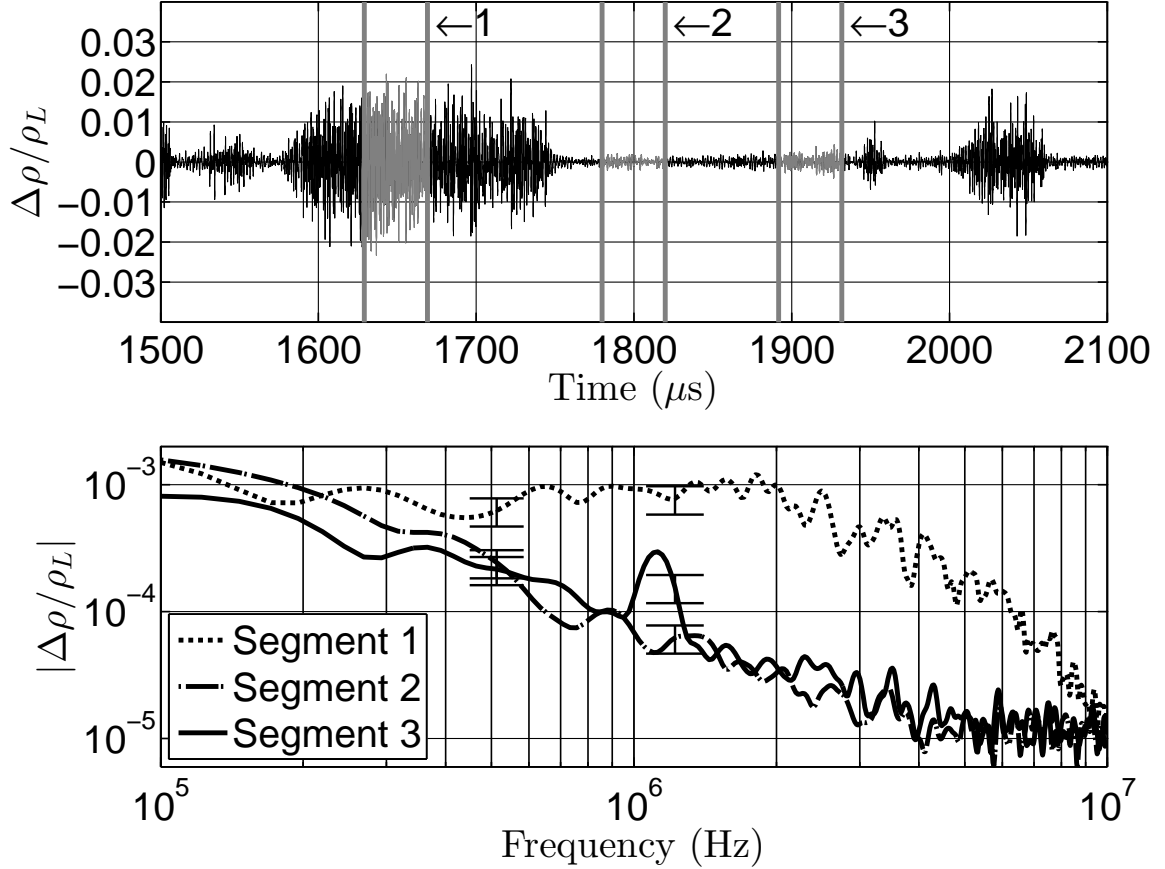


Figure 4.6: FLDI results from shot 2695, the band-pass filtered response (top) and spectral response from the three chosen segments (bottom).

highlighted. This shows the spectral content of the interrogated point of the boundary layer when minimal disturbances are detected (Segment 2), when a turbulent spot passes (Segment 1), and when a wave packet passes (Segment 3). The spectral content of the turbulent spot (Segment 1) shows broadband response; the wave packet (Segment 3) has a strong peak in response at 1.11 MHz.

The FLDI response for shot 2702 (Fig. 4.7) reveals interesting phenomena at 1300  $\mu\text{s}$  and 1810  $\mu\text{s}$ ; 30  $\mu\text{s}$  segments centered at 1300  $\mu\text{s}$ , 1600  $\mu\text{s}$ , and 1810  $\mu\text{s}$  are highlighted. This shows the spectral content of the interrogated point of the boundary layer when minimal disturbances are detected (Segment 2), when a turbulent spot passes (Segment 1), and when a wave packet passes (Segment 3). The spectral con-

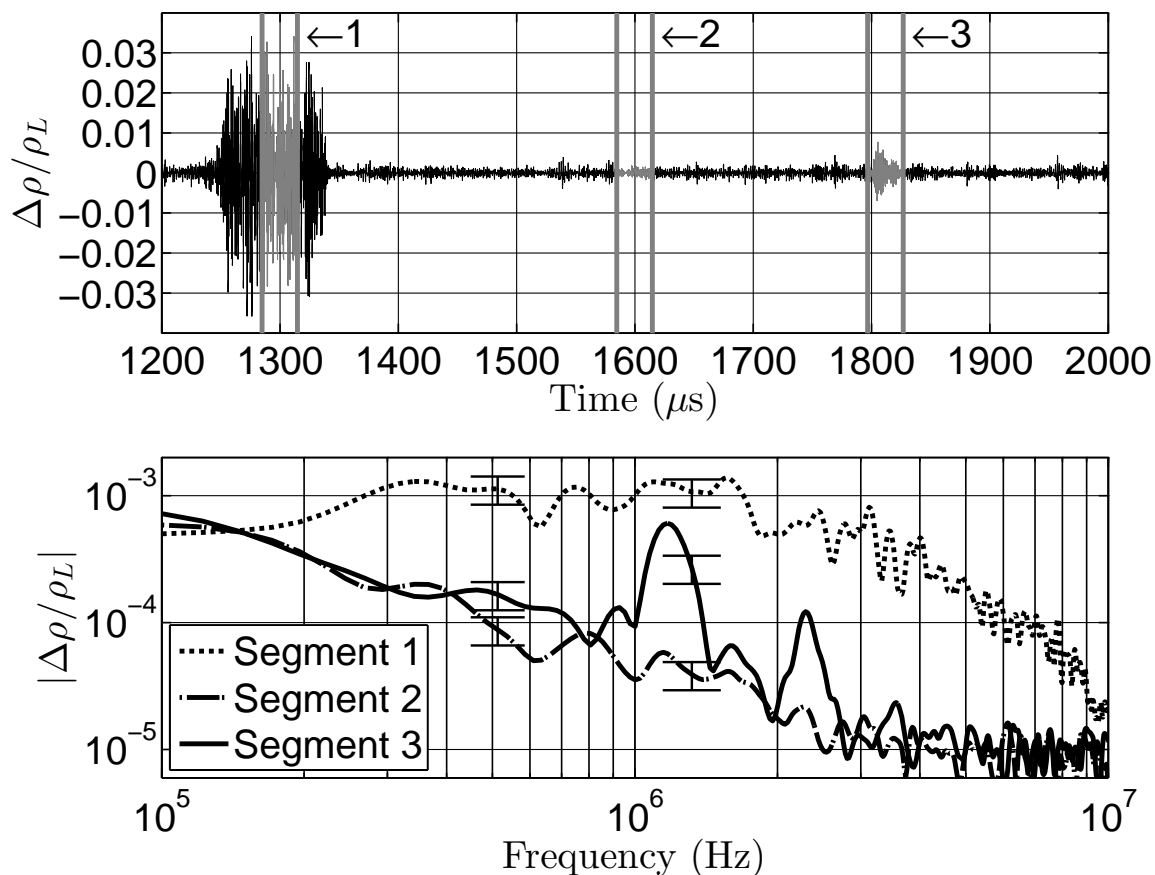


Figure 4.7: FLDI results from shot 2702, the band-pass filtered response (top) and spectral response from the three chosen segments (bottom).

tent of the turbulent spot (Segment 1) shows broadband response; the wave packet (Segment 3) has a strong peak in response at 1.17 MHz with a harmonic at 2.29 MHz. Zooming in (in time) on Segment 3 of Fig. 4.7 shows the wave packet in more detail (Fig. 4.8). The wave packet appears in the unprocessed and unfiltered trace (top), and is more prominent after the raw data are band-pass filtered and processed with Eq. 3.8 (bottom).

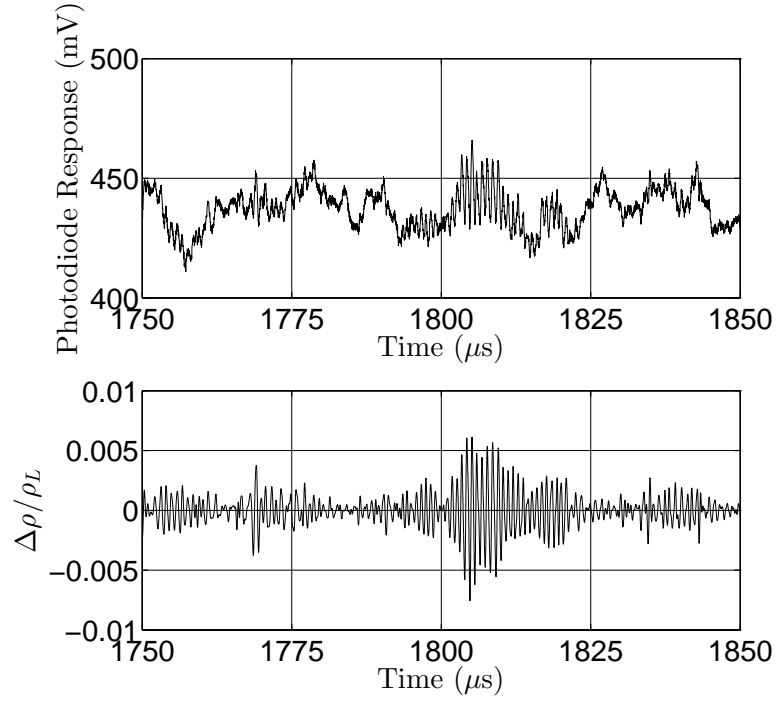


Figure 4.8: FLDI Results from shot 2702, zoomed into Segment 3 of Fig. 4.7, showing the unprocessed photodetector response (top), and the data after they are filtered and processed with Eq. 3.8 (bottom).

Table 4.3: Run Conditions - Single Point FLDI

| Shot | $P_R$ | $h_R$   | $T_R$ | $U_X$ | $\rho_X$             | $P_X$ | $T_{t/rX}$ | $T_{vX}$ | $M_X$ | $Re_X^{Unit}$ |
|------|-------|---------|-------|-------|----------------------|-------|------------|----------|-------|---------------|
|      | (MPa) | (MJ/kg) | (K)   | (m/s) | (kg/m <sup>3</sup> ) | (kPa) | (K)        | (K)      | (-)   | (1/m)         |
| 2695 | 48.4  | 6.9     | 4835  | 3416  | 0.081                | 22.4  | 955        | 950      | 5.50  | 6.8E+6        |
| 2696 | 46.0  | 7.0     | 4879  | 3440  | 0.076                | 21.5  | 977        | 975      | 5.47  | 6.4E+6        |
| 2697 | 49.3  | 8.4     | 5482  | 3724  | 0.071                | 25.5  | 1236       | 1243     | 5.26  | 5.6E+6        |
| 2702 | 49.7  | 8.4     | 5515  | 3739  | 0.071                | 25.7  | 1249       | 1256     | 5.25  | 5.6E+6        |
| 2704 | 49.5  | 8.4     | 5510  | 3737  | 0.071                | 25.7  | 1249       | 1256     | 5.25  | 5.6E+6        |
| 2705 | 50.0  | 8.4     | 5493  | 3728  | 0.072                | 26.0  | 1242       | 1248     | 5.25  | 5.7E+6        |

## 4.2.2 Discussion

The boundary-layer profiles for each of the shots in this test series are computed with the DPLR. The purpose of finding these profiles is to compare the scaling of the most unstable frequency ( $f_M \approx 0.7U_E/(2\delta)$ ) to the measured frequency (Demetriades, 1974, Stetson and Kimmel, 1992, Fedorov, 2011). These results are summarized in Table 4.4, where the scaling for shots 2695 and 2702 can be found along with other shots in which wave packets are detected. The interferometer was moved to a farther distance from the cone tip ( $s$ ) for two experiments (shots 2704 and 2705). The purpose of doing so was to make measurements at approximately the same edge conditions (as shot 2702), but where the boundary layer is thicker; a thicker boundary layer at the same edge velocity should decrease the frequency of a wave packet measured at the probe volume. A decrease of between 10-15% in the peak measured frequency ( $f_{peak}$ ) is evident in Table 4.4.

Table 4.4: Single Point Edge Conditions and Boundary Layer Instability Scaling

| Shot | $U_E$ | $\rho_E$             | $P_E$ | $T_{t/rE}$ | $T_{vE}$ | $M_E$ | $Re_E^{Unit}$ | $s$  | $\delta$ | $0.7\frac{U_E}{2\delta}$ | $f_{peak}$ |
|------|-------|----------------------|-------|------------|----------|-------|---------------|------|----------|--------------------------|------------|
|      | (m/s) | (kg/m <sup>3</sup> ) | (kPa) | (K)        | (K)      | (-)   | (1/m)         | (mm) | (mm)     | (MHz)                    | (MHz)      |
| 2695 | 3358  | 0.102                | 32.9  | 1119       | 991      | 4.99  | 7.4E+6        | 665  | 1.04     | 1.13                     | 1.11       |
| 2696 | 3382  | 0.096                | 31.5  | 1143       | 1015     | 4.97  | 7.0E+6        | 665  | 1.08     | 1.10                     | 1.11       |
| 2697 | 3661  | 0.089                | 36.7  | 1425       | 1323     | 4.81  | 6.2E+6        | 665  | 1.11     | 1.16                     | 1.12       |
| 2702 | 3676  | 0.089                | 36.9  | 1439       | 1339     | 4.81  | 6.1E+6        | 665  | 1.11     | 1.16                     | 1.17       |
| 2704 | 3673  | 0.089                | 37.0  | 1439       | 1338     | 4.81  | 6.1E+6        | 783  | 1.20     | 1.07                     | 0.98       |
| 2705 | 3665  | 0.090                | 37.4  | 1430       | 1330     | 4.81  | 6.2E+6        | 783  | 1.20     | 1.07                     | 1.03       |

Random error from the FLDI's imperfect focusing ability comes from the optical technique having to traverse the core flow and turbulent shear layer from the turbulent boundary layer on the nozzle wall (refer to Fig. 3.1). The core flow and turbulent shear layer could introduce additional noise to the measurement of the probe volume. The noise resulting from the fluctuations in the core flow and shear layer are bounded in frequency space by the spectral content of the quiescent windows of the signal as

in Segment 2 of Fig. 4.6 and Fig. 4.7, where minimal disturbances are detected in the boundary layer. Using a two-tailed hypothesis test, it is found that there is a statistically significant difference between the response of the FLDI when minimal disturbances are present (Segment 2), and when a wave packet is detected (Segment 3) in the frequency range of the acoustic instability (99.999% confidence interval). Additionally, the signal to noise ratio of the peak (Segment 3/Segment 2) is at least 5 in Fig. 4.6, and is at least 10 in Fig. 4.7. We conclude that the noise floor that is a result of the shear layer and core flow is sufficiently low, so that the FLDI technique can resolve the acoustic instability. Density disturbances in the boundary layer of less than 0.5%, or  $\approx 4e^{-5}$  kg/m<sup>3</sup> are observed at over 1 MHz.

The ability to make quantitative measurements of the acoustic instability with FLDI in a hypervelocity slender-body boundary layer is reproducibly demonstrated. This is notable because of the time scales (1-3 MHz) associated with the acoustic instability's fundamental and harmonic frequency for conditions available in T5. The error and noise floor associated with the measurement technique (FLDI) and facility are sufficiently low that an additional FLDI was placed downstream of the current FLDI described in this section to make acoustic instability growth rate measurements. The results from that work follow.

### **4.3 Double Point FLDI Measurement - Development**

In this section, the development efforts to make reliable two-point measurements of the instability on a slender body in hypervelocity flow are described. The two-point FLDI setup consists of two FLDI systems that probe a generator of the five degree half-angle cone with the intent of tracking the evolution of disturbances as they propagate downstream. The two-point FLDI development campaign was carried

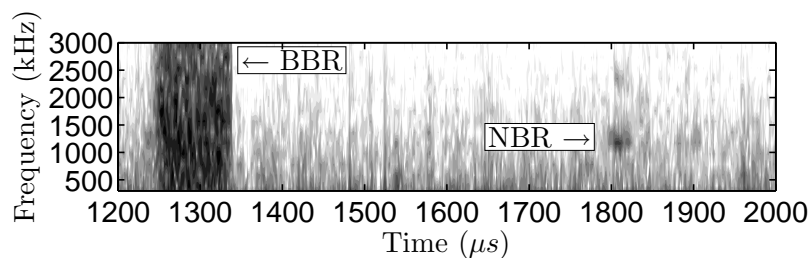
out largely during the experiments reported in [Parziale et al. \(2012b, 2013a\)](#) and [Jewell et al. \(2012, 2013\)](#). First, major technical impediments to making a successful measurement are highlighted. Then, some data from early and late in the development phase (dubbed “Dev 1” and “Dev 2”, respectively in section [A](#)) is presented for context. The data processing routine is described.

### 4.3.1 Shock Tube Fill Gas Quality and Cleaning Procedure

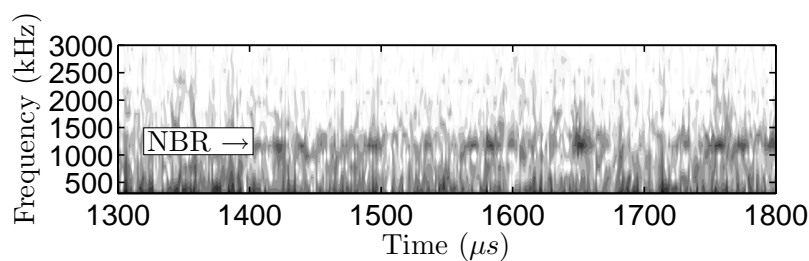
Throughout the testing campaign for this work, it became apparent that there was opportunity to increase the quality of the flow over the model from a technical standpoint. Improvement was achieved by using higher quality gas to fill the shock tube and cleaning the shock tube more thoroughly between experiments. Because consistent instability measurement results were obtained, the quality of the shock tube fill gas and shock tube cleaning procedure were fixed after shot 2760, concurrent with the conclusion of the development phase of the project.

There is no apparent record of what grade of gas was used to fill the shock tube in previous work, but it was most likely “Industrial,” as it was when this test campaign started. According to specification sheets for “Industrial” air from Air Liquide (the gas bottle supplier), there is a large bound on the relative O<sub>2</sub> to N<sub>2</sub> balance ( $\pm 2.5\%$  by partial pressure), and no clear quantification of total hydrocarbons (THC). According to the supplier, it is intended to be used for such purposes as powering pneumatic tools and inflating tires. Similarly loose specifications were found for “Industrial” grade N<sub>2</sub> and CO<sub>2</sub>. Throughout the development campaign, there was a switch to “Breathing Air,” then finally to the “ALPHAGAZ” line of gases. This last line of gases is intended to be used for research applications. The relative O<sub>2</sub> to N<sub>2</sub> balance is tighter ( $\pm 0.5\%$  by partial pressure), and the THC are specified to be less than 0.05 ppm. Specifications for N<sub>2</sub> and CO<sub>2</sub> at this grade were found to be similarly acceptable. For each experiment, the specification of gas is tabulated in section [A.1](#).

At the beginning of this test campaign, standard shock tube cleaning practice in T5 was to roll four shop towels into a cylinder and drag them through the shock tube. It became clear from the boundary-layer instability measurements that there were clear outlier instances of turbulent flow on the cone. In some instances, no other broad-band disturbances were registered by the FLDI during the steady flow test time beside a sporadic and unexplainable period of broadband response. To show these occurrences, spectrograms of two runs are compared. An example of sporadic response shows a large swath of broad-band response, followed by a period where minimal disturbances are detected, followed by a period of narrowband response (Fig 4.9(a)). An example of what is expected shows a stochastic but sensible series of narrowband peaks (Fig. 4.9(b)).



(a)



(b)

Figure 4.9: Arbitrary logarithmic units of change in density, the spectrum is estimated by the short time Fourier transform. Darker shading indicates larger amplitude. BBR is broadband response, NBR is narrowband response. Top: An example of sporadic response shows a large swath of broad-band response, followed by a period where minimal disturbances are detected, followed by a period of narrowband response (shot 2702). Bottom: An example of what is expected shows a stochastic but sensible series of narrowband peaks (shot 2789).

It was hypothesized that reducing the particulates in the shock tube prior to the run could reduce the number of unexpected occurrences of broadband response. The cleaning procedure between each experiment was changed to: 1) clean the shock-tube end with a Scotch-Brite pad, 2) clean the shock-tube end with acetone on a mop, 3) pass four shop towels rolled into a cylinder and drag them through the shock tube, the outer-most towel being misted with acetone, 4) repeat step 3 until the outermost towel does not become dirty after a pass through the shock tube. This procedure led to results as in Fig. 4.9(b).

During some experiments, the FLDI system would register near zero voltage just after the tunnel startup period (Fig. 4.10(a)), this behavior inhibits FLDI measurement. Vibration is eliminated as a candidate cause by accelerometer measurement (plots in section C). Small, constant amplitude vibrations begin at the test section  $\approx 100$  ms before the trigger. After  $\approx 4$  ms from the trigger<sup>5</sup> the vibration environment becomes very harsh, but this is after the end of the test time. Additionally, no gases used in these experiments have appreciably strong absorption lines at the wavelength of the FLDI laser (532 nm). It is concluded that the gas is exhibiting characteristics consistent with opacity. The opacity may be caused by material in the flow from an oxidation/ablation process in the shock tube or nozzle throat. The problem is more evident as the reservoir enthalpy is raised, and even more so as the reservoir pressure is raised. Consistently performing experiments nearer to the T5 performance limits leads to results as in Fig. 4.10(a). Following a rigorous cleaning procedure permits results as in Fig. 4.10(b) to be reproducibly demonstrated.

---

<sup>5</sup>The trigger is the primary shock wave registering a response by the reservoir pressure transducers. Steady flow over the cone begins  $\approx 1$  ms after the trigger.

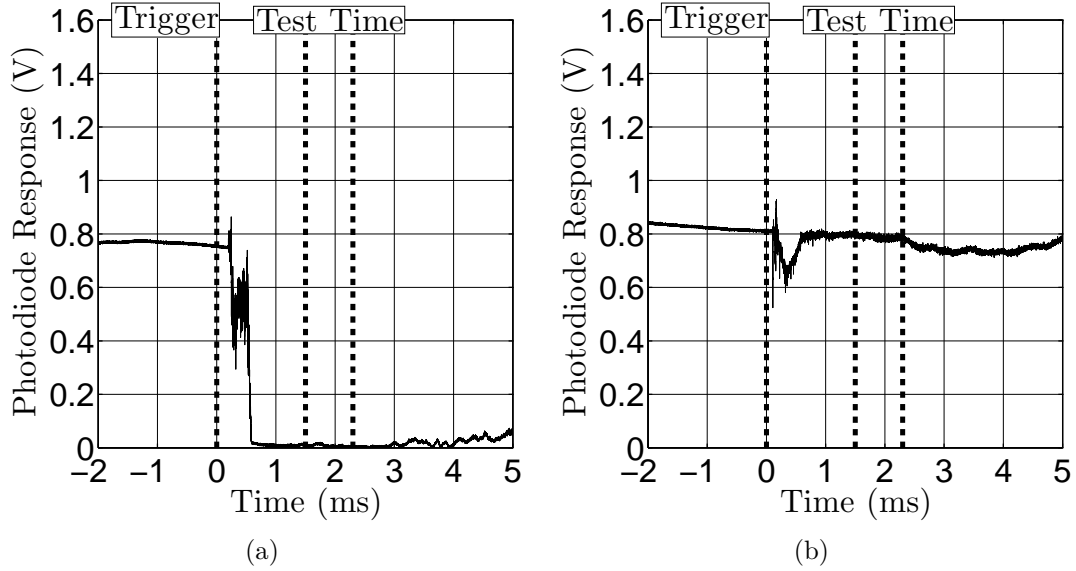


Figure 4.10: Raw time traces of photodiode response for the FLDI in Fig. 3.1. The ordinate range represents the peak (0.0 volts) and trough (1.6 volts) of a fringe; before each experiment the interferometer set to the middle of a fringe, 0.8 volts. The dashed lines represent the data acquisition system `Trigger` and the `Test Time` period. a: During startup period of shot 2726 ( $\text{CO}_2$ ) the flow becomes opaque. b: No opacity problems are evident for shot 2773 ( $\text{N}_2$ ).

### 4.3.2 Data and Discussion

Two shots from the development phase will be analyzed in this subsection (edge conditions found in Table 4.5). These two shots are selected for presentation because decisions pertaining to data processing and experimental methodology were based upon their results.

Table 4.5: Double Point Edge Conditions - Development

| Shot | $U_E$ | $\rho_E$                   | $P_E$ | $T_{t/rE}$ | $T_{vE}$ | $M_E$ | $Re_E^{Unit}$ | $y_{N_2}$ | $y_{O_2}$ | $y_{NO}$ | $y_N$ | $y_O$ |
|------|-------|----------------------------|-------|------------|----------|-------|---------------|-----------|-----------|----------|-------|-------|
|      | (m/s) | ( $\text{kg}/\text{m}^3$ ) | (kPa) | (K)        | (K)      | (-)   | (1/m)         | (-)       | (-)       | (-)      | (-)   | (-)   |
| 2711 | 3402  | 0.095                      | 31.9  | 1162       | 1036     | 4.96  | 6.88e6        | 0.73      | 0.19      | 0.08     | 0.00  | 0.00  |
| 2743 | 3799  | 0.095                      | 43.5  | 1575       | 1497     | 4.75  | 6.52e6        | 0.73      | 0.19      | 0.07     | 0.00  | 0.01  |

Initially, the data were analyzed in the same manner as in section 4.2. Certain windows of the test time that seemed interesting were selected, and spectral content of the signal in each of these windows was estimated. For example, for shot 2711, four

30  $\mu\text{s}$  windows in time are highlighted at 1630  $\mu\text{s}$ , 1745  $\mu\text{s}$ , 1890  $\mu\text{s}$ , and 2050  $\mu\text{s}$ , and their respective spectral content can be found in Fig 4.11(a). The four 30  $\mu\text{s}$  windows are displaced in time downstream to cover broadband responses in the boundary layer that appear to be end result of the content selected upstream (Fig. 4.11(b)). These results are consistent with a narrowband disturbance breaking down to a turbulent spot. These were the first data collected in T5 where disturbances are thought to have been successfully tracked from the upstream detector to the downstream detector. Although this result is interesting, it is unsatisfactory. Growth rate may not be measured with these data.

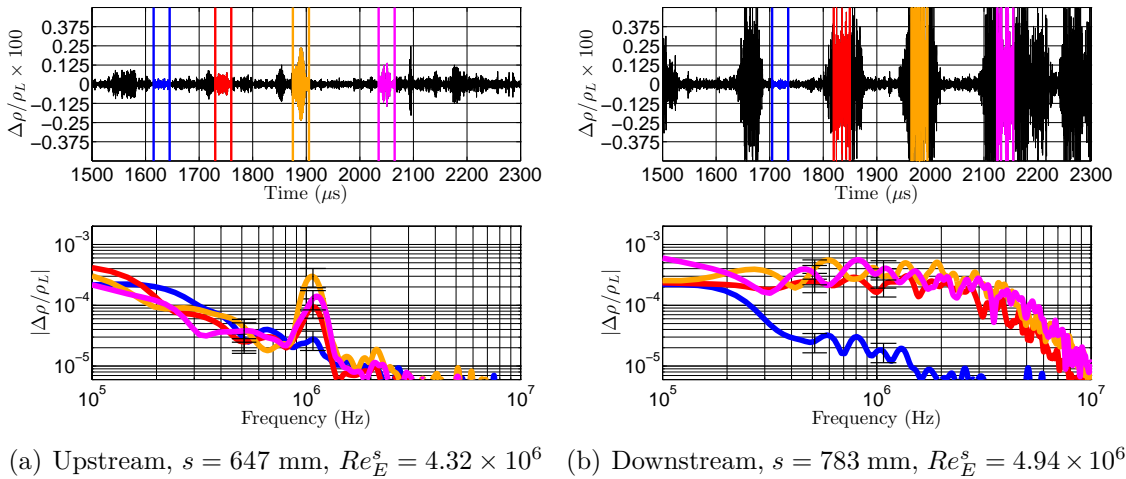


Figure 4.11: Windowed spectra shot 2711. Four 30  $\mu\text{s}$  windows highlight disturbances and corresponding spectra are plotted below for upstream (a) and downstream (b) probe volumes.

The detectors were realigned so that the distance along the generator of the cone ( $\Delta s$ ) was shorter. The purpose of this was to reduce the difference in Reynolds number between the detectors so that narrowband disturbances could be analyzed by each detector. The range of  $\Delta s$  is bounded by limited optical access.

The data for shot 2743 are analyzed with a similar windowed type manner in Fig. 4.12, with the probe volumes closer together. Nine windows highlight interesting narrowband disturbances in both the upstream and downstream detectors. The

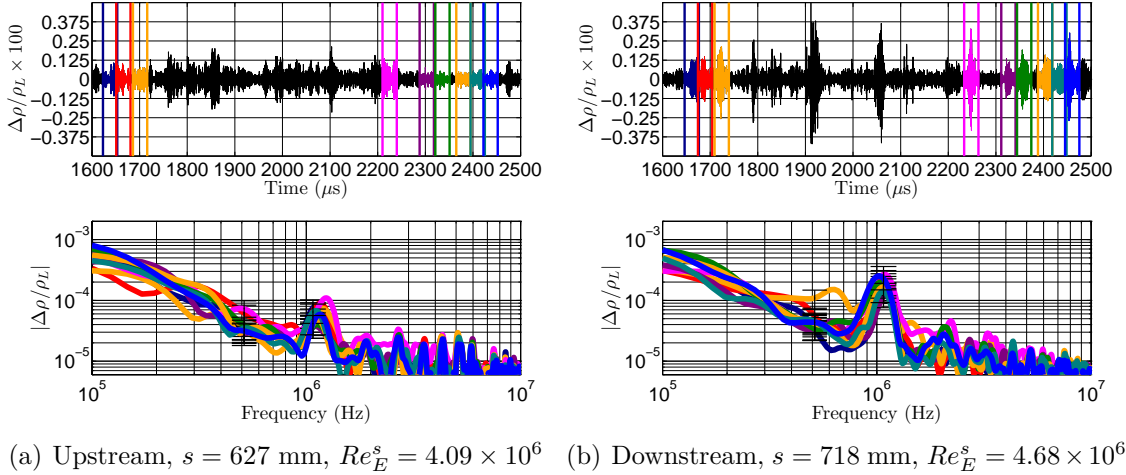


Figure 4.12: Windowed spectra shot 2743. Nine  $30 \mu\text{s}$  windows highlight disturbances and corresponding spectra are plotted below for upstream (a) and downstream (b) probe volumes.

narrowband peaks increase in amplitude and decrease in frequency. This behavior is consistent with an acoustic disturbance traveling downstream in the growing boundary layer.

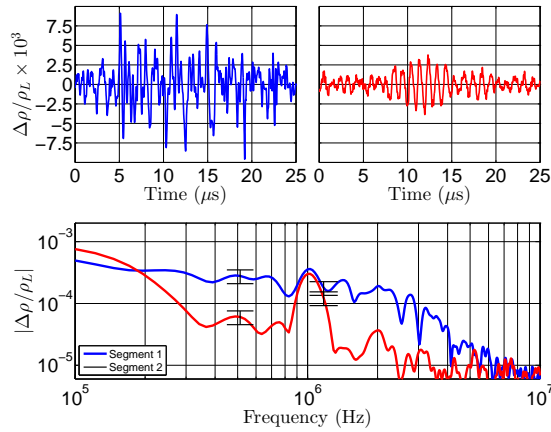


Figure 4.13: Narrowband vs. broadband disturbance from shot 2743. The top left time trace and corresponding spectrum (blue) indicate broadband response. The top right time trace and corresponding spectrum (red) indicate a narrowband disturbance. Both of these  $25 \mu\text{s}$  windows are selected from the downstream detector (Fig. 4.12(b)).

Individual windows were selected in the downstream data on the basis of discriminating against broadband response (as in Fig. 4.13). These windows were then displaced in time in the upstream detector. The time scale chosen to displace each of

the windows in Fig. 4.12(b) is a result of cross correlating the upstream and downstream disturbance signals (Fig. 4.14(b)). The ordinates in the cross-correlation plots are normalized by the square root of the product of the auto-covariances at zero lag, so that the maximum correlation would be unity if at any lag the signal upstream is identical to the signal downstream. A peak in cross-correlation occurs at a time-lag  $\tau=23.3 \mu\text{s}$ , and it is postulated that this effectively measures the correlation of the envelope of energy between the detectors, and could possibly be the group velocity of the narrowband disturbance between detectors. So, each of the windows in Fig. 4.12(b) are centered  $23.3 \mu\text{s}$  later in time than the windows in Fig. 4.12(a). There is no peak in the correlation in Fig. 4.14(a) indicating the inability of the algorithm to find a signal that is similar in each of the detectors. This would be consistent with attempting to cross-correlate signals that are as dissimilar as acoustic disturbances and turbulent spots, as is the case for the data in the upstream and downstream probe volumes for shot 2711.

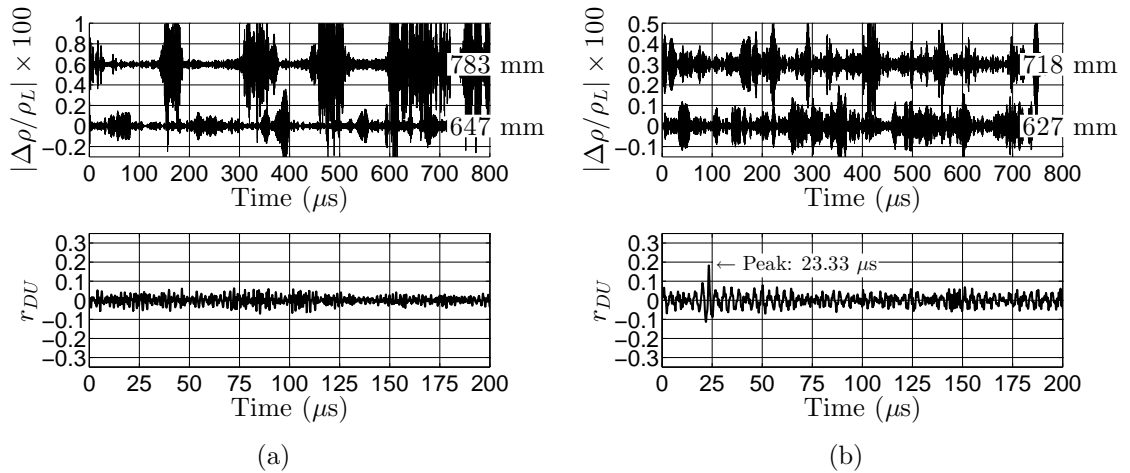


Figure 4.14: Time traces and cross-correlations of  $\Delta\rho/\rho_L$  for shots 2711 (a) and 2743 (b).

An additional method of inspecting the signals from the two-point FLDI technique is the spectrogram. This method of data processing provides much of the same information as the user-specified windowed spectra (Figs 4.11 and 4.12) but for the

entire test duration, allowing for the interpretation of disturbances with time. Evaluating the evolution of the spectrum throughout the run time is important because it is an indicator of the state of the boundary layer as well as an indicator of the quality of the data.

A spectrogram of shot 2711 is presented as Fig. 4.15. The narrowband disturbances can be seen to intermittently appear in the upstream trace at  $\approx 1.1$  MHz (Fig. 4.15, above), and no such narrowband disturbances can be found in the downstream detector (Fig. 4.15, below). There are periods in the downstream spectrogram where large broadband perturbations are recorded. This further motivated attempting to reduce the distance between the probe volumes ( $\Delta s$ ) so that narrowband disturbances could be measured in the upstream and downstream locations.

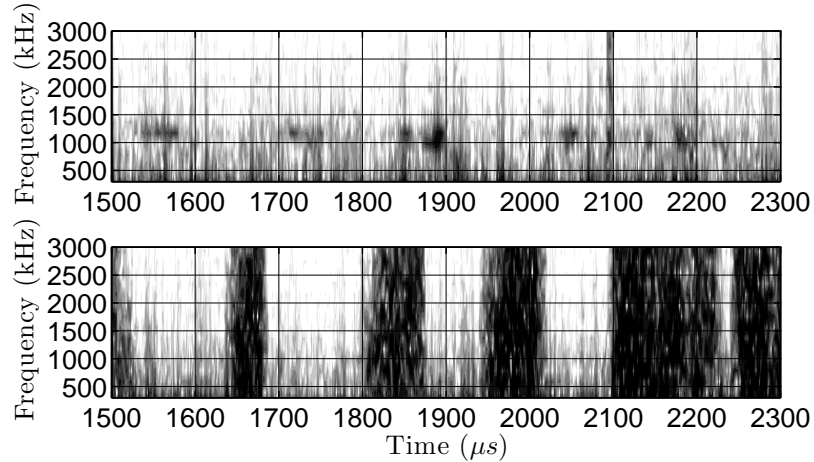


Figure 4.15: Spectrograms of shot 2711. Arbitrary logarithmic units of change in density, the spectrum is estimated by the short time Fourier transform. Darker shading indicates larger amplitude. Above: Upstream,  $s = 647$  mm,  $Re_E^s = 4.32 \times 10^6$ . Below: downstream,  $s = 783$  mm,  $Re_E^s = 4.94 \times 10^6$ .

A spectrogram of the upstream and downstream probe volumes for shot 2743 is presented as Fig. 4.16. In the upstream detector (Fig. 4.16, above), intermittent narrowband disturbances are registered throughout the test time at  $\approx 1.2$  MHz. These disturbances are seen to have larger amplitude in the downstream spectrogram (Fig. 4.16, below), although the correlation by transit time of the disturbances is

difficult to ascertain from this presentation. The disturbances in the downstream detector are also at a lower frequency  $\approx 1.1\text{MHz}$ . Two broadband periods appear in the downstream spectrogram; they are very short in duration. From this spectrogram, it appears that the disturbances are nearly at the point of break down to turbulence.

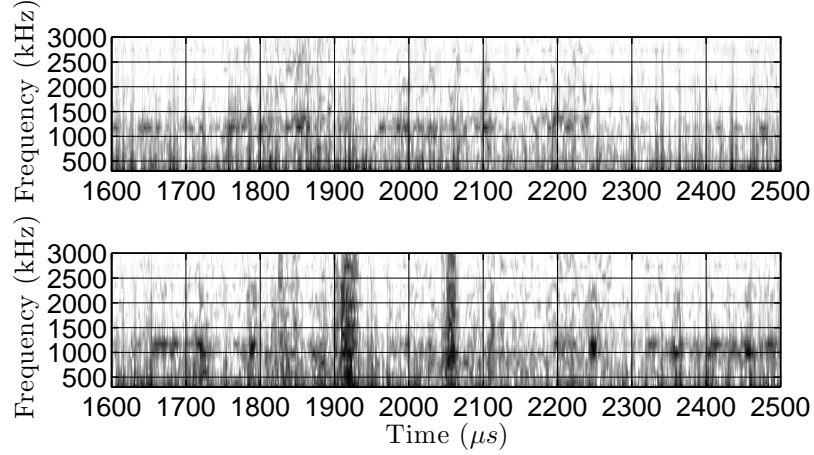


Figure 4.16: Spectrograms of shot 2743. Arbitrary logarithmic units of change in density, the spectrum is estimated by the short time Fourier transform. Darker shading indicates larger amplitude. Above: Upstream,  $s = 627$  mm,  $Re_E^s = 4.09 \times 10^6$ . Below: downstream,  $s = 718$  mm,  $Re_E^s = 4.68 \times 10^6$ .

The user-specified windowed spectra (Figs 4.11 and 4.12), correlations (Fig. 4.14), and spectrograms (Figs. 4.15 and 4.16) are valuable ways of data processing that provide a means of interpreting the FLDI data. These methods all lack a means of extracting information about the evolution of disturbances in the boundary layer in an unbiased manner; one way of achieving this goal is to analyze the time-averaged spectral content from the full test time.

The time-averaged spectra are computed using Welch's method with 50% overlapping  $10 \mu\text{s}$  Hann windows (Figs. 4.17(a) and 4.17(b)). For shot 2711, the peak at 1.1 MHz is evident in the upstream probe volume and the broadband spectral content in the downstream detector indicates turbulent bursts. For shot 2743, a strong narrowband peak in the upstream detector is clear at 1.2 MHz. There appears to be a peak in the downstream probe volume spectral content at 1.1 MHz, but the content

is being filled in around this peak. The next logical step after analyzing these data is to perform experiments at lower unit Reynolds number so that the effective spacing of the probe volumes is reduced. Those results form the basis of the data presented in the next section.

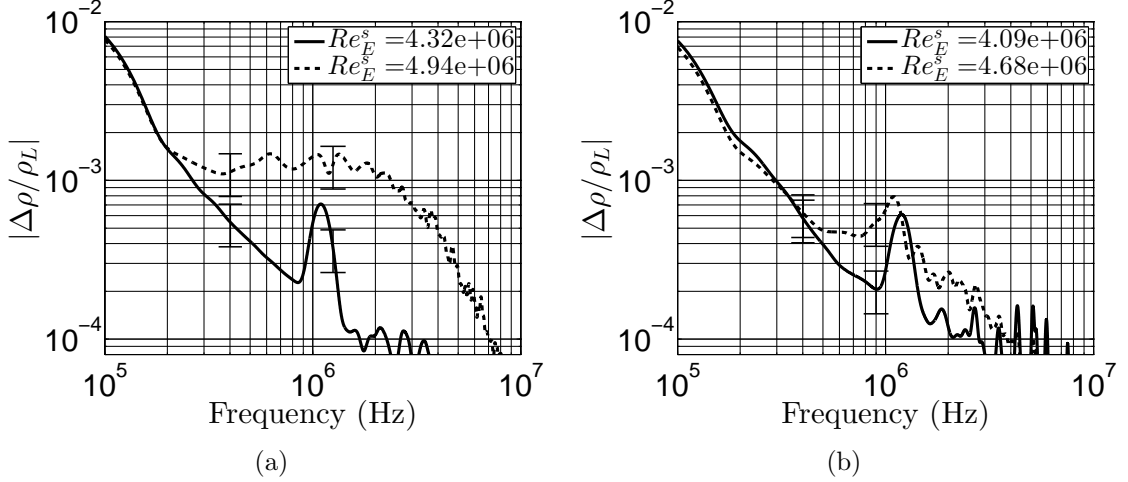


Figure 4.17: a: Spectrum estimate for shot 2711. b: Spectrum estimate for shot 2743.

An estimate of the most strongly amplified frequency is  $f \approx KU_E/(2\delta)$ . The frequency of the spectral peak at the upstream detector,  $f_U$ , is higher than the frequency of the spectral peak at the downstream detector,  $f_D$ ; as expected, the frequency is inversely proportional to the computed boundary-layer thickness (Table 4.6). This behavior is consistent with the hypothesis that as the effective waveguide grows in size, the frequency should decrease correspondingly. Additionally, if there is a peak in the cross-correlation, that time divided by probe volume spacing should indicate the group velocity of the narrowband disturbances. This velocity scale is nearly the edge velocity of the boundary layer (Table 4.6).

Table 4.6: Double Point Dev. Boundary Layer Instability Scaling

| Shot | $U_E$ | $\tau$     | $U_E/(\Delta s/\tau)$ | $\delta_U$ | $f_U$ | $2f_U\delta_U/U_E$ | $\delta_D$ | $f_D$ | $2f_D\delta_D/U_E$ |
|------|-------|------------|-----------------------|------------|-------|--------------------|------------|-------|--------------------|
|      | (m/s) | ( $\mu$ s) | (-)                   | (mm)       | (kHz) | (-)                | (mm)       | (kHz) | (-)                |
| 2711 | 3402  | -          | -                     | 1.06       | 1090  | 0.68               | 1.17       | -     | -                  |
| 2743 | 3799  | 23.3       | 0.97                  | 1.03       | 1200  | 0.65               | 1.11       | 1090  | 0.63               |

## 4.4 Double Point FLDI Measurement - Air

Air is used as the test gas in the series of experiments presented in this section. The reservoir pressure is held approximately constant, while the reservoir enthalpy is varied for two different series of shots. The two shot series are separated in Table 4.7 for organizational purposes as “lower enthalpy” (shots 2767-2764) and “higher enthalpy” (shots 2788-2787). In the lower and higher enthalpy series, the edge unit Reynolds number decreases when the reservoir pressure is held nominally constant and the reservoir enthalpy is increased.

Table 4.7: Double Point Edge Conditions - Development

| Shot | $U_E$ | $\rho_E$             | $P_E$ | $T_{t/rE}$ | $T_{vE}$ | $M_E$ | $Re_E^{Unit}$ | $y_{N_2}$ | $y_{O_2}$ | $y_{NO}$ | $y_N$ | $y_O$ |
|------|-------|----------------------|-------|------------|----------|-------|---------------|-----------|-----------|----------|-------|-------|
|      | (m/s) | (kg/m <sup>3</sup> ) | (kPa) | (K)        | (K)      | (-)   | (1/m)         | (-)       | (-)       | (-)      | (-)   | (-)   |
| 2767 | 3728  | 0.029                | 12.7  | 1505       | 1343     | 4.72  | 1.98e6        | 0.73      | 0.17      | 0.07     | 0.00  | 0.02  |
| 2766 | 3464  | 0.033                | 12.1  | 1248       | 1095     | 4.85  | 2.36e6        | 0.73      | 0.18      | 0.08     | 0.00  | 0.01  |
| 2765 | 3248  | 0.038                | 11.5  | 1039       | 900      | 5.00  | 2.82e6        | 0.73      | 0.19      | 0.08     | 0.00  | 0.01  |
| 2764 | 2982  | 0.037                | 8.3   | 776        | 725      | 5.33  | 2.99e6        | 0.73      | 0.19      | 0.07     | 0.00  | 0.00  |
| 2788 | 4425  | 0.067                | 46.1  | 2322       | 2281     | 4.49  | 4.03e6        | 0.74      | 0.16      | 0.07     | 0.00  | 0.03  |
| 2789 | 4244  | 0.076                | 47.1  | 2105       | 2062     | 4.55  | 4.73e6        | 0.73      | 0.17      | 0.07     | 0.00  | 0.02  |
| 2790 | 4199  | 0.079                | 47.3  | 2046       | 2001     | 4.57  | 4.94e6        | 0.73      | 0.17      | 0.07     | 0.00  | 0.02  |
| 2787 | 4062  | 0.079                | 43.2  | 1878       | 1819     | 4.63  | 5.08e6        | 0.73      | 0.18      | 0.07     | 0.00  | 0.02  |

The purpose of this campaign is to measure the incipient instability waves prior to the transition to fully turbulent flow. The ultimate goal is to determine the role of the acoustic instability in the transition process. The FLDI measurement volumes are located just upstream of the transition location to measure the instability waves. Boundary-layer transition is identified by departure from laminar surface heat-flux

rates measured by surface mounted heat-transfer gauges used in Jewell et al. (2012).

#### 4.4.1 Lower Enthalpy Conditions

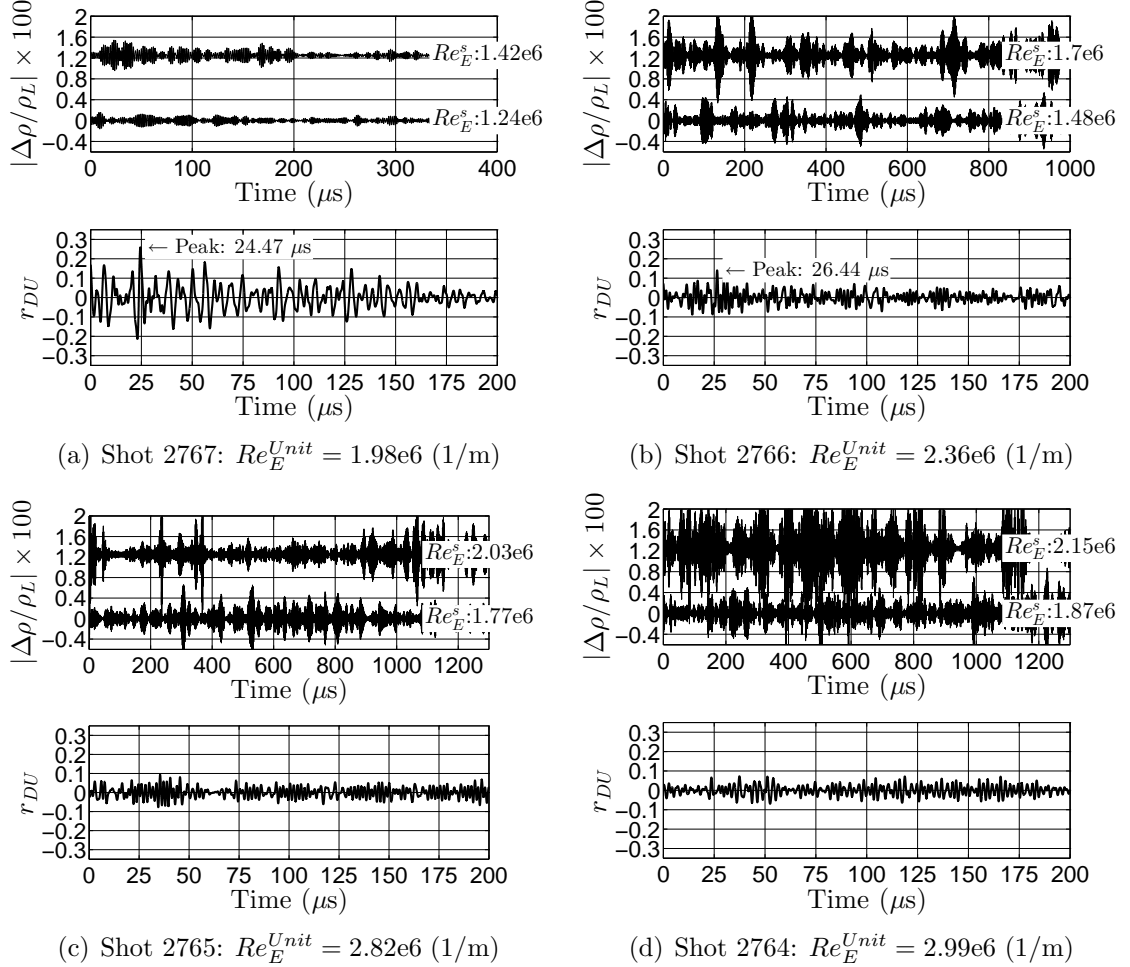


Figure 4.18: Time traces and cross-correlations of  $\Delta\rho/\rho_L$  for the lower enthalpy air shot series (conditions summarized in Table 4.7.)

For this shot series, the two FLDI probe volumes at  $627\pm 1$  mm and  $718\pm 1$  mm are positioned 37-57% of the boundary-layer thickness from the surface of the cone, respectively. All the probe locations can be found in Table B.

Band-pass filtered time traces of the non-dimensional fluctuations in density ( $\Delta\rho/\rho_L$ ) at two points in the boundary layer show an increase in RMS response as the edge unit Reynolds number is increased (top of each plot in Fig. 4.18). Cross-correlation

is used to estimate the extent to which the response at the upstream detector is related to the response at the downstream detector in a time-lag sense (bottom of each plot in Fig. 4.18). The ordinates in the cross-correlation plots are normalized by the square root of the product of the auto-covariences at zero lag, so that the maximum correlation would be unity if at any lag the signal upstream is identical to the signal downstream.

A peak in cross-correlation at a time-lag  $\tau$ , is nearly consistent with the time scale associated with the edge velocity and the detector spatial separation  $\Delta s$  (Table 4.8). These peaks in cross-correlation appear when both the upstream and downstream band-pass filtered time traces of  $\Delta\rho/\rho_L$  show low-amplitude, wave-packet-like behavior. This may indicate that the detectors are tracking wave packets that are traveling along the generator of the cone at approximately the edge velocity.

To further classify the signals, estimates of the power spectral density for each case are computed using Welch's method, with 50% overlapping  $20\ \mu\text{s}$  Hann windows (Fig. 4.19). As the Reynolds number is increased, a narrowband spectral peak increases in amplitude up to a certain value, slightly decreases in frequency, and then broadens out. This behavior is consistent with a fluid-dynamic instability increasing in amplitude in a thicker boundary layer, and then breaking down to turbulence. This assertion is supported by a corresponding departure from laminar surface heat-flux rates measured by surface mounted heat-transfer gauges (not shown). Note that there is a peak in the cross-correlation only when both detectors have a distinct narrowband spectral response. The peak in the cross-correlation indicates that there are discrete packets of narrowband disturbance that are traceable from the upstream detector to the downstream detector.

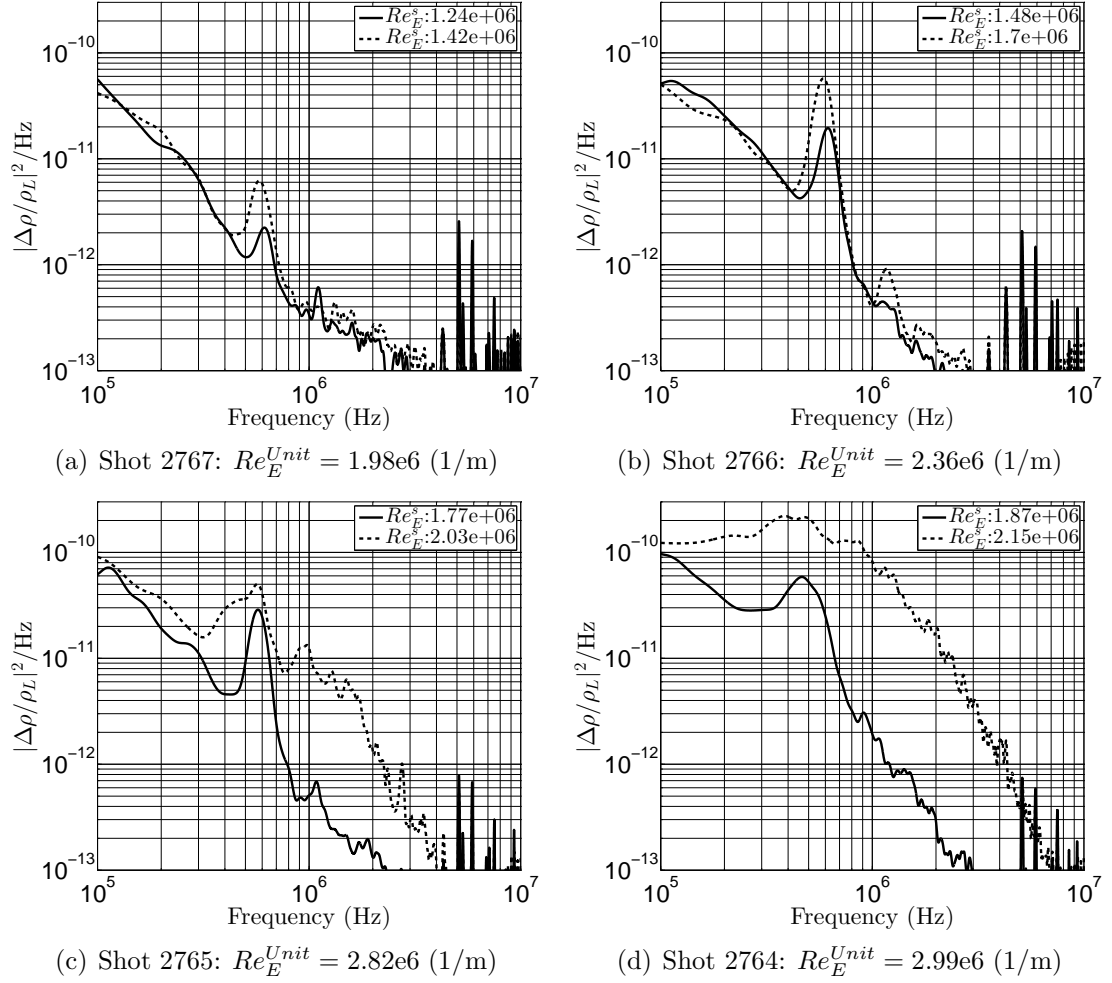


Figure 4.19: Power spectral density estimates of  $\Delta\rho/\rho_L$  for the lower enthalpy air shot series (conditions summarized in Table 4.7.)

#### 4.4.2 Higher Enthalpy Conditions

A second series of shots in air was conducted at higher reservoir pressure so that the reservoir enthalpy could be increased at a Reynolds number appropriate for instability measurement. These conditions appear as the conditions in the lower box in Table 4.7. Time traces and correlations are included for these experiments in Fig. 4.20. As the edge Reynolds number is increased, the RMS response of the FLDI probe volumes increases.

Power spectral density estimates are made for these experiments as well. They are computed using Welch's method, with 50% overlapping 10  $\mu s$  Hann windows and

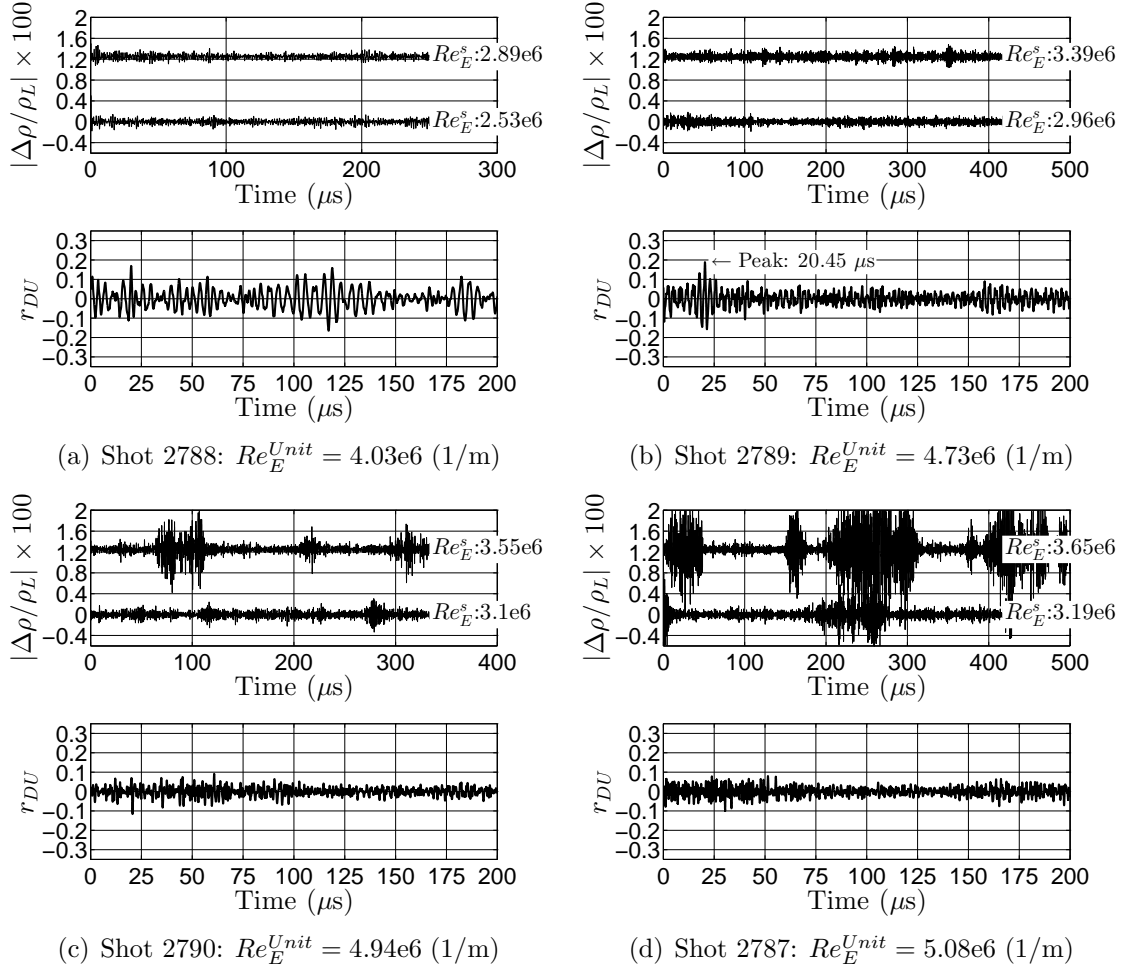


Figure 4.20: Time traces and cross-correlations of  $\Delta\rho/\rho_L$  for the higher enthalpy air shot series (conditions summarized in Table 4.7).

are presented in Fig. 4.21. Again, as the Reynolds number is increased, narrowband peaks appear to grow in amplitude, and then broadband behavior is observed. Note that making measurements of the instability at both probe volumes is more difficult at higher reservoir conditions (as in Fig. 4.21(b) versus Fig. 4.19(b)) because the non-dimensional distance between the detectors is higher.

The narrowband peaks observed in the spectral estimates are consistent with the acoustic mode first described by Mack (1984), for which an estimate of the most strongly amplified frequency is  $f \approx KU_E/(2\delta)$ . The frequency of the spectral peak at the upstream detector,  $f_U$ , is higher than the frequency of the spectral peak at

the downstream detector,  $f_D$ ; as expected, the frequency is inversely proportional to the computed boundary-layer thickness (Table 4.8). This behavior is consistent with the hypothesis that as the effective waveguide grows in size, the frequency should decrease correspondingly. Note that the dimensional narrowband spectral content is of higher frequency in Fig. 4.21 than Fig. 4.19, but the time scale is consistent for two disparate run conditions.

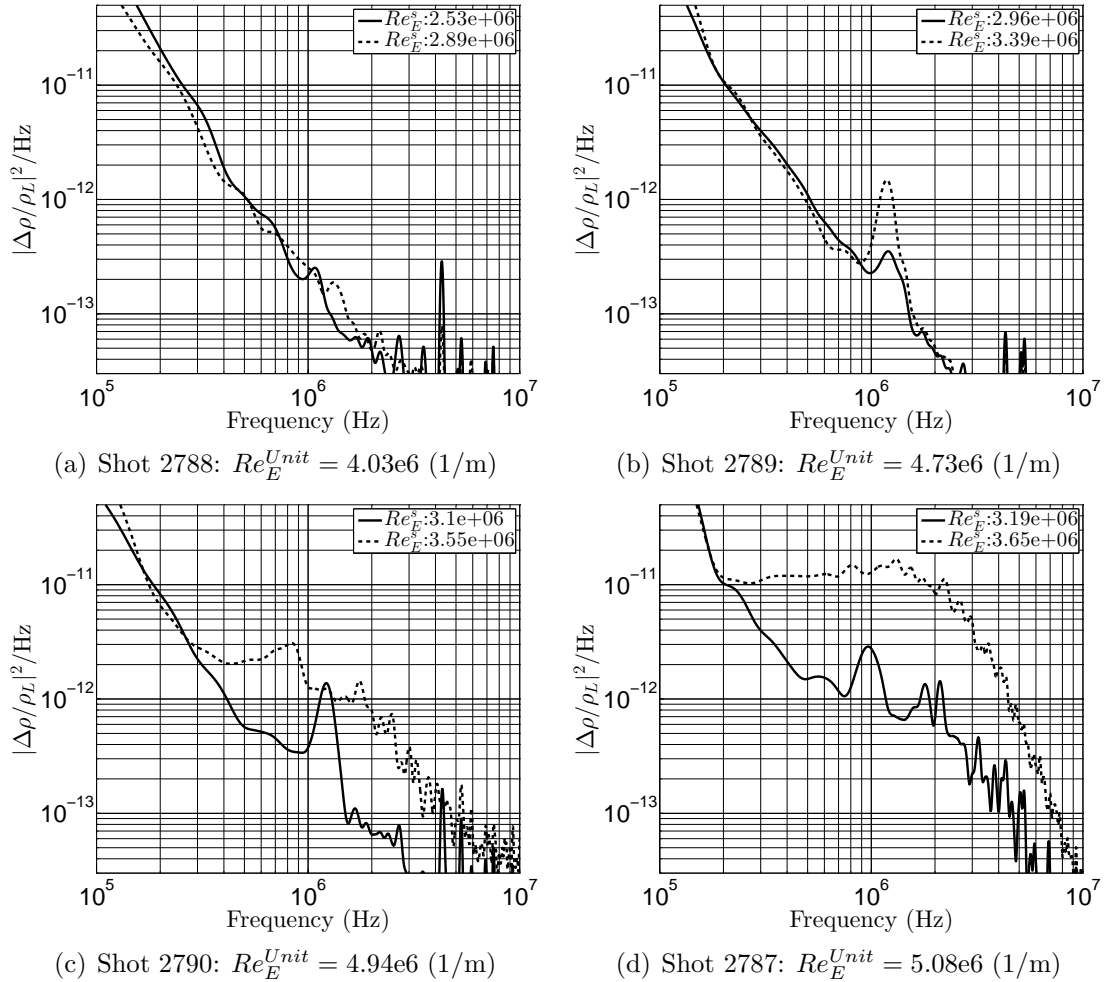


Figure 4.21: Power spectral density estimates of  $\Delta\rho/\rho_L$  for the higher enthalpy air shot series (conditions summarized in Table 4.7).

Table 4.8: Double Point Air Boundary Layer Instability Scaling

| Shot | $U_E$ | $\tau$     | $U_E/(\Delta s/\tau)$ | $\delta_U$ | $f_U$ | $2f_U\delta_U/U_E$ | $\delta_D$ | $f_D$ | $2f_D\delta_D/U_E$ |
|------|-------|------------|-----------------------|------------|-------|--------------------|------------|-------|--------------------|
|      | (m/s) | ( $\mu$ s) | (-)                   | (mm)       | (kHz) | (-)                | (mm)       | (kHz) | (-)                |
| 2767 | 3728  | 24.5       | 1.00                  | 1.91       | 620   | 0.63               | 2.04       | 580   | 0.63               |
| 2766 | 3464  | 26.4       | 1.00                  | 1.77       | 620   | 0.63               | 1.89       | 580   | 0.63               |
| 2765 | 3248  | -          | -                     | 1.67       | 580   | 0.64               | 1.79       | -     | -                  |
| 2764 | 2982  | -          | -                     | 1.72       | -     | -                  | 1.84       | -     | -                  |
| 2788 | 4425  | -          | -                     | 1.25       | -     | -                  | 1.34       | -     | -                  |
| 2789 | 4244  | 20.5       | 0.96                  | 1.17       | 1200  | 0.66               | 1.25       | 1180  | 0.69               |
| 2790 | 4199  | -          | -                     | 1.14       | 1200  | 0.65               | 1.22       | -     | -                  |
| 2787 | 4062  | -          | -                     | 1.14       | -     | -                  | 1.22       | -     | -                  |

### 4.4.3 Schlieren Visualization

High-speed schlieren cinematography from a conventional z-type setup, as in [Settles \(2001\)](#), also appears to capture the instability (Fig. 4.22). The 192x56 pixel images are recorded at 320k frames per second with a Vision Research Phantom v710. The light source is a high-power laser diode (905 nm, PN: 905D3S3J09R), pulsed for 12 ns by a LDP-V 50-100 V3 driver module from Laser Components. The center of the field of view is downstream of both FLDI detectors, approximately 780 mm from the tip of the cone. Ten frames are selected that bracket a frame in time when an interesting disturbance is observed in post-processing. An average is constructed, and 75 percent of the average is subtracted from each frame for contrast enhancement. The image shows the structures of the instability to be inclined at a 13-26 deg angle to the surface; it is noted to be similar to the results reported in [Kimmel et al. \(1996\)](#), [VanDercreek \(2010\)](#), and [Laurence et al. \(2012\)](#). "Structure angles for second-mode waves represent the inclination of a line of constant phase in the x-y plane" [Kimmel et al. \(1996\)](#); this is what we believe the structures in Fig. 4.22 to be.

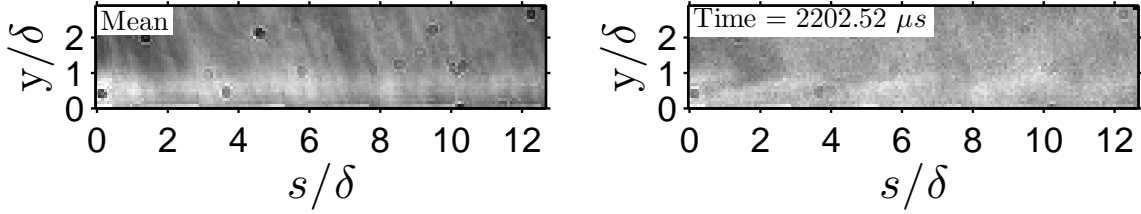


Figure 4.22: Schlieren images from shot 2766. On the left is the mean of ten frames, on the right is a snapshot of the instability. The time stamp indicates the delay from the pressure rise in the reservoir. The flow is from left to right. The calculated boundary-layer thickness (Table 4.8) and a length scale (allen key) placed in the image plane prior to the experiment are used to formulate the axes labels.

## 4.5 Double Point FLDI Measurement - $N_2$

Nitrogen is used as the test gas in the series of experiments presented in this section. The reservoir pressure is held approximately constant, while the reservoir enthalpy is varied for three different series of shots. The three shot series are separated in Table 4.9 for organizational purposes as “lower enthalpy” (shots 2774-2775), “medium enthalpy” (shots 2781-2778), and “higher enthalpy” (shots 2783-2782). The purpose of this campaign is to repeat the tests discussed in section 4.4 at as similar conditions as experimentally possible, but with a different test gas. This allows for the identification of any first-order effects that would significantly differentiate air and  $N_2$  as a test gas at these conditions. An additional goal was to attempt to make measurements of the acoustic instability at free-stream velocities in excess of 5 km/s. Again, the edge unit Reynolds number decreases when the reservoir pressure is held constant and the reservoir enthalpy is increased.

For this shot series, the two FLDI probe volumes at  $627 \pm 1$  mm and  $718 \pm 1$  mm are positioned 29-42% of the boundary-layer thickness from the surface of the cone, respectively. All the probe locations can be found in Table B.

Table 4.9: Double Point Edge Conditions - N<sub>2</sub>

| Shot | $U_E$ | $\rho_E$             | $P_E$ | $T_{t/rE}$ | $T_{vE}$ | $M_E$ | $Re_E^{Unit}$ | $y_{N_2}$ | $y_N$ |
|------|-------|----------------------|-------|------------|----------|-------|---------------|-----------|-------|
|      | (m/s) | (kg/m <sup>3</sup> ) | (kPa) | (K)        | (K)      | (-)   | (1/m)         | (-)       | (-)   |
| 2774 | 4054  | 0.020                | 6.9   | 1183       | 3303     | 5.76  | 1.72e6        | 0.99      | 0.01  |
| 2773 | 3859  | 0.020                | 6.0   | 1014       | 3136     | 5.93  | 1.83e6        | 1.00      | 0.00  |
| 2772 | 3665  | 0.021                | 5.4   | 876        | 3012     | 6.07  | 1.98e6        | 1.00      | 0.00  |
| 2775 | 3511  | 0.023                | 5.4   | 781        | 2924     | 6.16  | 2.25e6        | 1.00      | 0.00  |
| 2781 | 4793  | 0.045                | 29.8  | 2222       | 3360     | 4.95  | 3.11e6        | 0.99      | 0.01  |
| 2780 | 4624  | 0.049                | 28.7  | 1959       | 3300     | 5.10  | 3.61e6        | 0.99      | 0.01  |
| 2779 | 4389  | 0.050                | 24.4  | 1630       | 3200     | 5.32  | 4.03e6        | 1.00      | 0.00  |
| 2778 | 4194  | 0.050                | 20.3  | 1373       | 3082     | 5.54  | 4.15e6        | 1.00      | 0.00  |
| 2783 | 4917  | 0.052                | 38.1  | 2446       | 3263     | 4.84  | 3.44e6        | 0.99      | 0.01  |
| 2782 | 4792  | 0.056                | 37.1  | 2233       | 3252     | 4.95  | 3.85e6        | 0.99      | 0.01  |

### 4.5.1 Lower Enthalpy Conditions

The results for the nitrogen test series are qualitatively similar to those for air. An increase in RMS response of  $\Delta\rho/\rho_L$  as the edge unit Reynolds number is increased can be observed (top of each plot in Fig. 4.23). A peak in cross-correlation at a time-lag  $\tau$ , is nearly consistent with the time scale associated with the edge velocity and the detector spatial separation  $\Delta s$  (Table 4.10). These peaks in cross-correlation appear when both the upstream and downstream band-pass filtered time traces of  $\Delta\rho/\rho_L$  show low-amplitude, wave-packet-like behavior (Fig. 4.23). This may indicate that the detectors are tracking wave packets that are traveling along the generator of the cone at approximately the edge velocity. This is similar in behavior as in the air series presented in in section 4.4.

Welch’s method, with 50% overlapping 20  $\mu s$  Hann windows, is used to make estimates of the power spectral density for each case (Fig. 4.24). As the Reynolds number is increased, a narrowband spectral peak increases in amplitude until it saturates, and then broadens out, similar in behavior as in the air series presented in in section 4.4.

The narrowband peaks observed in the spectral estimates are again consistent with

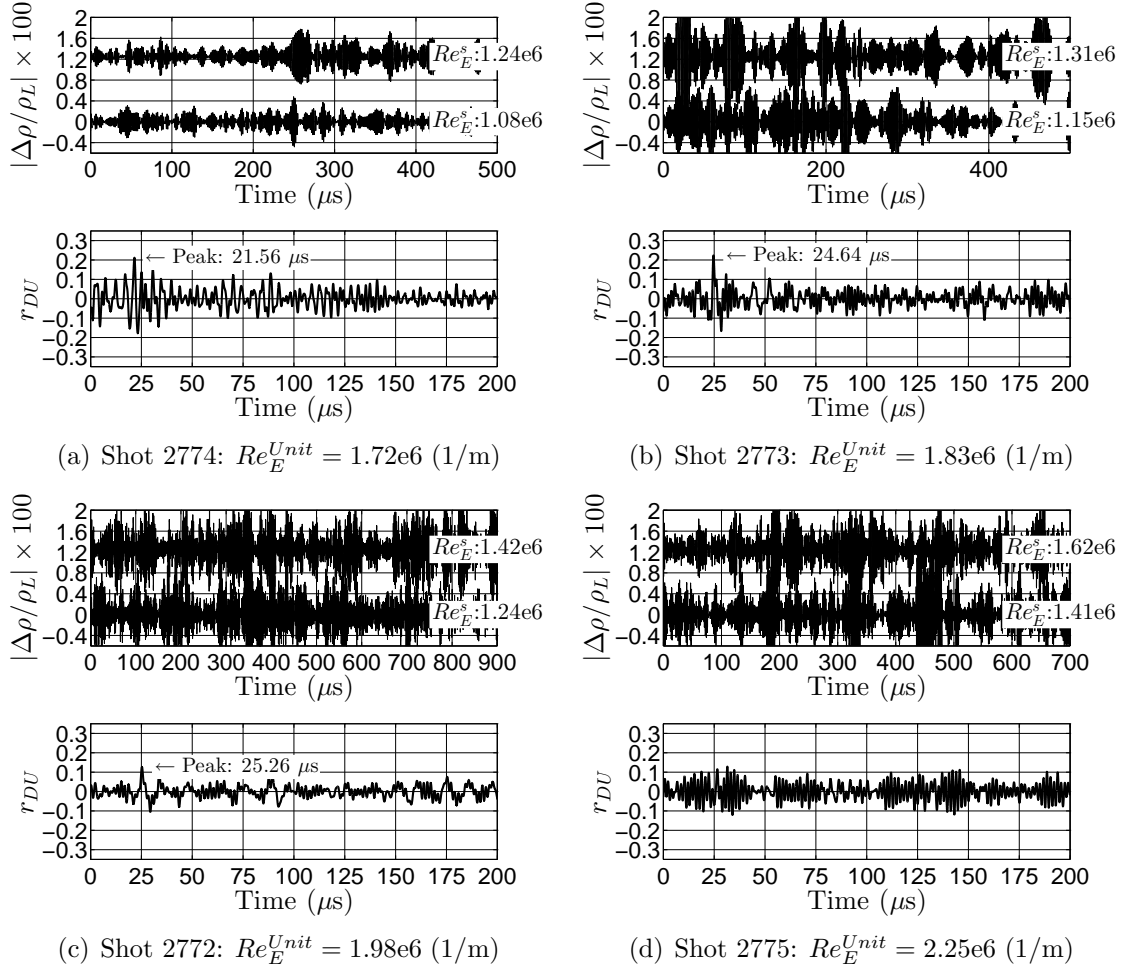


Figure 4.23: Time traces and cross-correlations of  $\Delta\rho/\rho_L$  for the lower enthalpy  $N_2$  shot series (conditions summarized in Table 4.9).

the acoustic mode. The frequency of the spectral peak at the upstream detector,  $f_U$ , is higher than the frequency of the spectral peak at the downstream detector,  $f_D$ ; the frequency is inversely proportional to the computed boundary-layer thickness (Table 4.10).

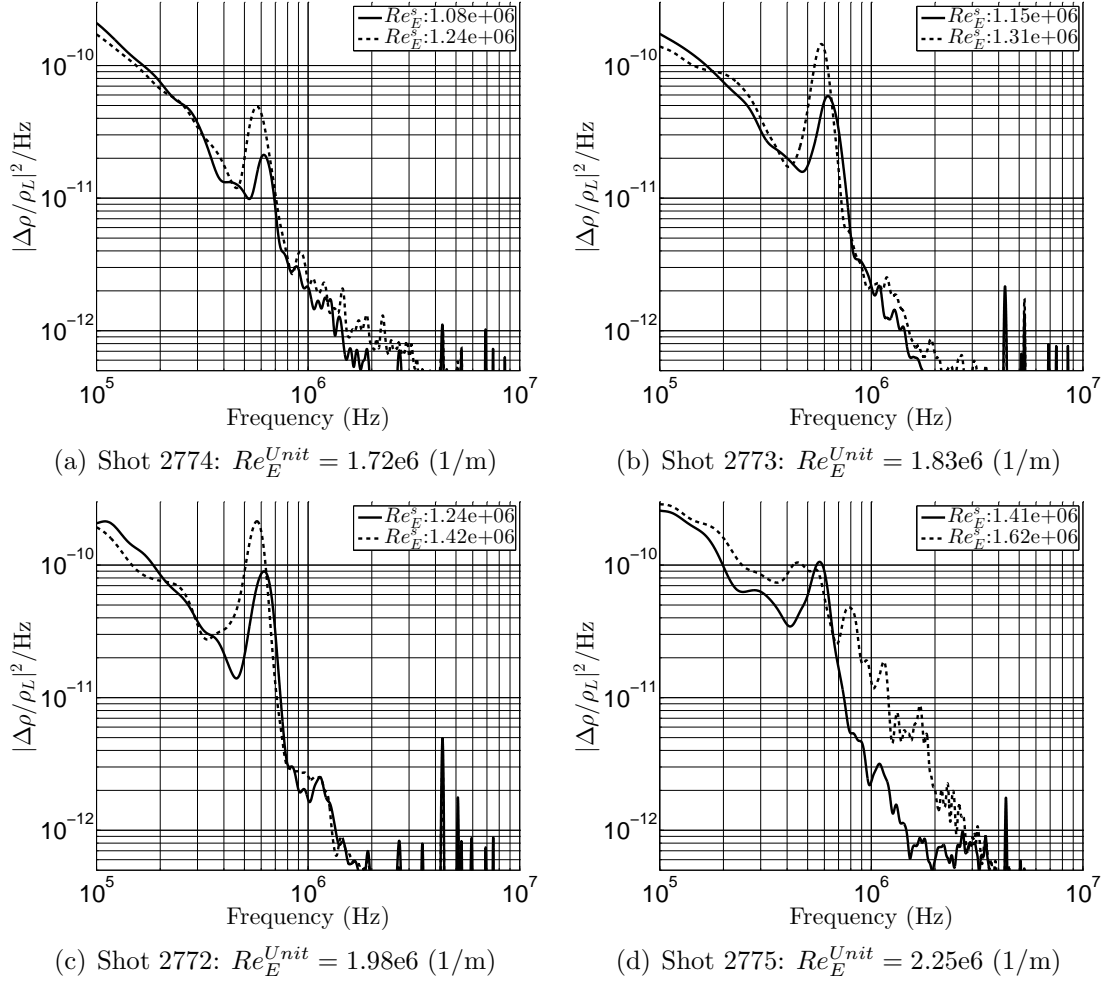


Figure 4.24: Power spectral density estimates of  $\Delta\rho/\rho_L$  for the lower enthalpy  $N_2$  shot series (conditions summarized in Table 4.9).

## 4.5.2 Moderate Enthalpy Conditions

As with the shots in air, a second series of shots in  $N_2$  was conducted at higher reservoir pressure so that the reservoir enthalpy could be increased at a Reynolds number appropriate for instability measurement. Again with increasing Reynolds number, the RMS fluctuations are observed to increase (Fig. 4.25). There are peaks in the cross-correlations when there are low-amplitude disturbances registered by both probe volumes. The velocity scale of transit of the disturbances between the detectors is again observed to be nearly the edge velocity (Table 4.9).

Welch's method, with 50% overlapping 10  $\mu s$  Hann, windows, is used to make

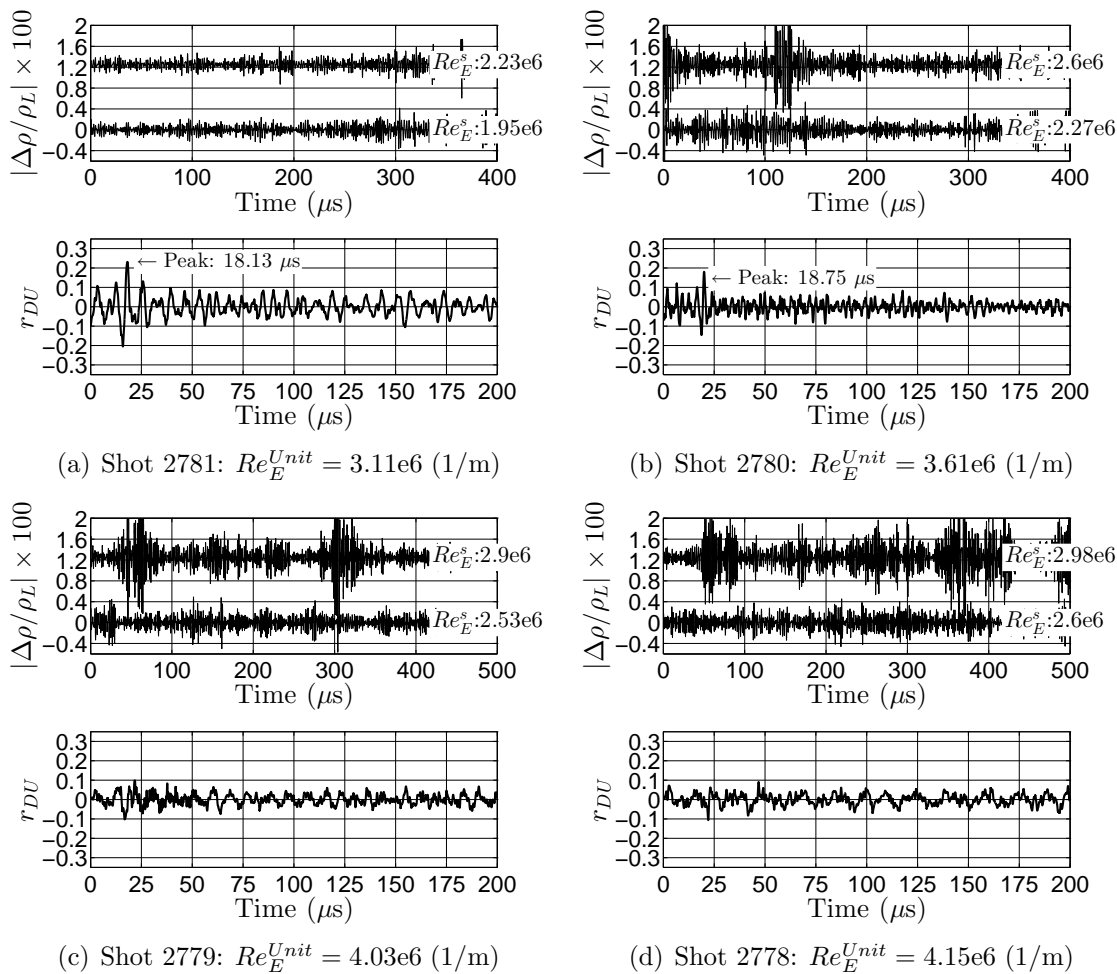


Figure 4.25: Time traces and cross-correlations of  $\Delta\rho/\rho_L$  for the medium enthalpy  $N_2$  shot series (conditions summarized in Table 4.9).

estimates of the power spectral density for each case (Fig. 4.26). The narrowband spectral peak increases in amplitude and decreases in frequency until it saturates, and then broadens out as the Reynolds number is increased.

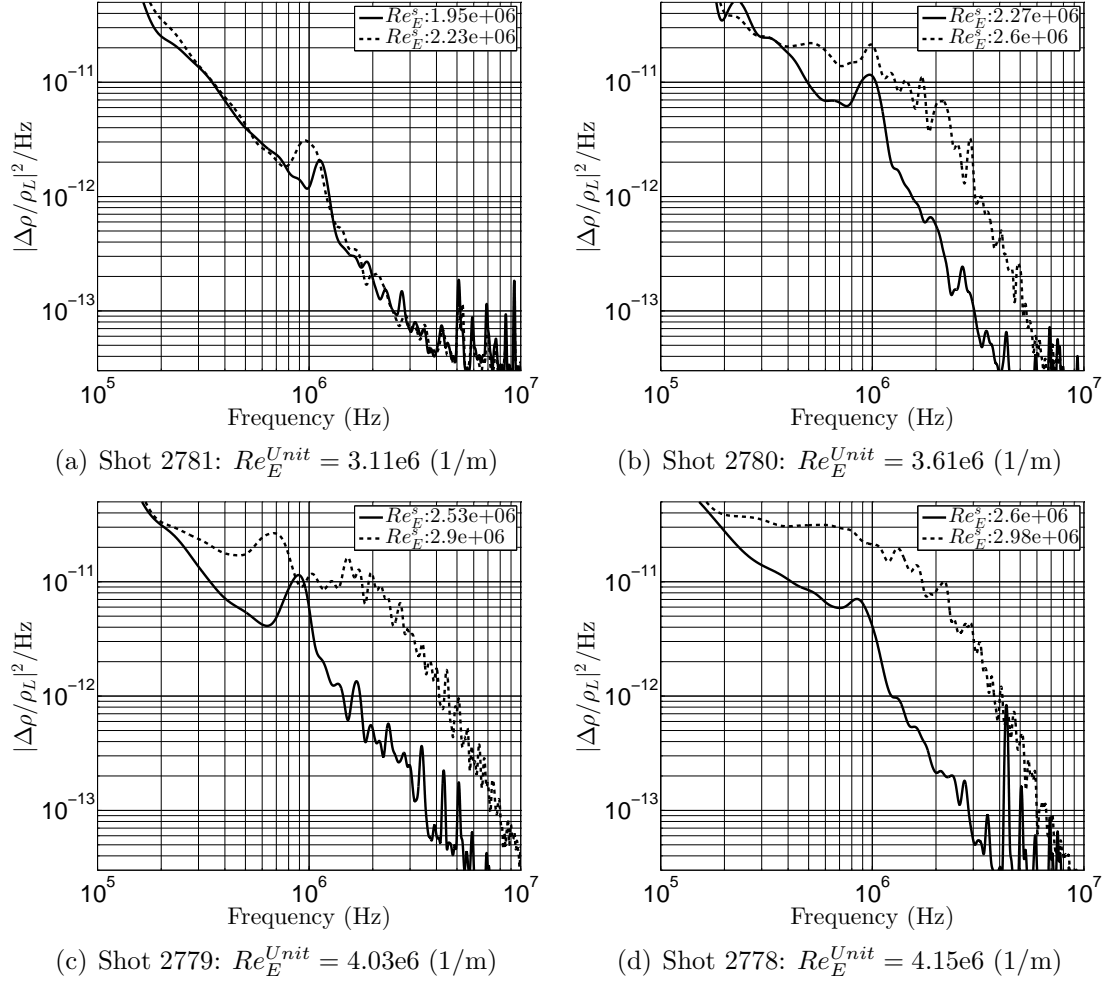


Figure 4.26: Time traces and cross-correlations of  $\Delta\rho/\rho_L$  for the medium enthalpy  $N_2$  shot series (conditions summarized in Table 4.7.)

### 4.5.3 Higher Enthalpy Conditions

In this subsection, the reservoir conditions were altered so that instability measurements were able to be made at free-stream velocities of  $> 5$  km/s (Table 4.7). Only two shots are included in this series as the high reservoir enthalpy and pressure required to make such measurements are closer to the performance envelope of T5, so the turnaround time of such shots is longer because of the more involved cleaning procedure that is required. The qualitative trends in increase in RMS response with increasing Reynolds number is consistent with all other experimental series (Fig. 4.27). The characteristic velocity ( $\Delta s/\tau$ ) that is observed from the correlation is again nearly

consistent with the edge velocity (Table 4.8) when there are low amplitude disturbances registered at the upstream and downstream detectors.

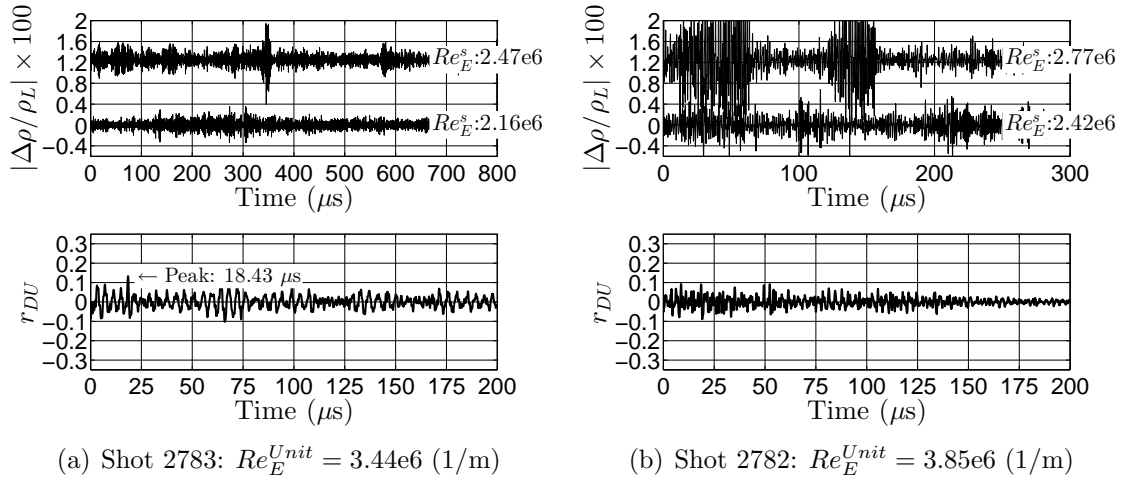


Figure 4.27: Time traces and cross-correlations of  $\Delta\rho/\rho_L$  for the higher enthalpy  $N_2$  shot series (conditions summarized in Table 4.7).

For these higher enthalpy cases, Welch's method, with 50% overlapping  $10 \mu s$  Hann windows, is used to make estimates of the power spectral density for each case (Fig. 4.28). The narrowband spectral peak increases in amplitude and decreases in frequency until it saturates, and then broadens out as the Reynolds number is increased.

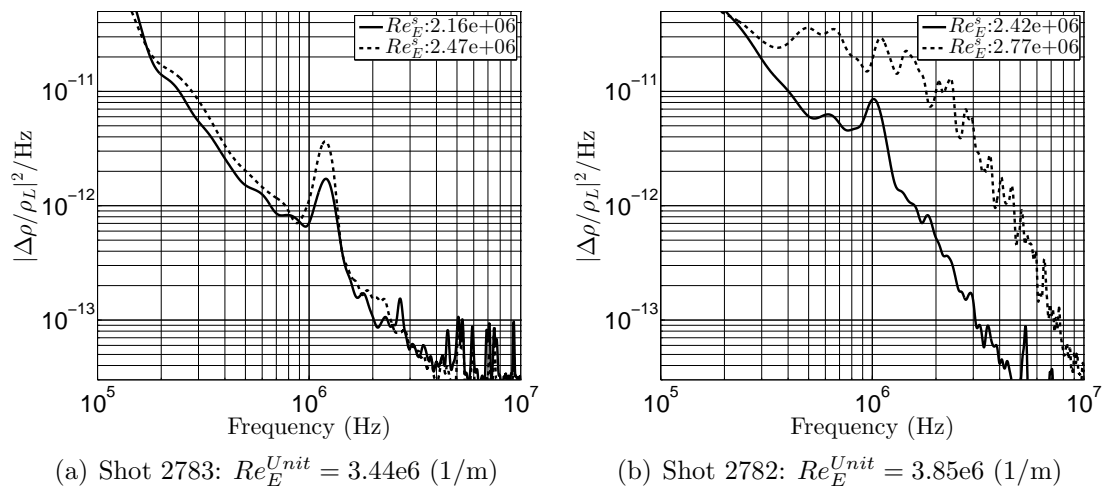


Figure 4.28: Power spectral density estimates of  $\Delta\rho/\rho_L$  for the higher enthalpy  $N_2$  shot series (conditions summarized in Table 4.7).

Table 4.10: Double Point N<sub>2</sub> Boundary Layer Instability Scaling

| Shot | $U_E$ | $\tau$     | $U_E/(\Delta s/\tau)$ | $\delta_U$ | $f_U$ | $2f_U\delta_U/U_E$ | $\delta_D$ | $f_D$ | $2f_D\delta_D/U_E$ |
|------|-------|------------|-----------------------|------------|-------|--------------------|------------|-------|--------------------|
|      | (m/s) | ( $\mu$ s) | (-)                   | (mm)       | (kHz) | (-)                | (mm)       | (kHz) | (-)                |
| 2774 | 4054  | 21.6       | 0.96                  | 2.37       | 620   | 0.72               | 2.54       | 570   | 0.71               |
| 2773 | 3859  | 24.6       | 1.04                  | 2.37       | 620   | 0.76               | 2.53       | 580   | 0.76               |
| 2772 | 3665  | 25.3       | 1.02                  | 2.32       | 630   | 0.80               | 2.49       | 570   | 0.77               |
| 2775 | 3511  | -          | -                     | 2.22       | 570   | 0.72               | 2.38       | -     | -                  |
| 2781 | 4793  | 18.1       | 0.95                  | 1.56       | 1100  | 0.71               | 1.67       | 960   | 0.67               |
| 2780 | 4624  | 18.8       | 0.96                  | 1.48       | 980   | 0.63               | 1.58       | -     | -                  |
| 2779 | 4389  | -          | -                     | 1.46       | 900   | 0.60               | 1.57       | -     | -                  |
| 2778 | 4194  | -          | -                     | 1.48       | -     | -                  | 1.58       | -     | -                  |
| 2783 | 4917  | 18.4       | 0.99                  | 1.44       | 1200  | 0.70               | 1.54       | 1200  | 0.75               |
| 2782 | 4792  | -          | -                     | 1.40       | -     | -                  | 1.49       | -     | -                  |

#### 4.5.4 Schlieren Visualization

High-speed schlieren cinematography from a conventional z-type setup, as in [Settles \(2001\)](#), also appears to capture the instability (Fig. 4.29). The 256x128 pixel images are recorded at 150k frames per second with a Vision Research Phantom v710. The light source is a high-power laser diode (905 nm, PN: 905D3S3J09R), pulsed for 12 ns by a LDP-V 50-100 V3 driver module from Laser Components. The center of the field of view is downstream of both FLDI detectors, approximately 780 mm from the tip of the cone. Ten frames that bracket a frame in time when an interesting disturbance is observed in post-processing are selected. An average is constructed, and 75 percent of the average is subtracted from each frame for contrast enhancement. The image shows the structures of the instability to be inclined at a 13-26 deg angle to the surface. It is noted to be similar to the results reported in [Kimmel et al. \(1996\)](#), [VanDercreek \(2010\)](#), and [Laurence et al. \(2012\)](#). "Structure angles for second-mode waves represent the inclination of a line of constant phase in the x-y plane" [Kimmel et al. \(1996\)](#); this is what we believe the structures in Fig. 4.22 to be.

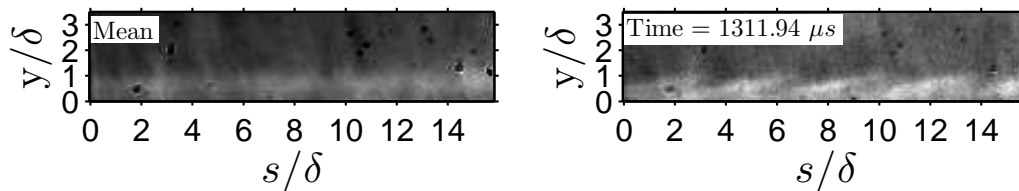


Figure 4.29: Schlieren image from shot 2773. On the left is the mean of ten frames, on the right is a snapshot of the instability. The time stamp indicates the delay from the pressure rise in the reservoir. The flow is from left to right. The calculated boundary-layer thickness (Table 4.10) and a length scale (allen key) placed in the image plane prior to the experiment are used to formulate the axes labels.

## 4.6 Double Point FLDI Measurement - CO<sub>2</sub>

Carbon dioxide is used as the test gas in the series of experiments presented in this section. The reservoir pressure is held approximately constant, while the reservoir enthalpy is varied for one series of shots. The conditions for this shot series are presented in Table 4.11. The purpose of this campaign is to repeat the tests discussed in sections 4.4 and 4.5 at as similar reservoir conditions as experimentally possible, but with a test gas that is understood to be more thermo-chemically active. Again, the edge unit Reynolds number decreases when the reservoir pressure is held constant and the reservoir enthalpy is increased.

Table 4.11: Double Point Edge Conditions - CO<sub>2</sub>

| Shot | $U_E$ | $\rho_E$             | $P_E$ | $T_{t/rE}$ | $T_{vE}$ | $M_E$ | $Re_E^{Unit}$ | $y_{CO_2}$ | $y_{O_2}$ | $y_{CO}$ | $y_C$ | $y_O$ |
|------|-------|----------------------|-------|------------|----------|-------|---------------|------------|-----------|----------|-------|-------|
|      | (m/s) | (kg/m <sup>3</sup> ) | (kPa) | (K)        | (K)      | (-)   | (1/m)         | (-)        | (-)       | (-)      | (-)   | (-)   |
| 2795 | 2549  | 0.086                | 23.6  | 1356       | 1356     | 4.10  | 5.07e6        | 0.85       | 0.06      | 0.10     | 0.00  | 0.00  |
| 2796 | 2518  | 0.090                | 24.2  | 1331       | 1331     | 4.10  | 5.34e6        | 0.86       | 0.05      | 0.09     | 0.00  | 0.00  |
| 2794 | 2512  | 0.091                | 24.3  | 1327       | 1327     | 4.10  | 5.39e6        | 0.86       | 0.05      | 0.09     | 0.00  | 0.00  |
| 2793 | 2398  | 0.098                | 24.0  | 1227       | 1227     | 4.11  | 5.97e6        | 0.90       | 0.04      | 0.06     | 0.00  | 0.00  |

Peaks in the cross correlations are observed when the disturbances at both detectors are of low amplitude (Fig. 4.30); this is consistent with the behavior observed in sections 4.4 and 4.5. The characteristic velocity ( $\Delta s/\tau$ ) is different from what was

tabulated for the air and nitrogen shots in Tables 4.8 and 4.10. For the air and  $N_2$  shots, the characteristic velocity scaled as  $U_E/(\Delta s/\tau) \approx 1$ . For the shots with  $CO_2$  as the test gas, the characteristic velocity scaled as  $U_E/(\Delta s/\tau) \approx 0.86$ .

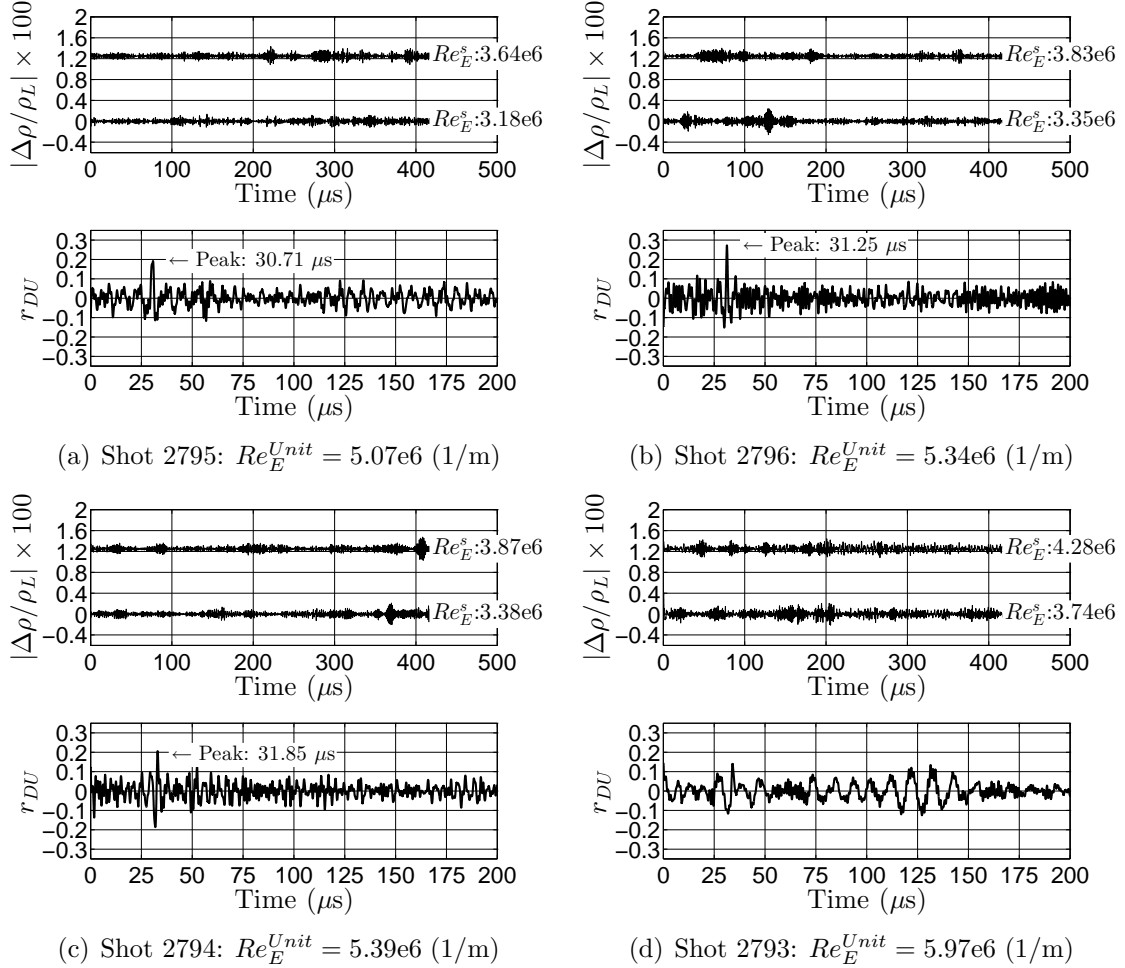


Figure 4.30: Time traces and cross-correlations of  $\Delta\rho/\rho_L$  for the  $CO_2$  shot series (conditions summarized in Table 4.11).

Welch's method, with 50% overlapping 20  $\mu s$  Hann windows, is used to make estimates of the power spectral density for each case (Fig. 4.31). As the Reynolds number is increased, a narrowband spectral peak increases in amplitude and decreases in frequency until it saturates, and then broadens out; this is qualitatively similar to behavior observed in the air and  $N_2$  experiments presented in sections 4.4 and 4.5.

The narrowband peaks observed in the spectral estimates are again consistent with

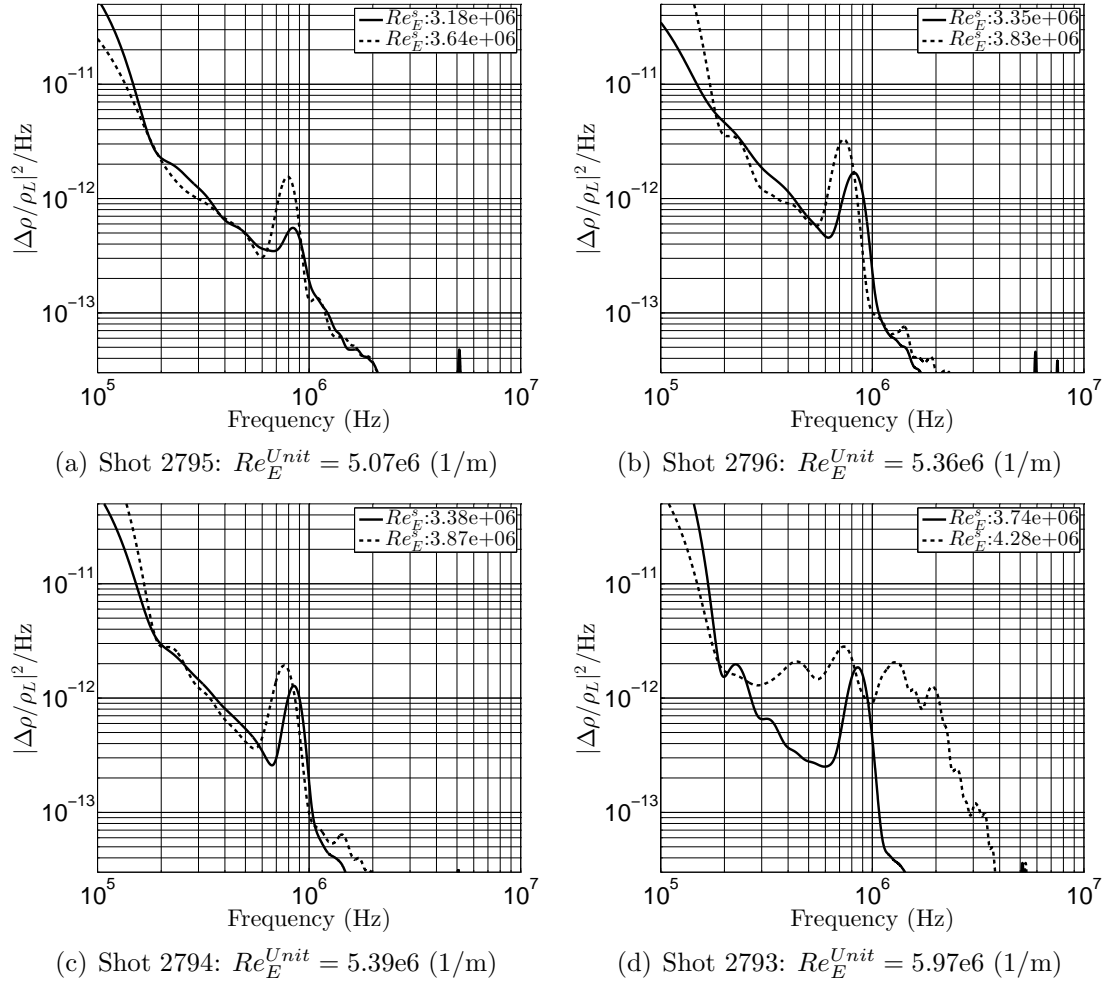


Figure 4.31: Power spectral density estimates of  $\Delta\rho/\rho_L$  for the CO<sub>2</sub> shot series (conditions summarized in Table 4.11).

the acoustic mode. The frequency of the spectral peak at the upstream detector,  $f_U$ , is higher than the frequency of the spectral peak at the downstream detector,  $f_D$ ; the frequency is inversely proportional to the computed boundary-layer thickness (Table 4.12).

Table 4.12: Double Point CO<sub>2</sub> Boundary Layer Instability Scaling

| Shot | $U_E$ | $\tau$     | $U_E/(\Delta s/\tau)$ | $\delta_U$ | $f_U$ | $2f_U\delta_U/U_E$ | $\delta_D$ | $f_D$ | $2f_D\delta_D/U_E$ |
|------|-------|------------|-----------------------|------------|-------|--------------------|------------|-------|--------------------|
|      | (m/s) | ( $\mu$ s) | (-)                   | (mm)       | (kHz) | (-)                | (mm)       | (kHz) | (-)                |
| 2795 | 2549  | 30.7       | 0.86                  | 1.02       | 840   | 0.67               | 1.10       | 780   | 0.67               |
| 2796 | 2518  | 31.3       | 0.87                  | 0.99       | 820   | 0.65               | 1.06       | 730   | 0.62               |
| 2794 | 2512  | 31.9       | 0.88                  | 0.99       | 840   | 0.66               | 1.06       | 750   | 0.63               |
| 2793 | 2398  | -          | -                     | 0.95       | 860   | 0.68               | 1.01       | -     | -                  |

# Chapter 5

## Analysis

In this chapter, the instability measurements presented in section 4 are analyzed. The methodology of data processing is described and the results are compared to stability calculations.

### 5.1 Experimental Amplification Factor

The determination of the amplification factor between the two probe volumes is described in this section. For a shot to be considered for amplification factor analysis, the results must exhibit the following behavior: 1) there is no significant departure from computed laminar heating rates, 2) there is a peak in the cross-correlations that indicates the existence of discrete packets, and 3) there is no spectral behavior that would indicate the wave packets are non-linear or turbulent.

#### 5.1.1 Methodology

To reduce the data, the amplification of disturbances is assumed to be 2-D, which is supported by the literature for this article geometry, orientation, and flow regime (Mack, 1984, Fedorov, 2011). Spatial amplification in the stream-wise direction is also assumed to be occurring at constant frequency between the detector stations; that is, the time-averaged amplitude at a given frequency in the upstream probe volume

spectrum may be related to the time-averaged amplitude at the same frequency in the downstream probe volume.

To make an estimate of the experimentally measured change in amplitude between stations we choose the amplification factor  $N$  to characterize density perturbations as

$$N = \ln(|A_D|/|A_U|) = \ln(|\Delta\rho_D|/|\Delta\rho_U|) = \frac{1}{2} \ln \left( \frac{|\Delta\rho_D/\rho_L|^2/\text{Hz}}{|\Delta\rho_U/\rho_L|^2/\text{Hz}} \right), \quad (5.1)$$

where the chosen disturbance amplitude ratio,  $A_D/A_U$ , is the density fluctuation ratio,  $|\Delta\rho_D|/|\Delta\rho_U|$ . There also must be sufficient signal to noise ratio (SNR) of the response at both detectors to make amplification factor measurements. An example of acceptable SNR is given for shot 2773 in Fig. 5.1(a); the frequency band in the spectrum which is deemed to have sufficient SNR is bounded by the two thick vertical lines. The results from this method of calculating the amplification factor can be found in Fig. 5.1(b). Note that the amplification factor discussed here is not synonymous with the “N factor of transition” that researchers use to estimate the transition location from stability calculations, the amplification factor computed using Eq. 5.1 and presented in Fig. 5.1 is a measure of the amplification of the disturbances in density between the two probe volumes.

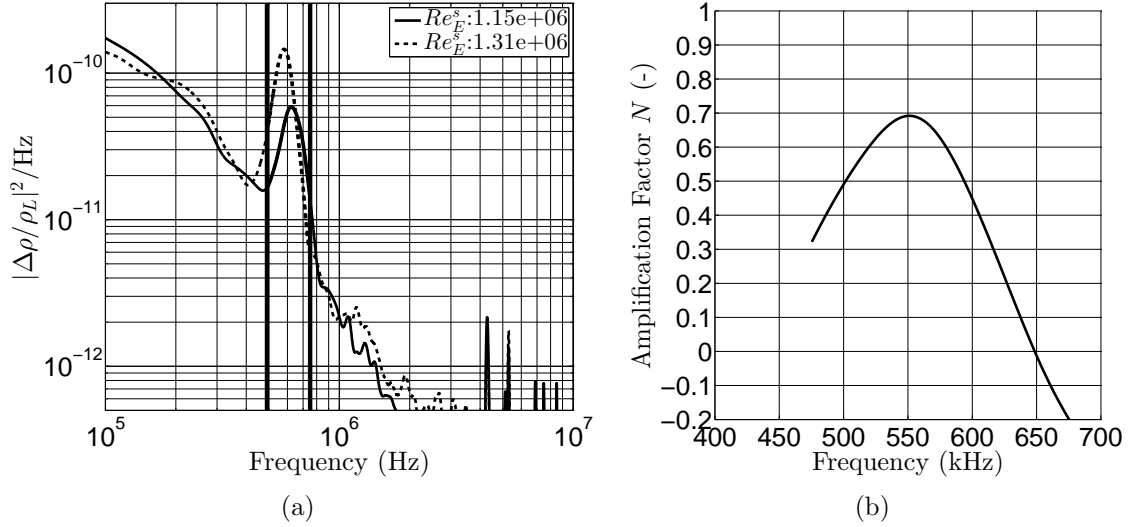


Figure 5.1: a: Example of amplification factor for shot 2773:  $N_2$ ,  $Re_E^{Unit} = 1.83e6$  (1/m). The acceptable SNR is located between the two thick vertical lines. b: the amplification factor computed from (a).

### 5.1.2 Uncertainty Estimate

The systematic error in the amplification factor is conservatively bounded to be less than 5%. This small error is due to the proportional nature of  $N = \ln(|\Delta\rho_D|/|\Delta\rho_U|)$ ; the systematic errors subtract from each other. The random error is estimated from the two  $\text{CO}_2$  experiments at nominally the same conditions (shots 2794 and 2796). At the maximum amplification factor, there is a difference of amplification of 10% and the peak is displaced 3.5% in frequency; these percentage values are used to represent the error estimate in the data.

### 5.1.3 Results

For each experiment performed with sufficient data quality, the amplification factor is computed (Fig. 5.2). The data are summarized in Table 5.1, along with the type of gas, the edge-unit Reynolds number  $Re_E^{Unit}$ , the edge Reynolds number based on the upstream detector location  $Re_E^U$ , and the edge Reynolds number based on the detector spacing  $Re_E^{\Delta s}$ . Also in Table 5.1 is the product of the angular frequency at

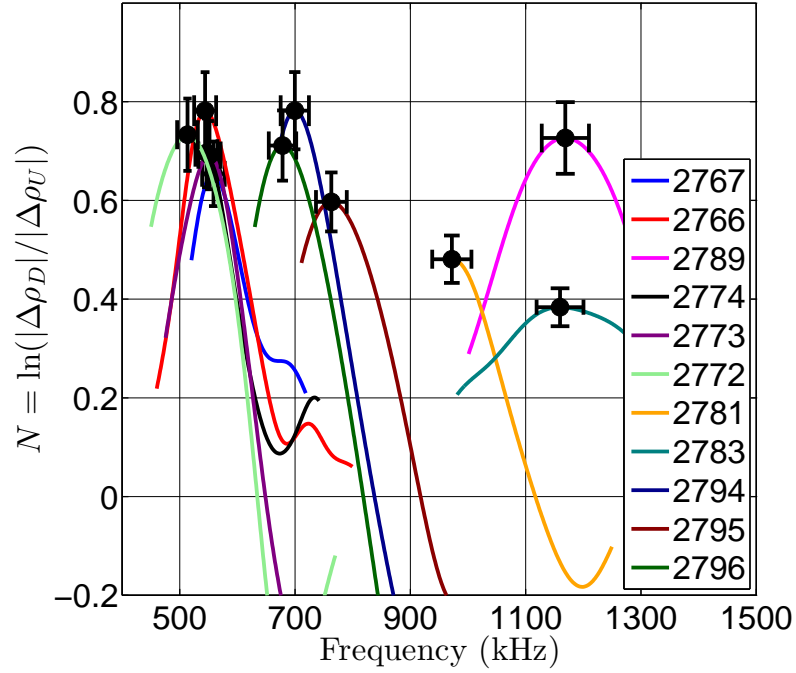


Figure 5.2: The amplification factor for all shots with sufficient signal to noise ratio.

maximum amplification and relaxation time of the gas constituent with the lowest characteristic vibrational temperature  $2\pi f_{N_{max}}\tau_{v,i}$ ,<sup>1</sup> the ratio of edge temperature to the characteristic vibrational temperature of the gas constituent with the lowest value

Table 5.1: Amplification Factor Data Summary

| Shot | Gas             | $Re_E^{Unit}$ | $Re_E^U$ | $Re_E^{\Delta s}$ | $M_E$ | $N_{max}$ | $f_{N_{max}}$ | $2\pi f_{N_{max}}\tau_{v,i}$ | $T_E/\Theta_{v,i}$ | $\lambda\alpha_c$ | $\lambda\sum_i\alpha_{r,i}$ | $\lambda\alpha_a$ |
|------|-----------------|---------------|----------|-------------------|-------|-----------|---------------|------------------------------|--------------------|-------------------|-----------------------------|-------------------|
|      |                 | (1/m)         | (-)      | (-)               | (-)   | (-)       | (kHz)         | (-)                          | (-)                | (-)               | (-)                         | (-)               |
| 2767 | Air             | 1.98e6        | 1.24e6   | 0.18e6            | 4.7   | 0.65      | 560           | 5.4e+02                      | 0.67               | 0.05              | 0.00                        | 0.05              |
| 2766 | Air             | 2.36e6        | 1.48e6   | 0.22e6            | 4.9   | 0.78      | 540           | 1.2e+03                      | 0.56               | 0.05              | 0.00                        | 0.05              |
| 2789 | Air             | 4.73e6        | 2.96e6   | 0.43e6            | 4.5   | 0.73      | 1170          | 9.1e+01                      | 0.94               | 0.04              | 0.00                        | 0.04              |
| 2774 | N <sub>2</sub>  | 1.72e6        | 1.08e6   | 0.16e6            | 5.8   | 0.70      | 550           | 1.0e+06                      | 0.35               | 0.09              | 0.00                        | 0.09              |
| 2773 | N <sub>2</sub>  | 1.83e6        | 1.15e6   | 0.17e6            | 5.9   | 0.69      | 550           | 3.5e+06                      | 0.30               | 0.10              | 0.00                        | 0.10              |
| 2772 | N <sub>2</sub>  | 1.98e6        | 1.24e6   | 0.18e6            | 6.1   | 0.73      | 510           | 1.1e+07                      | 0.26               | 0.10              | 0.00                        | 0.10              |
| 2781 | N <sub>2</sub>  | 3.11e6        | 1.95e6   | 0.28e6            | 5.0   | 0.48      | 970           | 7.9e+03                      | 0.65               | 0.05              | 0.00                        | 0.05              |
| 2783 | N <sub>2</sub>  | 3.44e6        | 2.16e6   | 0.31e6            | 4.8   | 0.38      | 1160          | 4.3e+03                      | 0.72               | 0.05              | 0.00                        | 0.05              |
| 2794 | CO <sub>2</sub> | 5.39e6        | 3.38e6   | 0.49e6            | 4.1   | 0.78      | 700           | 1.0e+01                      | 1.38               | 0.03              | 0.08                        | 0.10              |
| 2795 | CO <sub>2</sub> | 5.07e6        | 3.18e6   | 0.46e6            | 4.1   | 0.60      | 760           | 1.1e+01                      | 1.41               | 0.03              | 0.07                        | 0.10              |
| 2796 | CO <sub>2</sub> | 5.34e6        | 3.35e6   | 0.49e6            | 4.1   | 0.71      | 680           | 1.0e+01                      | 1.39               | 0.03              | 0.08                        | 0.11              |

$T_E/\Theta_{v,i}$ ,<sup>1</sup> and the acoustic attenuation per unit wavelength  $\lambda\alpha_a$ . The attenuation per wavelength ( $\lambda\alpha_a$ ) is computed by  $\alpha_a = \alpha_c + \sum_i \alpha_{r,i}$ ;  $\alpha_c$  is computed as in Eq. 1.6b, and  $\sum_i \alpha_{r,i}$  is computed with code described in Fujii and Hornung (2001, 2003).

The presentation of time scale ( $2\pi f_{N_{max}} \tau_{v,i}$ ) and temperature ratio ( $T_E/\Theta_{v,i}$ ) is intended to give a feel for the rate at which the gas is vibrationally relaxing and the extent to which the test gas is vibrationally excited. The N<sub>2</sub> experiments are relatively unexcited and have a large time scale mismatch. The Stokes-Kirchhoff (SK) attenuation is dominant, and is especially high for the N<sub>2</sub> shots with a lower edge density per Eq. 1.6b (edge conditions in Tables 4.7, 4.9, and 4.11).

In the air shots, the O<sub>2</sub> is closer in terms of time scale ( $\omega\tau$  is of order 100) and has a higher level of excitation, noting that the mass fraction of O<sub>2</sub> in the boundary layer is  $y_{O_2} \approx 0.18$ . Again, the Stokes-Kirchhoff (SK) attenuation is dominant.

For the CO<sub>2</sub> experiments, the time scale is mismatched by approximately one order of magnitude and exhibits appreciable vibrational excitation, noting that mass fraction of CO<sub>2</sub> is  $y_{CO_2} \approx 0.85$  in the boundary layer. This implies that the CO<sub>2</sub> experiments have the best chance to exhibit instability attenuation by relaxation effects. The Stokes-Kirchhoff (SK) attenuation is approximately half of the attenuation due to vibrational relaxation.

The amplification factors in Fig. 5.2 are all comparable to each other in terms of amplitude, and this is a manifestation of the SNR of the measurement technique. What is notable is that these similar amplification factors are observed during experiments with different Reynolds numbers and edge Mach numbers.

Three shots are selected and the amplification factor and attenuation coefficient are overlaid (Fig. 5.3). The linear slope of the acoustic attenuation for the air and N<sub>2</sub> cases exemplify the dominance of the SK terms. The uptick in attenuation for the CO<sub>2</sub> case at lower frequency is indicative of the vibrational relaxation terms.

---

<sup>1</sup>For air:  $\Theta_{v,O_2} = 2239$  K, for N<sub>2</sub>:  $\Theta_{v,N_2} = 3395$  K, and for CO<sub>2</sub>:  $\Theta_{v,CO_2} = 960$  K for the lowest energy doubly-degenerate mode.

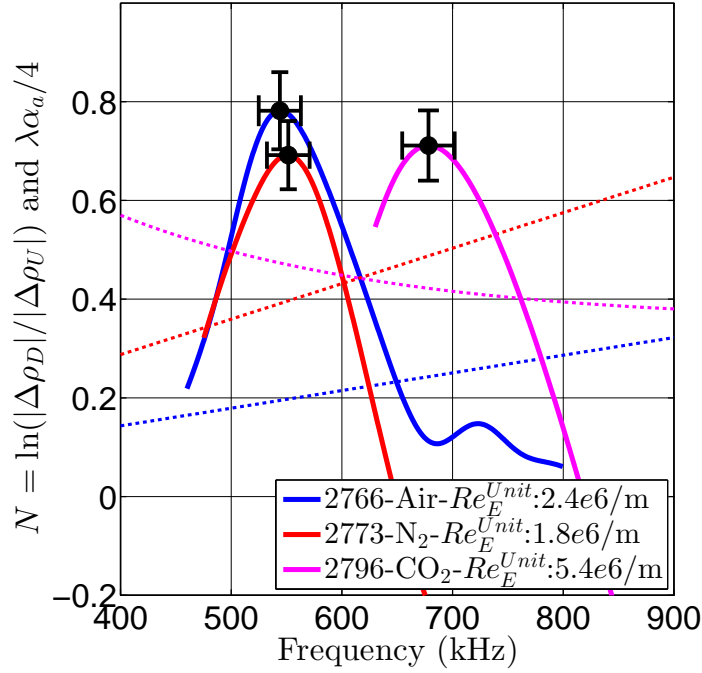


Figure 5.3: The amplification factor for three shots (solid lines) with the acoustic attenuation per wavelength (dotted lines).

## 5.2 PSE-Chem - Experiment Comparison

In this section, stability computations are compared with experimental results. Background is given to the stability calculations. The means by which data are extracted from the computations is described. Finally, examples of computational-experimental comparison are presented. Future work regarding improving the predictive capabilities of the computations is discussed.

### 5.2.1 Methodology

PSE-Chem is a part of the STABL software package described in [Johnson et al. \(1998\)](#), [Johnson \(2000\)](#), and [Wagnild \(2012\)](#). PSE-Chem analyzes the mean flow over the cone computed by DPLR. First, the method of normal modes is applied to the reacting Navier-Stokes equations, where it is assumed that the boundary layer is quasi-parallel, the gas is in thermo-chemical non-equilibrium, and the disturbances

have the form

$$q'(s, z, t) = \hat{q}(y) \exp(i(\alpha s + \beta z - \omega t)), \quad (5.2)$$

where  $q'$  is a disturbance at a position along the generator of the cone  $s$ , azimuthal position  $z$ , and time  $t$ . The amplitude of the disturbance is considered to be only a function of the wall-normal distance,  $\hat{q} = \hat{q}(y)$ . The stream-wise wave number is  $\alpha$ , the azimuthal wave number is  $\beta$ , and the angular frequency is  $\omega$ . The spatial linear stability problem is analyzed where the frequency ( $\omega$ ) is real and the wave numbers are complex ( $\alpha = \alpha_r + \alpha_i$ ); non-zero azimuthal wavenumbers ( $\beta$ ) are not considered in this analysis, as disturbance is assumed to be two-dimensional. The linear stability calculation results are then used as initial values for the parabolized stability equation (PSE) analysis, which is used to account for the non-parallel nature of the boundary layer. The procedure for the PSE analysis is found in [Johnson \(2000\)](#), which is builds on the work reported in [Herbert \(1993, 1997\)](#) and [Chang and Malik \(1994\)](#).

PSE-Chem is used to compute linear stability diagrams and amplification curves for cases corresponding to those in section 5.1.3. The linear stability diagrams are computed at the conditions summarized in Tables 4.7, 4.9, and 4.11. The amplification curves are computed from the upstream detector position on the cone at a spread of frequencies around those observed in the experiments. The amplification factor ( $N$ ) is computed as

$$N = \int_{s_U}^{s_D} \sigma ds, \quad (5.3a)$$

$$\sigma = -Im(\alpha) + \frac{1}{2E} \frac{dE}{ds}, \quad (5.3b)$$

$$E = \int_{\Omega} \bar{\rho} (|\hat{u}|^2 + |\hat{v}|^2 + |\hat{w}|^2) dV, \quad (5.3c)$$

where,  $s_U$  and  $s_D$  are the upstream and downstream probe volume locations,  $\sigma$  is the growth rate,  $\alpha$  is the wavenumber along a generator of the cone, and  $E$  is the

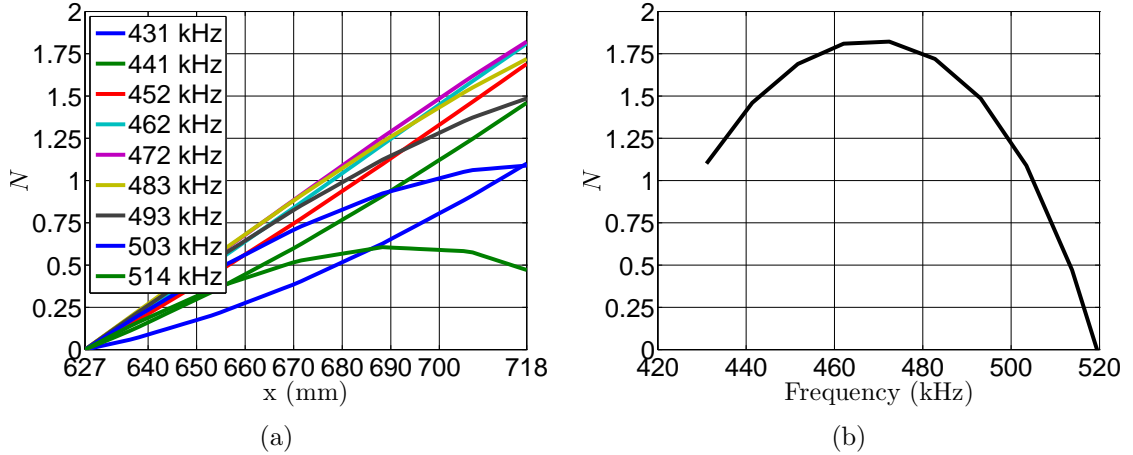


Figure 5.4: Example from shot 2773. a: Evolution of the amplification factor along the cone between the upstream and downstream probe volume locations, as in Eq. 5.3a. Note that different frequencies are amplified at different rates, and negative amplification factors are not shown. b: Computation of amplification factor for shot 2773 between the upstream and downstream probe volumes.

disturbance kinetic energy (Johnson, 2000). Other researchers have proposed that for compressible boundary layers there are more terms (namely thermodynamic) in the integrand of Eq. 5.3c, such as those in Mack (1984) or Hanifi et al. (1996); however, Schmid and Henningson (2001) note that “there is no obvious definition of disturbance measure,” so we omit the extra terms, as is the case with the default option in PSE-Chem. A fixed frequency is parameterized for each  $\sigma$  in Eq. 5.3a. An example of this is seen in Fig. 5.4(a) where different frequencies are amplified at different rates. If we take only the value at the downstream location, the result is Fig. 5.4(b); this is what we will compare our experimental amplification curves to.

## 5.2.2 Results

Comparisons of computational and experimental results are presented for five experiments of high data quality. For each experiment, there is a linear stability diagram included so that the evolution of most amplified disturbance along the cone may be appreciated. Additionally, there is a comparison of normalized density fluctuation

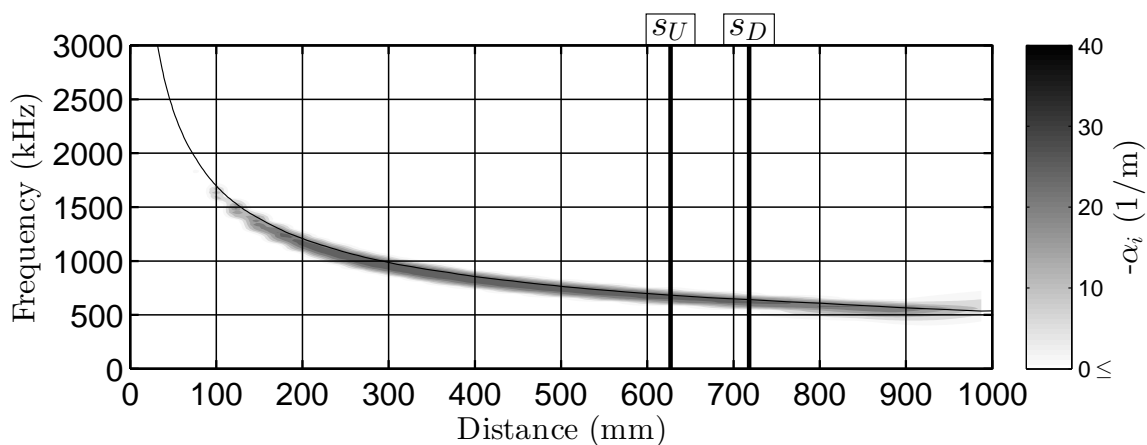
amplitude ( $|\Delta\rho|/\rho_L$ ) versus imaginary stream-wise wavenumber ( $\alpha_i$ ). Finally, the computational and experimental amplification factors are compared for each case.

The band at which frequencies are amplified is thin for shot 2766 relative to other cases, this is apparent from the linear stability diagram in Fig. 5.5(a). A line representing  $0.7U_E/(2\delta)$  in Fig. 5.5(a) illustrates how well the scaling of the most amplified frequency matches the computed value.

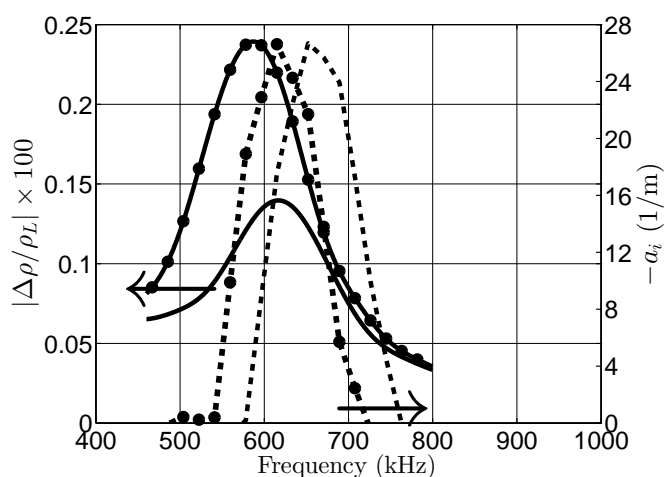
Two slices from the linear stability diagram are presented in Fig. 5.5(b) corresponding to the probe locations, which are marked on the linear stability diagram as  $s_U$  and  $s_D$ . It is observed that the computed  $\alpha_i$  is of higher frequency than the measured narrowband disturbances (Fig. 5.5(b)). The decrease in observed frequency at density fluctuation maximum between the upstream and downstream probe volumes is 5%, and this is similar to the computed decrease in frequency at the largest  $\alpha_i$ , 6%. The computational-experimental amplification factor comparison in Fig. 5.5(c) is poor in both amplitude and frequency.

The band at which frequencies are amplified is also relatively thin for shot 2773 relative to other cases, this is apparent from the linear stability diagram in Fig. 5.6(a). The line formed by  $0.7U_E/(2\delta)$  in Fig. 5.6(a) does not capture the value for the most amplified frequency as accurately as in the air case presented in Fig. 5.5(a), but the agreement with the trend is still apparent. Additionally, because of the lower unit Reynolds number in shot 2773 relative to shot 2766, the value of  $\alpha_i$  is lower.

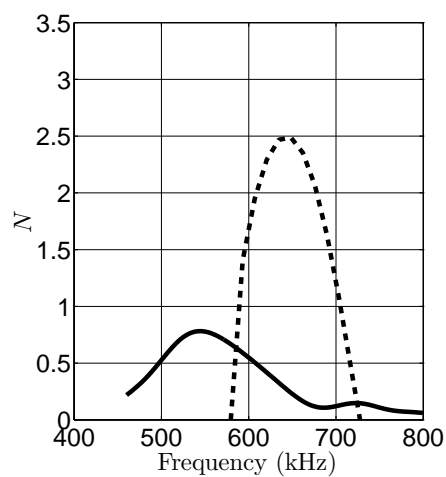
Slices from the linear stability diagram corresponding to the marked probe locations are presented in Fig. 5.6(b) along with the observed  $|\Delta\rho|/\rho_L$  for shot 2773. It is observed that the computed  $\alpha_i$  is of higher frequency than the measured narrowband disturbances (Fig. 5.6(b)). In this case, the decrease in the measured frequency at which there is maximum density fluctuation between the upstream and downstream probe volumes is 7%; this is similar to the computed decrease in frequency at the largest  $\alpha_i$  at 8%. Again, the computational-experimental amplification factor com-



(a)



(b)



(c)

Figure 5.5: Computational-experimental comparison for shot 2766, conditions summarized in Table 5.1. a: Linear stability diagram, darker shading indicating higher growth rate. A line representing  $0.7U_E/(2\delta)$  illustrates most amplified frequency scaling. Vertical lines denoted by  $s_U$  and  $s_D$  mark the upstream and downstream probe volume distance from the cone tip. b: Overlay of measured density disturbance amplitude from upstream (solid line, no markers) and downstream (solid line, markers) probe volumes, and computed growth rate at corresponding upstream (dashed line, no markers) and downstream (dashed line, markers) locations. c: Overlay of computed (dashed line) and measured (dotted line) amplification factor. Arrows are included to aid in indicating the appropriate ordinate.

parison in Fig. 5.6(c) is poor in both amplitude and frequency.

The neutral stability curve for shot 2796 (Fig. 5.7(a)) is apparently thicker than for shots 2773 (N<sub>2</sub>) or 2766 (air) at similar reservoir conditions, this is a result of the higher unit edge Reynolds number. The scaling of  $0.7U_E/(2\delta)$  under-predicts the most amplified frequency, but again the trend is consistent with the linear stability calculation. The higher unit edge Reynolds number for shot 2796 results in a higher computed growth rate than for shots 2773 or 2766. The computed stream-wise imaginary wavenumber ( $\alpha_i$ ) is of higher frequency than the measured density disturbances ( $|\Delta\rho|/\rho_L$ ), as seen in Fig. 5.7(b). The shift in frequency of the largest  $\alpha_i$  is 4% which is considerably smaller than the 10% decrease in frequency at the maximum  $|\Delta\rho|/\rho_L$  between the stations. The computational-experimental amplification factor comparison in Fig. 5.7(c) is poor in both amplitude and frequency, and there is greater disagreement than for the shots in air and N<sub>2</sub>.

Shot 2783 is a N<sub>2</sub> shot at nominally “higher” reservoir conditions than shot 2773, a N<sub>2</sub> at lower enthalpy and pressure. This results in a higher edge velocity and higher unit edge Reynolds number than shot 2773. The effect of  $Re_E^{Unit}$  on the stability of the flow is evident in the neutral stability curve as it is apparently thicker and of appreciably higher frequency (Fig. 5.8(a)). In Fig. 5.8(a), the line marked  $0.7U_E/(2\delta)$  is made white because of how well it agrees with the stability computation. The computed growth rate for shot 2783 is higher than for shot 2773. The computed stream-wise imaginary wavenumber ( $\alpha_i$ ) is of higher frequency than the measured density disturbances ( $|\Delta\rho|/\rho_L$ ), as seen in Fig. 5.8(b). The shift in frequency of the largest  $\alpha_i$  is 10%, which is considerably larger than the 1% decrease in frequency at the maximum  $|\Delta\rho|/\rho_L$  between the stations. The computational-experimental amplification factor comparison in Fig. 5.8(c) is poor in amplitude, but the maximum in frequency is nearly matched.

The discussion of shot 2773 relative to shot 2783 was intended to explore the

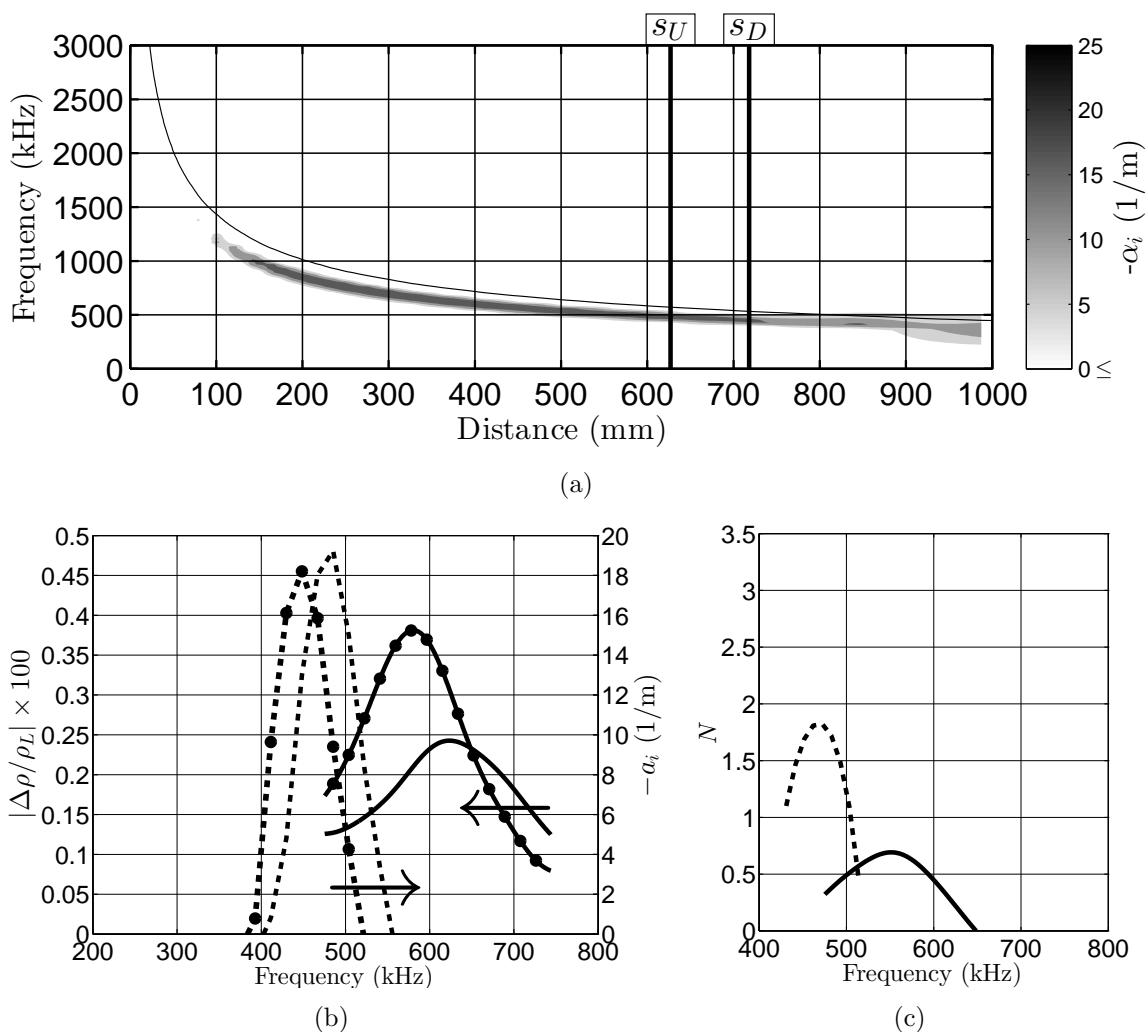
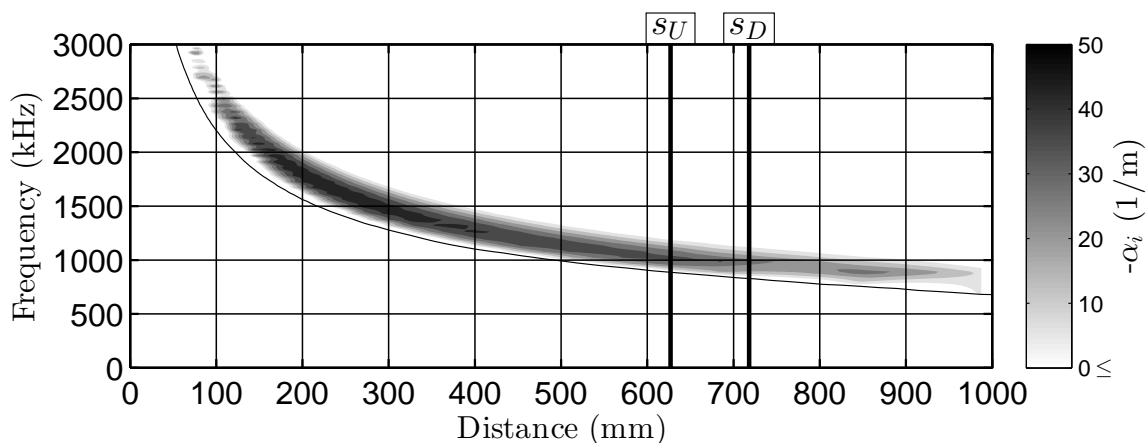
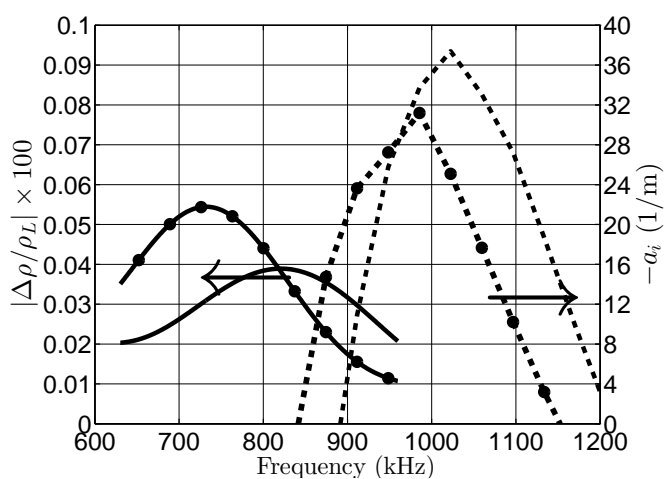


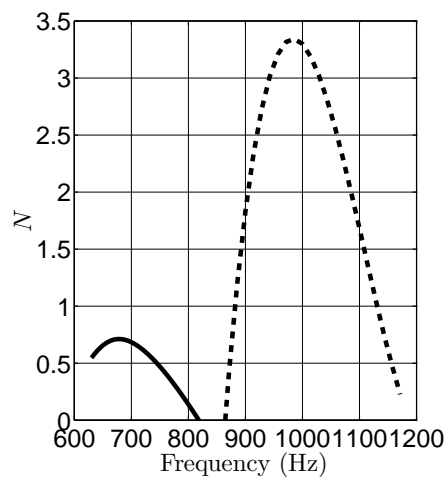
Figure 5.6: Computational-experimental comparison for shot 2773, conditions summarized in Table 5.1. a: Linear stability diagram, darker shading indicating higher growth rate. A line representing  $0.7U_E/(2\delta)$  illustrates most amplified frequency scaling. Vertical lines denoted by  $s_U$  and  $s_D$  mark the upstream and downstream probe volume distance from the cone tip. b: Overlay of measured density disturbance amplitude from upstream (solid line, no markers) and downstream (solid line, markers) probe volumes, and computed growth rate at corresponding upstream (dashed line, no markers) and downstream (dashed line, markers) locations. c: Overlay of computed (dashed line) and measured (dotted line) amplification factor. Arrows are included to aid in indicating the appropriate ordinate.



(a)



(b)



(c)

Figure 5.7: Computational-experimental comparison for shot 2796, conditions summarized in Table 5.1. a: Linear stability diagram, darker shading indicating higher growth rate. A line representing  $0.7U_E/(2\delta)$  illustrates most amplified frequency scaling. Vertical lines denoted by  $s_U$  and  $s_D$  mark the upstream and downstream probe volume distance from the cone tip. b: Overlay of measured density disturbance amplitude from upstream (solid line, no markers) and downstream (solid line, markers) probe volumes, and computed growth rate at corresponding upstream (dashed line, no markers) and downstream (dashed line, markers) locations. c: Overlay of computed (dashed line) and measured (dotted line) amplification factor. Arrows are included to aid in indicating the appropriate ordinate.

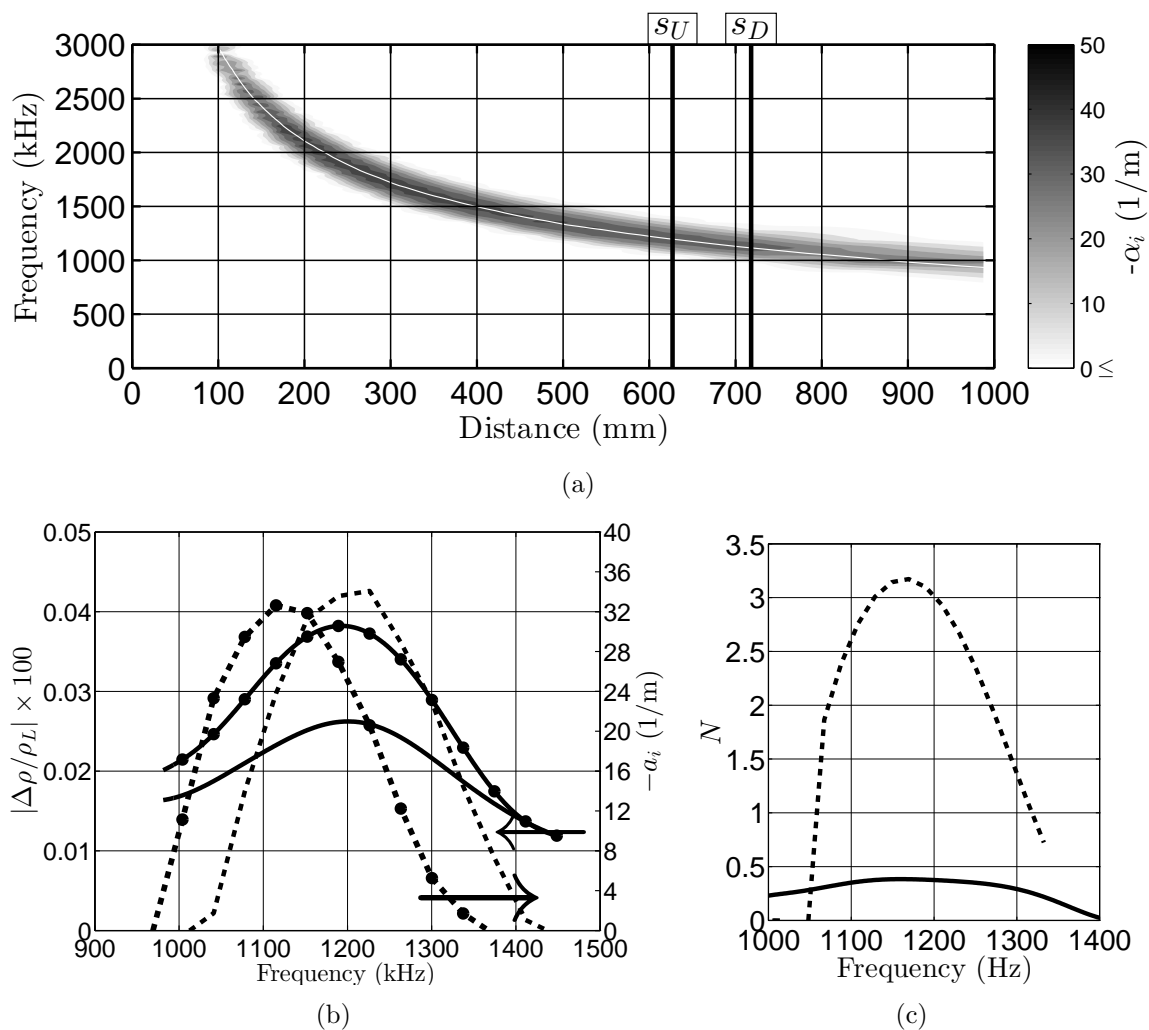
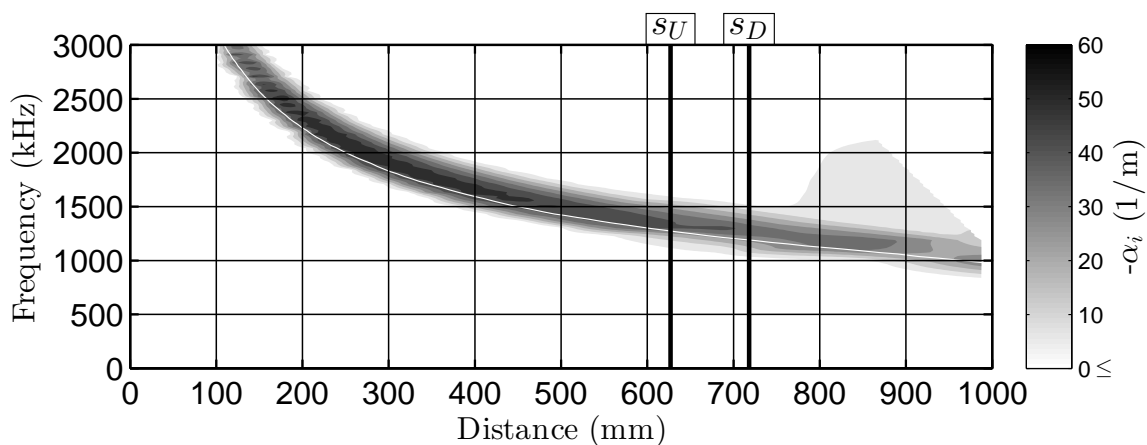


Figure 5.8: Computational-experimental comparison for shot 2783, conditions summarized in Table 5.1. a: Linear stability diagram, darker shading indicating higher growth rate. A line representing  $0.7U_E/(2\delta)$  illustrates most amplified frequency scaling. Vertical lines denoted by  $s_U$  and  $s_D$  mark the upstream and downstream probe volume distance from the cone tip. b: Overlay of measured density disturbance amplitude from upstream (solid line, no markers) and downstream (solid line, markers) probe volumes, and computed growth rate at corresponding upstream (dashed line, no markers) and downstream (dashed line, markers) locations. c: Overlay of computed (dashed line) and measured (dotted line) amplification factor. Arrows are included to aid in indicating the appropriate ordinate.

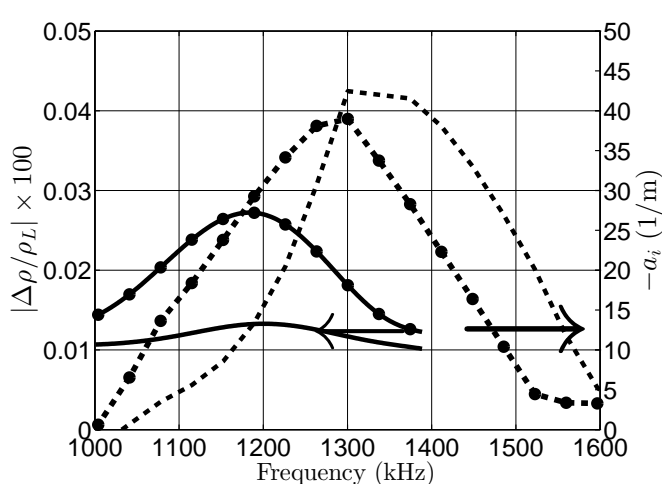
behavior of the same gas a disparate run conditions, the same is true of shot 2789 and shot 2766. Shot 2766 is an air shot at nominally “lower” reservoir conditions than shot 2789, an air experiment at higher enthalpy and pressure. This results in a higher edge velocity and higher unit edge Reynolds number than shot 2789. The effect on the stability of the flow is evident in the neutral stability curve in Fig. 5.9(a), as it is apparently thicker and of appreciably higher frequency as compared with shot 2766. Again, the line marked by  $0.7U_E/(2\delta)$  in Fig. 5.9(a) is made white because of how well it agrees with the stability computation. The maximum of the measured density disturbances ( $|\Delta\rho|/\rho_L$ ) occurs at a lower frequency than the computed growth rate for shot 2789. The decrease in frequency of the largest  $\alpha_i$  is similar to the decrease in frequency at the maximum  $|\Delta\rho|/\rho_L$  between the stations, 1%. The computational-experimental amplification factor comparison in Fig. 5.9(c) is poor in amplitude and frequency.

Several trends have become apparent following the analysis of the computational-experimental instability data. According to the computations, for the lower edge unit Reynolds number ( $Re_E^{Unit}$ ) flows, the band of frequencies that is most amplified is more narrow relative to high  $Re_E^{Unit}$  flows. For cases with a higher  $Re_E^{Unit}$ , there is a larger computed imaginary stream-wise wavenumber  $\alpha_i$ . The assertion that the boundary-layer disturbances should increase in amplitude and decrease in frequency as  $\propto 1/\delta$  is supported by the experimental and computational data.

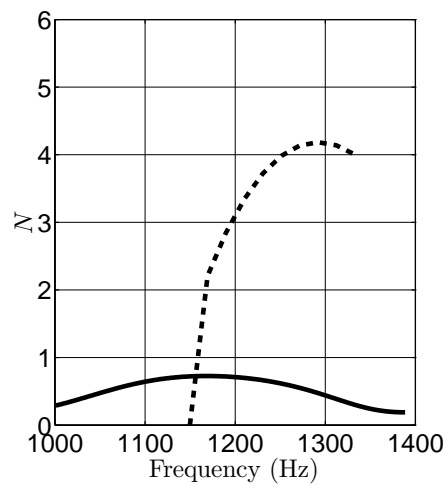
One significant discrepancy between the computational and the experimental data is that for air and CO<sub>2</sub> experiments, the computed imaginary stream-wise wavenumber  $\alpha_i$  has a maximum in frequency that is higher than the frequency at which there is a maximum in density disturbances ( $|\Delta\rho|/\rho_L$ ). This is not a sensible result because the maximum in amplification should occur at a lower frequency than the maximum amplitude for this flow field. Suppose that a disturbance evolves as two discrete fixed frequencies of 1500 kHz and 1300 kHz from  $s=400$  mm in in the linear stability di-



(a)



(b)



(c)

Figure 5.9: Computational-experimental comparison for shot 2789, conditions summarized in Table 5.1. a: Linear stability diagram, darker shading indicating higher growth rate. A line representing  $0.7U_E/(2\delta)$  illustrates most amplified frequency scaling. Vertical lines denoted by  $s_U$  and  $s_D$  mark the upstream and downstream probe volume distance from the cone tip. b: Overlay of measured density disturbance amplitude from upstream (solid line, no markers) and downstream (solid line, markers) probe volumes, and computed growth rate at corresponding upstream (dashed line, no markers) and downstream (dashed line, markers) locations. c: Overlay of computed (dashed line) and measured (dotted line) amplification factor. Arrows are included to aid in indicating the appropriate ordinate.

agram in Fig. 5.9(a), and follows linear spatial stability theory. The amplitude  $A$  of the disturbance at each frequency would evolve as  $(A) \propto \exp(\int -\alpha_i ds)$ , and higher frequencies would become more amplified at a downstream station, i.e. at  $s=600$  mm. The 1500 kHz disturbance would be integrated through a region with large  $-\alpha_i$  for a longer distance than the 1300 kHz disturbance. The  $N_2$  shots have the correct trend for the relative frequencies for the maxima in imaginary stream-wise wavenumber and density perturbations.

The reason for this disparity in frequency content is not clear at the time of this writing, but one strong candidate cause is the large systematic error in calculating the run conditions that was discussed in detail in section 2.5. An approximate estimate of the change in most strongly amplified frequency ( $f$ ) due to a change in static thermodynamic conditions and velocity can be had by using the scaling  $f \approx U_E/(2\delta)$  and the correlation found for the boundary-layer thickness (Eq. 2.5). Estimating the fractional change in  $f$  as  $df/f = d \ln f = dU_E/U_E - d\delta/\delta$  results in fractional changes of  $df/f \approx 15\text{-}20\%$ , which is a very large value if the spectral content is then going to be used to calculate the amplitudes of disturbances in the flow.

Incorrectly predicting the frequency at which there is a maximum in  $\alpha_i$  significantly alters the computation of the amplification factor frequency content; however, there is also a systematic under-prediction of the amplitude of the amplification ratio by the computations, even in the one case where the frequency content is correct (shot 2783, Fig. 5.8(c)). Instability growth in the non-linear regime would not follow a model based on linear theory (as is assumed in this calculations), but the disturbances exhibit no clear non-linear behavior, (large amplitude harmonics, sub-harmonics, or amplitudes over 0.5%). Examples of non-linear behavior in boundary layers dominated by the acoustic instability can be found in the power spectral density estimate of the FLDI results for shot 2790 (Fig. 4.21(c)) or the literature (Chokani, 1999, Chokani et al., 2005, Bountin et al., 2008).

A comparison of the measured frequency ( $f$ ) of the largest amplitude narrow-band disturbances scaled by the edge velocity ( $U_E$ ) and the calculated boundary layer thickness ( $\delta$ ) vs. the edge Reynolds number based on the distance from the cone tip is presented in Fig. 5.10, with the data from this work, [Stetson et al. \(1983\)](#), and [Demetriades \(1977\)](#). The data represent a collection of points over a range of edge Mach number  $M_E \approx 4.1$ -7.4, edge Reynolds number  $\approx 1$ -4.5e<sup>6</sup>, total enthalpy  $\approx 0.5$ -15 MJ/kg, wall temperature ( $T_W$ ) to reservoir temperature ( $T_R$ ) ratio  $T_W/T_R \approx 0.05$ -0.8, in air, N<sub>2</sub> and CO<sub>2</sub>. It is observed here that  $2f\delta/U_E$  has a range of 0.6-1.1 for these conditions.

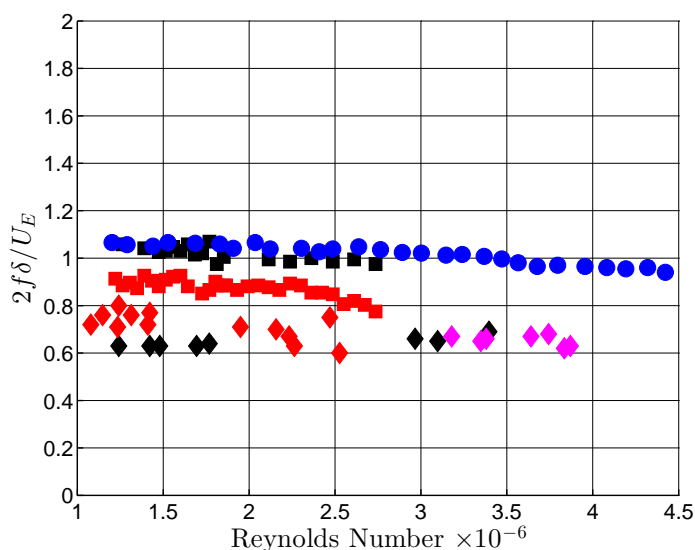


Figure 5.10: A comparison of the measured frequency of the largest amplitude narrow-band disturbances vs. the edge Reynolds number based on the distance from the cone tip with the data from this work (diamonds), [Stetson et al. \(1983\)](#) (circles), and [Demetriades \(1977\)](#) (squares). The data from this work for air are denoted by black diamonds and in Table 4.8, data for N<sub>2</sub> denoted by red diamonds and in Table 4.10, and data for CO<sub>2</sub> denoted by magenta diamonds and in Table 4.12. The blue filled circles are digitized and replotted from Fig. 14 from [Stetson et al. \(1983\)](#); this data is taken in a conventional hypersonic tunnel with a 7 degree-half angle cone at  $M_E = 6.8$  and a wall temperature ratio of  $T_W/T_R \approx 0.8$ . The squares are digitized and replotted from Table III from [Demetriades \(1977\)](#); this data is taken in a conventional hypersonic tunnel with a 4 degree-half angle cone at  $M_E = 7.4$  and a wall temperature ratio of  $T_W/T_R \approx 0.8$  (black squares) and  $T_W/T_R \approx 0.41$  (red squares).

The scatter in the [Stetson et al. \(1983\)](#) and [Demetriades \(1977\)](#) data is smaller than that of the present work; this is to be expected, as the data from the present work is recorded from reflected-shock tunnel experiments, and the data from [Stetson et al. \(1983\)](#) and [Demetriades \(1977\)](#) are collected from conventional hypersonic wind tunnel experiments. Of note in [Fig. 5.10](#) is no evidence of a strong trend in frequency vs. edge Reynolds number for any data set.

There is an observed shift in  $2f\delta/U_E$  that could be attributed to wall temperature ratio and edge Mach number. The value of  $2f\delta/U_E$  for a certain geometry is a function of (among other things) edge Mach number, because of the implication on disturbance-phase velocity ([Fig. 9.1 of Mack \(1984\)](#)), and boundary-layer temperature profile, because of the implication on disturbance wave number ([Fig. 10.9 of Mack \(1984\)](#)). It is observed in [Fig. 5.10](#) that  $2f\delta/U_E \approx 0.6-0.8$  for the wall-temperature ratio  $T_W/T_R \approx 0.05-0.10$ , and edge Mach number range  $M_E \approx 4.1-6.1$ . For wall-temperature ratio  $T_W/T_R \approx 0.41$  and edge Mach number  $M_E \approx 7.4$ ,  $2f\delta/U_E \approx 0.8-0.95$ . For wall-temperature ratio  $T_W/T_R \approx 0.8$  and edge Mach number  $M_E \approx 6.8-7.4$ ,  $2f\delta/U_E \approx 0.95-1.10$ . It is observed that wall temperature ratio could have a larger role in reducing  $2f\delta/U_E$  than edge Mach number does, but further investigation would be required to confirm this hypothesis.

# Chapter 6

## Conclusion

### 6.1 Introduction

The implication of boundary-layer transition on vehicle design is discussed in the context of a case study of the National Aerospace Plane (NASP). The marked effect of a poor understanding of the boundary-layer transition location was made apparent in a report from the Defense Science Review Board on the NASP in 1988, “[t]he largest uncertainty is the location of the point of transition from laminar to turbulent flow. Estimates range from 20% to 80% along the body span. That degree of uncertainty significantly affects the flow conditions at the engine inlet, aerodynamic heat transfer to the structure and skin friction. These in turn affect estimates of engine performance, structural heating and drag. The assumption made for the point of transition can affect the design vehicle gross take off weight by a factor of two or more... In view of the potential impact of uncertainties in the transition location, this is by far the single area of greatest technical risk in the aerodynamics of the NASP program” ([DSB, 1988](#)).

The path to transition to turbulence high-speed boundary layers is discussed, highlighting the recent developments in transient growth. The dominant mechanism that is believed to drive transition is introduced as the high-frequency modes discovered by [Mack \(1984\)](#). These modes are primarily acoustic in nature, are always

present if the edge Mach number is sufficiently large, and are the dominant instability mechanism when the wall temperature is sufficiently low compared to the recovery temperature.

Ray-tracing in high-speed boundary layers was used to explore the potential for acoustic energy trapping as function of edge Mach number, wall temperature ratio, and thermodynamic parameters. We proposed a figure of merit for acoustic energy trapping as the critical angle of inclination for rays originating in the boundary that are trapped, i.e., these rays always stay within the boundary layer. Using this concept, we find that an increasing amount of acoustic energy is trapped with increasing edge Mach number ( $M_E$ ), and decreasing wall temperature ratio ( $T_W/T_{ad}$ ). These trends agree qualitatively with the results of high-speed boundary-layer stability calculation by [Mack \(1984\)](#).

It is postulated that the fundamental driving principle of studying hypersonic slender-body boundary-layer instability at high enthalpy is characterizing the energy exchange between the thermo-chemical and fluid-mechanical processes. Thermo-chemical processes are only relevant at high-enthalpy conditions where the ordered kinetic energy of the flow is high enough so that chemical reactions and relaxation processes occur. If the fluid-mechanical and thermo-chemical processes proceed at comparable time scales, then energy exchange may take place. This energy exchange is explained as  $pdV$  work in the introduction, and a simple model discussing how acoustic energy is attenuated is presented following the formulation in [Pierce \(1989\)](#). Attenuation terms due to thermal-viscous dissipation and relaxation of the vibrational degree of freedom are included. The thermal-viscous dissipation, termed Stokes-Kirchhoff (SK) attenuation, was not previously considered in the literature pertaining to slender-body hypersonic boundary-layer instability damping.

## 6.2 Facility and Run Conditions

The test facility and method of calculating the run conditions is presented. Throughout the testing campaign for this work, it became apparent that there was opportunity to improve the quality of the flow over the model from a technical standpoint. Improvement was made by using higher quality gas to fill the shock tube and by cleaning the shock tube more thoroughly between experiments.

The methodology of calculating the run conditions is presented, namely the three stages: the reservoir, the nozzle, and then the mean flow over the cone. The propagation of bias error in these calculations is estimated. Examples highlighting the repeatability of experimentation in T5 are presented.

Example velocity and thermo-chemical boundary-layer profiles are provided for the mean flow over the 5 degree half-angle cone. It is observed that the gas is essentially chemically inactive on the time scale of one flow time over the model. The test gas is observed to be vibrationally inactive for  $N_2$  experiments, active on the time scale of one flow time over the model in air experiments, and active on the time scale of the boundary-layer thickness for  $CO_2$  experiments. The DPLR computations are favorably compared to perfect-gas similarity solutions.

## 6.3 FLDI Measurement Technique

To measure the acoustic instability on a slender body in a large-scale hypervelocity ground test (such as the T5 reflected-shock tunnel), six requirements of the diagnostic were identified: 1) high sensitivity to an unstable quantity in the boundary layer, 2) high temporal resolution of the measurement technique ( $> 10$  MHz), 3) high spatial resolution to resolve the small wavelength of the disturbance ( $< 1$  mm), 4) insensitivity to mechanical vibration, 5) the capability to have a small focal volume near the surface of the cone, and 6) a straightforward and repeatable means of extracting

quantitative data from the technique. The focused laser differential interferometer (FLDI) meets these requirements. For context, past research efforts to make instability measurements within a high-speed boundary layer are reviewed. The experimental setup, methodology of extracting quantitative results, and uncertainty estimates are described in detail.

The FLDI measurement setup was bench-tested. Firstly, a bench test experiment is designed and conducted to evaluate the sensitive region of the FLDI by traversal of a thin subsonic turbulent CO<sub>2</sub> jet through the horizontal span-wise direction along the direction of beam propagation. The  $1/e$  folding in RMS response of the FLDI to a subsonic CO<sub>2</sub> jet is  $\approx 10$  mm from the focus in the span wise direction. Secondly, to quantify the similarity in response of two FLDIs aligned along one generator of the cone, a disturbance is made by using a pulsed Nd:YAG laser which is focused to ionize a spot of gas and make a symmetric blast wave. This disturbance registered a difference in single shot peak response less of than 3.5% between the detectors.

## 6.4 Results

### 6.4.1 Tunnel Noise

Experimental results conducted to quantify the tunnel noise are presented. The measurements are made with the FLDI optical technique described in section 3. Motivation for such a survey is described, and the high-speed wind-tunnel noise literature is briefly reviewed. The results show the perturbations in density are not a strong function of the reservoir enthalpy. During one experiment, exceptional levels of noise were detected; this unique result is attributed to non-ideal operation of the shock tunnel. The present results indicate that RMS density fluctuations of  $\approx 1\%$  are achievable with attention to tunnel cleanliness. In addition, the spectral content of density fluctuation does not change throughout the test time.

### 6.4.2 Single and Double Point FLDI Developement

The ability to make quantitative measurements of the acoustic instability with FLDI in a hypervelocity slender-body boundary layer is reproducibly demonstrated. This is notable because of the time scales (1-3 MHz) associated with the acoustic instability's fundamental and harmonic frequency for conditions available in T5.

The development efforts to make reliable two-point measurements of the instability on a slender body in hypervelocity flow are described. The two-point FLDI setup consists of two FLDI systems that probe a generator of the five degree half-angle cone with the intent on tracking the evolution of disturbances as they propagate downstream. First, major technical impediments to making a successful measurement are highlighted. Then, some data from early and late in the development phase (dubbed “Dev 1” and “Dev 2”, respectively in section A) are presented for context. The data processing routine is described.

### 6.4.3 Double Point FLDI Measurements

The incipient instability waves prior to the transition to fully turbulent flow are measured in hypervelocity flow. The FLDI measurement volumes are located just upstream of the transition location to measure the instability waves.

Cross-correlations of the upstream and downstream FLDI probe volumes are estimated. A peak in cross-correlation at a time-lag,  $\tau$ , is nearly consistent with the time scale associated with the edge velocity and the detector spatial separation ( $\Delta s$ ) for the air and N<sub>2</sub> shots (Tables 4.8 and 4.10). The peak in cross-correlation for the CO<sub>2</sub> shots appears at a slightly faster time scale than the boundary-layer edge velocity (Table 4.12). These peaks in cross-correlation appear when both the upstream and downstream band-pass filtered time traces of  $\Delta\rho/\rho_L$  show low-amplitude, wave-packet-like behavior. This may indicate that the detectors are tracking wave packets

that are traveling along the generator of the cone at approximately the edge velocity.

## 6.5 Analysis

The methodology of determining the amplification factor between the two probe volumes is described. The amplification factors in Fig. 5.2 are all comparable in magnitude to each other, and this is a manifestation of the SNR of the measurement technique. Notably, these similar amplification factors are observed during experiments with different Reynolds numbers and edge Mach numbers.

The acoustic attenuation ( $\lambda\alpha_a$ ) is computed by  $\alpha_a = \alpha_c + \sum_i \alpha_{r,i}$ ;  $\alpha_c$  is computed as in Eq. 1.6b, and  $\sum_i \alpha_{r,i}$  is computed with code described in Fujii and Hornung (2001, 2003). The presentation of time scale ( $2\pi f_{N_{max}} \tau_{v,i}$ ) and temperature ratio ( $T_E/\Theta_{v,i}$ ) is intended to give a feel for the rate at which the gas is vibrationally relaxing and the extent to which the test gas is vibrationally excited.

The N<sub>2</sub> experiments are relatively unexcited and have a large time-scale mismatch. The Stokes-Kirchhoff (SK) attenuation is dominant, and is especially high for the N<sub>2</sub> shots with a lower edge density per Eq. 1.6b (edge conditions in Tables 4.7, 4.9, and 4.11). In the air shots, the O<sub>2</sub> vibrational relaxation is closest in terms of time scale ( $\omega\tau$  is of order 100), and has the highest level of excitation, and we note that the mass fraction of O<sub>2</sub> in the boundary layer is  $y_{O_2} \approx 0.18$ ; however, the Stokes-Kirchhoff (SK) attenuation is calculated to be dominant in air flows at these conditions.

For the CO<sub>2</sub> experiments, the time scale is mismatched by approximately one order of magnitude and exhibits appreciable vibrational excitation, noting that mass fraction of CO<sub>2</sub> is  $y_{CO_2} \approx 0.85$  in the boundary layer. This implies that the CO<sub>2</sub> experiments have the best chance to exhibit instability attenuation by relaxation effects. The Stokes-Kirchhoff (SK) attenuation is approximately half of the attenuation due to vibrational relaxation.

The scaling of  $2f\delta/U_E \approx 0.6-0.8$  appears to bound the measured frequency of the largest amplitude narrow-band disturbances (Fig. 5.10, Tables 4.8, 4.10, and 4.12) for the current data set. This scale of largest amplitude narrow-band disturbances is compared to the results reported in Stetson et al. (1983) and Demetriades (1977), and the range of  $2f\delta/U_E$  is expanded to 0.6-1.1. No strong trend in edge Reynolds number is evident for any data set for the  $2f\delta/U_E$  scaling. There is an observed shift in  $2f\delta/U_E$  that could be attributed to wall temperature ratio and edge Mach number. It is observed that wall temperature ratio could have a larger role in reducing  $2f\delta/U_E$  than edge Mach number does, but further investigation would be required to confirm this hypothesis. The change in  $2f\delta/U_E$  is possibly characteristic of the extreme velocity and sound-speed gradients typical of hypervelocity boundary layers.

Stability computations are compared with experimental results. The means by which data are extracted from the computations is described. The peak amplitude of the instability should increase in amplitude at a decreased frequency as it is tracked along the generator of the cone; these qualitative trends are observed for both the computations and experiments. A significant discrepancy between the computational and the experimental data is that for air and CO<sub>2</sub> experiments, the computed imaginary stream-wise wavenumber ( $\alpha_i$ ) has a maximum in frequency that is higher than the frequency at which there is a maximum in the density disturbances ( $|\Delta\rho|/\rho_L$ ). This is not a sensible result because the maximum in amplification should occur at a lower frequency for this flow field. The N<sub>2</sub> shots have the correct trend for the relative frequencies for the maxima in imaginary stream-wise wavenumber and density perturbations. The reason for this disparity in frequency content is not clear at the time of this writing, but one strong candidate cause is the large systemic error in calculating the run conditions that was discussed in detail in section 2.5. Incorrectly predicting the frequency at which there is a maximum in  $\alpha_i$  alters the computation of the amplification factor, so this may be one reason a poor prediction of the am-

plitude of the amplification ratio by the computations is observed. It should also be noted that normal-mode spatial stability analysis in conjunction with parabolized stability equation analysis is used to find the amplification of disturbances in the boundary layer. Recent developments in non-modal stability theory highlighted in [Trefethen et al. \(1993\)](#), [Schmid and Henningson \(2001\)](#), and [Schmid \(2007\)](#) may be able to provide a different approach to the problem which could lead to fruitful analysis of the experimental disturbance growth characterized in this work. Some high-speed compressible work has appeared in the literature, examples of which are [Hanifi et al. \(1996\)](#), [Tumin and Reshotko \(2003\)](#), and [Zuccher et al. \(2007\)](#). Specifically in [Zuccher et al. \(2007\)](#), the boundary layer on a sharp cone at supersonic edge Mach number is analyzed, and it is noted that the wall temperature has a strong effect on the results.

# Bibliography

- P. Adam. *Enthalpy Effects on Hypervelocity Boundary Layers*. PhD thesis, [California Institute of Technology](#), California, 1997. 22
- P. H. Adam and H. G. Hornung. Enthalpy Effects on Hypervelocity Boundary-layer Transition: Ground Test and Flight Data. *Journal of Spacecraft And Rockets*, 34(5):614–619, 1997. doi: [10.2514/2.3278](#). 22
- M. Azzazy, D. Modarress, and T. Hoefft. High sensitivity Density Fluctuation Detector. In *Proceedings of SPIE Vol. 569 High Speed Photography, Videography, and Photonics I/I*, San Diego, CA, 1985. SPIE. doi: [10.1117/12.949865](#). 53
- M. Azzazy, D. Modarress, and J. D. Trolinger. Feasibility Study of Optical Boundary Layer Transition Detection Method. [NASA-CR-178109](#), 1986. 53
- M. Azzazy, D. Modarress, and T. Hoefft. High-sensitivity Density Fluctuation Detector. *Journal of Physics E: Scientific Instruments*, 20(4):428, 1987. doi: [10.1088/0022-3735/20/4/017](#). 53
- E. P. Bartlett and R. M. Kendall. Nonsimilar Solution of the Multicomponent Laminar Boundary Layer by an Integral-Matrix Method. *AIAA Journal*, 6(6):1089–1097, 1968. doi: [10.2514/3.4678](#). 22
- T. G. Beckwith, R. D. Marangoni, and J. H. Lienhard. *Mechanical Measurements*. Pearson-Prentice Hall, Sixth edition, 2007. 43, 67

- J. Bélanger. *Studies of Mixing and Combustion in Hypervelocity Flows with Hot Hydrogen Injection*. PhD thesis, [California Institute of Technology](#), California, 1993. [28](#)
- D. C. Berridge. Measurements Of Second-Mode Instability Waves in Hypersonic Boundary Layers with a High-Frequency Pressure Transducer. Master's thesis, Purdue University, 2010. [51](#)
- A. Blanchard, J. Lachowicz, and S. Wilkinson. Performance of the NASA-Langley Mach 6 Quiet Wind Tunnel. *AIAA Journal*, 35(1):23–28, 1996. [doi: 10.2514/6.1996-441](#). [70](#)
- F.G. Blottner, M. Johnson, and M. Ellis. Chemically Reacting Viscous Flow Program for Multi-Component Gas Mixtures. *Sandia National Laboratory, SC-RR-70-754*, 1971. [doi: 10.2172/4658539](#). [21](#)
- L. R. Boedeker. Analysis and Construction of a Sharp Focusing Schlieren System. Master's thesis, Massachusetts Institute of Technology, Massachusetts, 1959. [51](#)
- M. Born and E. Wolf. *Principles of Optics*. Cambridge University Press, Sixth edition, 1997. [58](#)
- A. Bounitch, D. R. Lewis, and J. F. Lafferty. Improved Measurements of Tunnel Noise Pressure Fluctuations in the AEDC Hypervelocity Wind Tunnel No. 9. In *Proceedings of 49th AIAA Aerospace Sciences Meeting Including the New Horizons Forum and Aerospace Exposition*, Orlando, Florida, 2011. AIAA-2011-1200. [doi: 10.2514/6.2011-1200](#). [70](#)
- D. Bountin, A. Shipliyuk, and A. Maslov. Evolution of Nonlinear Processes in a Hypersonic Boundary Layer on a Sharp Cone. *Journal of Fluid Mechanics*, 611: 427–442, 2008. [doi: 10.1017/S0022112008003030](#). [128](#)

- S. Browne, J. Ziegler, and J. E. Shepherd. Numerical Solution Methods for Shock and Detonation Jump Conditions. GALCIT - FM2006-006, 2006. [27](#)
- M. Camac. CO<sub>2</sub> Relaxation Processes in Shock Waves. In *Fundamental Phenomena in Hypersonic Flow*, pages 195–215, Ithaca, NY, 1966. Cornell University Press. [20](#), [41](#)
- G. V. Candler. Hypersonic Nozzle Analysis Using an Excluded Volume Equation of State. In *Proceedings of 38th AIAA Thermophysics Conference*, Toronto, Ontario Canada, 2005. AIAA-2005-5202. doi: [10.2514/6.2005-5202](#). [28](#)
- K. M. Casper. Hypersonic Wind-Tunnel Measurements of Boundary-Layer Pressure Fluctuations. Master’s thesis, Purdue University, 2009. [51](#)
- S. Catrisa and B. Aupoix. Density Corrections for Turbulence Models. *Aerospace Science and Technology*, 4(1):1–11, 2000. [28](#)
- C.-L. Chang and M. R. Malik. Oblique-mode Breakdown and Secondary Instability in Supersonic Boundary Layers. *Journal of Fluid Mechanics*, 273(1):323–360, 1994. doi: [10.1017/S0022112094001965](#). [118](#)
- N. Chokani. Nonlinear Spectral Dynamics of Hypersonic Laminar Boundary Layer Flow. *Physics of Fluids*, 11(12):3846–3851, 1999. doi: [10.1063/1.870243](#). [128](#)
- N. Chokani, D. A. Bountin, A. N. Shplyuk, and A. A. Maslov. Nonlinear Aspects of Hypersonic Boundary-Layer Stability on a Porous Surface. *AIAA journal*, 43(1):149–155, 2005. doi: [10.2514/1.9547](#). [128](#)
- H. W. Coleman and W. G. Steele. *Experimentation and Uncertainty Analysis for Engineers*. John Wiley and Sons, Inc., Second edition, 1999. [43](#)
- S. H. Collicott, S. P. Schneider, and N. L. Messersmith. Review Of Optical Diagnostic Methods For Hypersonic Low-Noise Facilities. In *Proceedings of*

- 34th Aerospace Sciences Meeting and Exhibit*, Reno, NV, 1996. AIAA-96-0851. doi: [10.2514/6.1996-851](https://doi.org/10.2514/6.1996-851). 53
- A. Demetriades. Hypersonic Viscous Flow Over a Slender Cone. III - Laminar Instability and Transition. In *Proceedings of the 7th AIAA Fluid and Plasma Dynamics Conference*, number AIAA 74-535, Palo Alto, California, 1974. AIAA. doi: [10.2514/6.1974-535](https://doi.org/10.2514/6.1974-535). 81
- A. Demetriades. Laminar Boundary Layer Stability Measurements at Mach 7 Including Wall Temperature Effects. AFOSR-TR-77-1311, 1977. 6, 50, 129, 130, 137
- N. R. Draper and H. Smith. *Applied Regression Analysis*. Wiley-Interscience, 1998. 76
- DSB. Report of the Defense Science Board Task Force on the National Aerospace Plane (NASP). AD-A201 124, 1988. 2, 131
- DSB. Report of the Defense Science Board Task Force on the National Aerospace Plane (NASP). AD-A274 530, 1992. 2
- N.A. Ebrahim and H.G. Hornung. Nonequilibrium Nozzle Expansions of Carbon Dioxide from a High-Enthalpy Reservoir. *AIAA J*, 11(7):1369–1372, 1973. doi: [10.2514/3.50593](https://doi.org/10.2514/3.50593). 44
- N.A. Ebrahim and H.G. Hornung. High-Enthalpy Nonequilibrium Carbon Dioxide Nozzle and Wedge Flows: Experiment and Calculations. *AIAA J*, 13(7):845–846, 1975. doi: [10.2514/3.60456](https://doi.org/10.2514/3.60456). 44
- A. Fedorov. Transition and Stability of High-Speed Boundary Layers. *Annual Review of Fluid Mechanics*, 43:79–95, 2011. doi: [10.1146/annurev-fluid-122109-160750](https://doi.org/10.1146/annurev-fluid-122109-160750). 3, 4, 5, 42, 74, 81, 112

- A. Fedorov and A. Tumin. High-Speed Boundary-Layer Instability: Old Terminology and a New Framework. *AIAA Journal*, 49:1647–1657, 2011. doi: [10.2514/1.J050835](https://doi.org/10.2514/1.J050835). 4
- A.V. Fedorov. Receptivity of a High-Speed Boundary Layer to Acoustic Disturbances. *Journal of Fluid Mechanics*, 491:101–129, 2003. doi: [10.1017/S0022112003005263](https://doi.org/10.1017/S0022112003005263). 69
- K. Fujii. *An Experimental Investigation of the Attachment Line Boundary-Layer Transition on Swept Cylinders in Hypervelocity Flow*. PhD thesis, University of Tokyo, Tokyo, Japan, 2001. 23
- K. Fujii. Experiment of the Two-Dimensional Roughness Effect on Hypersonic Boundary-Layer Transition. *Journal of Spacecraft and Rockets*, 43(4):731–738, 2006. doi: [10.2514/1.17860](https://doi.org/10.2514/1.17860). 51
- K. Fujii and H. G. Hornung. A Procedure to Estimate the Absorption Rate of Sound Propagating Through High Temperature Gas. GALCIT Report FM 2001.004, 2001. 23, 116, 136
- K. Fujii and H. G. Hornung. Experimental Investigation of High-Enthalpy Effects on Attachment-Line Boundary-Layer Transition. *AIAA Journal*, 41(7):1282–1291, 2003. doi: [10.2514/2.2096](https://doi.org/10.2514/2.2096). 23, 116, 136
- K. Fujii, H. Noriaki, K. Tadao, T. Shoichi, N. Muneyoshi, I. Yukihiro, N. Akihiro, and O. Hiroshi. A Measurement of Instability Wave in the Hypersonic Boundary Layer on a Sharp Cone. In *Proceedings of the 41st AIAA Fluid Dynamics Conference and Exhibit*, Honolulu, Hawaii, 2011. AIAA-2011-3871. doi: [10.2514/6.2011-3871](https://doi.org/10.2514/6.2011-3871). 51
- G. A. Kriegsmann and E. L. Reiss. Acoustic Propagation in Wall Shear Flows and the Formation of Caustics. *Journal of The Acoustical Society Of America*. 7

- S. Garg and G. S. Settles. Measurements of a Supersonic Turbulent Boundary Layer by Focusing Schlieren Deflectometry. *Experiments in Fluids*, 25(3):254–264, 1998. doi: [10.1007/s003480050228](https://doi.org/10.1007/s003480050228). 51
- A. G. Gaydon and I. R. Hurle. *The Shock Tube in High-Temperature Chemical Physics*. Reinhold Publishing Corporation, first edition, 1963. 20
- P. Germain. *The Boundary Layer On a Sharp Cone in High-enthalpy Flow*. PhD thesis, [California Institute of Technology](https://www.proquest.com/docview/231111111), California, 1993. 21, 23
- P. D. Germain and H. G. Hornung. Transition on a Slender Cone in Hypervelocity Flow. *Experiments in Fluids*, 22:183–190, 1997. doi: [10.1007/s003480050036](https://doi.org/10.1007/s003480050036). 21, 22, 23
- R. R. Goodman and L. R. B. Duykers. Calculations of Convergent Zones in a Sound Channel. *The Journal of the Acoustical Society of America*, 34(7):960–962, 1962. doi: [10.1121/1.1918229](https://doi.org/10.1121/1.1918229). 8, 10
- D. G. Goodwin. An Open-Source, Extensible Software Suite for CVD Process Simulation. In *Proceedings of CVD XVI and EuroCVD Fourteen*, M Allendorf, F Maury, and F Teyssandier (Eds.), pages 155–162, 2003. 21, 27
- S. Gordon and B.J. McBride. Thermodynamic Data to 20000 K for Monatomic Gases. NASA TP-1999-208523, 1999. 27
- A. Hanifi, P. J. Schmid, and D. S. Henningson. Transient growth in compressible boundary layer flow. *Physics of Fluids*, 8(3):826–837, 1996. doi: [10.1063/1.868864](https://doi.org/10.1063/1.868864). 119, 138
- D. Heitmann, C. Kähler, R. Radespiel, T. Rödiger, H. Knauss, and S. Wagner. Non-Intrusive Generation of Instability Waves in a Planar Hypersonic Boundary Layer. *Experiments in Fluids*, 50:457–464, 2011. doi: [10.1007/s00348-010-0949-2](https://doi.org/10.1007/s00348-010-0949-2). 51

- T. Herbert. Parabolized Stability Equations. [AGARD-R-793](#), 1993. 118
- T. Herbert. Parabolized Stability Equations. *Annual Review of Fluid Mechanics*, 29 (1):245–283, 1997. doi: [10.1146/annurev.fluid.29.1.245](#). 118
- J. W. Hofferth, R. A. Humble, D. C. Floryan, and W. S. Saric. High-Bandwidth Optical Measurements of the Second-Mode Instability in a Mach 6 Quiet Tunnel. In *Proceedings of 51st AIAA Aerospace Sciences Meeting Including the New Horizons Forum and Aerospace Exposition*, Grapevine, Texas, 2013. AIAA 2013-0378. doi: [10.2514/6.2013-378](#). 52, 70
- H. G. Hornung. Performance Data of the New Free-Piston Shock Tunnel at GALCIT. In *Proceedings of 17th AIAA Aerospace Ground Testing Conference*, Nashville, TN, 1992. AIAA 1992-3943. doi: [10.2514/6.1992-3943](#). xv, 25, 47
- H. G. Hornung. Experimental Hypervelocity Flow Simulation, Needs, Achievements and Limitations. In *Proceedings of the First Pacific International Conference on Aero Sc. and Tech.*, Taiwan, 1993. 15, 29
- J. S. Jewell, I. A. Leyva, N. J. Parziale, and J. E. Shepherd. Effect of gas injection on transition in hypervelocity boundary layers. In *Proceedings of the 28th International Symposium on Shock Waves*, Manchester, UK, 2011. ISSW. 23
- J. S. Jewell, N. J. Parziale, I. A. Leyva, J. E. Shepherd, and H. G. Hornung. Turbulent Spot Observations within a Hypervelocity Boundary Layer on a 5-degree Half-Angle Cone. In *Proceedings of 42nd AIAA Fluid Dynamics Conference and Exhibit*, New Orleans, Louisiana, 2012. AIAA-2012-3062. doi: [10.2514/6.2012-3062](#). 23, 83, 94
- J. S. Jewell, R. M. Wagnild, I. A. Leyva, G. V. Candler, and J. E. Shepherd. Transition Within a Hypervelocity Boundary Layer on a 5-Degree Half-Angle Cone in Air/CO<sub>2</sub> Mixtures. In *51st AIAA Aerospace Sciences Meeting including the New*

- Horizons Forum and Aerospace Exposition*, Grapevine, Texas, 2013. AIAA-2013-0523. doi: [10.2514/6.2013-523](https://doi.org/10.2514/6.2013-523). 23, 83
- H. B. Johnson. *Thermochemical Interactions in Hypersonic Boundary Layer Stability*. PhD thesis, University of Minnesota, Minnesota, 2000. 28, 34, 39, 117, 118, 119
- H. B. Johnson, T. G Seipp, and G. V. Candler. Numerical Study of Hypersonic Reacting Boundary Layer Transition on Cones. *Physics of Fluids*, 10(13):2676–2685, 1998. doi: [10.1063/1.869781](https://doi.org/10.1063/1.869781). 34, 117
- J. M. Kendall. Wind-Tunnel Experiments Relating to Supersonic and Hypersonic Boundary-Layer Transition. *AIAA Journal*, 13(3):290–299, 1975. doi: [10.2514/3.49694](https://doi.org/10.2514/3.49694). 6, 50
- R. L. Kimmel, A. Demetriades, and J. C. Donaldson. Space-Time Correlation Measurements in a Hypersonic Transitional Boundary Layer. *AIAA Journal*, 34(12):2484–2489, 1996. doi: [10.2514/3.13428](https://doi.org/10.2514/3.13428). 50, 99, 107
- S. J. Kline and F. A. McClintock. Describing Uncertainties in Single Sample Experiments. *Mechanical Engineering*, 75:3–8, 1953. 43, 67
- A. J. Laderman and A. Demetriades. Detection of Boundary-Layer-Transition with a Laser-Beam. *AIAA Journal*, 14(1):102–104, 1976. doi: [10.2514/3.7058](https://doi.org/10.2514/3.7058). 52
- L. Landau and E. Teller. Zur Theorie der Schalldispersion. *Phys. Z. Sowjetunion*, 10(1), 1936. 39
- K. Y. Lau. Hypersonic Boundary-Layer Transition: Application to High-Speed Vehicle Design. *Journal of Spacecraft and Rockets*, 45(2):176–183, 2008. doi: [10.2514/1.31134](https://doi.org/10.2514/1.31134). 1
- S. J. Laurence, A. Wagner, K. Hannemann, V. Wartemann, H. Lüdeke, H. Tanno, and K. Itoh. Time-Resolved Visualization of Instability Waves in a Hypersonic

- Boundary Layer. *AIAA Journal*, 50(6):243–246, 2012. doi: [10.2514/1.56987](https://doi.org/10.2514/1.56987). 99, 107
- S. S. Lee, S.K. Lele, and P. Moin. Interaction of Isotropic Turbulence with Shock Waves: Effect of Shock Strength. *Journal of Fluid Mechanics*, 340:225–247, 1997. doi: [10.1017/S0022112097005107](https://doi.org/10.1017/S0022112097005107). 71
- I.A. Leyva, S.J. Laurence, A. K. Beierholm, H.G. Hornung, R. Wagnild, and G. Candler. Transition Delay in Hypervelocity Boundary Layers by Means of CO<sub>2</sub>/Acoustic Instability Interactions. In *Proceedings of 47th AIAA Aerospace Sciences Meeting Including the New Horizons Forum and Aerospace Exposition*, Orlando, Florida, 2009a. AIAA-2009-1287. doi: [10.2514/6.2009-1287](https://doi.org/10.2514/6.2009-1287). 23
- I.A. Leyva, S.J. Laurence, A. K. Beierholm, H.G. Hornung, R. Wagnild, and G. Candler. On the Impact of Injection Schemes on Transition in Hypersonic Boundary Layers. In *Proceedings of 16th AIAA/DLR/DGLR International Space Planes and Hypersonic Systems and Technologies Conference*, Bremen, Germany, 2009b. AIAA-2009-7204. doi: [10.2514/6.2009-7204](https://doi.org/10.2514/6.2009-7204). 23
- H. W. Liepmann and A. Roshko. *Elements of Gasdynamics*. John Wiley and Sons, Inc., 1957. 58
- T. C. Lin. Influence of Laminar Boundary-Layer Transition on Entry Vehicle Designs. *Journal of Spacecraft and Rockets*, 45(2):165–175, 2008. doi: [10.2514/1.30047](https://doi.org/10.2514/1.30047). 1
- L. M. Mack. Boundary-layer Linear Stability Theory. *AGARD Rep 709*, Special Course on Stability Transitional Laminar Flows 1984. 3, 4, 5, 6, 7, 15, 97, 112, 119, 130, 131, 132
- L. M. Mack. Stability of Axisymmetric Boundary layers on Sharp Cones at Hypersonic Mach Numbers. In *Proceedings of 19th AIAA Fluid Dynamics, Plasma*

- Dynamics and Lasers Conference*, Honolulu, Hawaii, 1987. AIAA-1987-1413. doi: [10.2514/6.1987-1413](https://doi.org/10.2514/6.1987-1413). 6
- K. Maheash, S.S. Lee, S.K. Lele, and P Moin. The Interaction of an Isotropic Field of Acoustic Waves with a Shock Wave. *Journal of Fluid Mechanics*, 300:383–407, 1995. doi: [10.1017/S0022112095003739](https://doi.org/10.1017/S0022112095003739). 71
- E. C. Marineau and H. G. Hornung. Study of Bow-Shock Wave Unsteadiness in Hypervelocity Flow from Reservoir Fluctuations. In *Proceedings of 48th AIAA Aerospace Sciences Meeting Including the New Horizons Forum and Aerospace Exposition*, Orlando, Florida, 2010. AIAA-2010-382. doi: [10.2514/6.2010-382](https://doi.org/10.2514/6.2010-382). 71
- MathWorks. stepwisefit documentation page. URL <http://www.mathworks.com>. 76
- B.J. McBride, M. J. Zehe, and S. Gordon. NASA Glenn Coefficients for Calculating Thermodynamic Properties of Individual Species. NASA TP-2002-211556, 2002. 21, 27
- M. McGilvray, P. A. Jacobs, R. G. Morgan, R. J. Gollan, and C. M. Jacobs. Helmholtz Resonance of Pitot Pressure Measurements in Impulsive Hypersonic Test Facilities. *AIAA*, 47(10):2430–2439, 2009. doi: [10.2514/1.42543](https://doi.org/10.2514/1.42543). 71
- D. McQuarrie. *Statistical Mechanics*. University Science Books, 2000. 15, 20
- R. C. Millikan and D. R. White. Systematics of Vibrational Relaxation. *The Journal of Chemical Physics*, 39(12):3209–3213, 1963. doi: [10.1063/1.1734182](https://doi.org/10.1063/1.1734182). 20, 41
- F. K. Moore. Unsteady Oblique Interaction of a Shock Wave with a Plane Disturbance. NACA TR-1165, 1954. 71
- M. V. Morkovin. Critical Evaluation of Transition From Laminar to Turbulent Shear Layers with Emphasis on Hypersonically Traveling Bodies. *AFFDL TR-68-149*, 1969. 69

- M. V. Morkovin, Reshotko E., and Herbert T. Transition in Open Flow Systems: A Reassessment. In *47th Annual Meeting of the Division of Fluid Dynamics*, volume 39, 1994. [3](#), [4](#)
- W. H. Munk. Sound Channel in an Exponentially Stratified Ocean, with Application to SOFAR. *Journal of The Acoustical Society Of America*, 55(2):220–226, 1974. doi: [10.1121/1.1914492](https://doi.org/10.1121/1.1914492). [9](#), [10](#)
- J. E. O’Hare. A Nonperturbing Boundary-Layer Transition Detector. In *Proceedings of SPIE 0569, High Speed Photography, Videography, and Photonics III*, pages 58–63, San Diego, California, 1985. doi: [10.1117/12.949864](https://doi.org/10.1117/12.949864). [53](#)
- N. J. Parziale, J. S. Jewell, J. E. Shepherd, and H. G. Hornung. Shock Tunnel Noise Measurement with Resonantly Enhanced Focused Schlieren Deflectometry. In *Proceedings of the 28th International Symposium on Shock Waves*, Manchester, UK, 2011. ISSW. [52](#)
- N. J. Parziale, J. S. Jewell, J. E. Shepherd, and H. G. Hornung. Optical Detection of Transitional Phenomena on Slender Bodies in Hypervelocity Flow. In *Proceedings of AVT-200 Specialists’ Meeting on Hypersonic Laminar-Turbulent Transition*, San Diego, California, 2012a. NATO. [52](#)
- N. J. Parziale, J. E. Shepherd, and H. G. Hornung. Reflected Shock Tunnel Noise Measurement by Focused Differential Interferometry. In *Proceedings of 42nd AIAA Fluid Dynamics Conference and Exhibit*, New Orleans, Louisiana, 2012b. AIAA-2012-3261. doi: [10.2514/6.2012-3261](https://doi.org/10.2514/6.2012-3261). [83](#)
- N. J. Parziale, J. E. Shepherd, and H. G. Hornung. Differential Interferometric Measurement of Instability at Two Points in a Hypervelocity Boundary Layer. In *Proceedings of 51st AIAA Aerospace Sciences Meeting Including the New Hori-*

- zons Forum and Aerospace Exposition*, Grapevine, Texas, 2013a. AIAA-2013-0521. doi: [10.2514/6.2013-521](https://doi.org/10.2514/6.2013-521). 83
- N. J. Parziale, J. E. Shepherd, and H. G. Hornung. Geometric Acoustics in High-Speed Boundary Layers. In *Proceedings of the 29th International Symposium on Shock Waves*, Madison, WI, 2013b. ISSW. 6
- N. J. Parziale, J. E. Shepherd, and H. G. Hornung. Differential Interferometric Measurement of Instability in a Hypervelocity Boundary Layer. *AIAA Journal*, 51(3): 750–754, 2013. doi: [10.2514/1.J052013](https://doi.org/10.2514/1.J052013). 77
- S. R. Pate. Supersonic Boundary-layer Transition - Effects of Roughness and Freestream Disturbances. *AIAA Journal*, 9(5):797–803, 1971a. doi: [10.2514/3.6278](https://doi.org/10.2514/3.6278). 70
- S. R. Pate. Measurements and Correlations of Transition Reynolds Numbers on Sharp Slender Cones at High Speeds. *AIAA Journal*, 9(6):1082–1090, 1971b. doi: [10.2514/3.49919](https://doi.org/10.2514/3.49919). 70
- S. R. Pate. Comparison of NASA Helium Tunnel Transition Data with Noise-Transition Correlation. *AIAA Journal*, 12(11):1615, 1974. doi: [10.2514/3.49564](https://doi.org/10.2514/3.49564). 70
- S. R. Pate and C. J. Schueler. Radiated Aerodynamic Noise Effects on Boundary-layer Transition in Supersonic and Hypersonic Wind Tunnels. *AIAA Journal*, 7(3): 450–457, 1969. doi: [10.2514/3.5128](https://doi.org/10.2514/3.5128). 70
- A. Paull and R. J. Stalker. Test flow disturbances in an expansion tube. *Journal of Fluid Mechanics*, 245:493–521, 1992. doi: [10.1017/S0022112092000569](https://doi.org/10.1017/S0022112092000569). 77
- A. D. Pierce. *Acoustics: An Introduction to its Physical Principles and Applications*. Acoustical Society of America, Second edition, 1989. 7, 9, 18, 20, 132

- A. Rasheed. *Passive Hypervelocity Boundary Layer Control Using an Acoustically Absorptive Surface*. PhD thesis, [California Institute of Technology](#), California, 2001. [22](#)
- A. Rasheed, H. G. Hornung, A. V. Fedorov, and N. D. Malmuth. Experiments on Passive Hypervelocity Boundary-layer Control Using an Ultrasonically Absorptive Surface. *AIAA J.*, 40(3):481–489, MAR 2002. doi: [10.2514/2.1671](#). [22](#)
- R. Reagan. Address Before a Joint Session of Congress on the State of the Union, 1986. [The American Presidency Project at University of California, Santa Barbara](#). [2](#)
- E. Reshotko. Boundary-Layer Stability and Transition. *Annual Review of Fluid Mechanics*, 8:311–349, 1976. doi: [10.1146/annurev.fl.08.010176.001523](#). [69](#)
- E. Reshotko. Transition Issues for Atmospheric Entry. *Journal of Spacecraft and Rockets*, 45(2):161–164, 2008. doi: [10.2514/1.29777](#). [3](#)
- T. Roediger, H. Knauss, Uwe Gaisbauer, E. Kraemer, S. Jenkins, and J. von Wolfersdorf. Time-Resolved Heat Transfer Measurements on the Tip Wall of a Ribbed Channel Using a Novel Heat Flux Sensor, Part I: Sensor and Benchmarks. *Journal of Turbomachinery*, 130(1), 2008. doi: [10.1115/1.2751141](#). [51](#)
- T. Roediger, H. Knauss, M. Estorf, S. P. Schneider, and B. V. Smorodsky. Hypersonic Instability Waves Measured Using Fast-Response Heat-Flux Gauges. *Journal of Spacecraft And Rockets*, 46(2):266–273, 2009. doi: [10.2514/1.37026](#). [51](#)
- N. R. Rotta. Effects of Nose Bluntness on the Boundary Layer Characteristics of Conical Bodies at Hypersonic Speeds. [AD-0645668](#) or NYU-AA-66-66, 1966. [60](#)
- S. Rufer and D. Berridge. Pressure Fluctuation Measurements in the NASA Langley 20-Inch Mach 6 Wind Tunnel. In *Proceedings of 42nd AIAA Fluid Dy-*

- namics Conference and Exhibit*, New Orleans, Louisiana, 2012. AIAA-2012-3262. doi: [10.2514/6.2012-3262](https://doi.org/10.2514/6.2012-3262). 70
- W. S. Saric, H. L. Reed, and E. J. Kerschen. Boundary Layer Receptivity to Freestream Disturbances. *Annual Review of Fluid Mechanics*, 34:291–319, 2002. doi: [10.1146/annurev.fluid.34.082701.161921](https://doi.org/10.1146/annurev.fluid.34.082701.161921). 69
- H. Schlichting. *Boundary-Layer Theory*. Springer, 2000. 3
- P. J. Schmid. Nonmodal Stability Theory. *Annual Review of Fluid Mechanics*, 39:129–162, 2007. doi: [10.1146/annurev.fluid.38.050304.092139](https://doi.org/10.1146/annurev.fluid.38.050304.092139). 138
- P. J. Schmid and D. S. Henningson. *Stability and Transition in Shear Flows*. Springer-Verlag, First edition, 2001. 3, 119, 138
- J. D. Schmisser and P. Erbland. Introduction: Assessment of Aerothermodynamic Flight Prediction Tools Through Ground and Flight Experimentation. *Progress in Aerospace Sciences*, 48-49:2–7, 2012. doi: [10.1016/j.paerosci.2011.09.004](https://doi.org/10.1016/j.paerosci.2011.09.004). 1
- S. P. Schneider. Effects of High-Speed Tunnel Noise on Laminar-Turbulent Transition. *Journal of Spacecraft and Rockets*, 38(3):323–333, 2001. doi: [10.2514/2.3705](https://doi.org/10.2514/2.3705). 69, 70
- S. P. Schneider. Hypersonic Laminar-Turbulent Transition on Circular Cones and Scramjet Forebodies. *Progress in Aerospace Sciences*, 40(1-2):1–50, 2004. doi: [10.1016/j.paerosci.2003.11.001](https://doi.org/10.1016/j.paerosci.2003.11.001). 1, 53, 69
- S. P. Schneider. Development of Hypersonic Quiet Tunnels. *Journal of Spacecraft and Rockets*, 45(4):641–664, 2008. doi: [10.2514/1.34489](https://doi.org/10.2514/1.34489). 70
- G. B. Schubauer and H. K. Skramstad. Laminar-Boundary-Layer Oscillations and Transition on a Flat Plate. [NACA-TR-909](https://naca.central.cmu.edu/bitstream/handle/1721.2/10700/1/NACA-TR-909.pdf), 1948. 3

- L. Schwelkart. The Hypersonic Revolution. Case Studies in the History of Hypersonic Technology. Volume 3: The Quest for the Orbital Jet: The National Aero-Space Plane Program (1983-1995). [ADA441126](#), 1997. 3
- G. S. Settles. *Schlieren and Shadowgraph Techniques*. Springer-Verlag Berlin Heidelberg, First edition, 2001. 99, 107
- A. E. Siegman. *Lasers*. University Science Books, 1986. 56
- G. Smeets. Laser Interferometer for High Sensitivity Measurements on Transient Phase Objects. *IEEE Transactions on Aerospace and Electronic Systems*, AES-8(2):186–190, 1972. doi: [10.1109/TAES.1972.309488](#). 52
- G. Smeets. Laser-Interferometer mit grossen, fokussierten Lichtbündeln für lokale Messungen. ISL - N 11/73, 1973. 52, 54
- G. Smeets. Verwendung eines Laser-Differentialinterferometers zur Bestimmung lokaler Schwankungsgrössen sowie des mittleren Dichteprofiles in einem turbulenten Freistrahle. ISL - N 20/74, 1974. 52
- G. Smeets. Flow Diagnostics by Laser Interferometry. *IEEE Transactions on Aerospace and Electronic Systems*, AES-13(2):82–90, 1977. doi: [10.1109/TAES.1977.308441](#). 52
- G. Smeets and A. George. Anwendungen des Laser-Differentialinterferometers in der Gasdynamik. ISL - N 28/73, Also translated by Goetz, A.: [ADA-307459](#), 1973. 52
- P. R. Spalart and S. R. Allmaras. A One-equation Turbulence Model for Aerodynamic Flows. In *Proceedings of 30th AIAA Aerospace Sciences Meeting and Exhibit*, Reno, Nevada, 1992. AIAA 1992-439. doi: [10.2514/6.1992-439](#). 28

- R. J. Stalker. Hypervelocity Aerodynamics with Chemical Nonequilibrium. *Annual Review of Fluid Mechanics*, 21:37–60, 1989. doi: [10.1146/annurev.fluid.21.1.37](https://doi.org/10.1146/annurev.fluid.21.1.37). 15, 29
- K. F. Stetson. Nosetip Bluntness Effects on Cone Frustum Boundary Layer Transition in Hypersonic Flow. In *Proceedings of the AIAA 16th Fluid and Plasma Dynamics Conference*, Danvers, Massachusetts, 1983. AIAA-83-1763. doi: [10.2514/6.1983-1763](https://doi.org/10.2514/6.1983-1763). 60
- K. F. Stetson, E. R. Thompson, J. C. Donaldson, and L. G. Siler. Laminar Boundary Layer Stability Experiments on a Cone at Mach 8, Part 1: Sharp Cone. In *Proceedings of the AIAA 16th Fluid and Plasma Dynamics Conference*, Danvers, Massachusetts, 1983. AIAA-83-1761. doi: [10.2514/6.1983-1761](https://doi.org/10.2514/6.1983-1761). 6, 50, 129, 130, 137
- K. F. Stetson, J. C. Donaldson, and L. G. Siler. Laminar Boundary Layer Stability Experiments on a Cone at Mach 8, Part 2: Blunt Cone. In *Proceedings of the 22nd AIAA Aerospace Sciences Meeting*, Reno, Nevada, 1984. AIAA-84-0006. doi: [10.2514/6.1984-6](https://doi.org/10.2514/6.1984-6). 6, 50
- K. F. Stetson, E. R. Thompson, J. C. Donaldson, and L. G. Siler. Laminar Boundary Layer Stability Experiments on a Cone at Mach 8, Part 5: Tests with a Cooled Model. In *Proceedings of the AIAA 20th Fluid and Plasma Dynamics Conference*, Buffalo, New York, 1989. AIAA-89-1895. doi: [10.2514/6.1989-1895](https://doi.org/10.2514/6.1989-1895). 6, 50
- K.F. Stetson and R. L. Kimmel. On Hypersonic Boundary-layer Stability. In *Proceedings of the 13th Aerospace Sciences Meeting and Exhibit*, Reno, NV, 1992. AIAA. 81
- N. Sudani and H. G. Hornung. Gasdynamical Detectors of Driver Gas Contamination

- in a High-Enthalpy Shock Tunnel. *AIAA*, 36(3):313–319, 1998. doi: [10.2514/2.383](https://doi.org/10.2514/2.383).  
75
- Taylor, G. I. and Maccoll, J. W. The Air Pressure on a Cone Moving at High Speeds. I. *Proceedings of the Royal Society of London. Series A, Containing Papers of a Mathematical and Physical Character*. 45
- P. A. Thompson. *Compressible-Fluid Dynamics*. McGraw-Hill, 1972. 7, 18, 19
- W. Tollmien. Über die Entstehung der Turbulenz. Also translated as The Production of Turbulence, 1931, [NACA-TM-609](https://naca.central.cmu.edu/bitstream/handle/171/10697/1/1929-10-1.pdf), 1929. 3
- L. N. Trefethen, A. E. Trefethen, S. C. Reddy, and T. A. Driscoll. Hydrodynamic Stability Without Eigenvalues. *Science*, 261(5121):578–584, 1993. URL <http://www.jstor.org/stable/2882016>. 138
- A. Tumin and E. Reshotko. Optimal Disturbances in Compressible Boundary Layers. *AIAA Journal*, 41(12):2357–2363, 2003. doi: [10.2514/2.6860](https://doi.org/10.2514/2.6860). 138
- C. P. VanDercreek. *Hypersonic Application of Focused Schlieren and Deflectometry*. PhD thesis, University of Maryland, College Park, Maryland, 2010. 51, 99, 107
- C. P. VanDercreek, M. S. Smith, and K. H. Yu. Focused Schlieren and Deflectometry at AEDC Hypervelocity Wind Tunnel No. 9. In *Proceedings of 27th AIAA Aerodynamic Measurement Technology and Ground Testing Conference*, Chicago, Illinois, 2010. AIAA 2010-4209. doi: [10.2514/6.2010-4209](https://doi.org/10.2514/6.2010-4209). 51
- W. G. Vincenti and C. H. Kruger. *Introduction to Physical Gas Dynamics*. Krieger Publishing Company, 1965. 17, 32
- R. M. Wagnild. *High Enthalpy Effects on Two Boundary Layer Disturbances in Supersonic and Hypersonic Flow*. PhD thesis, University of Minnesota, Minnesota, 2012. 28, 39, 117

- L. M. Weinstein. Large-Field High-Brightness Focusing Schlieren System. *AIAA Journal*, 31(7):1250–1255, 1993. doi: [10.2514/3.11760](https://doi.org/10.2514/3.11760). 51
- F. White. *Viscous Fluid Flow*. McGraw-Hill, second edition, 1991. 35
- F. White. *Viscous Fluid Flow*. McGraw-Hill, third edition, 2006. 10, 36
- M. J. Wright, G. V. Candler, and M. Prampolini. Data-parallel Lower-upper Relaxation Method for the Navier-Stokes Equations. *AIAA Journal*, 34(7):1371–1377, 1996. doi: [10.2514/3.13242](https://doi.org/10.2514/3.13242). 34
- R. L. Wright and E. V. Zoby. Flight Boundary Layer Transition Measurements on a Slender Cone at Mach 20. In *Proceedings of 10th Fluid and Plasmadynamics Conference*, Albuquerque, New Mexico, 1977. AIAA-1977-719. doi: [10.2514/6.1977-719](https://doi.org/10.2514/6.1977-719). 22
- S. Zuccher, I. Shalaev, A. Tumin, and E. Reshotko. Optimal Disturbances in the Supersonic Boundary Layer Past a Sharp Cone. *AIAA Journal*, 45(2):366–373, 2007. doi: [10.2514/1.22541](https://doi.org/10.2514/1.22541). 138

# Appendix A

## T5 Run Conditions

### A.1 Reservoir Conditions

Table A.1: Tunnel Noise Tunnel Run Parameters

| Shot | Gas   | $P_R$<br>(MPa) | $h_R$<br>(MJ/kg) | $P_1$<br>(kPa) | $P_{4i}$<br>(kPa) | $P_{4iAr}$<br>(kPa) | $P_{2R}$<br>(psi) | Dia<br>(mil) | $P_4$<br>(MPa) | $U_S$<br>(m/s) |
|------|-------|----------------|------------------|----------------|-------------------|---------------------|-------------------|--------------|----------------|----------------|
| 2684 | I Air | 46.6           | 8.0              | 85.0           | 116.0             | 17.5                | 1100              | 202/246      | 96             | 2844           |
| 2685 | I Air | 48.8           | 8.4              | 85.0           | 116.0             | 17.5                | 1100              | 203/246      | 107            | 2913           |
| 2686 | I Air | 49.5           | 13.9             | 45.0           | 116.0             | 6.0                 | 1120              | 213/248      | 112            | 3727           |
| 2687 | I Air | 49.3           | 15.9             | 35.0           | 116.0             | 0.0                 | 1130              | 211/246      | 111            | 3947           |
| 2688 | I Air | 52.4           | 17.1             | 35.0           | 116.0             | 0.0                 | 1130              | 211/246      | 111            | 4110           |
| 2689 | I Air | 52.0           | 17.9             | 35.0           | 116.0             | 0.0                 | 1130              | 212/246      | 112            | 4225           |
| 2690 | I Air | 50.8           | 17.2             | 35.0           | 116.0             | 0.0                 | 1130              | 209/245      | 98             | 4138           |
| 2691 | I Air | 41.8           | 5.5              | 150.0          | 118.0             | 19.0                | 1000              | 192/245      | 79             | 2439           |
| 2692 | I Air | 42.4           | 5.3              | 150.0          | 118.0             | 19.0                | 1000              | 191/244      | 76             | 2362           |
| 2693 | I Air | 49.6           | 8.6              | 80.0           | 116.0             | 17.5                | 1110              | 201/245      | 105            | 2927           |
| 2694 | I Air | 49.9           | 17.8             | 35.0           | 116.0             | 0.0                 | 1130              | 214/245      | 113            | 4225           |

Table A.2: Tunnel Noise Reservoir Conditions

| Shot | Gas   | $P_R$ | $h_R$   | $T_R$ | $\rho_R$             | $y_{N_2}$ | $y_{O_2}$ | $y_{NO}$ | $y_N$ | $y_O$ |
|------|-------|-------|---------|-------|----------------------|-----------|-----------|----------|-------|-------|
|      |       | (MPa) | (MJ/kg) | (K)   | (kg/m <sup>3</sup> ) | (-)       | (-)       | (-)      | (-)   | (-)   |
| 2684 | I Air | 46.6  | 8.03    | 5331  | 28.3                 | 0.702     | 0.084     | 0.137    | 0.001 | 0.076 |
| 2685 | I Air | 48.8  | 8.41    | 5499  | 28.6                 | 0.701     | 0.075     | 0.138    | 0.002 | 0.084 |
| 2686 | I Air | 49.5  | 13.92   | 7591  | 18.9                 | 0.684     | 0.013     | 0.093    | 0.039 | 0.170 |
| 2687 | I Air | 49.3  | 15.91   | 8141  | 17.0                 | 0.662     | 0.008     | 0.080    | 0.067 | 0.182 |
| 2688 | I Air | 52.4  | 17.14   | 8457  | 17.1                 | 0.646     | 0.007     | 0.075    | 0.086 | 0.186 |
| 2689 | I Air | 52.0  | 17.88   | 8616  | 16.5                 | 0.635     | 0.006     | 0.071    | 0.099 | 0.189 |
| 2690 | I Air | 50.8  | 17.23   | 8463  | 16.5                 | 0.644     | 0.006     | 0.074    | 0.088 | 0.187 |
| 2691 | I Air | 41.8  | 5.52    | 4200  | 33.9                 | 0.716     | 0.153     | 0.109    | 0.000 | 0.022 |
| 2692 | I Air | 42.4  | 5.28    | 4081  | 35.5                 | 0.719     | 0.160     | 0.104    | 0.000 | 0.018 |
| 2693 | I Air | 49.6  | 8.60    | 5583  | 28.5                 | 0.700     | 0.071     | 0.138    | 0.002 | 0.088 |
| 2694 | I Air | 49.9  | 17.75   | 8570  | 15.9                 | 0.637     | 0.006     | 0.071    | 0.097 | 0.189 |

Table A.3: Single Point Tunnel Run Parameters

| Shot | Gas    | $P_R$ | $h_R$   | $P_1$ | $P_{4i}$ | $P_{4iAr}$ | $P_{2R}$ | Dia     | $P_4$ | $U_S$ |
|------|--------|-------|---------|-------|----------|------------|----------|---------|-------|-------|
|      |        | (MPa) | (MJ/kg) | (kPa) | (kPa)    | (kPa)      | (psi)    | (mil)   | (MPa) | (m/s) |
| 2695 | I. Air | 48.4  | 6.9     | 115.1 | 118.0    | 16.5       | 1090     | 192/242 | 86    | 2655  |
| 2696 | I. Air | 46.0  | 7.0     | 114.7 | 118.0    | 16.5       | 1090     | 194/244 | 92    | 2703  |
| 2697 | I. Air | 49.3  | 8.4     | 85.0  | 116.0    | 17.5       | 1110     | 203/244 | 95    | 2899  |
| 2698 | I. Air | 50.1  | 8.4     | 85.2  | 116.0    | 17.5       | 1110     | 202/244 | 93    | 2899  |
| 2699 | I. Air | 50.3  | 8.5     | 85.1  | 116.0    | 17.5       | 1110     | 201/244 | 94    | 2913  |
| 2700 | I. Air | 49.4  | 13.4    | 50.0  | 116.0    | 6.0        | 1120     | 210/244 | 102   | 3681  |
| 2701 | I. Air | 48.5  | 8.6     | 85.0  | 116.0    | 17.5       | 1120     | 211/244 | 107   | 2956  |
| 2702 | I. Air | 49.7  | 8.4     | 85.0  | 116.0    | 17.5       | 1120     | 211/244 | 95    | 2913  |
| 2703 | I. Air | 48.5  | 8.5     | 85.2  | 116.0    | 17.5       | 1120     | 210/244 | 99    | 2927  |

Table A.4: Single Point Reservoir Conditions

| Shot | Gas    | $P_R$ | $h_R$   | $T_R$ | $\rho_R$             | $y_{N_2}$ | $y_{O_2}$ | $y_{NO}$ | $y_N$ | $y_O$ |
|------|--------|-------|---------|-------|----------------------|-----------|-----------|----------|-------|-------|
|      |        | (MPa) | (MJ/kg) | (K)   | (kg/m <sup>3</sup> ) | (-)       | (-)       | (-)      | (-)   | (-)   |
| 2695 | I. Air | 48.4  | 6.86    | 4835  | 33.3                 | 0.705     | 0.115     | 0.132    | 0.000 | 0.047 |
| 2696 | I. Air | 46.0  | 6.97    | 4879  | 31.3                 | 0.705     | 0.112     | 0.132    | 0.000 | 0.051 |
| 2697 | I. Air | 49.3  | 8.36    | 5482  | 29.0                 | 0.701     | 0.077     | 0.138    | 0.002 | 0.083 |
| 2698 | I. Air | 50.1  | 8.39    | 5495  | 29.4                 | 0.701     | 0.076     | 0.139    | 0.002 | 0.083 |
| 2699 | I. Air | 50.3  | 8.46    | 5525  | 29.3                 | 0.700     | 0.075     | 0.139    | 0.002 | 0.085 |
| 2700 | I. Air | 49.4  | 13.39   | 7424  | 19.5                 | 0.689     | 0.015     | 0.098    | 0.033 | 0.166 |
| 2701 | I. Air | 48.5  | 8.59    | 5572  | 27.9                 | 0.701     | 0.071     | 0.138    | 0.002 | 0.088 |
| 2702 | I. Air | 49.7  | 8.44    | 5515  | 29.0                 | 0.701     | 0.075     | 0.138    | 0.002 | 0.084 |
| 2703 | I. Air | 48.5  | 8.46    | 5517  | 28.3                 | 0.701     | 0.074     | 0.138    | 0.002 | 0.085 |

Table A.5: Double Point Tunnel Run Parameters - Dev 1 Air

| Shot | Gas   | $P_R$<br>(MPa) | $h_R$<br>(MJ/kg) | $P_1$<br>(kPa) | $P_{4i}$<br>(kPa) | $P_{4iAr}$<br>(kPa) | $P_{2R}$<br>(psi) | Dia<br>(mil) | $P_4$<br>(MPa) | $U_S$<br>(m/s) |
|------|-------|----------------|------------------|----------------|-------------------|---------------------|-------------------|--------------|----------------|----------------|
| 2704 | I Air | 49.5           | 8.4              | 85.2           | 116.0             | 17.5                | 1120              | 208/245      | 95             | 2913           |
| 2705 | I Air | 50.0           | 8.4              | 85.2           | 116.0             | 17.5                | 1120              | 210/245      | 96             | 2899           |
| 2706 | I Air | 49.0           | 9.2              | 84.8           | 116.0             | 11.0                | 1120              | 211/243      | 97             | 3093           |
| 2707 | I Air | 49.5           | 9.1              | 85.0           | 116.0             | 11.0                | 1120              | 210/242      | 99             | 3061           |
| 2708 | I Air | 50.3           | 7.7              | 100.0          | 116.0             | 17.5                | 1120              | 212/245      | 97             | 2804           |
| 2709 | I Air | 47.9           | 7.8              | 100.0          | 116.0             | 17.5                | 1120              | 211/243      | 108            | 2844           |
| 2710 | I Air | 45.9           | 7.1              | 115.0          | 118.0             | 16.5                | 1090              | 195/242      | 93             | 2727           |
| 2711 | I Air | 46.1           | 7.1              | 115.0          | 118.0             | 16.5                | 1090              | 197/242      | 94             | 2727           |
| 2712 | I Air | 42.8           | 7.1              | 100.0          | 118.0             | 17.5                | 1090              | 200/242      | 90             | 2715           |
| 2714 | I Air | 67.1           | 9.5              | 105.2          | 124.0             | 17.5                | 1500              | 200/242      | 107            | 3109           |
| 2715 | I Air | 68.5           | 10.5             | 87.0           | 124.0             | 17.5                | 1500              | 200/242      | 105            | 3226           |
| 2716 | I Air | 68.7           | 10.8             | 80.0           | 124.0             | 17.5                | 1500              | 200/242      | 107            | 3261           |
| 2717 | I Air | 70.0           | 10.6             | 82.0           | 124.0             | 17.5                | 1500              | 200/242      | 109            | 3226           |

Table A.6: Double Point Reservoir Conditions - Dev 1 Air

| Shot | Gas   | $P_R$<br>(MPa) | $h_R$<br>(MJ/kg) | $T_R$<br>(K) | $\rho_R$<br>(kg/m <sup>3</sup> ) | $y_{N_2}$<br>(-) | $y_{O_2}$<br>(-) | $y_{NO}$<br>(-) | $y_N$<br>(-) | $y_O$<br>(-) |
|------|-------|----------------|------------------|--------------|----------------------------------|------------------|------------------|-----------------|--------------|--------------|
| 2704 | I Air | 49.5           | 8.43             | 5510         | 28.9                             | 0.701            | 0.075            | 0.138           | 0.002        | 0.084        |
| 2705 | I Air | 50.0           | 8.39             | 5493         | 29.3                             | 0.701            | 0.076            | 0.138           | 0.002        | 0.083        |
| 2706 | I Air | 49.0           | 9.24             | 5842         | 26.6                             | 0.700            | 0.058            | 0.135           | 0.004        | 0.103        |
| 2707 | I Air | 49.5           | 9.10             | 5789         | 27.1                             | 0.700            | 0.061            | 0.136           | 0.003        | 0.100        |
| 2708 | I Air | 50.3           | 7.73             | 5217         | 31.5                             | 0.702            | 0.092            | 0.138           | 0.001        | 0.067        |
| 2709 | I Air | 47.9           | 7.82             | 5246         | 29.8                             | 0.702            | 0.090            | 0.137           | 0.001        | 0.070        |
| 2710 | I Air | 45.9           | 7.06             | 4917         | 30.9                             | 0.704            | 0.109            | 0.133           | 0.001        | 0.053        |
| 2711 | I Air | 46.1           | 7.07             | 4921         | 31.0                             | 0.704            | 0.109            | 0.133           | 0.001        | 0.053        |
| 2712 | I Air | 42.8           | 7.12             | 4930         | 28.7                             | 0.705            | 0.107            | 0.132           | 0.001        | 0.055        |
| 2714 | I Air | 67.1           | 9.50             | 6023         | 35.3                             | 0.697            | 0.056            | 0.140           | 0.004        | 0.102        |
| 2715 | I Air | 68.5           | 10.48            | 6435         | 33.1                             | 0.697            | 0.041            | 0.133           | 0.008        | 0.121        |
| 2716 | I Air | 68.7           | 10.83            | 6580         | 32.2                             | 0.697            | 0.036            | 0.130           | 0.010        | 0.127        |
| 2717 | I Air | 70.0           | 10.64            | 6507         | 33.3                             | 0.697            | 0.039            | 0.133           | 0.009        | 0.123        |

Table A.7: Double Point Tunnel Run Parameters - Dev 1 CO<sub>2</sub>

| Shot | Gas               | $P_R$<br>(MPa) | $h_R$<br>(MJ/kg) | $P_1$<br>(kPa) | $P_{4i}$<br>(kPa) | $P_{4iAr}$<br>(kPa) | $P_{2R}$<br>(psi) | Dia<br>(mil) | $P_4$<br>(MPa) | $U_S$<br>(m/s) |
|------|-------------------|----------------|------------------|----------------|-------------------|---------------------|-------------------|--------------|----------------|----------------|
| 2713 | I CO <sub>2</sub> | 35.8           | 8.3              | 60.0           | 110.0             | 11.0                | 975               | 192/242      | 81             | 3061           |

Table A.8: Double Point Reservoir Conditions - Dev 1 CO<sub>2</sub>

| Shot | Gas               | $P_R$ | $h_R$   | $T_R$ | $\rho_R$             | $y_{CO_2}$ | $y_{O_2}$ | $y_{CO}$ | $y_C$ | $y_O$ |
|------|-------------------|-------|---------|-------|----------------------|------------|-----------|----------|-------|-------|
|      |                   | (MPa) | (MJ/kg) | (K)   | (kg/m <sup>3</sup> ) | (-)        | (-)       | (-)      | (-)   | (-)   |
| 2713 | I CO <sub>2</sub> | 35.8  | 8.29    | 4157  | 36.2                 | 0.530      | 0.151     | 0.299    | 0.000 | 0.020 |

Table A.9: Double Point Tunnel Run Parameters - Dev 2 Air

| Shot | Gas     | $P_R$ | $h_R$   | $P_1$ | $P_{4i}$ | $P_{4iAr}$ | $P_{2R}$ | Dia     | $P_4$ | $U_S$ |
|------|---------|-------|---------|-------|----------|------------|----------|---------|-------|-------|
|      |         | (MPa) | (MJ/kg) | (kPa) | (kPa)    | (kPa)      | (psi)    | (mil)   | (MPa) | (m/s) |
| 2718 | I Air   | 70.1  | 10.1    | 82.0  | 124.0    | 17.5       | 1500     | 199/242 | 110   | 3125  |
| 2721 | B Air   | 58.3  | 10.4    | 60.9  | 110.0    | 17.5       | 1200     | -       | 107   | 3125  |
| 2739 | B Air   | 54.8  | 8.0     | 130.0 | 109.0    | 17.5       | 1200     | 201/242 | 101   | 2927  |
| 2740 | B Air   | 57.3  | 8.0     | 130.0 | 109.0    | 17.5       | 1200     | 202/242 | 103   | 2913  |
| 2741 | B Air   | 56.9  | 8.3     | 120.0 | 109.0    | 17.5       | 1200     | 203/242 | 101   | 2970  |
| 2742 | B Air   | 55.7  | 8.6     | 110.5 | 109.0    | 17.5       | 1210     | 203/242 | 102   | 3015  |
| 2743 | B Air   | 56.3  | 9.1     | 101.1 | 109.0    | 17.5       | 1210     | 203/242 | 105   | 3077  |
| 2744 | B Air   | 60.7  | 7.7     | 137.8 | 109.0    | 17.5       | 1210     | 203/242 | 98    | 2844  |
| 2746 | B Air   | 61.9  | 7.4     | 159.8 | 109.0    | 17.5       | 1210     | 201/244 | 100   | 2819  |
| 2752 | B Air   | 61.5  | 8.9     | 101.0 | 109.0    | 17.5       | 1210     | 202/242 | 96    | 2988  |
| 2753 | B Air   | 52.0  | 8.7     | 94.9  | 109.0    | 17.5       | 1210     | 203/244 | 92    | 2988  |
| 2755 | B Air   | 56.7  | 8.9     | 92.0  | 109.0    | 17.5       | 1210     | 203/244 | 102   | 2988  |
| 2757 | AG2 Air | 60.7  | 10.0    | 92.4  | 109.0    | 17.5       | 1210     | 203/245 | 96    | 3203  |

Table A.10: Double Point Reservoir Conditions - Dev 2 Air

| Shot | Gas     | $P_R$ | $h_R$   | $T_R$ | $\rho_R$             | $y_{N_2}$ | $y_{O_2}$ | $y_{NO}$ | $y_N$ | $y_O$ |
|------|---------|-------|---------|-------|----------------------|-----------|-----------|----------|-------|-------|
|      |         | (MPa) | (MJ/kg) | (K)   | (kg/m <sup>3</sup> ) | (-)       | (-)       | (-)      | (-)   | (-)   |
| 2718 | I Air   | 70.1  | 10.14   | 6301  | 34.8                 | 0.697     | 0.046     | 0.137    | 0.006 | 0.114 |
| 2721 | B Air   | 58.3  | 10.36   | 6344  | 28.5                 | 0.699     | 0.041     | 0.131    | 0.007 | 0.122 |
| 2739 | B Air   | 54.8  | 7.96    | 5332  | 33.5                 | 0.701     | 0.087     | 0.140    | 0.001 | 0.071 |
| 2740 | B Air   | 57.3  | 7.97    | 5346  | 34.9                 | 0.700     | 0.087     | 0.141    | 0.001 | 0.071 |
| 2741 | B Air   | 56.9  | 8.34    | 5501  | 33.4                 | 0.700     | 0.078     | 0.141    | 0.002 | 0.079 |
| 2742 | B Air   | 55.7  | 8.64    | 5623  | 31.8                 | 0.699     | 0.071     | 0.140    | 0.002 | 0.087 |
| 2743 | B Air   | 56.3  | 9.10    | 5816  | 30.8                 | 0.699     | 0.062     | 0.139    | 0.003 | 0.097 |
| 2744 | B Air   | 60.7  | 7.69    | 5232  | 38.0                 | 0.700     | 0.095     | 0.141    | 0.001 | 0.063 |
| 2746 | B Air   | 61.9  | 7.39    | 5105  | 40.0                 | 0.701     | 0.103     | 0.139    | 0.001 | 0.056 |
| 2752 | B Air   | 61.5  | 8.85    | 5731  | 34.3                 | 0.698     | 0.068     | 0.141    | 0.003 | 0.090 |
| 2753 | B Air   | 52.0  | 8.66    | 5617  | 29.7                 | 0.700     | 0.070     | 0.139    | 0.002 | 0.089 |
| 2755 | B Air   | 56.7  | 8.87    | 5722  | 31.7                 | 0.699     | 0.067     | 0.140    | 0.003 | 0.092 |
| 2757 | AG2 Air | 60.7  | 10.00   | 6207  | 30.6                 | 0.698     | 0.047     | 0.135    | 0.006 | 0.114 |

Table A.11: Double Point Tunnel Run Parameters - Dev 2 CO<sub>2</sub>

| Shot | Gas               | P <sub>R</sub><br>(MPa) | h <sub>R</sub><br>(MJ/kg) | P <sub>1</sub><br>(kPa) | P <sub>4i</sub><br>(kPa) | P <sub>4iAr</sub><br>(kPa) | P <sub>2R</sub><br>(psi) | Dia<br>(mil) | P <sub>4</sub><br>(MPa) | U <sub>S</sub><br>(m/s) |
|------|-------------------|-------------------------|---------------------------|-------------------------|--------------------------|----------------------------|--------------------------|--------------|-------------------------|-------------------------|
| 2719 | I CO <sub>2</sub> | 44.8                    | 7.7                       | 85.2                    | 120.0                    | 19.0                       | 975                      | 191/243      | 78                      | 2970                    |
| 2720 | I CO <sub>2</sub> | 59.3                    | 9.7                       | 55.0                    | 110.0                    | 17.5                       | 1200                     | 201/242      | 107                     | 3209                    |
| 2722 | I CO <sub>2</sub> | 60.3                    | 8.7                       | 66.0                    | 109.0                    | 17.5                       | 1200                     | 202/242      | 107                     | 3061                    |
| 2723 | I CO <sub>2</sub> | 54.3                    | 8.0                       | 71.0                    | 109.0                    | 17.5                       | 1200                     | 203/242      | 94                      | 2941                    |
| 2724 | I CO <sub>2</sub> | 53.2                    | 7.9                       | 75.0                    | 109.0                    | 17.5                       | 1200                     | 201/242      | 94                      | 2941                    |
| 2725 | I CO <sub>2</sub> | 57.0                    | 7.8                       | 82.0                    | 109.0                    | 17.5                       | 1200                     | 201/242      | 103                     | 2927                    |
| 2726 | I CO <sub>2</sub> | 57.8                    | 7.2                       | 95.0                    | 109.0                    | 17.5                       | 1200                     | 201/242      | 105                     | 2830                    |
| 2727 | I CO <sub>2</sub> | 57.1                    | 6.7                       | 114.7                   | 109.0                    | 17.5                       | 1200                     | 202/242      | 107                     | 2752                    |
| 2733 | I CO <sub>2</sub> | 56.6                    | 7.0                       | 135.0                   | 109.0                    | 17.5                       | 1200                     | -            | 107                     | 2857                    |
| 2734 | I CO <sub>2</sub> | 54.4                    | 6.1                       | 135.0                   | 109.0                    | 17.5                       | 1200                     | 201/242      | 105                     | 2632                    |
| 2745 | I CO <sub>2</sub> | 58.5                    | 9.7                       | 68.0                    | 109.0                    | 17.5                       | 1210                     | 202/242      | 99                      | 3261                    |
| 2747 | I CO <sub>2</sub> | 60.3                    | 9.4                       | 68.0                    | 109.0                    | 17.5                       | 1210                     | 201/244      | 100                     | 3194                    |
| 2751 | I CO <sub>2</sub> | 60.2                    | 9.0                       | 71.8                    | 109.0                    | 17.5                       | 1210                     | 202/242      | 96                      | 3144                    |
| 2754 | I CO <sub>2</sub> | 53.4                    | 9.4                       | 62.0                    | 109.0                    | 17.5                       | 1210                     | 102/244      | 96                      | 3211                    |
| 2756 | I CO <sub>2</sub> | 57.5                    | 8.7                       | 68.0                    | 109.0                    | 17.5                       | 1210                     | 203/245      | 105                     | 3079                    |

Table A.12: Double Point Reservoir Conditions - Dev 2 CO<sub>2</sub>

| Shot | Gas               | P <sub>R</sub><br>(MPa) | h <sub>R</sub><br>(MJ/kg) | T <sub>R</sub><br>(K) | ρ <sub>R</sub><br>(kg/m <sup>3</sup> ) | yCO <sub>2</sub><br>(-) | yO <sub>2</sub><br>(-) | yCO<br>(-) | yC<br>(-) | yO<br>(-) |
|------|-------------------|-------------------------|---------------------------|-----------------------|--|-------------------------|------------------------|------------|-----------|-----------|
| 2719 | I CO <sub>2</sub> | 44.8                    | 7.74                      | 4075                  | 47.5                                   | 0.587                   | 0.136                  | 0.263      | 0.000     | 0.014     |
| 2720 | I CO <sub>2</sub> | 59.3                    | 9.66                      | 4563                  | 51.8                                   | 0.433                   | 0.173                  | 0.361      | 0.000     | 0.033     |
| 2722 | I CO <sub>2</sub> | 60.3                    | 8.73                      | 4356                  | 57.5                                   | 0.510                   | 0.156                  | 0.312      | 0.000     | 0.022     |
| 2723 | I CO <sub>2</sub> | 54.3                    | 7.97                      | 4160                  | 55.9                                   | 0.573                   | 0.140                  | 0.272      | 0.000     | 0.015     |
| 2724 | I CO <sub>2</sub> | 53.2                    | 7.89                      | 4140                  | 55.3                                   | 0.579                   | 0.138                  | 0.268      | 0.000     | 0.015     |
| 2725 | I CO <sub>2</sub> | 57.0                    | 7.81                      | 4132                  | 59.6                                   | 0.589                   | 0.135                  | 0.261      | 0.000     | 0.014     |
| 2726 | I CO <sub>2</sub> | 57.8                    | 7.25                      | 4000                  | 64.1                                   | 0.641                   | 0.120                  | 0.229      | 0.000     | 0.010     |
| 2727 | I CO <sub>2</sub> | 57.1                    | 6.73                      | 3870                  | 67.0                                   | 0.688                   | 0.106                  | 0.198      | 0.000     | 0.007     |
| 2733 | I CO <sub>2</sub> | 56.6                    | 7.03                      | 3944                  | 64.3                                   | 0.660                   | 0.115                  | 0.216      | 0.000     | 0.009     |
| 2734 | I CO <sub>2</sub> | 54.4                    | 6.06                      | 3688                  | 69.0                                   | 0.749                   | 0.087                  | 0.160      | 0.000     | 0.004     |
| 2745 | I CO <sub>2</sub> | 58.5                    | 9.67                      | 4564                  | 51.0                                   | 0.431                   | 0.174                  | 0.362      | 0.000     | 0.033     |
| 2747 | I CO <sub>2</sub> | 60.3                    | 9.36                      | 4501                  | 54.1                                   | 0.457                   | 0.168                  | 0.346      | 0.000     | 0.029     |
| 2751 | I CO <sub>2</sub> | 60.2                    | 9.05                      | 4429                  | 55.6                                   | 0.483                   | 0.163                  | 0.329      | 0.000     | 0.025     |
| 2754 | I CO <sub>2</sub> | 53.4                    | 9.42                      | 4486                  | 47.8                                   | 0.448                   | 0.170                  | 0.351      | 0.000     | 0.030     |
| 2756 | I CO <sub>2</sub> | 57.5                    | 8.73                      | 4348                  | 54.8                                   | 0.508                   | 0.157                  | 0.313      | 0.000     | 0.022     |

Table A.13: Double Point Tunnel Run Parameters - Air

| Shot | Gas     | $P_R$<br>(MPa) | $h_R$<br>(MJ/kg) | $P_1$<br>(kPa) | $P_{4i}$<br>(kPa) | $P_{4iAr}$<br>(kPa) | $P_{2R}$<br>(psi) | Dia<br>(mil) | $P_4$<br>(MPa) | $U_S$<br>(m/s) |
|------|---------|----------------|------------------|----------------|-------------------|---------------------|-------------------|--------------|----------------|----------------|
| 2761 | AG2 Air | 28.2           | 5.5              | 90.1           | 50.0              | 16.5                | 500               | 136/181      | 53             | 2405           |
| 2762 | AG2 Air | 27.8           | 6.1              | 75.0           | 50.0              | 16.5                | 505               | 137/183      | 52             | 2492           |
| 2763 | AG2 Air | 27.8           | 6.6              | 60.3           | 50.0              | 16.5                | 500               | 135/183      | 51             | 2555           |
| 2764 | AG2 Air | 16.5           | 5.3              | 60.0           | 55.0              | 19.0                | 400               | 124/183      | 39             | 2374           |
| 2765 | AG2 Air | 17.5           | 6.5              | 60.0           | 55.0              | 8.0                 | 400               | 125/183      | 39             | 2693           |
| 2766 | AG2 Air | 17.0           | 7.6              | 45.1           | 55.0              | 8.0                 | 400               | 125/183      | 39             | 2873           |
| 2767 | AG2 Air | 16.6           | 9.0              | 35.0           | 55.0              | 8.0                 | 400               | 125/183      | 40             | 3128           |
| 2768 | AG2 Air | 25.2           | 9.3              | 45.0           | 50.0              | 10.0                | 500               | 138/183      | 51             | 3128           |
| 2769 | AG2 Air | 60.8           | 10.5             | 75.0           | 109.0             | 17.5                | 1210              | 202/243      | 94             | 3211           |
| 2770 | AG2 Air | 59.5           | 11.1             | 73.0           | 109.0             | 11.0                | 1210              | 200/243      | 96             | 3336           |
| 2771 | AG2 Air | 60.6           | 10.5             | 83.0           | 109.0             | 9.0                 | 1210              | 201/244      | 107            | 3264           |
| 2786 | AG2 Air | 53.6           | 10.0             | 85.0           | 109.0             | 17.5                | 1210              | 203/244      | 107            | 3228           |
| 2787 | AG2 Air | 53.6           | 10.7             | 80.0           | 109.0             | 15.0                | 1210              | 204/244      | 98             | 3336           |
| 2788 | AG2 Air | 54.7           | 13.1             | 65.0           | 109.0             | 5.0                 | 1210              | 204/244      | 99             | 3707           |
| 2789 | AG2 Air | 56.4           | 11.9             | 70.3           | 107.0             | 10.0                | 1210              | 204/244      | 99             | 3491           |
| 2790 | AG2 Air | 57.4           | 11.6             | 75.0           | 109.0             | 10.0                | 1200              | 205/244      | 99             | 3451           |

Table A.14: Double Point Reservoir Conditions - Air

| Shot | Gas     | $P_R$<br>(MPa) | $h_R$<br>(MJ/kg) | $T_R$<br>(K) | $\rho_R$<br>(kg/m <sup>3</sup> ) | $Y_{N_2}$<br>(-) | $Y_{O_2}$<br>(-) | $Y_{NO}$<br>(-) | $Y_N$<br>(-) | $Y_O$<br>(-) |
|------|---------|----------------|------------------|--------------|----------------------------------|------------------|------------------|-----------------|--------------|--------------|
| 2761 | AG2 Air | 28.2           | 5.55             | 4179         | 22.9                             | 0.717            | 0.150            | 0.107           | 0.000        | 0.026        |
| 2762 | AG2 Air | 27.8           | 6.06             | 4415         | 21.2                             | 0.713            | 0.135            | 0.116           | 0.000        | 0.036        |
| 2763 | AG2 Air | 27.8           | 6.59             | 4644         | 19.9                             | 0.710            | 0.119            | 0.123           | 0.000        | 0.049        |
| 2764 | AG2 Air | 16.5           | 5.28             | 4009         | 14.0                             | 0.721            | 0.156            | 0.098           | 0.000        | 0.025        |
| 2765 | AG2 Air | 17.5           | 6.48             | 4532         | 12.8                             | 0.713            | 0.119            | 0.116           | 0.000        | 0.052        |
| 2766 | AG2 Air | 17.0           | 7.55             | 4950         | 11.1                             | 0.710            | 0.087            | 0.121           | 0.001        | 0.082        |
| 2767 | AG2 Air | 16.6           | 9.02             | 5513         | 9.4                              | 0.710            | 0.050            | 0.114           | 0.003        | 0.122        |
| 2768 | AG2 Air | 25.2           | 9.32             | 5726         | 13.7                             | 0.707            | 0.049            | 0.120           | 0.004        | 0.120        |
| 2769 | AG2 Air | 60.8           | 10.46            | 6397         | 29.5                             | 0.698            | 0.040            | 0.131           | 0.008        | 0.123        |
| 2770 | AG2 Air | 59.5           | 11.10            | 6649         | 27.4                             | 0.698            | 0.032            | 0.124           | 0.011        | 0.135        |
| 2771 | AG2 Air | 60.6           | 10.51            | 6415         | 29.3                             | 0.698            | 0.039            | 0.130           | 0.008        | 0.124        |
| 2786 | AG2 Air | 53.6           | 10.04            | 6194         | 27.0                             | 0.700            | 0.045            | 0.131           | 0.006        | 0.118        |
| 2787 | AG2 Air | 53.6           | 10.69            | 6457         | 25.6                             | 0.699            | 0.036            | 0.126           | 0.009        | 0.130        |
| 2788 | AG2 Air | 54.7           | 13.14            | 7374         | 21.9                             | 0.690            | 0.016            | 0.103           | 0.029        | 0.162        |
| 2789 | AG2 Air | 56.4           | 11.87            | 6931         | 24.5                             | 0.696            | 0.024            | 0.115           | 0.017        | 0.147        |
| 2790 | AG2 Air | 57.4           | 11.56            | 6817         | 25.6                             | 0.697            | 0.027            | 0.119           | 0.014        | 0.142        |

Table A.15: Double Point Tunnel Run Parameters - N<sub>2</sub>

| Shot | Gas                | P <sub>R</sub><br>(MPa) | h <sub>R</sub><br>(MJ/kg) | P <sub>1</sub><br>(kPa) | P <sub>4i</sub><br>(kPa) | P <sub>4iAr</sub><br>(kPa) | P <sub>2R</sub><br>(psi) | Dia<br>(mil) | P <sub>4</sub><br>(MPa) | U <sub>S</sub><br>(m/s) |
|------|--------------------|-------------------------|---------------------------|-------------------------|--------------------------|----------------------------|--------------------------|--------------|-------------------------|-------------------------|
| 2772 | AG1 N <sub>2</sub> | 16.7                    | 8.0                       | 45.0                    | 55.0                     | 8.0                        | 400                      | 125/183      | 36                      | 2958                    |
| 2773 | AG1 N <sub>2</sub> | 16.7                    | 9.0                       | 40.0                    | 55.0                     | 6.0                        | 400                      | 125/183      | 37                      | 3144                    |
| 2774 | AG1 N <sub>2</sub> | 16.7                    | 10.1                      | 35.0                    | 55.0                     | 5.0                        | 405                      | 126/183      | 39                      | 3336                    |
| 2775 | AG1 N <sub>2</sub> | 17.4                    | 7.3                       | 52.0                    | 55.0                     | 9.0                        | 400                      | 126/283      | 39                      | 2819                    |
| 2776 | AG1 N <sub>2</sub> | 45.9                    | 7.2                       | 130.0                   | 110.0                    | 16.5                       | 950                      | 190/245      | 76                      | 2767                    |
| 2777 | AG1 N <sub>2</sub> | 37.7                    | 8.8                       | 85.0                    | 110.0                    | 16.5                       | 965                      | 190/244      | 80                      | 3079                    |
| 2778 | AG1 N <sub>2</sub> | 41.4                    | 10.7                      | 72.0                    | 110.0                    | 10.0                       | 955                      | 189/244      | 79                      | 3374                    |
| 2779 | AG1 N <sub>2</sub> | 42.3                    | 12.0                      | 60.0                    | 110.0                    | 10.0                       | 970                      | 189/244      | 79                      | 3532                    |
| 2780 | AG1 N <sub>2</sub> | 44.5                    | 13.6                      | 50.0                    | 110.0                    | 10.0                       | 1025                     | 188/244      | 75                      | 3730                    |
| 2781 | AG1 N <sub>2</sub> | 43.4                    | 15.0                      | 50.0                    | 110.0                    | 0.0                        | 1025                     | 189/244      | 80                      | 3977                    |
| 2782 | AG1 N <sub>2</sub> | 53.9                    | 14.8                      | 50.0                    | 110.0                    | 10.0                       | 1210                     | 201/243      | 93                      | 3849                    |
| 2783 | AG1 N <sub>2</sub> | 53.3                    | 15.9                      | 50.0                    | 110.0                    | 5.0                        | 1205                     | 203/244      | 99                      | 4030                    |
| 2784 | AG1 N <sub>2</sub> | 60.4                    | 16.1                      | 50.0                    | 124.0                    | 5.0                        | 1500                     | 204/244      | 100                     | 4003                    |
| 2785 | AG1 N <sub>2</sub> | 61.8                    | 16.2                      | 50.0                    | 124.0                    | 5.1                        | 1500                     | 211/244      | 107                     | 4003                    |

Table A.16: Double Point Reservoir Conditions - N<sub>2</sub>

| Shot | Gas                | P <sub>R</sub><br>(MPa) | h <sub>R</sub><br>(MJ/kg) | T <sub>R</sub><br>(K) | ρ <sub>R</sub><br>(kg/m <sup>3</sup> ) | Y <sub>N<sub>2</sub></sub><br>(-) | Y <sub>N</sub><br>(-) |
|------|--------------------|-------------------------|---------------------------|-----------------------|--|-----------------------------------|-----------------------|
| 2772 | AG1 N <sub>2</sub> | 16.7                    | 7.99                      | 6159                  | 9.0                                    | 0.988                             | 0.012                 |
| 2773 | AG1 N <sub>2</sub> | 16.7                    | 8.99                      | 6601                  | 8.3                                    | 0.977                             | 0.023                 |
| 2774 | AG1 N <sub>2</sub> | 16.7                    | 10.13                     | 7006                  | 7.7                                    | 0.961                             | 0.039                 |
| 2775 | AG1 N <sub>2</sub> | 17.4                    | 7.27                      | 5778                  | 10.1                                   | 0.994                             | 0.006                 |
| 2776 | AG1 N <sub>2</sub> | 45.9                    | 7.17                      | 5769                  | 26.7                                   | 0.996                             | 0.004                 |
| 2777 | AG1 N <sub>2</sub> | 37.7                    | 8.85                      | 6658                  | 18.8                                   | 0.984                             | 0.016                 |
| 2778 | AG1 N <sub>2</sub> | 41.4                    | 10.73                     | 7411                  | 18.1                                   | 0.961                             | 0.039                 |
| 2779 | AG1 N <sub>2</sub> | 42.3                    | 12.00                     | 7800                  | 17.3                                   | 0.941                             | 0.059                 |
| 2780 | AG1 N <sub>2</sub> | 44.5                    | 13.64                     | 8230                  | 16.8                                   | 0.914                             | 0.086                 |
| 2781 | AG1 N <sub>2</sub> | 43.4                    | 14.98                     | 8506                  | 15.5                                   | 0.889                             | 0.111                 |
| 2782 | AG1 N <sub>2</sub> | 53.9                    | 14.84                     | 8565                  | 19.2                                   | 0.895                             | 0.105                 |
| 2783 | AG1 N <sub>2</sub> | 53.3                    | 15.89                     | 8769                  | 18.2                                   | 0.876                             | 0.124                 |
| 2784 | AG1 N <sub>2</sub> | 60.4                    | 16.09                     | 8862                  | 20.4                                   | 0.874                             | 0.126                 |
| 2785 | AG1 N <sub>2</sub> | 61.8                    | 16.16                     | 8885                  | 20.8                                   | 0.873                             | 0.127                 |

Table A.17: Double Point Tunnel Run Parameters - CO<sub>2</sub> - AR:100

| Shot | Gas                 | P <sub>R</sub><br>(MPa) | h <sub>R</sub><br>(MJ/kg) | P <sub>1</sub><br>(kPa) | P <sub>4i</sub><br>(kPa) | P <sub>4iAr</sub><br>(kPa) | P <sub>2R</sub><br>(psi) | Dia<br>(mil) | P <sub>4</sub><br>(MPa) | U <sub>S</sub><br>(m/s) |
|------|---------------------|-------------------------|---------------------------|-------------------------|--------------------------|----------------------------|--------------------------|--------------|-------------------------|-------------------------|
| 2791 | SFE CO <sub>2</sub> | 17.6                    | 8.8                       | 22.0                    | 50.0                     | 7.0                        | 400                      | 127/183      | 40                      | 3111                    |
| 2792 | SFE CO <sub>2</sub> | 18.3                    | 6.8                       | 32.0                    | 50.0                     | 7.0                        | 405                      | 118/182      | 40                      | 2742                    |
| 2793 | SFE CO <sub>2</sub> | 22.7                    | 4.6                       | 50.0                    | 77.0                     | 14.0                       | 540                      | 115/183      | 34                      | 2224                    |
| 2794 | SFE CO <sub>2</sub> | 23.2                    | 5.3                       | 47.0                    | 77.0                     | 11.5                       | 545                      | 117/183      | 35                      | 2392                    |
| 2795 | SFE CO <sub>2</sub> | 22.6                    | 5.5                       | 41.0                    | 77.0                     | 11.5                       | 545                      | 116/182      | 34                      | 2431                    |
| 2796 | SFE CO <sub>2</sub> | 23.1                    | 5.3                       | 47.0                    | 77.0                     | 11.5                       | 545                      | 118/183      | 35                      | 2402                    |

Table A.18: Double Point Reservoir Conditions - CO<sub>2</sub> - AR:100

| Shot | Gas                 | P <sub>R</sub><br>(MPa) | h <sub>R</sub><br>(MJ/kg) | T <sub>R</sub><br>(K) | ρ <sub>R</sub><br>(kg/m <sup>3</sup> ) | y <sub>CO<sub>2</sub></sub><br>(-) | y <sub>O<sub>2</sub></sub><br>(-) | y <sub>CO</sub><br>(-) | y <sub>C</sub><br>(-) | y <sub>O</sub><br>(-) |
|------|---------------------|-------------------------|---------------------------|-----------------------|--|------------------------------------|-----------------------------------|------------------------|-----------------------|-----------------------|
| 2791 | SFE CO <sub>2</sub> | 17.6                    | 8.83                      | 4134                  | 17.2                                   | 0.461                              | 0.167                             | 0.343                  | 0.000                 | 0.029                 |
| 2792 | SFE CO <sub>2</sub> | 18.3                    | 6.81                      | 3717                  | 21.9                                   | 0.648                              | 0.118                             | 0.224                  | 0.000                 | 0.010                 |
| 2793 | SFE CO <sub>2</sub> | 22.7                    | 4.61                      | 3179                  | 35.3                                   | 0.860                              | 0.049                             | 0.089                  | 0.000                 | 0.001                 |
| 2794 | SFE CO <sub>2</sub> | 23.2                    | 5.28                      | 3375                  | 33.0                                   | 0.801                              | 0.070                             | 0.127                  | 0.000                 | 0.003                 |
| 2795 | SFE CO <sub>2</sub> | 22.6                    | 5.50                      | 3433                  | 31.2                                   | 0.779                              | 0.077                             | 0.141                  | 0.000                 | 0.003                 |
| 2796 | SFE CO <sub>2</sub> | 23.1                    | 5.31                      | 3384                  | 32.7                                   | 0.797                              | 0.071                             | 0.129                  | 0.000                 | 0.003                 |

## A.2 Nozzle Exit Conditions

Table A.19: Tunnel Noise Nozzle Exit Conditions

| Shot | $U_X$ | $\rho_X$             | $P_X$ | $T_X$ | $T_{vX}$ | $M_X$ | $y_{N_2}$ | $y_{O_2}$ | $y_{NO}$ | $y_N$ | $y_O$ |
|------|-------|----------------------|-------|-------|----------|-------|-----------|-----------|----------|-------|-------|
|      | (m/s) | (kg/m <sup>3</sup> ) | (kPa) | (K)   | (K)      | (-)   | (-)       | (-)       | (-)      | (-)   | (-)   |
| 2684 | 3677  | 0.059                | 18.9  | 1113  | 1116     | 5.47  | 0.731     | 0.187     | 0.076    | 0.000 | 0.005 |
| 2685 | 3753  | 0.059                | 20.3  | 1181  | 1183     | 5.42  | 0.732     | 0.187     | 0.075    | 0.000 | 0.006 |
| 2686 | 4629  | 0.041                | 24.6  | 2014  | 2016     | 5.00  | 0.736     | 0.148     | 0.067    | 0.000 | 0.049 |
| 2687 | 4891  | 0.036                | 25.0  | 2248  | 2250     | 4.94  | 0.738     | 0.128     | 0.062    | 0.000 | 0.072 |
| 2688 | 5047  | 0.036                | 27.1  | 2405  | 2406     | 4.90  | 0.740     | 0.119     | 0.058    | 0.000 | 0.083 |
| 2689 | 5136  | 0.035                | 27.1  | 2481  | 2482     | 4.89  | 0.741     | 0.111     | 0.055    | 0.000 | 0.093 |
| 2690 | 5055  | 0.035                | 26.2  | 2402  | 2404     | 4.90  | 0.740     | 0.116     | 0.058    | 0.000 | 0.086 |
| 2691 | 3114  | 0.071                | 14.1  | 683   | 694      | 5.93  | 0.733     | 0.193     | 0.074    | 0.000 | 0.001 |
| 2692 | 3053  | 0.075                | 14.0  | 646   | 657      | 5.98  | 0.733     | 0.194     | 0.072    | 0.000 | 0.001 |
| 2693 | 3790  | 0.059                | 20.9  | 1216  | 1218     | 5.39  | 0.732     | 0.186     | 0.074    | 0.000 | 0.007 |
| 2694 | 5118  | 0.034                | 25.8  | 2451  | 2453     | 4.90  | 0.741     | 0.110     | 0.056    | 0.000 | 0.093 |

Table A.20: Single Point Nozzle Exit Conditions

| Shot | $U_X$ | $\rho_X$             | $P_X$ | $T_X$ | $T_{vX}$ | $M_X$ | $y_{N_2}$ | $y_{O_2}$ | $y_{NO}$ | $y_N$ | $y_O$ |
|------|-------|----------------------|-------|-------|----------|-------|-----------|-----------|----------|-------|-------|
|      | (m/s) | (kg/m <sup>3</sup> ) | (kPa) | (K)   | (K)      | (-)   | (-)       | (-)       | (-)      | (-)   | (-)   |
| 2695 | 3416  | 0.081                | 22.4  | 955   | 950      | 5.50  | 0.731     | 0.189     | 0.078    | 0.000 | 0.002 |
| 2696 | 3440  | 0.076                | 21.5  | 977   | 975      | 5.47  | 0.731     | 0.189     | 0.078    | 0.000 | 0.002 |
| 2697 | 3724  | 0.071                | 25.5  | 1236  | 1243     | 5.26  | 0.732     | 0.187     | 0.075    | 0.000 | 0.006 |
| 2698 | 3729  | 0.072                | 26.0  | 1241  | 1248     | 5.25  | 0.732     | 0.187     | 0.075    | 0.000 | 0.006 |
| 2699 | 3742  | 0.073                | 26.5  | 1257  | 1264     | 5.24  | 0.732     | 0.187     | 0.075    | 0.000 | 0.006 |
| 2700 | 4529  | 0.049                | 29.8  | 2028  | 2040     | 4.89  | 0.735     | 0.152     | 0.068    | 0.000 | 0.045 |
| 2701 | 3765  | 0.069                | 25.5  | 1278  | 1287     | 5.22  | 0.732     | 0.186     | 0.074    | 0.000 | 0.007 |
| 2702 | 3739  | 0.071                | 25.7  | 1249  | 1256     | 5.25  | 0.732     | 0.187     | 0.075    | 0.000 | 0.006 |
| 2703 | 3741  | 0.069                | 25.2  | 1253  | 1260     | 5.24  | 0.732     | 0.186     | 0.075    | 0.000 | 0.007 |

Table A.21: Double Point Nozzle Exit Conditions - Dev 1 Air

| Shot | $U_X$ | $\rho_X$             | $P_X$ | $T_X$ | $T_{vX}$ | $M_X$ | $y_{N_2}$ | $y_{O_2}$ | $y_{NO}$ | $y_N$ | $y_O$ |
|------|-------|----------------------|-------|-------|----------|-------|-----------|-----------|----------|-------|-------|
|      | (m/s) | (kg/m <sup>3</sup> ) | (kPa) | (K)   | (K)      | (-)   | (-)       | (-)       | (-)      | (-)   | (-)   |
| 2704 | 3737  | 0.071                | 25.7  | 1249  | 1256     | 5.25  | 0.732     | 0.187     | 0.075    | 0.000 | 0.006 |
| 2705 | 3728  | 0.072                | 26.0  | 1242  | 1248     | 5.25  | 0.732     | 0.187     | 0.075    | 0.000 | 0.006 |
| 2706 | 3883  | 0.066                | 26.6  | 1394  | 1404     | 5.15  | 0.733     | 0.184     | 0.073    | 0.000 | 0.010 |
| 2707 | 3859  | 0.067                | 26.9  | 1373  | 1382     | 5.16  | 0.733     | 0.184     | 0.073    | 0.000 | 0.010 |
| 2708 | 3599  | 0.077                | 25.1  | 1118  | 1121     | 5.35  | 0.731     | 0.188     | 0.077    | 0.000 | 0.004 |
| 2709 | 3616  | 0.073                | 23.9  | 1134  | 1138     | 5.33  | 0.731     | 0.188     | 0.077    | 0.000 | 0.004 |
| 2710 | 3459  | 0.075                | 21.7  | 994   | 992      | 5.46  | 0.731     | 0.189     | 0.078    | 0.000 | 0.002 |
| 2711 | 3461  | 0.076                | 21.8  | 995   | 993      | 5.46  | 0.731     | 0.189     | 0.078    | 0.000 | 0.002 |
| 2712 | 3468  | 0.070                | 20.3  | 1005  | 1003     | 5.44  | 0.731     | 0.188     | 0.078    | 0.000 | 0.003 |
| 2714 | 3946  | 0.087                | 36.3  | 1445  | 1454     | 5.14  | 0.733     | 0.186     | 0.073    | 0.000 | 0.008 |
| 2715 | 4112  | 0.082                | 38.6  | 1619  | 1629     | 5.05  | 0.733     | 0.181     | 0.073    | 0.000 | 0.013 |
| 2716 | 4170  | 0.080                | 39.2  | 1680  | 1690     | 5.02  | 0.733     | 0.179     | 0.073    | 0.000 | 0.015 |
| 2717 | 4140  | 0.082                | 39.7  | 1648  | 1658     | 5.04  | 0.733     | 0.180     | 0.073    | 0.000 | 0.014 |

Table A.22: Double Point Nozzle Exit Conditions - Dev 1 CO<sub>2</sub>

| Shot | $U_X$ | $\rho_X$             | $P_X$ | $T_X$ | $T_{vX}$ | $M_X$ | $y_{CO_2}$ | $y_{O_2}$ | $y_{CO}$ | $y_C$ | $y_O$ |
|------|-------|----------------------|-------|-------|----------|-------|------------|-----------|----------|-------|-------|
|      | (m/s) | (kg/m <sup>3</sup> ) | (kPa) | (K)   | (K)      | (-)   | (-)        | (-)       | (-)      | (-)   | (-)   |
| 2713 | 3056  | 0.080                | 30.1  | 1737  | 1737     | 4.21  | 0.717      | 0.100     | 0.180    | 0.000 | 0.002 |

Table A.23: Double Point Nozzle Exit Conditions - Dev 2 Air

| Shot | $U_X$ | $\rho_X$             | $P_X$ | $T_X$ | $T_{vX}$ | $M_X$ | $y_{N_2}$ | $y_{O_2}$ | $y_{NO}$ | $y_N$ | $y_O$ |
|------|-------|----------------------|-------|-------|----------|-------|-----------|-----------|----------|-------|-------|
|      | (m/s) | (kg/m <sup>3</sup> ) | (kPa) | (K)   | (K)      | (-)   | (-)       | (-)       | (-)      | (-)   | (-)   |
| 2718 | 4057  | 0.086                | 39.3  | 1563  | 1574     | 5.08  | 0.733     | 0.183     | 0.073    | 0.000 | 0.011 |
| 2721 | 4082  | 0.071                | 33.0  | 1595  | 1605     | 5.05  | 0.733     | 0.179     | 0.073    | 0.000 | 0.015 |
| 2739 | 3650  | 0.082                | 27.5  | 1159  | 1164     | 5.33  | 0.731     | 0.188     | 0.076    | 0.000 | 0.004 |
| 2740 | 3654  | 0.086                | 29.0  | 1164  | 1169     | 5.32  | 0.731     | 0.188     | 0.076    | 0.000 | 0.004 |
| 2741 | 3725  | 0.083                | 29.7  | 1236  | 1242     | 5.26  | 0.732     | 0.188     | 0.075    | 0.000 | 0.005 |
| 2742 | 3781  | 0.079                | 29.4  | 1291  | 1296     | 5.22  | 0.733     | 0.187     | 0.074    | 0.000 | 0.006 |
| 2743 | 3865  | 0.076                | 30.5  | 1375  | 1383     | 5.17  | 0.733     | 0.186     | 0.073    | 0.000 | 0.008 |
| 2744 | 3597  | 0.094                | 30.1  | 1109  | 1111     | 5.37  | 0.731     | 0.189     | 0.077    | 0.000 | 0.003 |
| 2746 | 3537  | 0.098                | 30.0  | 1051  | 1052     | 5.43  | 0.731     | 0.189     | 0.078    | 0.000 | 0.002 |
| 2752 | 3824  | 0.085                | 32.7  | 1329  | 1337     | 5.20  | 0.733     | 0.187     | 0.073    | 0.000 | 0.006 |
| 2753 | 3781  | 0.074                | 27.7  | 1296  | 1304     | 5.21  | 0.733     | 0.186     | 0.074    | 0.000 | 0.007 |
| 2755 | 3824  | 0.078                | 30.3  | 1333  | 1341     | 5.19  | 0.733     | 0.187     | 0.073    | 0.000 | 0.007 |
| 2757 | 4024  | 0.077                | 34.3  | 1539  | 1548     | 5.07  | 0.733     | 0.182     | 0.073    | 0.000 | 0.012 |

Table A.24: Double Point Nozzle Exit Conditions - Dev 2 CO<sub>2</sub>

| Shot | $U_X$<br>(m/s) | $\rho_X$<br>(kg/m <sup>3</sup> ) | $P_X$<br>(kPa) | $T_X$<br>(K) | $T_{vX}$<br>(K) | $M_X$<br>(-) | $y_{CO_2}$<br>(-) | $y_{O_2}$<br>(-) | $y_{CO}$<br>(-) | $y_C$<br>(-) | $y_O$<br>(-) |
|------|----------------|----------------------------------|----------------|--------------|-----------------|--------------|-------------------|------------------|-----------------|--------------|--------------|
| 2719 | 2999           | 0.106                            | 38.4           | 1718         | 1718            | 4.20         | 0.763             | 0.085            | 0.151           | 0.000        | 0.001        |
| 2720 | 3283           | 0.120                            | 53.4           | 2013         | 2013            | 4.16         | 0.673             | 0.115            | 0.208           | 0.000        | 0.004        |
| 2722 | 3161           | 0.132                            | 54.0           | 1904         | 1904            | 4.17         | 0.726             | 0.098            | 0.174           | 0.000        | 0.002        |
| 2723 | 3047           | 0.126                            | 47.7           | 1785         | 1784            | 4.19         | 0.762             | 0.085            | 0.151           | 0.000        | 0.001        |
| 2724 | 3035           | 0.124                            | 46.6           | 1772         | 1771            | 4.19         | 0.765             | 0.084            | 0.149           | 0.000        | 0.001        |
| 2725 | 3033           | 0.135                            | 50.2           | 1773         | 1773            | 4.19         | 0.774             | 0.081            | 0.144           | 0.000        | 0.001        |
| 2726 | 2949           | 0.144                            | 50.5           | 1696         | 1695            | 4.20         | 0.806             | 0.070            | 0.124           | 0.000        | 0.001        |
| 2727 | 2866           | 0.149                            | 49.3           | 1611         | 1611            | 4.22         | 0.831             | 0.061            | 0.108           | 0.000        | 0.000        |
| 2733 | 2915           | 0.144                            | 49.2           | 1659         | 1659            | 4.21         | 0.816             | 0.067            | 0.117           | 0.000        | 0.000        |
| 2734 | 2753           | 0.153                            | 46.0           | 1482         | 1482            | 4.25         | 0.858             | 0.052            | 0.090           | 0.000        | 0.000        |
| 2745 | 3285           | 0.118                            | 52.5           | 2011         | 2011            | 4.16         | 0.671             | 0.116            | 0.210           | 0.000        | 0.004        |
| 2747 | 3244           | 0.125                            | 54.4           | 1983         | 1983            | 4.16         | 0.690             | 0.110            | 0.197           | 0.000        | 0.003        |
| 2751 | 3202           | 0.128                            | 54.1           | 1943         | 1943            | 4.16         | 0.708             | 0.104            | 0.186           | 0.000        | 0.002        |
| 2754 | 3241           | 0.110                            | 47.4           | 1958         | 1958            | 4.17         | 0.678             | 0.113            | 0.205           | 0.000        | 0.004        |
| 2756 | 3156           | 0.125                            | 51.2           | 1894         | 1894            | 4.17         | 0.722             | 0.099            | 0.177           | 0.000        | 0.002        |

Table A.25: Double Point Nozzle Exit Conditions - Air

| Shot | $U_X$<br>(m/s) | $\rho_X$<br>(kg/m <sup>3</sup> ) | $P_X$<br>(kPa) | $T_X$<br>(K) | $T_{vX}$<br>(K) | $M_X$<br>(-) | $y_{N_2}$<br>(-) | $y_{O_2}$<br>(-) | $y_{NO}$<br>(-) | $y_N$<br>(-) | $y_O$<br>(-) |
|------|----------------|----------------------------------|----------------|--------------|-----------------|--------------|------------------|------------------|-----------------|--------------|--------------|
| 2761 | 3111           | 0.048                            | 9.5            | 686          | 720             | 5.91         | 0.732            | 0.192            | 0.075           | 0.000        | 0.001        |
| 2762 | 3227           | 0.048                            | 11.2           | 800          | 803             | 5.67         | 0.731            | 0.190            | 0.077           | 0.000        | 0.002        |
| 2763 | 3344           | 0.047                            | 12.4           | 906          | 902             | 5.52         | 0.731            | 0.188            | 0.078           | 0.000        | 0.003        |
| 2764 | 3035           | 0.029                            | 5.4            | 639          | 725             | 5.97         | 0.733            | 0.191            | 0.074           | 0.000        | 0.002        |
| 2765 | 3304           | 0.030                            | 7.8            | 881          | 891             | 5.53         | 0.731            | 0.185            | 0.078           | 0.000        | 0.006        |
| 2766 | 3525           | 0.027                            | 8.3            | 1066         | 1075            | 5.34         | 0.731            | 0.180            | 0.078           | 0.000        | 0.012        |
| 2767 | 3792           | 0.023                            | 8.9            | 1293         | 1305            | 5.18         | 0.733            | 0.168            | 0.073           | 0.000        | 0.026        |
| 2768 | 3864           | 0.034                            | 13.9           | 1379         | 1388            | 5.12         | 0.733            | 0.173            | 0.073           | 0.000        | 0.021        |
| 2769 | 4101           | 0.073                            | 34.6           | 1615         | 1625            | 5.04         | 0.733            | 0.179            | 0.073           | 0.000        | 0.015        |
| 2770 | 4202           | 0.069                            | 34.7           | 1722         | 1732            | 4.99         | 0.733            | 0.175            | 0.072           | 0.000        | 0.019        |
| 2771 | 4108           | 0.073                            | 34.7           | 1625         | 1634            | 5.03         | 0.733            | 0.179            | 0.073           | 0.000        | 0.015        |
| 2786 | 4026           | 0.067                            | 29.9           | 1535         | 1547            | 5.08         | 0.733            | 0.180            | 0.073           | 0.000        | 0.014        |
| 2787 | 4132           | 0.064                            | 30.6           | 1643         | 1655            | 5.02         | 0.733            | 0.176            | 0.073           | 0.000        | 0.018        |
| 2788 | 4501           | 0.055                            | 32.9           | 2012         | 2022            | 4.89         | 0.735            | 0.157            | 0.069           | 0.000        | 0.039        |
| 2789 | 4316           | 0.062                            | 33.6           | 1838         | 1849            | 4.94         | 0.734            | 0.168            | 0.071           | 0.000        | 0.027        |
| 2790 | 4271           | 0.064                            | 33.7           | 1789         | 1800            | 4.96         | 0.734            | 0.171            | 0.072           | 0.000        | 0.024        |

Table A.26: Double Point Nozzle Exit Conditions - N<sub>2</sub>

| Shot | U <sub>X</sub> | ρ <sub>X</sub>       | P <sub>X</sub> | T <sub>X</sub> | T <sub>vX</sub> | M <sub>X</sub> | y <sub>N<sub>2</sub></sub> | y <sub>N</sub> |
|------|----------------|----------------------|----------------|----------------|-----------------|----------------|----------------------------|----------------|
|      | (m/s)          | (kg/m <sup>3</sup> ) | (kPa)          | (K)            | (K)             | (-)            | (-)                        | (-)            |
| 2772 | 3725           | 0.016                | 3.2            | 686            | 3038            | 6.97           | 0.998                      | 0.002          |
| 2773 | 3923           | 0.015                | 3.6            | 804            | 3163            | 6.78           | 0.996                      | 0.004          |
| 2774 | 4121           | 0.015                | 4.3            | 952            | 3331            | 6.53           | 0.993                      | 0.007          |
| 2775 | 3568           | 0.017                | 3.1            | 609            | 2948            | 7.10           | 0.999                      | 0.001          |
| 2776 | 3582           | 0.044                | 8.2            | 617            | 2583            | 7.08           | 1.000                      | 0.000          |
| 2777 | 3928           | 0.034                | 8.2            | 813            | 2897            | 6.76           | 0.999                      | 0.001          |
| 2778 | 4264           | 0.038                | 12.8           | 1121           | 3113            | 6.24           | 0.997                      | 0.003          |
| 2779 | 4463           | 0.039                | 15.8           | 1347           | 3246            | 5.95           | 0.995                      | 0.005          |
| 2780 | 4703           | 0.039                | 19.0           | 1628           | 3388            | 5.69           | 0.992                      | 0.008          |
| 2781 | 4875           | 0.036                | 20.0           | 1846           | 3503            | 5.52           | 0.987                      | 0.013          |
| 2782 | 4874           | 0.045                | 24.9           | 1855           | 3410            | 5.52           | 0.990                      | 0.010          |
| 2783 | 5001           | 0.042                | 25.7           | 2027           | 3479            | 5.40           | 0.986                      | 0.014          |
| 2784 | 5037           | 0.046                | 28.9           | 2070           | 3439            | 5.39           | 0.987                      | 0.013          |
| 2785 | 5047           | 0.047                | 29.7           | 2086           | 3433            | 5.38           | 0.987                      | 0.013          |

Table A.27: Double Point Nozzle Exit Conditions - CO<sub>2</sub>

| Shot | U <sub>X</sub> | ρ <sub>X</sub>       | P <sub>X</sub> | T <sub>X</sub> | T <sub>vX</sub> | M <sub>X</sub> | y <sub>CO<sub>2</sub></sub> | y <sub>O<sub>2</sub></sub> | y <sub>CO</sub> | y <sub>C</sub> | y <sub>O</sub> |
|------|----------------|----------------------|----------------|----------------|-----------------|----------------|-----------------------------|----------------------------|-----------------|----------------|----------------|
|      | (m/s)          | (kg/m <sup>3</sup> ) | (kPa)          | (K)            | (K)             | (-)            | (-)                         | (-)                        | (-)             | (-)            | (-)            |
| 2791 | 3094           | 0.038                | 14.1           | 1624           | 1627            | 4.32           | 0.632                       | 0.128                      | 0.234           | 0.000          | 0.006          |
| 2792 | 2789           | 0.049                | 14.7           | 1422           | 1425            | 4.29           | 0.758                       | 0.087                      | 0.154           | 0.000          | 0.001          |
| 2793 | 2437           | 0.079                | 18.4           | 1166           | 1168            | 4.28           | 0.898                       | 0.037                      | 0.065           | 0.000          | 0.000          |
| 2794 | 2552           | 0.073                | 18.7           | 1261           | 1263            | 4.27           | 0.861                       | 0.050                      | 0.088           | 0.000          | 0.000          |
| 2795 | 2589           | 0.069                | 18.1           | 1288           | 1290            | 4.28           | 0.847                       | 0.055                      | 0.097           | 0.000          | 0.000          |
| 2796 | 2558           | 0.073                | 18.6           | 1265           | 1267            | 4.27           | 0.859                       | 0.051                      | 0.090           | 0.000          | 0.000          |

### A.3 Edge Conditions

Table A.28: Single Point Edge Conditions

| Shot | $U_E$ | $\rho_E$             | $P_E$ | $T_E$ | $T_{vE}$ | $M_E$ | $Re_E^{Unit}$ | $y_{N_2}$ | $y_{O_2}$ | $y_{NO}$ | $y_N$ | $y_O$ |
|------|-------|----------------------|-------|-------|----------|-------|---------------|-----------|-----------|----------|-------|-------|
|      | (m/s) | (kg/m <sup>3</sup> ) | (kPa) | (K)   | (K)      | (-)   | (1/m)         | (-)       | (-)       | (-)      | (-)   | (-)   |
| 2695 | 3358  | 0.102                | 32.9  | 1119  | 991      | 4.99  | 7.44          | 0.731     | 0.189     | 0.078    | 0.000 | 0.002 |
| 2696 | 3382  | 0.096                | 31.5  | 1143  | 1015     | 4.97  | 6.96          | 0.731     | 0.189     | 0.078    | 0.000 | 0.002 |
| 2697 | 3661  | 0.089                | 36.7  | 1425  | 1323     | 4.81  | 6.15          | 0.732     | 0.187     | 0.075    | 0.000 | 0.006 |
| 2698 | 3667  | 0.090                | 37.4  | 1430  | 1330     | 4.81  | 6.24          | 0.732     | 0.187     | 0.075    | 0.000 | 0.006 |
| 2699 | 3679  | 0.091                | 38.0  | 1447  | 1349     | 4.80  | 6.26          | 0.732     | 0.187     | 0.075    | 0.000 | 0.006 |
| 2700 | 4452  | 0.060                | 41.9  | 2348  | 2300     | 4.48  | 3.59          | 0.737     | 0.159     | 0.064    | 0.000 | 0.039 |
| 2701 | 3702  | 0.086                | 36.6  | 1472  | 1373     | 4.79  | 5.92          | 0.732     | 0.187     | 0.074    | 0.000 | 0.007 |
| 2702 | 3676  | 0.089                | 36.9  | 1439  | 1339     | 4.81  | 6.13          | 0.732     | 0.187     | 0.075    | 0.000 | 0.006 |
| 2703 | 3679  | 0.087                | 36.2  | 1442  | 1342     | 4.81  | 5.99          | 0.732     | 0.187     | 0.075    | 0.000 | 0.006 |

Table A.29: Double Point Edge Conditions - Dev 1 Air

| Shot | $U_E$ | $\rho_E$             | $P_E$ | $T_E$ | $T_{vE}$ | $M_E$ | $Re_E^{Unit}$ | $y_{N_2}$ | $y_{O_2}$ | $y_{NO}$ | $y_N$ | $y_O$ |
|------|-------|----------------------|-------|-------|----------|-------|---------------|-----------|-----------|----------|-------|-------|
|      | (m/s) | (kg/m <sup>3</sup> ) | (kPa) | (K)   | (K)      | (-)   | (1/m)         | (-)       | (-)       | (-)      | (-)   | (-)   |
| 2704 | 3673  | 0.089                | 37.0  | 1439  | 1338     | 4.81  | 6.13          | 0.732     | 0.187     | 0.075    | 0.000 | 0.006 |
| 2705 | 3665  | 0.090                | 37.4  | 1430  | 1330     | 4.81  | 6.25          | 0.732     | 0.187     | 0.075    | 0.000 | 0.006 |
| 2706 | 3818  | 0.082                | 37.9  | 1599  | 1512     | 4.73  | 5.56          | 0.733     | 0.185     | 0.073    | 0.000 | 0.010 |
| 2707 | 3794  | 0.084                | 38.3  | 1575  | 1488     | 4.74  | 5.73          | 0.733     | 0.185     | 0.073    | 0.000 | 0.009 |
| 2708 | 3539  | 0.097                | 36.3  | 1296  | 1184     | 4.88  | 6.86          | 0.731     | 0.188     | 0.077    | 0.000 | 0.004 |
| 2709 | 3555  | 0.091                | 34.7  | 1313  | 1200     | 4.87  | 6.43          | 0.731     | 0.188     | 0.077    | 0.000 | 0.004 |
| 2710 | 3400  | 0.095                | 31.7  | 1161  | 1035     | 4.96  | 6.86          | 0.731     | 0.189     | 0.078    | 0.000 | 0.002 |
| 2711 | 3402  | 0.095                | 31.9  | 1162  | 1036     | 4.96  | 6.88          | 0.731     | 0.189     | 0.078    | 0.000 | 0.002 |
| 2712 | 3409  | 0.088                | 29.7  | 1172  | 1044     | 4.95  | 6.34          | 0.731     | 0.188     | 0.078    | 0.000 | 0.003 |
| 2714 | 3879  | 0.108                | 51.8  | 1649  | 1590     | 4.74  | 7.33          | 0.733     | 0.187     | 0.073    | 0.000 | 0.007 |
| 2715 | 4044  | 0.102                | 54.5  | 1842  | 1799     | 4.66  | 6.63          | 0.733     | 0.183     | 0.073    | 0.000 | 0.011 |
| 2716 | 4100  | 0.099                | 55.2  | 1913  | 1874     | 4.63  | 6.37          | 0.733     | 0.181     | 0.072    | 0.000 | 0.013 |
| 2717 | 4071  | 0.102                | 56.0  | 1875  | 1835     | 4.65  | 6.64          | 0.733     | 0.182     | 0.073    | 0.000 | 0.012 |

Table A.30: Double Point Edge Conditions - Dev 1 CO<sub>2</sub>

| Shot | $U_E$ | $\rho_E$             | $P_E$ | $T_E$ | $T_{VE}$ | $M_E$ | $Re_E^{Unit}$ | $y_{CO_2}$ | $y_{O_2}$ | $y_{CO}$ | $y_C$ | $y_O$ |
|------|-------|----------------------|-------|-------|----------|-------|---------------|------------|-----------|----------|-------|-------|
|      | (m/s) | (kg/m <sup>3</sup> ) | (kPa) | (K)   | (K)      | (-)   | (1/m)         | (-)        | (-)       | (-)      | (-)   | (-)   |
| 2713 | 3008  | 0.099                | 39.1  | 1834  | 1834     | 4.04  | 5.36          | 0.718      | 0.100     | 0.179    | 0.000 | 0.002 |

Table A.31: Double Point Edge Conditions - Dev 2 Air

| Shot | $U_E$ | $\rho_E$             | $P_E$ | $T_E$ | $T_{VE}$ | $M_E$ | $Re_E^{Unit}$ | $y_{N_2}$ | $y_{O_2}$ | $y_{NO}$ | $y_N$ | $y_O$ |
|------|-------|----------------------|-------|-------|----------|-------|---------------|-----------|-----------|----------|-------|-------|
|      | (m/s) | (kg/m <sup>3</sup> ) | (kPa) | (K)   | (K)      | (-)   | (1/m)         | (-)       | (-)       | (-)      | (-)   | (-)   |
| 2718 | 3989  | 0.107                | 55.6  | 1779  | 1734     | 4.68  | 7.09          | 0.733     | 0.184     | 0.073    | 0.000 | 0.010 |
| 2721 | 4014  | 0.088                | 46.7  | 1819  | 1764     | 4.65  | 5.75          | 0.733     | 0.181     | 0.073    | 0.000 | 0.013 |
| 2739 | 3589  | 0.103                | 39.7  | 1339  | 1236     | 4.87  | 7.21          | 0.731     | 0.188     | 0.076    | 0.000 | 0.004 |
| 2740 | 3592  | 0.108                | 42.0  | 1344  | 1245     | 4.87  | 7.58          | 0.731     | 0.189     | 0.076    | 0.000 | 0.004 |
| 2741 | 3661  | 0.104                | 42.7  | 1423  | 1331     | 4.82  | 7.18          | 0.732     | 0.188     | 0.075    | 0.000 | 0.005 |
| 2742 | 3718  | 0.098                | 42.2  | 1482  | 1393     | 4.79  | 6.79          | 0.733     | 0.188     | 0.074    | 0.000 | 0.006 |
| 2743 | 3799  | 0.095                | 43.5  | 1575  | 1497     | 4.75  | 6.52          | 0.733     | 0.187     | 0.073    | 0.000 | 0.007 |
| 2744 | 3537  | 0.118                | 43.7  | 1285  | 1182     | 4.91  | 8.37          | 0.731     | 0.189     | 0.077    | 0.000 | 0.003 |
| 2746 | 3477  | 0.124                | 43.7  | 1222  | 1115     | 4.95  | 8.90          | 0.731     | 0.189     | 0.078    | 0.000 | 0.002 |
| 2752 | 3761  | 0.106                | 46.8  | 1522  | 1446     | 4.78  | 7.34          | 0.733     | 0.188     | 0.073    | 0.000 | 0.006 |
| 2753 | 3717  | 0.092                | 39.7  | 1489  | 1398     | 4.78  | 6.35          | 0.733     | 0.187     | 0.074    | 0.000 | 0.006 |
| 2755 | 3760  | 0.098                | 43.4  | 1528  | 1447     | 4.77  | 6.75          | 0.733     | 0.187     | 0.073    | 0.000 | 0.007 |
| 2757 | 3956  | 0.095                | 48.6  | 1755  | 1698     | 4.67  | 6.29          | 0.733     | 0.183     | 0.073    | 0.000 | 0.011 |

Table A.32: Double Point Edge Conditions - Dev 2 CO<sub>2</sub>

| Shot | $U_E$ | $\rho_E$             | $P_E$ | $T_E$ | $T_{vE}$ | $M_E$ | $Re_E^{Unit}$ | $y_{CO_2}$ | $y_{O_2}$ | $y_{CO}$ | $y_C$ | $y_O$ |
|------|-------|----------------------|-------|-------|----------|-------|---------------|------------|-----------|----------|-------|-------|
|      | (m/s) | (kg/m <sup>3</sup> ) | (kPa) | (K)   | (K)      | (-)   | (1/m)         | (-)        | (-)       | (-)      | (-)   | (-)   |
| 2719 | 2952  | 0.130                | 49.8  | 1808  | 1808     | 4.03  | 7.07          | 0.764      | 0.085     | 0.150    | 0.000 | 0.001 |
| 2720 | 3232  | 0.147                | 69.1  | 2138  | 2138     | 3.98  | 7.59          | 0.676      | 0.115     | 0.206    | 0.000 | 0.003 |
| 2722 | 3112  | 0.162                | 69.9  | 2011  | 2011     | 4.00  | 8.50          | 0.728      | 0.098     | 0.173    | 0.000 | 0.002 |
| 2723 | 3000  | 0.155                | 61.7  | 1879  | 1879     | 4.02  | 8.33          | 0.763      | 0.085     | 0.151    | 0.000 | 0.001 |
| 2724 | 2988  | 0.153                | 60.3  | 1865  | 1865     | 4.02  | 8.23          | 0.766      | 0.084     | 0.149    | 0.000 | 0.001 |
| 2725 | 2985  | 0.166                | 65.0  | 1865  | 1865     | 4.03  | 8.91          | 0.775      | 0.081     | 0.143    | 0.000 | 0.001 |
| 2726 | 2904  | 0.177                | 65.4  | 1780  | 1780     | 4.04  | 9.65          | 0.806      | 0.070     | 0.123    | 0.000 | 0.000 |
| 2727 | 2822  | 0.184                | 63.9  | 1690  | 1690     | 4.05  | 10.20         | 0.831      | 0.061     | 0.108    | 0.000 | 0.000 |
| 2733 | 2869  | 0.177                | 63.8  | 1742  | 1742     | 4.04  | 9.72          | 0.816      | 0.067     | 0.117    | 0.000 | 0.000 |
| 2734 | 2710  | 0.190                | 59.8  | 1555  | 1555     | 4.08  | 10.79         | 0.858      | 0.052     | 0.090    | 0.000 | 0.000 |
| 2745 | 3233  | 0.144                | 68.0  | 2137  | 2137     | 3.98  | 7.47          | 0.674      | 0.116     | 0.208    | 0.000 | 0.003 |
| 2747 | 3194  | 0.153                | 70.3  | 2102  | 2102     | 3.98  | 7.95          | 0.693      | 0.109     | 0.196    | 0.000 | 0.002 |
| 2751 | 3152  | 0.157                | 69.9  | 2056  | 2056     | 3.99  | 8.20          | 0.710      | 0.104     | 0.185    | 0.000 | 0.002 |
| 2754 | 3191  | 0.134                | 61.3  | 2076  | 2076     | 3.99  | 7.03          | 0.681      | 0.113     | 0.203    | 0.000 | 0.003 |
| 2756 | 3107  | 0.154                | 66.2  | 2000  | 2000     | 4.00  | 8.10          | 0.724      | 0.099     | 0.176    | 0.000 | 0.002 |

Table A.33: Double Point Edge Conditions - Air

| Shot | $U_E$ | $\rho_E$             | $P_E$ | $T_E$ | $T_{vE}$ | $M_E$ | $Re_E^{Unit}$ | $y_{N_2}$ | $y_{O_2}$ | $y_{NO}$ | $y_N$ | $y_O$ |
|------|-------|----------------------|-------|-------|----------|-------|---------------|-----------|-----------|----------|-------|-------|
|      | (m/s) | (kg/m <sup>3</sup> ) | (kPa) | (K)   | (K)      | (-)   | (1/m)         | (-)       | (-)       | (-)      | (-)   | (-)   |
| 2761 | 3058  | 0.061                | 14.6  | 828   | 726      | 5.29  | 4.86          | 0.732     | 0.192     | 0.075    | 0.000 | 0.001 |
| 2762 | 3172  | 0.061                | 16.8  | 952   | 815      | 5.11  | 4.64          | 0.731     | 0.190     | 0.077    | 0.000 | 0.002 |
| 2763 | 3286  | 0.059                | 18.3  | 1068  | 922      | 5.00  | 4.37          | 0.731     | 0.188     | 0.078    | 0.000 | 0.003 |
| 2764 | 2982  | 0.037                | 8.3   | 776   | 725      | 5.33  | 2.99          | 0.733     | 0.191     | 0.074    | 0.000 | 0.002 |
| 2765 | 3248  | 0.038                | 11.5  | 1039  | 900      | 5.00  | 2.82          | 0.731     | 0.186     | 0.078    | 0.000 | 0.006 |
| 2766 | 3464  | 0.033                | 12.1  | 1248  | 1095     | 4.85  | 2.36          | 0.731     | 0.180     | 0.078    | 0.000 | 0.012 |
| 2767 | 3728  | 0.029                | 12.7  | 1505  | 1343     | 4.72  | 1.98          | 0.733     | 0.169     | 0.073    | 0.000 | 0.025 |
| 2768 | 3799  | 0.043                | 19.9  | 1593  | 1457     | 4.69  | 2.89          | 0.733     | 0.174     | 0.073    | 0.000 | 0.020 |
| 2769 | 4032  | 0.091                | 48.9  | 1841  | 1790     | 4.65  | 5.93          | 0.733     | 0.181     | 0.073    | 0.000 | 0.013 |
| 2770 | 4132  | 0.085                | 48.8  | 1964  | 1919     | 4.60  | 5.40          | 0.734     | 0.178     | 0.072    | 0.000 | 0.017 |
| 2771 | 4040  | 0.091                | 49.0  | 1851  | 1801     | 4.64  | 5.90          | 0.733     | 0.181     | 0.073    | 0.000 | 0.013 |
| 2786 | 3959  | 0.083                | 42.4  | 1754  | 1687     | 4.67  | 5.49          | 0.733     | 0.182     | 0.073    | 0.000 | 0.013 |
| 2787 | 4062  | 0.079                | 43.2  | 1878  | 1819     | 4.63  | 5.08          | 0.733     | 0.178     | 0.072    | 0.000 | 0.016 |
| 2788 | 4425  | 0.067                | 46.1  | 2322  | 2281     | 4.49  | 4.03          | 0.737     | 0.164     | 0.065    | 0.000 | 0.034 |
| 2789 | 4244  | 0.076                | 47.1  | 2105  | 2062     | 4.55  | 4.73          | 0.735     | 0.173     | 0.070    | 0.000 | 0.023 |
| 2790 | 4199  | 0.079                | 47.3  | 2046  | 2001     | 4.57  | 4.94          | 0.734     | 0.175     | 0.071    | 0.000 | 0.021 |

Table A.34: Double Point Edge Conditions - N<sub>2</sub>

| Shot | $U_E$ | $\rho_E$             | $P_E$ | $T_E$ | $T_{vE}$ | $M_E$ | $Re_E^{Unit}$ | $y_{N_2}$ | $y_N$ |
|------|-------|----------------------|-------|-------|----------|-------|---------------|-----------|-------|
|      | (m/s) | (kg/m <sup>3</sup> ) | (kPa) | (K)   | (K)      | (-)   | (1/m)         | (-)       | (-)   |
| 2772 | 3665  | 0.021                | 5.4   | 876   | 3012     | 6.07  | 1.98          | 0.998     | 0.002 |
| 2773 | 3859  | 0.020                | 6.0   | 1014  | 3136     | 5.93  | 1.83          | 0.996     | 0.004 |
| 2774 | 4054  | 0.020                | 6.9   | 1183  | 3303     | 5.76  | 1.72          | 0.993     | 0.007 |
| 2775 | 3511  | 0.023                | 5.4   | 781   | 2924     | 6.16  | 2.25          | 0.999     | 0.001 |
| 2776 | 3525  | 0.060                | 14.1  | 790   | 2564     | 6.15  | 5.82          | 1.000     | 0.000 |
| 2777 | 3864  | 0.045                | 13.6  | 1023  | 2873     | 5.92  | 4.08          | 0.999     | 0.001 |
| 2778 | 4194  | 0.050                | 20.3  | 1373  | 3082     | 5.54  | 4.15          | 0.997     | 0.003 |
| 2779 | 4389  | 0.050                | 24.4  | 1630  | 3200     | 5.32  | 4.03          | 0.995     | 0.005 |
| 2780 | 4624  | 0.049                | 28.7  | 1959  | 3300     | 5.10  | 3.61          | 0.992     | 0.008 |
| 2781 | 4793  | 0.045                | 29.8  | 2222  | 3360     | 4.95  | 3.11          | 0.987     | 0.013 |
| 2782 | 4792  | 0.056                | 37.1  | 2233  | 3252     | 4.95  | 3.85          | 0.991     | 0.009 |
| 2783 | 4917  | 0.052                | 38.1  | 2446  | 3263     | 4.84  | 3.44          | 0.987     | 0.013 |
| 2784 | 4953  | 0.057                | 42.8  | 2498  | 3202     | 4.82  | 3.76          | 0.988     | 0.012 |
| 2785 | 4961  | 0.058                | 43.9  | 2520  | 3189     | 4.81  | 3.80          | 0.988     | 0.012 |

Table A.35: Double Point Edge Conditions - CO<sub>2</sub>

| Shot | $U_E$ | $\rho_E$             | $P_E$ | $T_E$ | $T_{vE}$ | $M_E$ | $Re_E^{Unit}$ | $y_{CO_2}$ | $y_{O_2}$ | $y_{CO}$ | $y_C$ | $y_O$ |
|------|-------|----------------------|-------|-------|----------|-------|---------------|------------|-----------|----------|-------|-------|
|      | (m/s) | (kg/m <sup>3</sup> ) | (kPa) | (K)   | (K)      | (-)   | (1/m)         | (-)        | (-)       | (-)      | (-)   | (-)   |
| 2791 | 3045  | 0.047                | 18.5  | 1727  | 1727     | 4.12  | 2.69          | 0.633      | 0.128     | 0.234    | 0.000 | 0.005 |
| 2792 | 2745  | 0.060                | 19.1  | 1502  | 1502     | 4.11  | 3.48          | 0.758      | 0.087     | 0.154    | 0.000 | 0.001 |
| 2793 | 2398  | 0.098                | 24.0  | 1227  | 1227     | 4.11  | 5.97          | 0.898      | 0.037     | 0.065    | 0.000 | 0.000 |
| 2794 | 2512  | 0.091                | 24.3  | 1327  | 1327     | 4.10  | 5.39          | 0.861      | 0.050     | 0.088    | 0.000 | 0.000 |
| 2795 | 2549  | 0.086                | 23.6  | 1356  | 1356     | 4.10  | 5.07          | 0.847      | 0.055     | 0.097    | 0.000 | 0.000 |
| 2796 | 2518  | 0.090                | 24.2  | 1331  | 1331     | 4.10  | 5.34          | 0.859      | 0.051     | 0.090    | 0.000 | 0.000 |

## Appendix B

# Probe-Volume Locations and Boundary-Layer Thicknesses

$s_U$  is the distance from the cone tip to the upstream probe volume;  $n_U$  is the wall-normal distance of the upstream probe volume;  $\delta_U$  is the calculated boundary-layer thickness<sup>1</sup> at the upstream probe volume;  $s_D$  is the distance from the cone tip to the downstream probe volume;  $n_D$  is the wall-normal distance of the downstream probe volume;  $\delta_D$  is the calculated boundary-layer thickness at the upstream probe volume.

Table B.1: Probe Volume Locations and Boundary Layer Thicknesses.

| Shot | $s_U$ | $n_U$  | $\delta_U$        | $n_U/\delta_U$    | $s_D$ | $n_D$ | $\delta_D$ | $n_D/\delta_D$    |                   |     |
|------|-------|--------|-------------------|-------------------|-------|-------|------------|-------------------|-------------------|-----|
|      | (mm)  | (thou) | ( $\mu\text{m}$ ) | ( $\mu\text{m}$ ) | (-)   | (mm)  | (thou)     | ( $\mu\text{m}$ ) | ( $\mu\text{m}$ ) | (-) |
| 2695 | 665   | 25     | 635               | 1040              | 0.61  | -     | -          | -                 | -                 | -   |
| 2696 | 665   | 25     | 635               | 1078              | 0.59  | -     | -          | -                 | -                 | -   |
| 2697 | 665   | 25     | 635               | 1107              | 0.57  | -     | -          | -                 | -                 | -   |
| 2698 | 665   | 30     | 762               | 1103              | 0.69  | -     | -          | -                 | -                 | -   |
| 2699 | 665   | 32     | 813               | 1097              | 0.74  | -     | -          | -                 | -                 | -   |
| 2700 | 665   | 22     | 559               | 1365              | 0.41  | -     | -          | -                 | -                 | -   |
| 2701 | 665   | 22     | 559               | 1126              | 0.50  | -     | -          | -                 | -                 | -   |

*Continued on next page*

<sup>1</sup>In this work,  $\delta$  refers to  $\delta_{99}$ , where the local velocity in the boundary layer is 99% of the velocity at the boundary-layer edge.

Table B.1 – *Continued from previous page*

| Shot | $s_U$ | $n_U$  | $\delta_U$        | $n_U/\delta_U$ | $s_D$ | $n_D$  | $\delta_D$        | $n_D/\delta_D$ |      |      |
|------|-------|--------|-------------------|----------------|-------|--------|-------------------|----------------|------|------|
|      | (mm)  | (thou) | ( $\mu\text{m}$ ) | (-)            | (mm)  | (thou) | ( $\mu\text{m}$ ) | (-)            |      |      |
| 2702 | 665   | 25     | 635               | 1107           | 0.57  | -      | -                 | -              | -    |      |
| 2703 | 665   | 25     | 635               | 1126           | 0.56  | -      | -                 | -              | -    |      |
| 2704 | 647   | 25     | 635               | 1091           | 0.58  | 783    | 25                | 635            | 1201 | 0.53 |
| 2705 | 647   | 25     | 635               | 1084           | 0.59  | 783    | 25                | 635            | 1197 | 0.53 |
| 2706 | 647   | 25     | 635               | 1137           | 0.56  | 783    | 25                | 635            | 1255 | 0.51 |
| 2707 | 647   | 25     | 635               | 1124           | 0.57  | 783    | 25                | 635            | 1235 | 0.51 |
| 2708 | 647   | 25     | 635               | 1047           | 0.61  | 783    | 25                | 635            | 1154 | 0.55 |
| 2709 | 647   | 25     | 635               | 1082           | 0.59  | 783    | 25                | 635            | 1197 | 0.53 |
| 2710 | 647   | 25     | 635               | 1066           | 0.60  | 783    | 25                | 635            | 1175 | 0.54 |
| 2711 | 647   | 25     | 635               | 1065           | 0.60  | 783    | 25                | 635            | 1172 | 0.54 |
| 2712 | 647   | 25     | 635               | 1109           | 0.57  | 783    | 25                | 635            | 1224 | 0.52 |
| 2713 | 647   | 25     | 635               | 991            | 0.64  | 783    | 25                | 635            | 1097 | 0.58 |
| 2714 | 647   | 25     | 635               | 985            | 0.64  | 783    | 25                | 635            | 1087 | 0.58 |
| 2715 | 647   | 25     | 635               | 1022           | 0.62  | 783    | 25                | 635            | 1125 | 0.56 |
| 2716 | 647   | 25     | 635               | 1035           | 0.61  | 783    | 25                | 635            | 1146 | 0.55 |
| 2717 | 647   | 25     | 635               | 1019           | 0.62  | 783    | 25                | 635            | 1121 | 0.57 |
| 2739 | 627   | 25     | 635               | 1002           | 0.63  | 718    | 25                | 635            | 1076 | 0.59 |
| 2741 | 627   | 25     | 635               | 994            | 0.64  | 718    | 25                | 635            | 1060 | 0.60 |
| 2742 | 627   | 25     | 635               | 1023           | 0.62  | 718    | 25                | 635            | 1099 | 0.58 |
| 2743 | 627   | 25     | 635               | 1035           | 0.61  | 718    | 25                | 635            | 1106 | 0.57 |
| 2744 | 627   | 25     | 635               | 935            | 0.68  | 718    | 25                | 635            | 998  | 0.64 |
| 2745 | 627   | 25     | 635               | 820            | 0.77  | 718    | 25                | 635            | 876  | 0.72 |
| 2751 | 627   | 25     | 635               | 783            | 0.81  | 718    | 25                | 635            | 840  | 0.76 |
| 2752 | 627   | 25     | 635               | 982            | 0.65  | 718    | 25                | 635            | 1054 | 0.60 |
| 2753 | 627   | 25     | 635               | 1053           | 0.60  | 718    | 25                | 635            | 1125 | 0.56 |
| 2754 | 627   | 25     | 635               | 848            | 0.75  | 718    | 25                | 635            | 911  | 0.70 |
| 2757 | 627   | 25     | 635               | 1038           | 0.61  | 718    | 25                | 635            | 1106 | 0.57 |
| 2761 | 627   | 25     | 635               | 1338           | 0.47  | 718    | 25                | 635            | 1425 | 0.45 |
| 2762 | 627   | 36     | 914               | 1320           | 0.69  | 718    | 38                | 965            | 1416 | 0.68 |

*Continued on next page*

Table B.1 – *Continued from previous page*

| Shot | $s_U$ | $n_U$  | $\delta_U$        | $n_U/\delta_U$ | $s_D$ | $n_D$  | $\delta_D$        | $n_D/\delta_D$ |      |      |
|------|-------|--------|-------------------|----------------|-------|--------|-------------------|----------------|------|------|
|      | (mm)  | (thou) | ( $\mu\text{m}$ ) | (-)            | (mm)  | (thou) | ( $\mu\text{m}$ ) | (-)            |      |      |
| 2763 | 627   | 36     | 914               | 1331           | 0.69  | 718    | 38                | 965            | 1422 | 0.68 |
| 2764 | 627   | 36     | 914               | 1723           | 0.53  | 718    | 38                | 965            | 1844 | 0.52 |
| 2765 | 627   | 36     | 914               | 1668           | 0.55  | 718    | 38                | 965            | 1789 | 0.54 |
| 2766 | 627   | 36     | 914               | 1774           | 0.52  | 718    | 38                | 965            | 1891 | 0.51 |
| 2767 | 627   | 36     | 914               | 1906           | 0.48  | 718    | 38                | 965            | 2039 | 0.47 |
| 2768 | 627   | 21     | 533               | 1561           | 0.34  | 718    | 24                | 610            | 1679 | 0.36 |
| 2769 | 627   | 18     | 457               | 1064           | 0.43  | 718    | 20                | 508            | 1137 | 0.45 |
| 2770 | 627   | 18     | 457               | 1103           | 0.41  | 718    | 20                | 508            | 1178 | 0.43 |
| 2771 | 627   | 18     | 457               | 1065           | 0.43  | 718    | 20                | 508            | 1147 | 0.44 |
| 2772 | 627   | 37     | 940               | 2318           | 0.41  | 718    | 39                | 991            | 2488 | 0.40 |
| 2773 | 627   | 37     | 940               | 2366           | 0.40  | 718    | 39                | 991            | 2534 | 0.39 |
| 2774 | 627   | 37     | 940               | 2366           | 0.40  | 718    | 39                | 991            | 2542 | 0.39 |
| 2775 | 627   | 37     | 940               | 2224           | 0.42  | 718    | 39                | 991            | 2384 | 0.42 |
| 2776 | 627   | 18     | 457               | 1371           | 0.33  | 718    | 22                | 559            | 1477 | 0.38 |
| 2777 | 627   | 18     | 457               | 1574           | 0.29  | 718    | 22                | 559            | 1684 | 0.33 |
| 2778 | 627   | 18     | 457               | 1481           | 0.31  | 718    | 22                | 559            | 1580 | 0.35 |
| 2779 | 627   | 18     | 457               | 1464           | 0.31  | 718    | 22                | 559            | 1574 | 0.35 |
| 2780 | 627   | 18     | 457               | 1483           | 0.31  | 718    | 22                | 559            | 1585 | 0.35 |
| 2781 | 627   | 18     | 457               | 1556           | 0.29  | 718    | 22                | 559            | 1667 | 0.34 |
| 2782 | 627   | 18     | 457               | 1395           | 0.33  | 718    | 22                | 559            | 1491 | 0.37 |
| 2783 | 627   | 18     | 457               | 1439           | 0.32  | 718    | 22                | 559            | 1543 | 0.36 |
| 2784 | 627   | 18     | 457               | 1371           | 0.33  | 718    | 22                | 559            | 1477 | 0.38 |
| 2785 | 627   | 18     | 457               | 1362           | 0.34  | 718    | 22                | 559            | 1452 | 0.38 |
| 2786 | 627   | 18     | 457               | 1113           | 0.41  | 718    | 22                | 559            | 1196 | 0.47 |
| 2787 | 627   | 18     | 457               | 1142           | 0.40  | 718    | 22                | 559            | 1222 | 0.46 |
| 2788 | 627   | 18     | 457               | 1252           | 0.37  | 718    | 22                | 559            | 1337 | 0.42 |
| 2789 | 627   | 18     | 457               | 1166           | 0.39  | 718    | 22                | 559            | 1248 | 0.45 |
| 2790 | 627   | 18     | 457               | 1142           | 0.40  | 718    | 22                | 559            | 1224 | 0.46 |

# Appendix C

## Test-Section Vibration

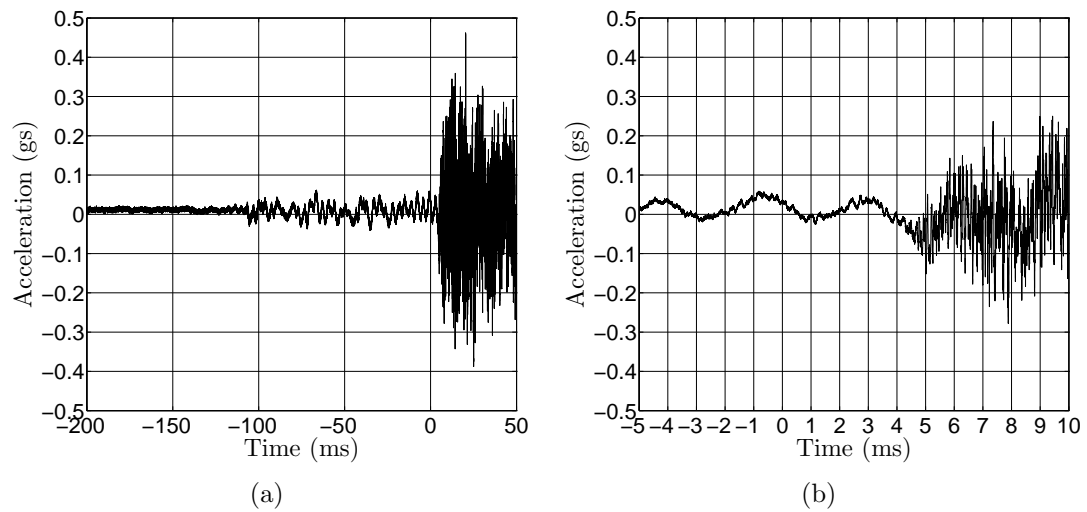


Figure C.1: Shot 2678. Test section vibration as measured by a PCB353b18 accelerometer, with a PCB483 signal conditioner. The accelerometer was placed on the breadboard that is fixed to the south side of the test-section, and is oriented in the vertical direction.